

**MAGNETIZATION DYNAMICS IN MATERIALS WITH HIGH
MAGNETIC ANISOTROPY**

Thesis submitted for the degree of
Doctor of Philosophy (Science)

in

Physics (Experimental)

by

Semanti Pal

Department of Physics

University of Calcutta

2014

To my loving family and mentor.....

Abstract

This thesis focuses on the investigation of the magnetization processes of magnetic materials with high magnetic anisotropies over various timescales from femto and picoseconds to quasistatic processes. The quasistatic magnetic properties are measured by the vibrating sample magnetometer (VSM) and static magneto-optical Kerr effect (static MOKE) magnetometer. The ultrafast magnetization dynamics is measured by a custom-built time-resolved MOKE (TR-MOKE) microscope. The experimental results are modeled by the solution of the Landau-Lifshitz-Gilbert (LLG) equation under the frameworks of the macrospin formalism, discrete dipole approximation method, plane wave method and micromagnetic simulations. We have investigated the effects of varying Co layer thickness in Co/Pd multilayers on PMA and the corresponding precession frequency and Gilbert damping and established a correlation between the PMA and damping. When these multilayers are patterned to form antidot lattices, the magnetization dynamics changes significantly due to the presence of shell modes at the boundaries of the holes where a regular multilayer structure is destroyed due to the gallium ion bombardment during the fabrication. We have further studied the standing spin-wave spectra in the Co/Pt multilayers with varying Co layer thickness and varying no. of bilayer repeats. The bulk and surface spin-wave modes and their dependences on the magnetic environments at various surface and interface are investigated. In the FePt/NiFe exchange spring samples, the effect of the spin-twist structures on the dynamic magnetic properties is investigated thoroughly. Starting from the magnetization dynamics of single ferromagnets of varying aspect ratio, we have also studied the quasistatic and ultrafast magnetization dynamics of ferromagnetic nanowire arrays with varying aspect ratios. The competition between magnetocrystalline and shape anisotropies in magnetic nanowires and the corresponding effects on the quasistatic magnetization reversal mechanisms is investigated thoroughly.

List of publications

This thesis is based upon the following publications and manuscripts:

1. Tunable magnonic frequency and damping in $[\text{Co}/\text{Pd}]_8$ multilayers with variable Co layer thickness

S. Pal, B. Rana, O. Hellwig, T. Thomson, and A. Barman

Appl. Phys. Lett. **98**, 082501 (2011)

2. Correlation between perpendicular magnetic anisotropy and Gilbert damping in $[\text{Co}/\text{Pd}]_8$ multilayers with variable Co layer thickness

S. Pal, B. Rana, O. Hellwig, T. Thomson, and A. Barman

Allied Publishers, New Delhi, India (2011)

3. Magnetization reversal dynamics in Co nanowires with competing magnetic anisotropies

S. Pal, S. Saha, D. Polley, and A. Barman

Solid State Commun. **151**, 1994 (2011)

4. Time-resolved measurement of spin-wave spectra in CoO capped $[\text{Co}(t)/\text{Pt}(7\text{\AA})]_{n-1}$ Co(t) multilayer systems

S. Pal, B. Rana, S. Saha, R. Mandal, O. Hellwig, J. Romero-Vivas, S. Mamica, J. W. Klos, M. Mruczkiewicz, M. L. Sokolovskyy, M. Krawczyk, and A. Barman

J. Appl. Phys. **111**, 07C507 (2012)

5. Effect of spin-twist structure on the spin-wave dynamics of the $\text{Fe}_{55}\text{Pt}_{45}/\text{Ni}_{80}\text{Fe}_{20}$ exchange-coupled bi-layers with varying $\text{Ni}_{80}\text{Fe}_{20}$ thickness

S. Pal, S. Barman, O. Hellwig, and A. Barman

J. Appl. Phys. **115**, 17D105 (2014)

6. Optically induced spin-wave dynamics in [Co/Pd]₈ antidot lattices with perpendicular magnetic anisotropy

S. Pal, P. Gruszecki, J. W. Klos, K. Das, O. Hellwig, M. Krawczyk, and A. Barman

(Submitted)

7. All optical excitation and detection of spin-waves in ferromagnetic nanowires with high aspect ratio

S. Pal, S. Saha, M.V. Kamalakar, and A. Barman

(Manuscript to be submitted)

The following publications are not included in the thesis:

1. Magnetization reversal dynamics in clusters of Ni nanoparticles

B. Rana, M. Agrawal, **S. Pal**, and A. Barman

J. Appl. Phys. **107**, 09B513 (2010)

2. Micromagnetic study of size-dependent picosecond dynamics in single nanomagnets

S. Pal, D. Kumar, and A. Barman

J. Phys. D: Appl. Phys. **44**,105002 (2011)

3. All-optical excitation and detection of collective picosecond dynamics of ordered arrays of nanomagnets with varying areal density

B. Rana, **S. Pal**, S. Barman, Y. Fukuma, Y. Otani, and A. Barman

Appl. Phys. Express **4**, 113003 (2011)

4. Detection of picosecond magnetization dynamics of 50 nm magnetic dots down to the single dot regime

B. Rana, D. Kumar, S. Barman, **S. Pal**, Y. Fukuma, Y. Otani, and A. Barman

ACS Nano **5**, 9559 (2011)

5. Anisotropy in collective precessional dynamics in arrays of Ni₈₀Fe₂₀ nanoelements

B. Rana, D. Kumar, S. Barman, **S. Pal**, R. Mandal, Y. Fukuma, Y. Otani, and A. Barman

J. Appl. Phys. **111**, 07D503 (2012)

6. Optically induced tunable magnetization dynamics in nanoscale Co antidot lattices

R. Mandal, S. Saha, D. Kumar, S. Barman, **S. Pal**, K. Das, A. K. Raychaudhuri, Y. Fukuma, Y. Otani, and A. Barman

ACS Nano **6**, 3397 (2012)

7. Local control of magnetic damping in ferromagnetic/non-magnetic bilayers by interfacial intermixing induced by focused ion-beam irradiation

J. A. King, A. Ganguly, D.M. Burn, **S. Pal**, E.A. Sallabank, T.P.A. Hase, A.T. Hindmarch, A. Barman, and D. Atkinson

Appl. Phys. Lett. **104**, 242410 (2014)

Acknowledgements

There are several individuals and groups, without whose support, this work would have never been completed. First and foremost, I would like to thank Prof. Anjan Barman, my Ph.D. supervisor, for all of the guidance he has given to me during all these years, above and beyond the call of duty. I started working with him with zero experimental and a very little theoretical knowledge on this field of research. I am sincerely thankful to him for the patience he showed in repeatedly teaching every experimental and computational tools including even the simplest PowerPoint presentations, explaining concepts and phenomena from different aspects and for always making time for me in his busy schedule. He showed me how to build a lab comprising of extremely sophisticated experimental equipments from few empty rooms and how to maintain a healthy and friendly lab environment. He gave me the opportunity to have multiple exchange visits to very good labs and to attend very useful national and international conferences. I have learned a tremendous amount from him which will help me not only in my professional life, but in my personal life too.

I gratefully acknowledge the unconditional love, support, guidance, encouragement and sense of humor of my parents and sister that kept me going through all those frustrating days of data analysis. They had to sacrifice a lot and even I could spend a very little time with them during the course my Ph.D. but they never complained. They are the biggest strength of mine. I am indebted to Dr. Bitasta Chanda for her constant guidance since my 10th standard. She is the best teacher cum friend in this world and I am very fortunate to have her in my life. I am thankful to Nitish for his support throughout my works.

Dr. Saswati Barman taught me the LLG Micromagnetic Simulator and helped a lot in the simulation works. I always thank her for her moral support during the Ph.D. days. My thesis would have never been completed without the help of Dr. Maciej Krawczyk. Working with such a nice person like him is an experience I shall cherish forever. I would like to thank him for all his support during the analyses of my works. Discussions with him have always been very helpful for me. Special thanks to Dr. Olav Hellwig and Dr. M. V. Kamalakar for providing with high quality samples for my works. I would like to thank Dr. Matteo Franchin for helping me with MayaVI and NMAG softwares. Dr. Gianluca Gubbiotti gave me

an opportunity to visit his lab. During that short visit, discussions with him helped me to have better understanding of my works.

I would like to specially acknowledge Bivas, my labmate, who always helped me a lot to learn the experimental techniques. After my mentor, he is the person, from whom I learnt lab attitudes. My labmate Dheeraj helped me in the numerical analysis of the experimental results. However, beyond all the academic help, I would like to specially thank him for standing by me through all the ups and downs. Milan gave me useful experimental tips during his short stay in our group. I am thankful to Susmita, Debanjan and Arnab for their support in the experimental works. Above all, thank you Bivas, Dheeraj, Milan, Susmita, Arnab and Debanjan for maintaining the very cheerful and friendly environment in the lab which made life easier during the Ph.D. days. Arabinda Da taught me the formatting of thesis in Microsoft Office Word, without those tips, writing thesis would have been very difficult for me. I would also like to acknowledge the help and support from Kausik, Samiran, Ruma, Chandrima, Bipul, Kallol, Pinaki Da, Sabari Da and Jaivardhan Da. Apart from my labmates, I am thankful to my brothers Animesh, Nirnay, Arghya and a very special friend Raghav for always making me smile and for all the academic help they provided. Debanjan, Arnab and specially Nirnay helped me a lot with the proof correction of this thesis.

Finally, I thank the S. N. Bose National Centre for Basic Sciences for giving me an opportunity to work. Thanks to University Grant Commission for providing me with junior and senior research fellowships. Thanks to various funding agencies including Department of Science and Technology, Government of India under Grant Nos. SR/NM/NS-09/2007, INT/EC/CMS (24/233552) and INT/JP/JST/P-23/09; and Department of Information Technology, Govt. of India under Grant No. 1(7)2010/M & C for the funding towards development of experimental set ups I used during my Ph.D. study.

Semanti Pal

S. N. Bose National Centre for Basic Sciences,
Salt Lake, Kolkata, India.

Preface

Magnetic nanostructures with high anisotropies have inspired technological progress within magnetic data storage, spintronics, magnetic logic and magnonic crystals. Recent development in fabrication technology resulted in the emergence of new synthetic materials with designed high perpendicular magnetic anisotropy (PMA) structures, exchange spring magnets, magnetic nanowires and more recently spin transfer torque MRAM (STT-MRAM). The high speed operation and thermal stability of the above devices demand optimization of various material parameters and understanding and control of magnetization processes at various time-scales.

In this thesis, we have investigated the magnetization processes of magnetic materials with high magnetic anisotropies over various time-scales from femto and picoseconds to quasistatic processes. We studied magnetic materials including Co/Pd and Co/Pt continuous multilayers with varying Co layer thickness and varying no. of bilayer repeats, FePt/NiFe exchange spring magnets with varying NiFe layer thickness, patterned Co/Pd multilayers and magnetic nanowires. The samples are prepared by various techniques including ultra high vacuum magnetron sputtering, lithography and electrodeposition through nanoporous templates. The initial characterizations of the samples are done by the X-ray diffraction (XRD), scanning electron microscopy (SEM) and energy dispersive X-ray (EDX). The interface roughness and thickness of individual layer in multilayers are studied by X-ray reflectivity (XRR) technique and subsequent modeling of the experimental data. The static magnetic properties are measured by the vibrating sample magnetometer (VSM) and static magneto-optical Kerr effect (static MOKE) magnetometer.

The ultrafast magnetization dynamics is measured by a custom-built time-resolved MOKE (TR-MOKE) technique in a two-color optical pump-probe set up developed in our laboratory. The experimental results will be modeled by the solution of the Landau-Lifshitz-Gilbert (LLG) equation under the frameworks of the macrospin formalism, discrete dipole approximation method, plane wave method and micromagnetic simulations. We have investigated the effects of varying Co layer thickness in Co/Pd multilayers on PMA and the corresponding precession frequency and Gilbert damping. As a collective precession of

the whole multilayer stack is observed, macrospin formalism is used to analyze the experimental results. Since both PMA and Gilbert damping have their origins in the spin-orbit coupling, correlation between the two is investigated and a linear correlation is obtained primarily due to the interfacial $d-d$ hybridization. The effects of two-magnon scattering, spin pumping and alloying at the interfaces are investigated on the above phenomena. When these multilayers are patterned to form antidot lattices, the magnetization dynamics changes significantly. The spin-wave spectra depend strongly on the areal density of holes. Due to the gallium ion bombardment during the fabrication of holes in the focused ion beam milling technique, the material properties at the boundary of holes are modified and new shell modes are found in this region. The coupling of these shell modes also gives rise to new modes in these multilayered antidots with PMA. We have further studied the standing spin-wave spectra in the Co/Pt multilayers with varying Co layer thickness and varying no. of bilayer repeats. The experimental results are modeled by the discrete dipole approximation (DDA) method. The bulk and surface spin-wave modes and their dependences on the magnetic environments at various surfaces and interfaces are investigated. Both symmetric and anti-symmetric modes are observed from the calculations of the spin-wave profiles in the out-of-plane direction across the multilayers. In the FePt/NiFe exchange spring samples, the presence of a hard magnetic layer at the bottom of a soft magnetic layer induces a very high anisotropy and pinning of NiFe moments at the interface. At various values and directions of bias magnetic field a spin-twist structure within the NiFe layers may occur, whose nature will depend on the thickness of the NiFe layer. The effect of the spin-twist structures on the dynamic magnetic properties of the NiFe layers is investigated thoroughly. Rich spin-wave spectra are observed; whose frequency shows a strong dependence on the NiFe layer thickness. The important features of the experimental results are reasonably reproduced by micromagnetic simulations. For thinner samples, the magnetization dynamics are found to be primarily governed by the formation of stripe domain in the FePt layer and with increasing thickness of the NiFe layer, the effect of the spin-twist structure within this layer comes into play. As the thickness of NiFe layer increases further, the effect of the spin-twist structure in determining the dynamic mode profile decreases. We have also studied the quasistatic and ultrafast magnetization dynamics on ferromagnetic nanowires with varying

aspect ratios. The competition between magnetocrystalline and shape anisotropies in magnetic nanowires and the corresponding effects on the quasistatic magnetization reversal mechanisms is investigated thoroughly. Finally the precessional dynamics in Ni nanowires arrays is studied. Multiple spin-wave modes are observed. The experimental results are modeled by micromagnetic simulations and the origins of the different spin-wave modes are investigated.

List of abbreviations

AD	: Antidot
ADL	: Antidot lattice
DDA	: Discrete dipole approximation
DW	: Domain-wall
Eqn.	: Equation
ES	: Exchange spring
FFT	: Fast Fourier transform
Fig.	: Figure
FM	: Ferromagnet/Ferromagnetic
LLG	: Landau-Lifshitz-Gilbert
ML	: Multilayer
MO	: Microscope objective
MOKE	: Magneto-optical Kerr effect
MRAM	: Magnetic random-access memory
N. A.	: Numerical aperture
NW	: Nanowire
OBD	: Optical bridge detector
OOMMF	: Object oriented micromagnetic framework
PMA	: Perpendicular magnetic anisotropy

PWM	: Plane wave method
Py	: Permalloy ($\text{Ni}_{80}\text{Fe}_{20}$)
rf	: Radio-frequency
SO	: Spin-orbit
STT	: Spin-transfer torque
TR-MOKE	: Time-resolved magneto-optical Kerr effect

List of symbols

α	: Damping constant
γ	: Gyromagnetic ratio
λ	: Wavelength
τ	: Time constant
ξ	: Spin-orbit interaction energy
K	: Anisotropy
K_{eff}	: Effective anisotropy
M	: Magnetization
M_s	: Saturation magnetization
m	: Unit vector of magnetization
t_{Co}	: Co layer thickness
H	: Magnetic field
H_{eff}	: Effective magnetic field
f	: Frequency
A	: Exchange stiffness constant

List of tables

<u>Table number and caption</u>	<u>Page no.</u>
Table 2.1: Eigen frequencies for some standard shapes.	41
Table 3.1: Different simulator packages.	62
Table 4.1: Chemical composition of the electrolytic solution.	73
Table 4.2: Components of the TR-MOKE magnetometer.	83
Table 6.1: Variation of demagnetization, slow and fast remagnetization times with t_{Co} .	123
Table 7.1: Exchange integrals (J_{Co-Co} , J_{Co-Pt} , J_{Pt-Pt}), magnetic moments (μ_{Co} , μ_{Pt}), anisotropy constants at interfaces ($K_{u,i}$) and average anisotropy fields (H_{ani}) used for calculations of SW spectra in $[Co(tCo)/Pt(7\text{\AA})]_{n-1} Co(tCo)$ MLs.	136
Table 7.2: Anisotropy constants at external surfaces ($K_{u,S1}$, $K_{u,S2}$, $K_{u,S3}$) used for calculations of the SW spectra in $[Co(tCo)/Pt(7\text{\AA})]_n Co(tCo)$ MLs by assuming the same values on both surfaces.	137
Table 9.1: Demagnetizaion, fast and slow remagnetization times for different samples.	160

List of figures

<u>Figure number and caption</u>	<u>Page no.</u>
Fig. 2.1: Co-ordinate system used for a cubic system.	15
Fig. 2.2: Schematic describing Lorentz decomposition method to calculate the dipolar fields on a moment at a position i .	18
Fig. 2.3: Schematic diagram of spin configuration of an FM-AFM bilayer at different stages.	22
Fig. 2.4: Different types of domain-walls - (a) 180° domain-wall, (b) 90° domain-wall and (c) Bloch wall.	26
Fig. 2.5: Illustration of flux closure structure assumed in the ring model.	27
Fig. 2.6: (a) Cylindrical co-ordinate system used. (b)-(d) Various magnetization reversal modes in an infinite cylinder: (b) coherent rotation, (c) curling and (d) buckling.	28
Fig. 2.7: Schematic showing the directions of the applied bias field and the demagnetizing factors in an infinite cylinder with respect to the co-ordinate system used.	29
Fig. 2.8: Hysteresis loops for applied field (a) parallel, (b) perpendicular and (c) at 45° to the long-axis of an elongated particle.	30
Fig. 2.9: Magnetization dynamics at various time-scales.	33
Fig. 2.10: Magnetization precession about the applied bias field (a) without damping and (b) with damping.	34
Fig. 2.11: Co-ordinate systems used for (a) an ellipsoid, (b) a plane and (c) a cylinder.	40

Fig. 2.12: (a) Geometry for the Kerr rotation (θ_k) and Kerr ellipticity (ε_k). (b-d) Different MOKE geometries – (b) Longitudinal MOKE, (c) Transverse MOKE and (d) Polar MOKE. i = incident electric field vector, r = reflected electric field vector, k = induced (due to MOKE effect) orthogonal component in the reflected electric field vector (both in and out of phase to r). 48

Fig. 2.13: The incident light - linearly polarized along the +X direction and propagating along Z direction. 49

Fig. 3.1: Example of a square rod under the DDA model. The rod has a dimension $2La \times 2La \times (N-1)a$, where a is the lattice constant. All the moments in each lattice plane point to the Z direction due to the applied bias field H_0 . M_s is the static magnetization of the sample and $\mathbf{m} = \mathbf{M}/M_s$. The magnetostatic waves are assumed to propagate along the Z direction. 55

Fig. 3.2: Discretization of a sample into (a) cuboidal cells following finite difference method (FDM) and (b) tetrahedral cells following finite element method (FEM). 62

Fig. 4.1: Schematic of the sputtering technique. 70

Fig. 4.2: Arrangement of the electron gun, ion gun and sample in the chamber (a) before and (b) after the evacuation. 71

Fig. 4.3: A typical electrodeposition cell. 72

Fig. 4.4: Nanowire fabrication procedure: (a) gold coating on one face of the template by sputtering. (b) Deposition of metal ions through the pores of the template. (c) Nanowires after dissolution of templates. 74

Fig. 4.5: Schematic diagram of the scanning electron microscope (SEM). 75

Fig. 4.6: Interaction of accelerated electrons with a sample and emission of X-rays is shown schematically. 76

- Fig. 4.7: Schematic diagrams of (a) X-ray diffraction and (b) X-ray diffractometer are shown. 77
- Fig. 4.8: The principle of X-ray reflectivity (XRR). 79
- Fig. 4.9: Schematic diagram of Vibrating Sample Magnetometer (VSM). 80
- Fig. 4.10: (Upper panel) A photograph of the all optical time-resolved magneto-optical Kerr effect (TR-MOKE) microscope in our laboratory in the S. N. Bose national Centre for Basic Sciences. (Lower panel) An enlarged view of the detection procedure. The important components in the set up are labeled in the figures. 82
- Fig. 4.11: (a) Schematic diagram of mode matching between diode laser mode volume and TEM₀₀ mode volume of Millenia. (b) Schematic diagram of Millenia laser head. The figures are reproduced from Ref. [224]. 86
- Fig. 4.12: Absorption and emission spectra of Ti-sapphire crystal. The figure is reproduced from Ref. [222]. 88
- Fig. 4.13: A schematic of the beam path inside the folded cavity of Tsunami. The figure is reproduced from Ref. [222]. 88
- Fig. 4.14: The four prism arrangement used for dispersion compensation in Tsunami laser. 89
- Fig. 4.15: A schematic diagram of the SHG unit and the optical path inside it are shown. The figure is reproduced from Ref. [223]. 90
- Fig. 4.16: A schematic diagram of an all optical time-resolved magneto-optical Kerr effect (TR-MOKE) microscope with collinear pump-probe geometry. 93
- Fig. 4.17: Schematic diagram of the collinear geometry of pump and probe beams focused by a microscope objective (MO) on the sample surface with (a) in-plane and (b) out-of-plane bias field (H) geometry. 95

- Fig. 4.18: Schematic diagram of the optical bridge detector unit is shown. 96
- Fig. 4.19: A typical mode-locked power spectrum of the output beam from Tsunami. 99
- Fig. 4.20: Schematic diagrams of (a) alignment procedure of the retro-reflector, (b) a kinematic mirror mount along with the screws on it and (c-d) alignment procedure of probe beam (c) just after the retro-reflector and (d) after the polarizer. 101
- Fig. 4.21: A schematic diagram showing the alignment procedure of the microscope objective. 104
- Fig. 4.22: The reflectivity signal obtained from a Si(100) wafer as a function of the time delay between the pump and the probe beams. The decay of the reflectivity signal after the zero delay can be fitted with a double exponential decay function to obtain the time constant of the longer decay which is about 220 ps in our case. 106
- Fig. 4.23: A schematic diagram of static magneto-optical Kerr effect (Static MOKE) microscope along with the direction of the applied bias field H . 107
- Fig. 6.1: X-Ray reflectivity data and the extracted thickness and interface roughness values for $[\text{Co}(t_{\text{Co}})/\text{Pd}(0.9\text{nm})]_8$ MLs. 121
- Fig. 6.2: (a) Dependence of magnetic anisotropy field and the saturation magnetization on the Co layer thickness t_{Co} in $[\text{Co}/\text{Pd}]_8$ multilayer films, as measured by static magnetometry. (b) Hysteresis loops from the multilayer samples obtained from polar MOKE measurement. (c) The time-resolved reflectivity and Kerr rotation signals and the corresponding FFT spectra from the multilayer sample with $t_{\text{Co}} = 0.5$ nm, showing the frequencies of phonon and the precession of magnetization, respectively. 122
- Fig. 6.3: (a) The time-resolved Kerr rotation data after background 124

subtraction and (b) the corresponding FFT spectra are shown for $[\text{Co}/\text{Pd}]_8$ films with different Co layer thickness t_{Co} . The solid lines in Fig. 6.3(a) correspond to the fit with eqn. (6.2). The applied bias fields are also shown in the figure.

Fig. 6.4: (a) The bias field dependence of experimental precession frequency (symbols) and the calculated frequencies (solid line) with eqn. (6.1) are shown for multilayers with different Co layer thickness. (b) The geometry for the macrospin model is shown. (c) The damping coefficient α (symbols: experimental data, solid line: linear fit) is plotted as a function of $1/t_{\text{Co}}$. The extracted perpendicular magnetic anisotropy (K_{eff}) and the saturation magnetization M_s (filled squares: from TR-MOKE, open circles: from static magnetometry) are plotted as a function of t_{Co} . The dashed line shows the calculated M_s values, while the dotted line corresponds to the linear fit to K_{eff} vs t_{Co} . 125

Fig. 6.5: The damping coefficient α is plotted as a function of K_{eff} (symbols) and the dotted line corresponds to the linear fit. 127

Fig. 7.1: (a) P-MOKE loops for a series of $[\text{Co}(t_{\text{Co}})/\text{Pt}(7\text{\AA})]_{n-1} \text{Co}(t_{\text{Co}})$ samples. (b) The experimental and fitted X-ray reflectivity results from the multilayer sample with $t_{\text{Co}} = 0.8$ nm. (c) The time-resolved reflectivity and Kerr rotation data and the corresponding FFT spectra are shown for the multilayer with $t_{\text{Co}} = 0.6$ nm at a bias field of 2.47 kOe. 132

Fig. 7.2: Time-resolved Kerr rotation data and the corresponding FFT spectra for $[\text{Co}(t_{\text{Co}})/\text{Pt}(7\text{\AA})]_{n-1} \text{Co}(t_{\text{Co}})$ multilayers with $n \times t_{\text{Co}} = 40 \times 0.2$ nm, 13×0.6 nm and 10×0.8 nm at bias magnetic field $H = 2.47$ kOe. 133

Fig. 7.3: (a) Model structure of the Co/Pt ML film with PMA used in the calculations. The lateral sizes of the ML film are $2000a \times 2000a$, where a is the in-plane lattice constant. Bias magnetic field \mathbf{H} is rotated 10° from the surface normal of the film. The anisotropy constants on surface layers ($K_{\text{u},S1}$, $K_{\text{u},S2}$, 135

$K_{u,S3}$) and at the interfaces ($K_{u,i}$) are different from zero. (b) TR-MOKE relative intensities calculated with the DDA method for the ML with $t_{Co} = 0.6$ nm at $H = 2.47$ kOe. (c) The profiles of SWs with lower frequencies from the spectra shown in (b). Mode number m and corresponding frequency of the mode are listed on the right.

Fig. 7.4: Relative intensities calculated with the DDA method for $[\text{Co}(t_{Co})/\text{Pt}(7\text{\AA})]_{n-1}\text{Co}(t_{Co})$ ML with (a) $t_{Co} = 0.8$ nm ($n = 10$) and asymmetric magnetic anisotropies at surfaces, (b) $t_{Co} = 0.8$ nm with symmetric magnetic anisotropies at surfaces and (c) $t_{Co} = 0.2$ nm ($n = 40$) with symmetric surfaces. The magnetic field assumed in calculations was $H = 2.47$ kOe. 138

Fig. 8.1: (a) ADL fabrication procedure and typical scanning electron micrographs of ADLs with lattice constant $a =$ (i) 500 nm, (ii) 400 nm, (iii) 300 nm and (iv) 200 nm. (b) Measurement geometry. 143

Fig. 8.2: (a) Typical TR-MOKE signal and corresponding SW spectra for ADL with $a = 400$ nm. (b) Areal density dependence of the TR-MOKE signal with the bi-exponential background subtracted and the SW spectra of the ADLs at $\mu_{0H} = 0.084$ T. 145

Fig. 8.3: (a) Dependence of frequency of SW mode on H for continuous Co/Pd ML. The TR-MOKE data (symbol), fit to the Kittel formula (solid line) and the PWM results (dashed line) using the same parameters are shown. (b) Dependence of frequencies of SW modes on H for ADLs with $a = 200$ nm (dots) along with the results from PWM calculations (solid lines) and continuous ML (dashed line). 146

Fig. 8.4: (a) Dependence of the frequency of SWs in ADL on the lattice constant at $\mu_{0H} = 0.084$ T for the bunch of the lowest modes. The horizontal dashed line marks the FMR frequency of the continuous ML. Vertical dashed lines marks the periods investigated experimentally in this chapter. (b) The unit cell of the ADL used in the PWM calculations. (c) Amplitude of the 149

dynamical component of the magnetization vector in ADL for five modes with the lowest frequencies for $a = 200$ nm.

Fig. 8.5. (a) Dependence of the frequency of SW excitations in ADL with shells (ADLS) on the lattice constant at $\mu_{0H} = 0.084$ T. The horizontal dashed line marks the FMR frequency of the continuous ML, the dashed green lines point the two frequencies of the ADL taken from Fig. 8.4(a). The symbols represent frequencies extracted from the TR-MOKE data (Fig. 8.2(b)). Vertical dotted lines marks the periods investigated experimentally in this chapter. (b) The unit cell of the ADLS. (c) and (d) Amplitude of the dynamical component of the magnetization vector in ADLS. The profiles of the few modes with lowest frequencies for $a = 200$ nm and 500 nm are shown. 151

Fig. 8.6: The amplitude of the SW with the lowest frequency (the first mode) in ADLS across the center of the unit cell along x axis for $a = 200, 300$ and 500 nm. The grey area marks the antidot position within the unit cell. 153

Fig. 9.1: Time-resolved Kerr rotation data showing (a) the ultrafast demagnetization for all samples and (b) magnetization precession and corresponding FFT power spectra at a bias field of 1.0 kOe for $S80$. (c) Bias field dependence of mode 1 and the corresponding Kittel fit for $S80$. 159

Fig. 9.2: (a) Experimentally obtained SW spectra for samples with varying $\text{Ni}_{80}\text{Fe}_{20}$ layer thickness t for $H = 1$ kOe, (b) simulated SW modes for bare $\text{Ni}_{80}\text{Fe}_{20}$ films with varying thickness and (c) simulated SW frequencies for $\text{Fe}_{55}\text{Pt}_{45}/\text{Ni}_{80}\text{Fe}_{20}$ bi-layers. Schematics show the directions of the applied bias field (H) and the pulsed field ($h(t)$) as used in the simulations. The intensities of the lower frequency mode in $S10$, lowest and highest frequency modes in $S20$ were magnified 8 times as shown next to those peaks for visual clarity. 161

Fig. 9.3: (a) Simulated static magnetic configurations of bare $\text{Fe}_{55}\text{Pt}_{45}$ thin film ($S0$) and $\text{Fe}_{55}\text{Pt}_{45}/\text{Ni}_{80}\text{Fe}_{20}$ bi-layers with varying $\text{Ni}_{80}\text{Fe}_{20}$ layer thickness ($S10, S20, S50$ and $S80$). Magnified views of parts of $S10$ and $S50$ are shown to 163

elaborate the spin-twist structure inside the $\text{Ni}_{80}\text{Fe}_{20}$ layer. (b) The color map used for Fig. 9.3(a). (c) The effective magnetic field used inside the $\text{Ni}_{80}\text{Fe}_{20}$ layer (as a function of the distance from the $\text{Fe}_{55}\text{Pt}_{45}/\text{Ni}_{80}\text{Fe}_{20}$ interface) in the simulations.

Fig. 9.4: (a) Static magnetic state of the sample *S20* with the black dashed line, along which the internal field distribution is calculated and (b) Internal field distribution at $z = 35$ nm for the sample *S20* under different configurations. 165

Fig. 9.5: Region-wise extraction of precession frequencies from (a) *S0*, (b) *S10*, (c) *S20* and (d) *S80*. The static magnetic states are not in scale for better visual clarity. 167

Fig. 10.1: Scanning electron micrographs of Co NWs with different aspect ratios: (a) 60, (b) 49.5, (c) 18.1, and (d) 6.8. (e) The EDX spectrum and (f) the XRD data obtained from the electrodeposited Co NWs. 173

Fig. 10.2: (a) Experimental and (b) simulated $M-H$ curves of Co NWs with different aspect ratio (R). The red lines correspond to the $M-H$ curves with H applied parallel to the long-axis of the NW and the black lines correspond to the $M-H$ curves with H applied perpendicular to the long-axis of the NW. 175

Fig. 10.3: Vector maps of magnetization reversal in a Co NW with $R = 20$. The magnetic field is applied along (a) the long-axis and (b) the short-axis of the NW. The coordinate system and the color map indicating the direction of the magnetization are shown next to the images. 177

Fig. 10.4: Vector maps of magnetization reversal in a Co NW with $R = 7$. The magnetic field is applied along (a) the long-axis and (b) the short-axis of the NW. The coordinate system and the color map indicating the direction of the magnetization are as shown in Fig. 10.3. 178

Fig. 10.5: Vector maps of magnetization reversal in a Co NW with $R = 2.5$. The magnetic field is applied along (a) the long-axis and (b) the short-axis of the 179

NW. The coordinate system and the color map indicating the direction of the magnetization are as shown in Fig. 10.3.

Fig. 11.1: (a) Hysteresis loops for the Ni nanowire (NW) array along the long and two typical short axes directions. (b) Schematic showing the NW array. The wire axis is along the Z axis and the black arrows show different directions along which the short-axis loops were measured. The direction of the applied bias field H during the TR-MOKE measurements is also shown. (c) Typical time-resolved Kerr ellipticity data from the sample showing ultrafast demagnetization and fast remagnetization at $H = 1.5$ kOe. 185

Fig. 11.2: (a) Typical experimental and simulated spin-wave (SW) spectra for NWs with $d = 35$ nm at $H = 1.0$ kOe. (b) Dependence of the experimental (points) and simulated (lines) SW modes on the bias field H . (c) A right circular cylinder of radius r and length $2nr$. 186

Fig. 11.3: Power and phase distributions of different modes with the view plane in Z vs. X-Y plane for $H = 1.5$ kOe. The color scales for power and phase distributions are shown in the first column of the table. 189

Fig. 11.4: Power and phase distributions of the highest frequency mode for different bias field values. The color scales for power and phase distributions are shown in the first column of the table. 190

Contents

Abstract.....	iii
List of publications	iv
Acknowledgements	vii
Preface.....	ix
List of abbreviations	xii
List of symbols	xiv
List of tables.....	xv
List of figures	xvi
1. Introduction	1
2. Theoretical background.....	11
2.1. Introduction.....	11
2.2. Ferromagnetism.....	11
2.2.1. Classical approach – Curie-Weiss Law	11
2.2.2. Quantum mechanical approach – Exchange interaction	12
2.1.3. Spin-orbit coupling	12
2.3. Anisotropy.....	13
2.3.1. Magnetic anisotropy at macroscopic level.....	13
2.3.2. Magnetic anisotropy at microscopic level - Dipolar interaction	17
2.3.3. Magnetic anisotropy at microscopic level – Spin-orbit coupling.....	19
2.3.4. Perpendicular magnetic anisotropy (PMA).....	20
2.3.5. Exchange anisotropy	21
2.4. Energy terms in ferromagnetic systems.....	23
2.4.1. Zeeman energy.....	23
2.4.2. Magnetostatic energy.....	23

2.4.3.	Exchange energy	24
2.4.4.	Magnetocrystalline anisotropy energy.....	25
2.5.	Magnetic domains and domain-walls.....	25
2.6.	Magnetization reversal and various reversal modes	26
2.6.1.	Coherent rotation of magnetization	29
2.6.2.	Magnetization curling	30
2.6.3.	Magnetization buckling.....	31
2.7.	Magnetization dynamics at various time-scales and the Landau-Lifshitz-Gilbert (LLG) equation.....	32
2.8.	Ultrafast demagnetization.....	35
2.8.1.	The three temperature model.....	35
2.8.2.	Elliott-Yafet (EY)-type of phonon scattering.....	36
2.8.3.	Spin-flip Coulomb scattering.....	37
2.8.4.	Relativistic quantum electrodynamic processes	37
2.8.5.	Laser induced spin-flip	37
2.8.6.	Super-diffusive spin transport.....	38
2.9.	Ferromagnetic resonance and the macrospin model: Kittel formula	39
2.10.	Spin-waves.....	41
2.10.1.	Exchange SWs	43
2.10.2.	Exchange SW in thin films - perpendicular standing spin-wave modes.....	44
2.10.3.	Dipolar SWs	45
2.11.	Magneto-optical Kerr effect (MOKE)	47
2.11.1.	Physical origin	49
2.11.2.	Phenomenological origin.....	50
2.10.3.	Quantum mechanical origin	52

3.	Numerical methods	54
3.1.	Introduction.....	54
3.2.	Discrete dipole approximation (DDA) method	55
3.3.	Plane wave method (PWM)	58
3.4.	Micromagnetic simulations	61
3.5.	Calculations of power and phase profiles of resonant modes	66
4.	Fabrication, synthesis, characterization and measurement techniques	68
4.1.	Introduction.....	68
4.2.	Fabrication	69
4.2.1.	Sputtering	69
4.2.2.	Focused ion beam (FIB) milling	70
4.3.	Synthesis.....	72
4.4.	Characterization techniques	74
4.4.1.	Scanning electron microscopy (SEM)	74
4.4.2.	Energy dispersive X-ray (EDX)	76
4.4.3.	X-ray diffraction (XRD).....	77
4.4.4.	X-ray reflectivity (XRR)	78
4.4.5.	Vibrating sample magnetometer (VSM)	79
4.5.	Measurement techniques	81
4.5.1.	Introduction.....	81
4.5.2.	Time resolved magneto-optical Kerr effect (TR-MOKE) microscope.....	82
4.5.3.	Static magneto-optical Kerr effect microscope (Static MOKE)	107
5.	Literature survey.....	109
5.1.	Introduction.....	109
5.2.	Magnetic multilayers.....	110

5.3. Exchange-spring magnets	113
5.4. Magnetic nanowires	115
6. Correlation between perpendicular magnetic anisotropy and Gilbert damping in [Co/Pd] ₈ multilayers with variable Co layer thickness	119
6.1. Introduction.....	119
6.2. Sample fabrication	120
6.3. Characterization and measurement of quasistatic and ultrafast magnetization dynamics	120
6.4. Results and discussions	121
6.5. Conclusions.....	128
7. Time-resolved measurement of spin-wave spectra in CoO capped [Co(<i>t_{Co}</i>)/Pt(7Å)] _n - ₁ Co(<i>t_{Co}</i>) multilayer systems.....	129
7.1. Introduction.....	129
7.2. Sample fabrication and characterization	130
7.3. Measurements of the quasistatic and ultrafast magnetization dynamics	131
7.4. Results and discussions	132
7.5. Conclusions.....	140
8. Optically induced spin-wave dynamics in [Co/Pd] ₈ antidot lattices with perpendicular magnetic anisotropy	141
8.1. Introduction.....	141
8.2. Sample fabrication	143
8.3. Measurement of ultrafast magnetization dynamics	144
8.4. Results and discussions	144
8.5. Conclusions.....	154
9. Effect of the spin-twist structure on the spin-wave dynamics in Fe ₅₅ Pt ₄₅ /Ni ₈₀ Fe ₂₀ exchange coupled bi-layers with varying Ni ₈₀ Fe ₂₀ thickness.....	156

9.1. Introduction.....	156
9.2. Sample fabrication	157
9.3. Measurement of ultrafast magnetization dynamics	158
9.4. Results and discussions	159
9.5. Conclusions.....	168
10. Magnetization reversal dynamics in Co nanowires with competing magnetic anisotropies.....	170
10.1. Introduction	170
10.2. Sample preparation.....	171
10.3. Characterization and measurement of the quasistatic magnetic properties.....	172
10.4. Results and discussions	172
10.5. Conclusions.....	179
11. All optical excitation and detection of spin-waves in high aspect ratio ferromagnetic nanowires	181
11.1. Introduction	181
11.2. Sample preparation.....	183
11.3. Measurement of quasistatic and ultrafast magnetization dynamics	183
11.4. Results and discussions	184
11.5. Conclusions.....	191
12. Summary and future perspective	192
12.1. Summary.....	192
12.2. Future perspectives.....	196
Bibliography.....	198

1. Introduction

The study of spin-waves (SWs) and active control and manipulation of spin degree of freedom in nanomagnets have become one of the most important topics of research in modern science due to its increasing impact on the present and future technologies [1-3]. Since the invention of hard disks, the technology of magnetic read-write never ceased to evolve. Magnetic data storage offers non-volatility and long term stability of magnetic states. Recent technologies have helped us to investigate and tailor SW excitations in patterned arrays of ordered ferromagnets (FMs), which enhance opportunities in the above fields of research. In the past decade, it has been suggested that SWs may be used to carry and process information. Due to their relatively low speed of propagation as opposed to light, SWs with frequencies in the range of GHz have wavelengths in the nanometer regime, making them an ideal candidate for nanoscale on-chip data communications. This emerging research field is called 'magnonics' and the corresponding artificial crystals are called as the 'magnonic crystals'. The advantage of these devices are non-volatility, faster data processing speed, less power consumption and increased integration densities as compared to the conventional semiconductor devices.

The hard-disk industry has been using longitudinal recording successfully for five decades. However, it is understood that 'superparamagnetism' will interfere with the progress of the hard-disk industry. Superparamagnetism occurs when the microscopic magnetic grains become so tiny that random thermal vibrations at room temperature cause them to lose their magnetic orientations. Though the antiferromagnetically coupled (AFC) media [4-5] helped to achieve higher storage density by obstructing the superparamagnetism effect, eventually, it was found that magnetic materials with high magnetic anisotropies are even superior candidates than the AFC media in this field. As a result, materials with high anisotropy caught significant attention. This magnetic anisotropy can have different origins. It can originate intrinsically from the crystalline structure of the material. Materials such as Co, CoCr, CoPt, CoCrPt have very high magnetocrystalline anisotropy. Specific shapes of the element can also give rise to anisotropies in the systems. For example, in thin films, the plane of the film is the easy axis for magnetization. Again in high aspect ratio

Chapter 1

nanowires, the wire axis is the easy axis of magnetization. For device applications, it is always desirable to have systems with tunable anisotropies. In case of nanowires, the anisotropy can be controlled by controlling the aspect ratio of the nanowire [6]. Now a days, the technology of nanofabrication has achieved unprecedented efficiency in manipulating material structure and properties and helped us to achieve some very important structures with designed high anisotropies: i) structures with high perpendicular magnetic anisotropy (PMA), ii) exchange spring (ES) magnets and iii) magnetic nanowires with varying aspect ratio. The most crucial problem in the application of the high anisotropy materials is that very high field is required to switch the magnetization [7]. To overcome this difficulty, new techniques are being invented. One of them is the thermally assisted recording (TAR) or heat assisted magnetic recording (HAMR) [8]. In this method, low switching field can be achieved by reducing the anisotropy of the material by heating the sample. Recent developments showed that spin-transfer torque (STT) can be used to flip the active elements in magnetic random-access memory (MRAM). STT-MRAM can replace conventional MRAM due to low current requirements, thermal stability and reduced cost. The reduction of its write current density and increase of thermal stability is the basis for current academic research in spin electronics and magnetic multilayers with perpendicular magnetic anisotropy are thought to be ideal candidates for this.

In this thesis, we have studied the magnetization processes over various time-scales ranging from static and quasistatic processes such as equilibrium spin configurations and magnetization reversal to femto and picoseconds processes such as ultrafast demagnetization, remagnetization, magnetization precession and damping of magnetic materials with high magnetic anisotropy. The materials investigated include Co/Pd and Co/Pt continuous multilayers with varying Co layer thickness and varying no. of bilayers repeats, FePt/NiFe ES magnets with varying NiFe layer thickness, patterned Co/Pd multilayers and ferromagnetic nanowires. In this introduction, we shall present a brief review of the research on the static and quasistatic properties of the aforesaid systems. The review of the dynamic properties will be presented in a later chapter.

Chapter 1

The technological progress with magnetic thin film media started to face difficulties in the 1980s due to the polycrystalline nature of the films. The physical properties (especially, the magnetic ones) of these media are strongly dependent on the microstructures of the film such as grain morphology, crystallographic orientation and grain size [9]. Eventually, it was found that instead of single layer thin films, the multilayer (ML) magnetic thin films can enhance device performance significantly due to the larger grain density as well as decreased magnetic exchange coupling between the magnetic layers and the grains in each magnetic layer [10-12]. Due to the very high and tunable anisotropy, the PMA-MLs emerged as potential candidates in storage industry as soon as perpendicular data recording was found to be more efficient than the longitudinal recording [7, 13-14]. After the pioneering work by Néel [15], it was known that surface discontinuities influence the magnetic anisotropies in thin films. Hence in MLs with ultrathin component layers, the interface anisotropy contribution can dominate over the bulk contribution to give a preferential perpendicular orientation of the magnetization. PMA was first observed in Co/Pd MLs [16-17] in 1985. The study was made with fixed Pd layer thickness (t_{Pd}). From VSM measurements, it was found that the ML becomes hard to magnetize in the film plane for Co layer thickness (t_{Co}) $< 12 \text{ \AA}$ and shows perpendicular easy axis of magnetization. The samples were heated to 400°C , which caused alloying and/or mixing at the originally sharp interfaces. As the Co/Pd alloy structures do not exhibit PMA [18], this heating resulted in the in plane easy axis of magnetization for the samples. Hence, it was inferred that rather than the crystalline anisotropy, the surface anisotropy at the Co/Pd interface and the strain in the Co layer is responsible for the PMA. Also, it was observed that the saturation magnetization of the Co/Pd ML structure is significantly higher than the value that could be expected if it was assumed that the magnetic moments reside in the Co layer only. This implies that some magnetic moment gets induced in the Pd layer also due to the ferromagnetic coupling between the Co and Pd electrons. The PMA depends not only on t_{Co} , but on the thickness of the Pd layer (t_{Pd}) also. For $t_{Pd} < 6.7 \text{ \AA}$, no multilayer reflection was observed and hence PMA is not expected [19]. Beyond all the phenomenological explanations, Magnetic Circular X-ray Dichroism (MCXD) study at the Co $L_{2,3}$ and $M_{2,3}$ core edges in Co/Pt ML shows a strongly enhanced perpendicular Co orbital moment and this is believed to drive the PMA in these MLs [20]. The magnetic and magneto-optical properties

Chapter 1

of PMA-MLs are very sensitive to the preparation method and conditions, the sublayer and total film thicknesses. The magnetization reversal studies on Co/Pd MLs by direct observation of domain structure, using a magneto-optic microscope, as well as magnetization viscosity measurement with time, shows that the reversal mechanism depends strongly on t_{Co} . The reversal mechanism was found to change from domain wall motion dominated reversal to nucleation dominated reversal as t_{Co} changes from 2 to 4 Å [21]. This observation was confirmed by Monte-Carlo simulations. Study of magnetization reversal of Co/Pt MLs in ultra-short time-scale reveals the presence of ring domains [22]. The magnetic reversal behavior is quite interesting for CoO capped Co/Pt MLs that are exchange biased perpendicular to the film plane [23]. The nucleation properties of reverse domains in the ascending and descending branches of the hysteresis loops are significantly different for these samples. Another very important property of the PMA-MLs is the observation of antisymmetric magneto-resistance (MR). All popular MRs, such as giant magneto-resistance (GMR) [24-26], tunnelling magneto-resistance (TMR) [27-28], anisotropic magneto-resistance (AMR) [29-33] etc. are symmetric with respect to the magnetic field H . However, in Co/Pt MLs, MR antisymmetric with respect to H can be observed due to the mutual perpendicular orientations of the domain walls, current and the sample magnetization [34].

Antidot lattice (ADL) structures have been proposed as a method for data storage with the recording bits trapped between consecutive holes along the intrinsic hard axis of the magnetic material. To date, most of the works have been concentrated on the magnetic antidot arrays with in-plane anisotropy [35]. However, the shifting of the data storage technology from the longitudinal to the perpendicular recording mode indicates that the ADs can be considered as the potential magnetic recording media only when the anisotropy is perpendicularly oriented [36]. Hence, patterned PMA-MLs have also attracted large attention along with the bit-patterned media and thermally assisted magnetic recording. The study of percolated perpendicular media (PPM) was started since 2006 [36-37]. Fabrication of PPM was attempted by the routes of co-deposition of magnetic materials and non-magnetic oxides [38-39], magnetic films on anodized alumina templates [40-41], deposition of hard magnetic materials on arrays of non-magnetic nanoparticles [42],

Chapter 1

deposition of hard magnetic films on nanoporated membranes fabricated by an organic/inorganic self-assembly process [43-44] and sputtering [45]. It is very important to keep an eye on the surface flatness during the fabrication [45]. It was observed that with increasing areal density of pinning sites, the medium coercivity increases [36]. The intergranular exchange coupling results in a very steep slope in the hysteresis loop. It was observed that if the defect diameters are smaller than the domain wall (DW) width, then no pinning occurs [37]. The exchange coupling constant of the medium significantly influences the medium coercivity and the reversal mechanism [46]. If the value of the exchange coupling constant exceeds a threshold value, then the DWs cannot be pinned using non-magnetic pinning sites. However, the switching time is independent of the damping constant of the PPM. Calculation of energy barrier is also performed to estimate the thermal stability [37, 47]. Study of magnetic properties on antidots based on Co/Pd MLs with varying Co layer thicknesses claims antiferromagnetic coupling to be responsible for the PMA in these structures [48].

On the other hand, ES magnets [49], based on the interfacial exchange coupling of soft and hard FM layers, have emerged as potential candidates for the application in a broad range of fields [50-51]. The term exchange spring refers to the reversible demagnetization curves that are often observed in these structures. Initially, the research on ES systems started in the field of permanent magnets [49]. It was found that if we combine a hard magnet with high coercive field with a soft magnet with high saturation magnetization, the maximum energy product of this exchange coupled system becomes significantly high. This makes these ES systems suitable for permanent magnet application. However, gradually the attention shifted towards its application in the storage industry as the soft magnetic phase can significantly improve the writability of the media without compromising the thermal stability [52]. As a result, GMR effects, magnetization reversal, coercivity tuning and mapping spin configurations become very interesting fields of research. Basically, by controlling the anisotropy direction in the hard layer, one can have parallel or perpendicular ES magnet. However, the shifting of the storage industry from longitudinal to perpendicular recording has encouraged interest in perpendicular ES magnets [53]. The spins in the hard magnet is pinned due to the very high anisotropy. With increasing distance from the interface into the soft layer, the effective exchange coupling decreases

Chapter 1

and the spins in the soft layer forms a characteristic spin-twist structure under the application of an external field. There have been a lot of studies [54-57], both numerical and experimental; to probe this spin-twist structure in the ES magnets as this twisted spin structure influences the sample properties. GMR and AMR effects can be distinctly observed in ES systems [58]. In DyFe₂/YFe₂ ML system, a spin-twist structure can be observed upto 20 Å in the soft YFe₂ layer above a certain bending field. Due to the AMR effect, a dip in the MR near the coercive field of the system is observed when the field was increased from a large negative value. However, when the field is increased beyond the bending field, both magnetization and MR increase significantly. This increase in MR is due to ES induced GMR. Hence, in ES magnets also, the spin-transfer torque may play a role. Magnetization reversal in ES systems [59-65] is a very interesting phenomenon. The thickness of the soft layer plays an important role in coercivity reduction and magnetization reversal in these samples. With the increase of the soft magnetic layer thickness, the system properties changes from that of a rigid magnet to an ES magnet [55]. Accordingly, the magnetization reversal mechanism also changes [60]. Magnetization reversal studies on ES bi-layers with varying soft layer thickness shows that the shapes of the hysteresis loops change systematically as a result of the change in the effective exchange coupling. It is obvious that the soft magnet will switch at a lower field (reversible switching) as compared to the switching field for the hard layer magnetization (irreversible switching). However, interestingly it is observed that contrary to common belief, the reversible twist of the soft layer is not pinned at the soft/hard magnet interface, but penetrates significantly into the hard layer [59]. When the soft magnet is reversed under the influence of a small field, a DW is created at the interface of the hard and soft phases. With increasing field, this DW can propagate through the hard magnet causing magnetization reversal. This phenomenon is called as “DW assisted” reversal. Here, the field required to reverse the magnetization of the hard layer in the bi-layer is lesser than that of bare hard layer. One can also have “microwave assisted reversal” in ES magnets. In this case, microwave is used to induce large amplitude precession to result in magnetization switching by overcoming a metastable state. Since DW is also a metastable state, microwave assisted DW reversal [61] can be induced in ES bi-layers to reduce the switching time significantly.

Chapter 1

The discovery of novel magnetic and transport properties such as conductance and flux quantization [66-67] and GMR [68] in magnetic nanowires (NWs) for dimensions in the nanometer regime led to its potential applications in the fields of magnetic storage, field sensors, logic devices and magnonic crystals and hence triggered large interest in NWs. Densely packed ordered arrays of magnetic NWs with large aspect ratios (R) may overcome the superparamagnetic limit due to the large volumes of the individual NWs and large shape anisotropy along the wire axis, associated with larger areal density. Initially, most of the works were concentrated on the fabrication of NWs under different conditions and investigation of the shape anisotropy. However, gradually the attention shifted to the study of magnetic properties, particularly magnetic hysteresis, reversal mechanism, magnetization dynamics and DWs [69-70]. Magnetization reversal being hysteric, involves metastable energy barriers. As a result, both the static magnetization reversal and dynamic reversal became interesting topics of study [71]. The classical Néel-Brown model for rotation in unison can safely explain the magnetization reversal in single domain particles [72-73]. However, in magnetic wires [74-76] and elongated particles [77-79], inhomogeneous reversal modes like nucleation of reversed domain followed by the propagation of the DW, come into the picture. In these structures, the thickness of the DW (λ_w) is an important parameter. It was suggested theoretically that for a NW with diameter $d < \sqrt{\pi\lambda_w}$, all spins should reverse in unison (coherent rotation). For a NW with diameter $d > \sqrt{\pi\lambda_w}$, the reversal should involve curling mode. In both cases all the spins reverse simultaneously suppressing all the thermal effects in infinitely long wires. However, it was later found that the formation of 2π -DW can lead to a finite energy barrier even in infinite wires. Nucleation of DW was also proposed to be responsible for the magnetization reversal in NWs of finite length. For a NW with diameter $d > \sqrt{\pi\lambda_w}$, even smaller energy barrier results if the nucleation of the π -DW starts at the end of the wire. The activation energy associated with the reversal process was found to be proportional to the wire cross-section and independent of the wire length. Subsequent experimental and theoretical studies also suggest that the reversal in NWs generally starts at the ends or at defects [74, 76, 79-81]. In contrast to Fe and Ni NWs, the presence of two competing anisotropies: i) the

Chapter 1

shape anisotropy along the wire axis and ii) the magnetocrystalline anisotropy (in hcp Co) perpendicular to the wire axis in Co NWs makes the reversal process complicated. Furthermore, when the NWs are placed in an array, the interwire interaction influences both the reversal process and switching field. Magnetization reversal studies by DC-magnetization and micro-SQUID magnetometry reveals that the reversal mechanism of an array of NWs is different from that of the single wire. Deviation from curling mode and pinning of DWs at imperfections was also observed. Magnetic force microscopy measurements on arrays of Fe NWs also support the effect of interwire dipolar interaction in reversal processes [82]. Hysteresis loops of individual wires were found to be rectangular. In an array, each wire is placed in a spatially varying dipolar field of its neighborhood and as a result, the hysteresis loop of the array is significantly broadened. Depending upon the aspect ratio R and d , the ground state changes from single domain state to multidomain state through vortex formation [83].

The high speed of operation and thermal stability of all devices demand optimization of various material parameters and understanding and control of magnetization processes at various time-scales. To be more specific, a thorough understanding of the precessional dynamics is crucial. The magnetization dynamics depends significantly on the magnetic ground state of the system. In continuous and patterned MLs, the dynamics is strongly influenced by the sublayer thicknesses. The exchange coupling between the layers strongly affects the dynamics. Both precession frequency and damping get affected. Depending on the layer thicknesses, single or multiple SW modes can be observed. Also the number of sublayers plays a crucial role in determining the SW modes in the MLs. In case of NWs, the dynamics is significantly affected by the interwire dipolar coupling. The dispersion relation depends strongly on the competition between the shape anisotropy, magnetocrystalline anisotropy and the dipolar interaction. At the same time, the finite width and the periodicity of the wire influence the SW modes in the NW system.

To study these potentially exciting phenomena, the foremost challenge faced is the fabrication of high quality samples. Extremely sophisticated techniques are required to deposit ultrathin multiple layers with sharp interfaces. Presence of a magnetic field affects the growth of a ferromagnetic layer and hence can be used to control the fabrication process. Popular methods for the fabrication of MLs are molecular beam epitaxy (MBE) and

Chapter 1

magnetron sputtering. Magnetic materials exhibit high surface energy because of the partially filled *d*-shells. The growth of the interface of MLs is dominantly governed by the surface and interface energy terms. So it is essential to understand these forces for growing MLs with monolayer level control. A systematic layer-by-layer growth is rare for MLs due to misfit strain energy and the Stranski-Krastanov growth mode *i.e.*, formation of islands is more common. To suppress this island growth, it is required to take the route of non-equilibrium growth at low temperatures [84]. Nanolithography has always been very popular for the fabrication of nanoscale magnetic structures including NWs [85-86]. However, this process is slow, expensive and not suitable for large area production. On the other hand, electrodeposition through nanoporous templates [87] is a very efficient and cost-effective method to produce large aspect ratio NWs at large scales with different diameters, lengths and crystallinity.

To investigate the magnetization dynamics, different techniques in the frequency, wave-vector and time domains were invented. The conventional ferromagnetic resonance (FMR) [88] is a frequency domain technique where the sample is excited at a particular frequency. The external bias field is swept to probe the magnetization dynamics through the resonance. Vector network analyzer based FMR (VNA-FMR) is also a frequency domain technique [89-90] but with very high frequency resolution over a broad band of frequency. Here, the bias field is kept fixed and the excitation frequency is varied from MHz to GHz range to measure the dynamic magnetic response. To incorporate spatial resolution, spatially resolved FMR is also developed [91]. On the other hand, the Brillouin light scattering (BLS) technique [92] has emerged as a very efficient technique to measure the magnetization dynamics in the wave-vector domain. Recent developments of space-resolved and time-resolved BLS techniques have taken the application of BLS to the next level. By BLS technique, a precise measurement of the SW dispersion with wave-vector can be obtained. Pulse inductive microwave magnetometry (PIMM) is a time domain measurement technique. However, the time resolution is limited to tens of picoseconds. The time-resolved magneto-optical Kerr effect (TR-MOKE) [93] microscopy offers very high time resolution along with a spatial resolution in the sub- μm regime. With the time-resolution of the order of sub-hundred femtosecond (limited by the pulse width of the laser), the ultrafast magnetization dynamics can be probed quite efficiently. Further by

Chapter 1

incorporating a scanning microscope with the TR-MOKE, time-resolved scanning Kerr microscopy (TR-SKM) [94-96] was developed to image the time-evolution of spatial distribution of magnetization in confined magnetic elements. Magnetoresistive methods [97] and X-ray [98] microscopy are also showing potentials of achieving very high spatio-temporal resolution.

2. Theoretical background

2.1. Introduction

The invention of magnetic media and recording equipment is the basis of the present day technological revolution. Along with this, the ultrafast optical microscopy has emerged as one of the best techniques to investigate various properties suitable for modern applications of the material under study. As a result, magnetism and ultrafast optical microscopy have become very active and interesting fields of research. Magnetic materials were found to be a major test bed for the development of the ultrafast optical microscopy. There are primarily three different sources of magnetic moment in a free atom. The diamagnetism is observed due to the change in the orbital moment induced by some external magnetic field. On the other hand, both spin and orbital angular momentum play a role in the occurrence of paramagnetism, ferromagnetism, antiferromagnetism and ferrimagnetism. Among these, the ferromagnetic materials are found to possess most challenging and interesting properties to be explored by the ultrafast optical microscopy. Ferromagnets (FMs) have characteristic demagnetization times in femtosecond range, relaxation times in low picoseconds range, precession frequency varying over a broad range, domain-wall width and spin-wave wavelengths in the nanometer range – all these properties make FMs to be the most exciting candidate to be studied by the ultrafast optical microscopy.

2.2. Ferromagnetism

2.2.1. Classical approach – Curie-Weiss Law

According to Weiss [99], there are two competing energy contributions in a FM – i) the internal field or the “Weiss field” which favors parallel orientation of magnetic moments and ii) free magnetic poles on the surface which cause demagnetization. The competition between these two energy terms makes the FM to break up into small domains for the

Chapter 2

minimization of the free energy. In this classical framework, the Curie-Weiss law [100] describes the ferromagnetic susceptibility.

$$\chi_f = \frac{C}{T - T_c} \quad (2.1)$$

From the law, one can infer that below the Curie temperature (T_c), FMs show spontaneous magnetization. Eventually, Heisenberg [101], Dorfman [102] and Frenkel [103] managed to find the quantum mechanical origin of this “Weiss field” – the exchange interaction! This is the consequence of the antisymmetrization requirement for electron wavefunction.

2.2.2. Quantum mechanical approach – Exchange interaction

The exchange interaction is a direct consequence of the Coulombic interaction energy and Pauli Exclusion Principle. The concept of direct exchange can be explained on the basis of Heitler-London model of hydrogen molecule [100]. In this model, the wavefunctions of two electrons are written as $\psi(\mathbf{r}_1, s_1)$ and $\psi(\mathbf{r}_2, s_2)$, where \mathbf{r}_i 's are spatial and s_i 's are spin states. The exclusion principle demands that upon overlap, the resultant wavefunction must be antisymmetric. This can be achieved by the spatial or spin part of the wavefunction $\psi = \varphi\chi$ where φ is the spatial and χ is the spin part. For two nuclei a and b , the exchange integral is given by:

$$J_{12} = \int \varphi_a^*(1)\varphi_b^*(2)\mathcal{H}_{12}\varphi_a(2)\varphi_b(1)d\tau_1d\tau_2 \quad (2.2)$$

The above discussion was for electrons with direct overlapping of wavefunctions, *i.e.*, the interaction is direct exchange. One can have indirect exchange also. Later, it was understood that on top of these contributions, magnetic anisotropy and magneto-dipole interaction also play crucial role in determining domain structures in FMs.

2.1.3. Spin-orbit coupling

Spin-orbit (SO) coupling is basically the interaction of spin and orbital moments. An electron orbiting a nucleus with velocity \mathbf{v} experiences a field:

$$\mathbf{B} = \frac{\mathbf{r} \times \mathbf{v}}{rc^2} \frac{dV(r)}{dr} \quad (2.3)$$

Chapter 2

where $V(r)$ is the potential experienced by the electron and $\mathbf{r} \times \mathbf{v}$ is the classical angular momentum. The SO interaction energy is given by:

$$E_{SO} = -\frac{1}{2} \boldsymbol{\mu}_s \cdot \mathbf{B} \quad (2.4)$$

Substituting eqn. (2.3) in eqn. (2.4) one can derive:

$$E_{SO} = \frac{e\hbar^2}{2m_e r c^2} \frac{dV(r)}{dr} \mathbf{l} \cdot \mathbf{s} \quad (2.5)$$

2.3. Anisotropy

The non-relativistic quantum mechanics safely describes the basic properties of a FM. But in this formalism, the free energy is independent of the direction of magnetization. On the other hand, practically it is observed that the magnetization generally lies in some preferred direction with respect to the crystalline axes or/and to the external shape of the body. This property is called the “magnetic anisotropy”. The anisotropy energy term is essentially a correction to the total energy. The origin of this term lies in the relativistic correction to the total Hamiltonian. The introduction of the *dipole-dipole interaction* and *spin-orbit coupling* terms breaks the rotational invariance with respect to the spin quantization axis and hence gives rise to the magnetic anisotropy [104].

2.3.1. Magnetic anisotropy at macroscopic level

First, we will take the thermodynamic approach to give a phenomenological description of magnetic anisotropy. Throughout the description, the temperature of the FM will be assumed well below the Curie temperature to neglect magnetic fluctuations. Let us define Ω_M as the unit vector of magnetization \mathbf{M} of a FM under the influence of a bias field H . The components of Ω_M are α_1 , α_2 and α_3 with $\alpha_1^2 + \alpha_2^2 + \alpha_3^2 = 1$. Under some approximation, the thermodynamic potential G of the system can be reduced to a function of Ω_M only.

$$G = G(\Omega_M) \quad (2.6)$$

Chapter 2

2.3.1.1. Shape and magnetocrystalline anisotropies

A very common origin of magnetic anisotropy is the anisotropic shape of the element. This is called the shape anisotropy. However, when the shape of the body is isotropic but still the magnetization prefers to remain aligned to a particular crystal axis, then the anisotropy is termed as the magnetocrystalline anisotropy. Thus the total anisotropy energy of a system can be expressed as:

$$G(\Omega_M) = G_{cryst}(\Omega_M) + G_{shape}(\Omega_M) \quad (2.7)$$

The first term denotes the energy for the magnetocrystalline anisotropy contribution and hence is an intrinsic property of the material chosen. It arises mainly from the SO coupling. Dipolar interaction has a little contribution in it. The second term, on the other hand, is the contribution from the shape anisotropy and depends on the geometry of the sample. The shape anisotropy arises entirely from the dipolar interaction.

From symmetry arguments, one can deduce a form of $G_{Cryst}(\Omega_M)$. This term can be expanded in the successive powers of α_i 's:

$$G_{Cryst}(\Omega_M) = b_0(H_M) + \sum_{i,j} b_{ij}(H_M)\alpha_i\alpha_j + \sum_{i,j,k,l} b_{ijkl}(H_M)\alpha_i\alpha_j\alpha_k\alpha_l \quad (2.8)$$

+

Where H_M is the component of the external field along Ω_M . In the above expansion, only terms even in Ω_M are kept to satisfy the time reversal symmetry. It is observed that terms in this type of expansion converge very quickly. So, only few terms are enough to describe the magnetocrystalline anisotropy. Due to crystalline symmetry, one can establish relationships between coefficients in eqn. (2.8). As a result, number of independent parameters is reduced. In cubic systems like Ni and Fe, this results in the suppression of terms of order 2 and the first non vanishing term is of order 4:

$$G_{cryst}(\Omega_M) = K_0 + K_1(\alpha_1^2\alpha_2^2 + \alpha_2^2\alpha_3^2 + \alpha_3^2\alpha_1^2) + K_2\alpha_1^2\alpha_2^2\alpha_3^2 \quad (2.9)$$

+ $K_3(\alpha_1^2\alpha_2^2 + \alpha_2^2\alpha_3^2 + \alpha_3^2\alpha_1^2)^2 + \dots$

The co-ordinate axes are taken along the cubic axes as shown in Fig. 2.1.

Chapter 2

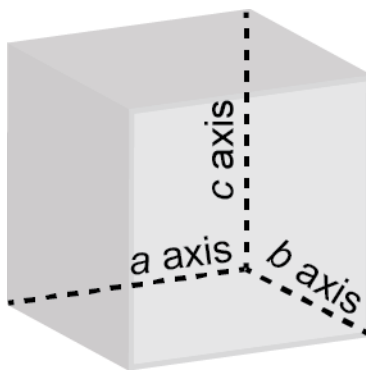


Fig. 2.1: Co-ordinate system used for a cubic system.

For hcp systems like Co, eqn. (2.8) reduces to:

$$G_{cryst}(\Omega_M) = K_0 + K_1 \sin^2 \theta + K_2 \sin^4 \theta + (K_3 + K'_3 \cos(6\varphi)) \sin^6 \theta + \dots \dots \dots \quad (2.10)$$

Here, φ and θ are angles with respect to the a and c axes, respectively. It is to be noted that the anisotropy constant K 's are a bit misleading, such as, K_1 is of order 4 in cubic system but of order 2 in hcp systems. Also, as an hcp structure has lower symmetry than a cubic structure, the magnitude of magnetocrystalline anisotropy is higher in hcp structures than the cubic structures.

2.3.1.2. Volume and interface anisotropies

In case of systems with smaller dimensions like ultrathin films, the effect of the surface (or interface) has to be taken into account. In this case, the total thermodynamic potential is written as a sum of a volume term and a surface (or interface) term:

$$G(\Omega_M) = \int dV G^V(\Omega_M) + \int dS G^S(\Omega_M)$$

$G^V(\Omega_M)$ and $G^S(\Omega_M)$ are energy densities per unit volume and interfacial area, respectively. The second term depends on the materials in contact and the crystalline orientation.

The interface anisotropy was first pointed out by Néel [15] due to the lowered symmetry of the interface as compared to the bulk. The expression of the surface contribution to the magnetocrystalline anisotropy is:

Chapter 2

$$G_{cryst}^S(\Omega_M) = K_1^S \sin^2\theta + (K_2^S + K_2'^S \cos(4\varphi)) \sin^4\theta + \dots \dots \dots \dots \quad (2.11)$$

The sign of K_1^S can be positive or negative depending on the interface under consideration. If it is positive, then, for ultrathin films, this contribution may dominate over the volume contribution to give a preferential perpendicular direction of magnetization. This is of immense importance in present day technology and we will discuss about it in some more details later.

2.3.1.3. Strain induced anisotropy and magnetostriction

In reality, the G value of a material is also a function of the strain tensor ε which we neglected in eqn. (2.6) under some approximation to give a simple description of different anisotropy terms. Hence,

$$G \equiv G(\Omega_M, \varepsilon) \quad (2.12)$$

A system under strain acquires some anisotropy energy due to the change in the *magneto-elastic energy*. Under small deformation, one can expand $G(\Omega_M, \varepsilon)$ in a power series of α and ε to get an expression for the strain induced anisotropy. It is important to note that during the fabrication of ultrathin films/multilayers, there can be huge strain due to the epitaxial growth on a substrate with different lattice parameters. So, this strain induced anisotropy plays a crucial role in ultrathin films. It is also evident that under strain the symmetry of the material will be lowered. So, new terms in the anisotropy are expected which may be forbidden in the unstrained state.

On the other hand, as the magneto-elastic energy is linear with respect to ε , the system tries to lower its energy by acquiring an anisotropic non-zero strain. This is known as the magnetostriction. The strain depends on the direction of magnetization and the magnitude is given by the competition between the elastic and magneto-elastic energy terms.

Chapter 2

2.3.2. Magnetic anisotropy at microscopic level - Dipolar interaction

While investigating the microscopic origin of magnetic anisotropy, we will first start with the dipolar interaction. For an itinerant FM like Fe, Co and Ni, the expression for the dipole-dipole Hamiltonian is given after Jansen [105]:

$$\mathcal{H}_{dip} = \frac{\mu_B^2}{2} \iint dr dr' \frac{1}{|r - r'|^3} \times \left(\hat{\mathbf{m}}(r) \cdot \hat{\mathbf{m}}(r') - 3 \frac{[(r - r') \cdot \hat{\mathbf{m}}(r)][(r - r') \cdot \hat{\mathbf{m}}(r')]}{|r - r'|^2} \right)$$

where $\hat{\mathbf{m}}(r)$ is the magnetization density operator expressed in terms of μ_B per unit volume. The corresponding energy E_{dip} is calculated under Hartree approximation. Now, for 3d transition metals, the magnetization distribution around each atomic shell is almost spherical. Hence, while calculating E_{dip} , we can safely ignore the higher order multipolar terms and keep the dipolar term only to obtain for the i^{th} atom:

$$E_{dip} = \frac{\mu_B^2}{2} \sum_{i \neq j} \frac{1}{r_{ij}^3} \left(m_i \cdot m_j - 3 \frac{(r_{ij} \cdot m_i)(r_{ij} \cdot m_j)}{r_{ij}^2} \right) \quad (2.13)$$

Under the assumption of dominating exchange interaction, eqn. (2.13) is further simplified as:

$$E_{dip} = \frac{\mu_B^2}{2} \sum_{i \neq j} \frac{m_i \cdot m_j}{r_{ij}^3} (1 - 3 \cos^2 \theta_{ij}) \quad (2.14)$$

where, θ_{ij} is the angle between Ω_M and the direction u_{ij} of the atom pair (i, j) .

2.3.2.1. Dipolar shape anisotropy

A close look to eqn. (2.14) reveals that the energy converges very slowly as r_{ij}^{-3} . Hence, the dipolar field $H_{dip}(i)$ on a moment m_i depends significantly on the moments located at the boundary of the sample, giving rise to the *shape anisotropy*. According to Lorentz, H_{dip} can be calculated by dividing the sample in two parts as shown in Fig. 2.2: i) a spherical cavity of radius R where the discrete moment distribution is retained and ii) the rest of the sample, where the discrete moment distribution can be approximated by a continuous distribution of magnetization $\mathbf{M}(\mathbf{r})$. If the magnetization is uniform, then only the surface carries some pseudo charges. In that case, we have:

Chapter 2

$$H_{dip}(i) = H_{cav} + H_L + H_d \quad (2.15)$$

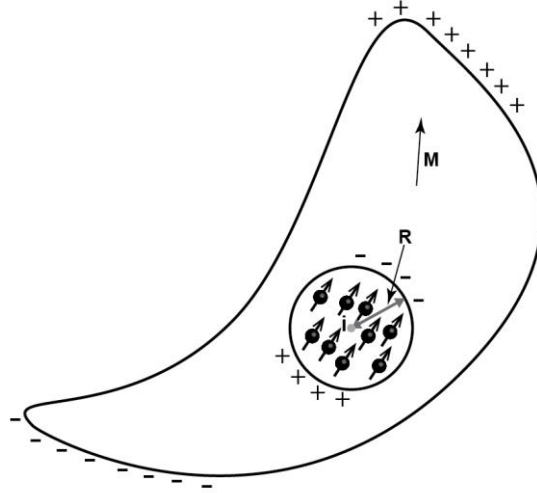


Fig. 2.2: Schematic describing Lorentz decomposition method to calculate the dipolar fields on a moment at a position i .

H_{cav} is the field due to the dipoles inside the spherical cavity, $H_L = \frac{4}{3}\pi M$ is the Lorentz field due to the charges on the cavity surface and H_d is the demagnetizing field due to the pseudo charges on the external surface. The first two terms in eqn. (2.15) converge rapidly and hence do not contribute to the shape anisotropy. The shape anisotropy is entirely controlled by the demagnetizing field H_d . The expression for the shape anisotropy is given by:

$$G_{shape}(\Omega_M) = -\frac{1}{2} \int dV \vec{M}(r) \cdot \vec{H}_d(r) \quad (2.16)$$

The magnitude $M(r)$ is constant throughout the sample except at the interface. Due to the presence of a different material, the magnitude of $M(r)$ is modified due to proximity effect. Hence, again it is possible to split the total shape anisotropy into volume and surface terms.

2.3.2.2. Dipolar crystalline anisotropy

The first two terms in eqn. (2.15) contribute to the magnetocrystalline anisotropy. As can be seen from eqn. (2.14), dipolar energy involves terms of order 2 with respect to Ω_M . However, in structures with higher symmetry like cubic, terms of order 2 are forbidden but

Chapter 2

allowed in structures with lower symmetry like hcp. So the contribution of dipolar interaction to the magnetocrystalline anisotropy is zero in case of cubic systems but non-zero in case of hcp systems. However, under strain, the symmetry of cubic systems is lowered (as discussed in section 2.3.1.3.) and in that case one might have the contribution of dipolar interaction also to the crystalline anisotropy.

2.3.3. Magnetic anisotropy at microscopic level – Spin-orbit coupling

The Pauli Hamiltonian or the Schrödinger equation with relativistic correction is given by:

$$\mathcal{H}_{Pauli} = \frac{p^2}{2m} - e\Phi - \frac{p^4}{8m^3c^2} + \frac{e\hbar^2}{8m^2c^2} \text{div.} \mathbf{E} + \frac{e\hbar}{4m^2c^2} \boldsymbol{\sigma} \cdot (\mathbf{E} \times \mathbf{p}) \quad (2.17)$$

Here, the first two terms are the non-relativistic kinetic energy and potential energy, third term is the relativistic mass-velocity correction, fourth term is the Darwin term and the last term takes care of the SO coupling. However, the orbital motion is directly linked to the lattice and hence this term contributes significantly to the magnetocrystalline anisotropy.

The SO term survives only near the nucleus. Hence, here also the potential can be safely approximated to be spherically symmetric. Then, the SO Hamiltonian can be expressed as:

$$\begin{aligned} \mathcal{H}_{SO} &= - \frac{e\hbar}{4m^2c^2r} \frac{d\Phi}{dr} \boldsymbol{\sigma} \cdot (\mathbf{r} \times \mathbf{p}) \\ &= - \frac{e\hbar^2}{2m^2c^2r} \frac{d\Phi}{dr} \mathbf{l} \cdot \mathbf{s} \\ &= \xi(r) \mathbf{l} \cdot \mathbf{s} \end{aligned} \quad (2.18)$$

Since in FMs, the magnetism is due to the d electrons, $\xi(r)$ can be replaced with the radial average ξ over d -orbital. Hence eqn. (2.18) finally reads:

$$\mathcal{H}_{SO} = \xi \mathbf{l} \cdot \mathbf{s}$$

The effect of the SO coupling is to remove the quenching of orbital angular momentum. As a result, the value of the gyromagnetic ratio g changes from 2. However, as the effect is rather small, g always remains close to 2.

Chapter 2

Now, as already mentioned, the effect of this term is small, hence a popular way is to use the perturbation theory to analyze this effect. To calculate the anisotropy constant of order n , one needs to use perturbation theory of order n . It is sufficient to use 2nd order perturbation theory for hcp structures and ultrathin films and it is evident that 4th order perturbation theory is required for cubic systems.

For 2nd order perturbation theory, the change in energy is given by:

$$\Delta E_{SO} = \sum_{exc} \frac{|\langle exc | \mathcal{H}_{SO} | gr \rangle|^2}{E_{gr} - E_{exc}}$$

Here “ gr ” and “ exc ” refer to the ground and excited states. Thus, a very crude estimate of K_1 for uniaxial system is given by:

$$K_1 \sim \frac{\xi^2}{W} \quad (2.19)$$

W being the width of the d band. For a cubic system, using 4th order anisotropy:

$$K_1 \sim \frac{\xi^4}{W^3} \quad (2.20)$$

So, in general, anisotropy constant of order n is given by the n^{th} power of $\frac{\xi}{W}$ and hence converges rapidly.

2.3.4. Perpendicular magnetic anisotropy (PMA)

The PMA is presently a very interesting topic of research [106-109]. In section 2.3.1.2., we have introduced PMA. Strong PMA can be realized in Co based MLs where the Co layer thickness is less than 12 Å. The PMA is significant in X/Co/X MLs where X = Pd, Pt, Au and Ir, whereas this effect is quite weak for X = Cu and Ag. The investigation of origin of PMA has attracted huge attention. Few proposed explanations for this are: reduced coordination symmetry, altered electronic structure, localized epitaxial strain at the interface and electronic band-structure interactions. For a bare Co film, the out-of-plane d_{z^2} and d_{xz} , d_{yz} states located near the Fermi energy (E_F) show less dispersion due to less overlap of neighboring Co atoms. However, because of strong interaction between Co atoms in the

Chapter 2

film plane, the in-plane d_{xy} and $d_{x^2-y^2}$ states show significant dispersion. In contact with a non-magnetic material, the energies and wave-functions of out-of-plane states change due to interfacial hybridization. These hybridizations are sensitive to the local interface structure and affect the SO coupling perturbation, which in turn changes the magnetocrystalline anisotropy energy. The PMA increases with the strength of the hybridization.

Pd d bands have higher energy than Cu d bands. The energies of the Pd d states are close to that of the antibonding out-of-plane Co d states and at the same time, in contact with Co, the Pd $4d$ orbitals have lesser localization. As a result, strong hybridization occurs at the Co/Pd interface within -1.5-0.5 eV with respect to E_F . These hybridized states are shifted upwards in terms of energy. Now, it is known that the anisotropy energy is closely related to the anisotropy of the orbital magnetic moment which is simply the difference of parallel and perpendicular orbital moments: $\Delta m_{orb} = m_{orb}^{\parallel} - m_{orb}^{\perp}$. Because of the strong hybridization at Co/Pd interface, a significant spin polarization of the Co d band occurs and m_{orb}^{\perp} is significantly enhanced. This enhanced perpendicular moment causes PMA by modifying the SO coupling.

In contrast, the interface Cu d states have more localized orbitals and much lower energy with respect to the Co d orbitals. Hence, they have less overlap, *i.e.*, weak hybridization which in turn weakens the PMA.

2.3.5. Exchange anisotropy

Exchange bias or exchange anisotropy was discovered in 1956 by Meiklejohn and Bean [110]. This type of anisotropy is found in a FM if the interface of a FM/AFM (AFM: Antiferromagnet) ML is cooled in the presence of a static magnetic field H through the Néel temperature (T_N) of the AFM. The Curie temperature (T_C) of the FM should be larger than T_N . The exchange anisotropy is a unidirectional anisotropy. The hysteresis loop of the ML system, when field cooled at temperature $T < T_N$, has an increased coercivity H_c and at the same time, shifts along the field axis. This loop shift is generally termed as the *exchange bias* H_E . Both these effects disappear at $T \approx T_N$. This confirms that the presence of the AFM is essential to observe the exchange anisotropy. The exchange bias properties disappear if

Chapter 2

the FM/AFM interface is cooled at zero field from demagnetized state. However, the properties are retained if it is cooled at zero field from a remanent state.

The unidirectional nature of the exchange anisotropy can be explained by incorporating exchange interaction at the interface [111]. As shown in Fig. 2.3(i), the spins in the FM get aligned to the applied bias field H at $T_N < T < T_C$, while the spins in the AFM remain randomly oriented. As the sample is cooled to $T < T_N$ in the presence of H , the spins in AFM at the FM/AFM interface gets aligned along the direction of the spins in the FM due to exchange coupling as illustrated in Fig. 2.3(ii). The rest of the spins rearrange themselves according to the antiferromagnetic ordering to produce zero net magnetization. Now, as we start to reverse H , the spins in the FM starts to rotate. For sufficiently high anisotropy, the spins in the AFM do not rotate.

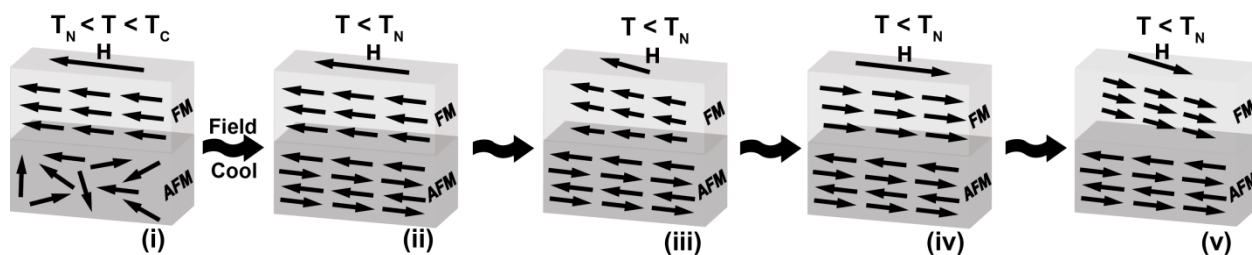


Fig. 2.3: Schematic diagram of spin configuration of an FM-AFM bilayer at different stages.

As elaborated in Fig. 2.3(iii), the interfacial exchange interaction at the FM/AFM interaction tries to align the spins in the FM along the direction of the spins in the AFM at the interface, *i.e.*, exert a microscopic torque on the spins in the FM. Therefore, the spins in the FM have only one stable configuration implying unidirectional anisotropy. Thus, higher H is required to fully reverse the spins in the FM layer in FM/AFM bilayer than in a bare FM of similar thickness. Fig. 2.3(iv) presents the case where the spins in the FM are fully reversed. Now if H is brought back to the original direction, then the spins in the FM will rotate at smaller fields due to the interaction with the AFM. This interlayer exchange interaction hence gives rise to an additional field and as a result, the hysteresis loop is shifted in the field axis.

Chapter 2

2.4. Energy terms in ferromagnetic systems

Both static and dynamic properties of a magnetic system depend on the interplay between different energy contributions present. The total energy of a FM in the presence of an external field can be written as:

$$E = E_Z + E_{demag} + E_{ex} + E_{ani}$$

Where:

E_Z = Zeeman energy

E_{demag} = Magnetostatic energy

E_{ex} = Exchange energy

E_{ani} = Magnetocrystalline anisotropy energy

2.4.1. Zeeman energy

The energy of a magnetic system with magnetization M in the presence of an external field H is given by:

$$E_Z = -\mathbf{M} \cdot \mathbf{H} \quad (2.21)$$

In the continuum limit, this becomes:

$$E_Z = - \int \mathbf{M} \cdot \mathbf{H} dV \quad (2.22)$$

Hence the Zeeman energy reaches its minimum value when M is aligned along H .

2.4.2. Magnetostatic energy

Magnetostatic fields arise naturally from a magnetization distribution because of the influence of its own field. This effect results in magnetization structures (*e.g.* magnetic domains) on a length scale larger than few atomic spacing. In spite of being much weaker than the exchange interaction, it plays a crucial role in FMs. The corresponding energy can be written as:

$$E_{demag} = -\frac{1}{2} \mathbf{H}_d \cdot \mathbf{M} \quad (2.23)$$

where \mathbf{H}_d is the demagnetizing field expressed in term of the demagnetizing factors N_d 's:

Chapter 2

$$H_d = -\mathbf{N}_d \cdot \mathbf{M} \quad (2.24)$$

Combining eqns (2.23) and (2.24), we have:

$$E_{demag} = \frac{1}{2} N_d M^2 \quad (2.25)$$

In the continuum limit, eqn. (2.23) changes to:

$$E_{demag} = -\frac{1}{2} \int \mathbf{H}_d \cdot \mathbf{M} dV \quad (2.26)$$

2.4.3. Exchange energy

As described in section 2.2.2., the exchange interaction originates from the overlapping electronic wavefunctions. This can be phenomenologically described by the Heisenberg exchange Hamiltonian. Considering nearest neighbor interaction only, the exchange Hamiltonian of an atom i with its neighbors can be written as:

$$\mathcal{H}_{ex} = -2 \sum_j J_{ij} \mathbf{S}_i \cdot \mathbf{S}_j \quad (2.27)$$

If the exchange is isotropic and equal to a constant value J , then

$$\mathcal{H}_{ex} = -2J \sum_j \mathbf{S}_i \cdot \mathbf{S}_j \quad (2.28)$$

Hence, for the entire sample, the exchange energy will be:

$$E_{ex} = -2J \sum_{i \neq j} \mathbf{S}_i \cdot \mathbf{S}_j \quad (2.29)$$

In the continuum model, eqn. (2.29) can be written as:

$$E_{ex} = A \int (\nabla \mathbf{m})^2 dV \quad (2.30)$$

where \mathbf{m} is a continuous vector quantity and A is called the exchange stiffness constant defined as:

$$A = \frac{2JS^2}{a} \quad (2.31)$$

Chapter 2

where a is the lattice constant. The typical values of A for Ni, Co, Fe and permalloy ($\text{Ni}_{80}\text{Fe}_{20}$) are 9×10^{-12} J/m, 30×10^{-12} J/m, 21×10^{-12} J/m and 13×10^{-12} J/m, respectively.

2.4.4. Magnetocrystalline anisotropy energy

As discussed in section 2.3., anisotropy reflects the existence of a preferential direction of magnetization in a material. Following eqn. (2.9), the expression for anisotropy energy for a *cubic* system can be written as:

$$E_{ani} = K_0 + K_1(\alpha_1^2\alpha_2^2 + \alpha_2^2\alpha_3^2 + \alpha_3^2\alpha_1^2) + K_2\alpha_1^2\alpha_2^2\alpha_3^2 \quad (2.32)$$

On the other hand, using eqn. (2.10), one can deduce the expression for anisotropy energy for a *uniaxial* system:

$$E_{ani} = K_0 + K_1\sin^2\theta + K_2\sin^4\theta \quad (2.33)$$

2.5. Magnetic domains and domain-walls

Every system tries to remain in the minimum energy state. Now, considering eqn. (2.25), it is evident that M has to be reduced to minimize the magnetostatic self-energy. As a result, the system tries to break into domains. In each domain, the property of spontaneous magnetization is retained and the exchange interaction dominates which aligns spins in certain direction. A sample will be in multidomain or single domain state depending on the applied bias field and/or dimensions. One can have different types of domain patterns in various samples. Few examples are: checkerboard domain pattern, circular domain, wavy domain, surface domain and fir-tree domain. *Bubble domains* are a special kind of circular domains created in ferromagnetic films with PMA in the presence of a perpendicular bias field. Formation of stripe domains is observed in magnetic thin films with a rotatable magnetic anisotropy.

The spins do not change their directions abruptly from one domain to another. As elaborated in Fig. 2.4, the spins gradually change direction from domain I to domain II. The reason is that the exchange energy increases with the increase in angle between neighboring spins. An abrupt change in the angle would result in a huge increase of exchange energy. So, to minimize the total free energy of the system, there exists a

Chapter 2

transition region from domain I to domain II and this region is called as the *domain-wall* (DW).

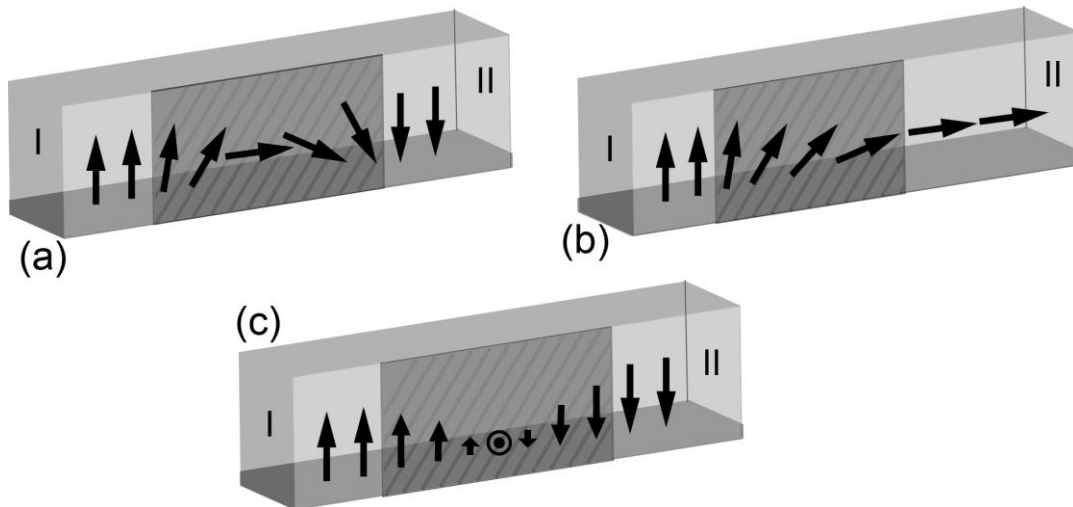


Fig. 2.4: Different types of domain-walls - (a) 180° domain-wall, (b) 90° domain-wall and (c) Bloch wall.

If the normal component of magnetization is continuous across the DW, then the DWs are primarily classified into two types: i) 180° DWs, illustrated in Fig. 2.4(a), which separate two domains with opposite spin directions and ii) 90° DWs, illustrated in Fig. 2.4(b), which separate two domains with spins making an angle 90° . The existence of surface free poles does not affect the rotation of spins in bulk samples. However, they have significant effect in thinner samples. Due to this contribution, in case of very thin films, spin rotation in a plane parallel to the film surface involves less magnetostatic energy than the spin rotation in a plane parallel to the wall. The first case is called as the Néel wall, schematically shown in Fig. 2.4(a), and the second one is called the Bloch wall and is shown in Fig. 2.4(c).

2.6. Magnetization reversal and various reversal modes

Magnetization reversal is one among the various magnetic processes which have attracted tremendous attention. The time required for an element to switch its magnetization direction is becoming important as the operational speeds of the devices have now reached the GHz regime. The reversal mechanism and associated modes are of particular interest.

Chapter 2

These reversal modes depend primarily on the shape of the element and the direction of the applied field.

Below a critical size, when an element is in the single domain state, the magnetization reversal occurs in unison over the whole element [112-113]. The calculations for the critical size are done by using the Ring model. Energies of the single domain configuration and a configuration which tends to a flux closure structure are compared at a zero external field.

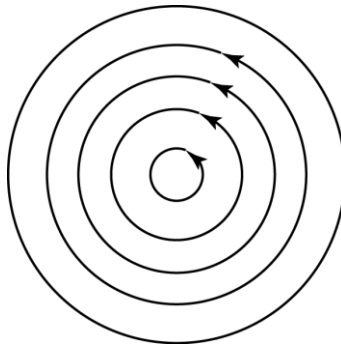


Fig. 2.5: Illustration of flux closure structure assumed in the ring model.

Assuming flux closure structure as shown in Fig. 2.5, the expression for the critical size is given by [114]:

$$\frac{N_z M_s^2 R_c^2}{6A} = \ln \frac{4R_c}{a} - 1 \quad (2.34)$$

Where M_s = saturation magnetization, R_c = critical radius, a = lattice constant, N_z = demagnetizing factor along the polar axis and A = exchange stiffness constant. However, there are three very important issues with this model:

- i) This model assumes that once the system is in the single domain state at zero field, it will always remain in the saturated state for all field values – which is not always true.
- ii) The configurations, which are used for the calculation of R_c , are to a good approximation close to the minimum energy state but actually not strictly in the minimum energy state always. This affects the stability of the states and may lead to erroneous results.
- iii) The method of comparing energies does not allow the existence of hysteresis and hence, loses its reliability as hysteresis is of fundamental interest in a FM.

Chapter 2

As a result, in most cases, this model significantly overestimates the coercivity. Avoiding these serious issues, various reversal modes in magnetic structures can be investigated under few very simple assumptions:

- i) The element does not have structural imperfections.
- ii) Exchange energy (E_{ex}), anisotropy energy (E_{ani}), Zeeman energy (E_z) and magnetostatic energy (E_{demag}) are considered, other energy terms are neglected.
- iii) The analyses are valid only below the Curie temperature.
- iv) Only static ferromagnetism is considered.

Under these assumptions, the magnetic properties of structures like infinite cylinders, spheres or prolate ellipsoids can be studied quite accurately. Consider an *infinite cylinder* of radius R and cylindrical co-ordinates (r, φ, z) (as shown in Fig. 2.6 with respect to the Cartesian co-ordinates) with the bias field H applied along the Z direction. For H higher than the saturation field, the cylinder will be in saturated state, *i.e.*, in single domain state. As H is decreased, the minimum energy state can be obtained by finding proper direction cosine vector $\alpha_i(r, \varphi, z)$. However, for an infinite cylinder, using symmetry considerations, the rigorous job of finding α_i for every H value can be avoided. In that case, the reversal can occur via three mechanisms as illustrated in Fig. 2.6:

- (b) Coherent rotation
- (c) Curling
- (d) Buckling

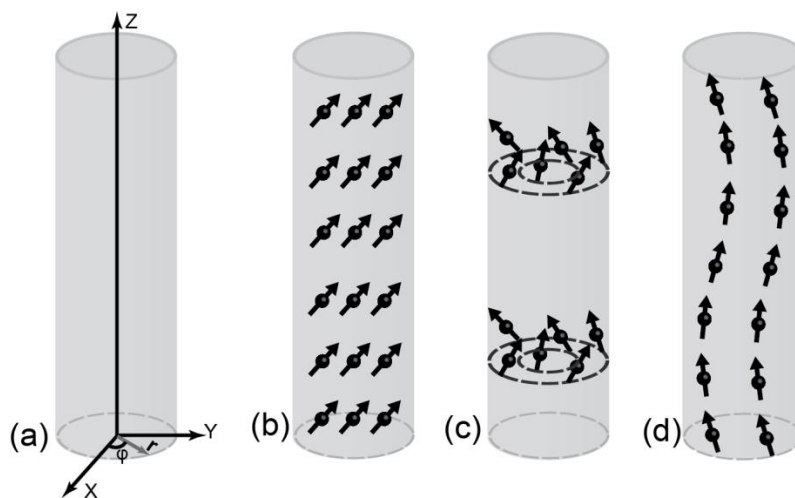


Fig. 2.6: (a) Cylindrical co-ordinate system used. (b)-(d) Various magnetization reversal modes in an infinite cylinder: (b) coherent rotation, (c) curling and (d) buckling.

Chapter 2

2.6.1. Coherent rotation of magnetization

The expression for the coercive field (H_c) can be easily obtained in this case [113, 115]. Suppose the angle between the long-axis (Z direction, in our case) and H is θ , N_z and N_i are the demagnetizing factors along Z direction and any other direction perpendicular to Z respectively as shown in Fig. 2.7.

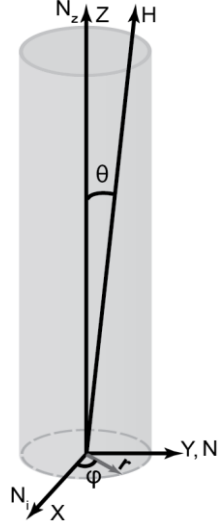


Fig. 2.7: Schematic showing the directions of the applied bias field and the demagnetizing factors in an infinite cylinder with respect to the co-ordinate system used.

For infinite cylinder, $N_z = 0$ and $N_i = 2\pi$. The energy of the system is then,

$$F_{mag} = \frac{1}{2} M_s^2 (N_z \cos^2 \theta + N_i \sin^2 \theta) + H M_s \cos \theta \quad (2.35)$$

The contributions of the demagnetizing factors are incorporated in the first term whereas the second term takes into account the contribution of the external field H . Minimization of F_{mag} with respect to θ gives:

$$\frac{dF_{mag}}{d\theta} = M_s^2 (N_i - N_z) \cos \theta \sin \theta - H M_s \sin \theta = 0 \quad (2.36)$$

$$M_s (N_i - N_z) \cos \theta = H$$

Chapter 2

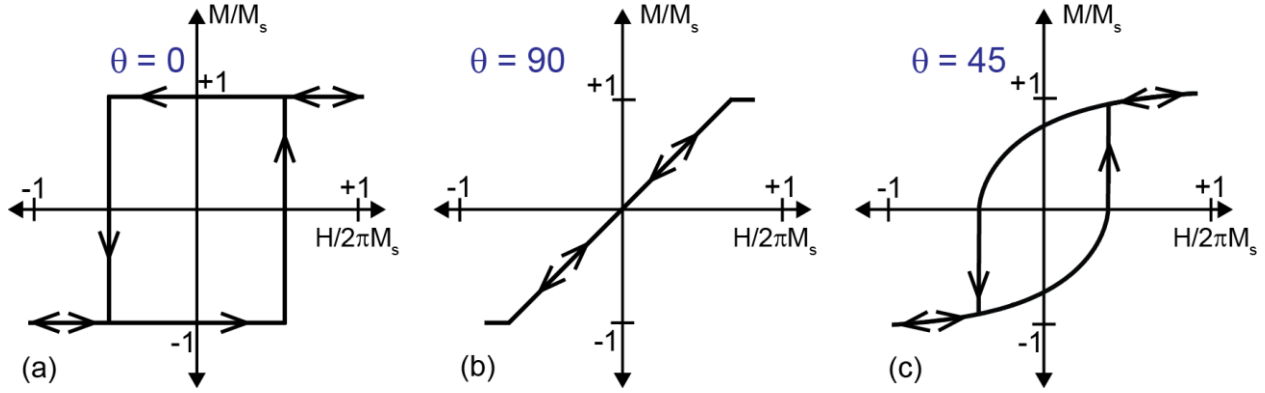


Fig. 2.8: Hysteresis loops for applied field (a) parallel, (b) perpendicular and (c) at 45° to the long-axis of an elongated particle.

Hence, the maximum coercive field can be obtained for the limiting case $\theta = 0$ (similar to the case shown in Fig. 2.8). Putting $N_i = 2\pi$ and $N_z = 0$, this becomes:

$$H_c = 2\pi M_s \quad (2.37)$$

2.6.2. Magnetization curling

Curling mode is favorable as it reduces the magnetostatic self-energy of the system due to its vortex-like flux closure structure. However, it involves more exchange energy as $\nabla M \neq 0$. In this case, the reversal occurs via rotation of spins from Z axis in a plane perpendicular to the radius. Hence, the rotation angle ω is independent of φ and z , and depends on r only. Setting $E_{demag} = 0$, we have the total energy per unit volume[114]:

$$\bar{E} = \frac{1}{\pi R^2} \int_{a/2}^R (E_{ex} + E_z) 2\pi r dr \quad (2.38)$$

Where a is the lattice constant. By substituting the direction cosines,

$$\alpha_x = \sin \omega \cos \varphi, \quad \alpha_y = \sin \omega \sin \varphi, \quad \alpha_z = \cos \omega$$

we obtain,

$$E_x = A[(d\omega/dr)^2 + (1/(r)^2)\sin^2\omega]$$

and

$$E_z = -HM_s \cos \omega$$

Along with these two equations, we make the following substitutions:

Chapter 2

$$x = r/R, \quad R_0 = A^{1/2}/M_s, \quad S = R/R_0, \quad h = \frac{H}{2\pi M_s}$$

Using above equations, eqn. (2.38) can be written as:

$$\bar{E} = \frac{2A}{R^2} \int_{a/2R}^1 \left[x \left(\frac{d\omega}{dr} \right)^2 + \frac{\sin^2 \omega}{x} - 2\pi S^2 h x \cos \omega \right] dx \quad (2.39)$$

Using Euler differential equation, this integral can be minimized:

$$\frac{d^2 \omega}{dx^2} + \frac{1}{x} \frac{d\omega}{dx} - \left(h\pi S^2 + \frac{\cos \omega}{x^2} \right) \sin \omega = 0 \quad (2.40)$$

The solution reaches minimum for a certain range of h values for the trivial solution $\omega = 0$. The value of h , at which the solution starts to deviate from the minimum, is called as the reduced nucleation field h_n . For small angles $\omega \ll 1$, eqn. (2.40) can be linearized to Bessel equation:

$$\frac{d^2 \omega}{dx^2} + x^{-1} \frac{d\omega}{dx} - (h\pi S^2 + x^{-2}) \omega = 0 \quad (2.41)$$

The solution is a combination of Bessel and Neumann functions of the first order. Assuming $a/2R \ll 1$, a simple form of the nucleation field h_n is obtained with a valid approximation of $\omega = 0$ at $x = 0$:

$$h_n = 1.08S^{-2}$$

An alternative solution of eqn. (2.41) can be obtained by graphical methods and it states that the magnetization reverses completely at $\omega = \pi$, the second trivial solution of eqn. (2.40).

2.6.3. Magnetization buckling

In this case, the spin rotation is along X direction and the deviation is a periodic function (period = $2T$) of Z. The angle of deviation ω is defined as:

$$\omega = \sum_{m=1}^{\infty} \omega_{2m-1} \cos \left[(2m-1) \frac{\pi}{T} z \right] \quad (2.42)$$

Substituting the direction cosines and solving for the total energy, one obtains the expression for the nucleation field:

$$h_n = -1.29S^{-\frac{2}{3}}$$

Chapter 2

Among the three mechanisms, the system chooses the one with the most positive h_n . It is observed that for $S > 1.1$, curling is the favorable mechanism whereas buckling occurs for $S < 1.1$. However, the transition from curling to buckling mode is not abrupt. The mechanism is quite complicated for $S = 1$, where a mixed mechanism occurs and reduces h_n . Coherent rotation is actually a special case of buckling for $S \ll 1$. In long cylindrical nanowires, vortex wall assisted reversal is observed. This is often termed as *localized curling mode*. At the end of the wire, a vortex is nucleated and it traverses through the wire reversing the entire magnetization. As the diameter reduces, transverse wall mode becomes the primary mechanism for magnetization reversal. This mode is often called as the *corkscrew mode*. However, reversal involving vortex wall mode is faster than the corkscrew mode [116-117].

Similarly, calculations can be performed for spheres or prolate ellipsoids and depending on the structure one can have different magnetization reversal modes like *fanning* [118] etc.

2.7. Magnetization dynamics at various time-scales and the Landau-Lifshitz-Gilbert (LLG) equation

Magnetization dynamics occurs over a broad range of time-scales ranging from μs to fs and is schematically shown in Fig. 2.9. The slowest dynamics is the domain-wall motion. The typical time-scale of this process is few ns to hundred μs . Precession of magnetization is a faster dynamics [119] and it occurs within 10-100 ps and gets damped in sub-ns to tens of ns time. So the spin-waves in ferromagnetic materials can propagate within few hundreds of ps to tens of ns before it gets damped out. Within similar time-scales, we have two more phenomena: reversal of spins as used in magnetic recording (few ps – few hundred ps) and vortex core switching (few tens of ps – several ns). Apart from the fundamental exchange interaction (~ 10 fs), SO coupling and spin-transfer-torque (~ 10 fs – 1 ps), the fastest magnetization dynamics is the laser induced ultrafast demagnetization. When a femtosecond laser pulse falls on a magnetized ferromagnetic sample, an ultrafast demagnetization is observed [120] within about 500 fs. The physics behind this ultrafast demagnetization is still a topic of intense debate. Different physical mechanisms are

Chapter 2

considered to play an important role for the demagnetization process. This includes the excitation of stoner pairs [121], SO coupling [122], coupling with the electromagnetic field via a terahertz emission [123], and scattering of spins with impurity centers or phonons [124]. The demagnetization is followed by a very fast partial recovery of magnetization within 1-10 ps. This occurs due to the exchange of energy from hot electrons and spins to the lattice. This can be phenomenologically described by a three temperature model [120, 125]. After this fast recovery, there is a slow recovery of magnetization due to the diffusion of electron and lattice heat to the surroundings (such as substrate) [126-127].

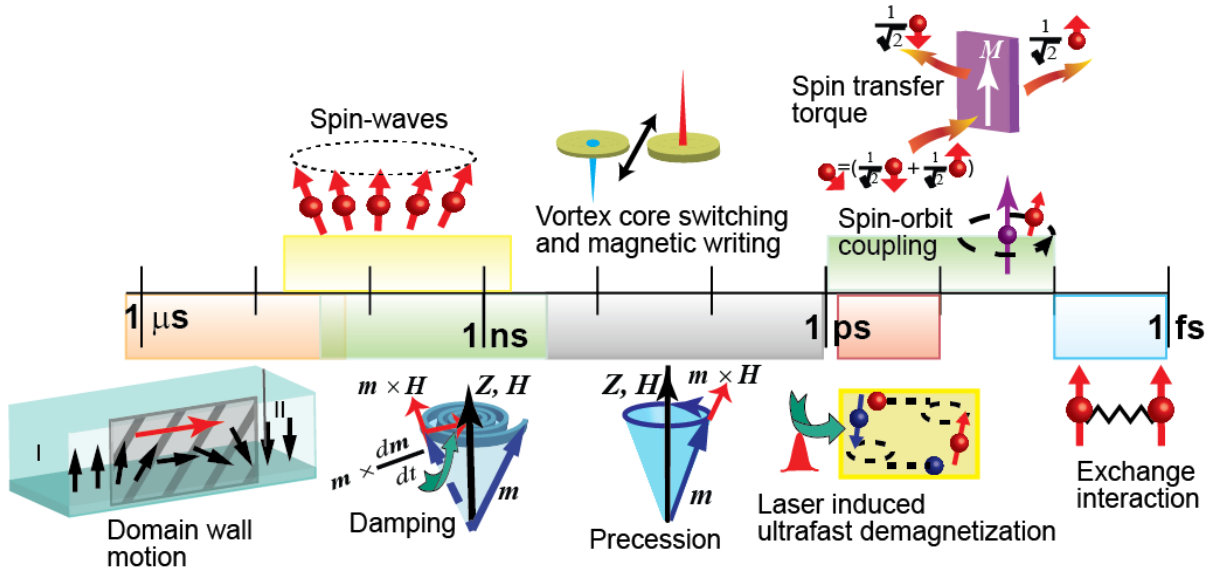


Fig. 2.9: Magnetization dynamics at various time-scales.

The precessional motion is guided by the Landau-Lifshitz-Gilbert (LLG) equation. The LLG equation can be derived using the spin commutation relations on the spin operator and the Zeeman Hamiltonian and combining that with the Classical Mechanics and Electromagnetism [128]. Here, we will present the final form only. When the magnetization (M) of the sample is at an angle to an effective external field (H_{eff}), then it experiences a torque and starts to precess around H_{eff} and finally gets aligned to H_{eff} . The LLG equation is derived from quantum mechanical arguments [129-130]. The first form of the equation as suggested by Landau and Lifshitz was:

$$\frac{d\mathbf{m}}{dt} = -\gamma(\mathbf{m} \times \mathbf{H}_{eff}) \quad (2.43)$$

Chapter 2

with

$$\mathbf{m} = \mathbf{M}/M_s$$

where γ is the gyromagnetic ratio.

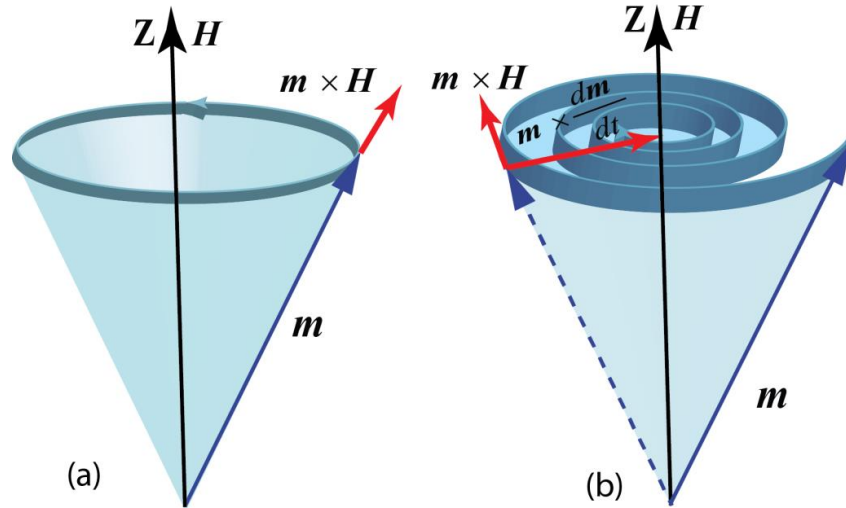


Fig. 2.10: Magnetization precession about the applied bias field (a) without damping and (b) with damping.

This equation implies an undamped precession of the tip of the magnetization vector around H_{eff} . However, this is in contrast to the practical situation where M finally gets aligned to H_{eff} . So, a damping term has to be added to the eqn. (2.43). Landau and Lifshitz proposed the damping term to be [131]:

$$-\lambda \mathbf{m} \times (\mathbf{m} \times \mathbf{H}_{eff})$$

Whereas, Gilbert suggested [132-133]

$$\alpha \left(\mathbf{m} \times \frac{d\mathbf{m}}{dt} \right)$$

Hence, incorporating the damping term, we arrive at the LLG equation:

$$\frac{d\mathbf{m}}{dt} = -\gamma(\mathbf{m} \times \mathbf{H}_{eff}) + \alpha \left[\mathbf{m} \times \frac{d\mathbf{m}}{dt} \right] \quad (2.44)$$

Here in the equation, the first term governs the precessional motion of the magnetic moment whereas the second term takes into account the damping. γ is the gyromagnetic ratio and α is the Gilbert damping.

2.8. Ultrafast demagnetization

The discovery of ultrafast demagnetization in 1996 [120] in Ni films led to tremendous research as it resulted in two new challenges - i) understanding of magnetization dynamics in an extremely non-equilibrium regime and ii) controlling the material properties in the sub-picosecond timescale which will lead to significant progress in the spintronics industry. After 1996, this ultrafast demagnetization was observed in many materials. However, in spite of its technological importance, the underlying physical mechanism remained highly controversial. There are various theories proposed for this and below, we will discuss about few of them.

2.8.1. The three temperature model

In 1996, the first observation of the ultrafast demagnetization in Ni under the excitation of a 60 fs laser pulse was explained phenomenologically by a three-temperature model (3TM) [120]. This is basically an extension of the two-temperature model introduced by S. I. Anisimov in 1974 [134]. In 3TM, it is assumed that the system consists of three thermalized reservoirs for exchanging energy, namely, the electron, lattice and spin systems at temperatures T_e , T_l and T_s respectively. The absorbed energy creates hot electrons within the system. During this transient hot electron regime, spin dependent electron scattering modifies the spin population. Hence this induces a spin dynamics associated with T_s different from T_e and T_l and leads to the ultrafast demagnetization. The temporal evolution of the system can be described by three coupled differential equations:

$$C_e(T_e) \frac{dT_e}{dt} = -g_{el}(T_e - T_l) - g_{es}(T_e - T_s) + P(t) \quad (2.45)$$

$$C_s(T_s) \frac{dT_s}{dt} = -g_{es}(T_s - T_e) - g_{sl}(T_s - T_l) \quad (2.46)$$

$$C_l(T_l) \frac{dT_l}{dt} = -g_{el}(T_l - T_e) - g_{sl}(T_l - T_s) \quad (2.47)$$

With C_e = Electronic specific heat of the material concerned

Chapter 2

C_s = Magnetic contribution to the specific heat

C_l = Lattice contribution to the specific heat

g_{el} = Electron-lattice interaction constant

g_{sl} = Spin-lattice interaction constant

g_{es} = Electron-spin interaction constant

$P(t)$ = Laser source term

2.8.2. Elliott-Yafet (EY)-type of phonon scattering

The 3TM model discussed in the previous section provides a phenomenological description only and does not consider the transfer of angular momentum. The ultrafast transfer of angular momentum was first proposed by Zhang and Hübner [135] without incorporating the lattice degree of freedom. To explicitly incorporate the dissipation of angular momentum during the ultrafast demagnetization, the 3TM model is extended [125, 136]. Throughout the calculations, it is assumed that the electronic system is in full internal equilibrium. It is proposed that the spin relaxation is mediated by EY-like processes, with a spin-flip probability a_{sf} for electron-phonon momentum scattering events. The equation for magnetization dynamics thus becomes:

$$\frac{dm}{dt} = Rm \frac{T_l}{T_c} \left(1 - m \coth \left(\frac{mT_c}{T_e} \right) \right) \quad (2.48)$$

Where $m = M/M_s$

T_c = Curie temperature

R = Material specific scaling factor for demagnetization rate with

$$R \propto a_{sf} \frac{T_c^2}{\mu_{at}}$$

μ_{at} = Atomic magnetic moment

Chapter 2

Hence, the excess energy of the electron system provides the energy for the demagnetization and the angular momentum is dissipated via the interaction with the lattice.

2.8.3. Spin-flip Coulomb scattering

This is another theory based on the EY interactions. The EY mechanism states that due to the presence of spin-orbit (SO) interaction, the spin does not remain a good quantum number. So, whenever an electron is scattered in a momentum-dependent scattering mechanism, the spin admixture is changed. In the previous section, the (quasi)elastic electron-phonon scattering was considered to be responsible for the EY mechanism. One can think of the electron-electron Coulomb scattering [137] also. Not being a (quasi)elastic process, this scattering process offers more phase space for transition from minority to majority bands than for electron-phonon scattering. The model developed describes the scattering dynamics by Boltzmann scattering integrals for the momentum-dependent dynamical distribution functions in various bands.

2.8.4. Relativistic quantum electrodynamic processes

This theory primarily focuses on what happens at the very first stage when a femtosecond laser beam falls on a saturated FM material [138]. According to this theory, at the very beginning, the photon field interacts with electronic charges and spins. The material polarization induced by the photon field interacts coherently with the spins and modifies the angular momentum non-linearly in less than 50 fs. The origin of this coherent interaction lies in relativistic quantum electrodynamics, beyond the SO interaction involving ionic potentials. In the second stage, relaxation of electrons and spins to thermalized populations takes place and incoherent processes like demagnetization occurs. This can be clearly distinguished from the previously mentioned coherent interaction. Finally, for longer time delays, the energy exchange between charges and spins with the lattice becomes important.

2.8.5. Laser induced spin-flip

This theory [139-140] combines *ab initio* electronic many-body theory with quantum optics to give more insight on the coherent process occurring at the very beginning when

Chapter 2

the laser light falls on the material (as discussed in the previous section). In this theory, calculations show that for every elementary on-site process of optically induced magnetization switching, light acts as a local angular momentum reservoir at ultrashort time-scales. Light does not take away the total angular momentum change in the material but takes a part of it (with the use of orbital momentum via SO interaction as a converter) and triggers its redistribution. The entire process is extremely complicated as the light absorbed at every single site does not involve only the driving laser pulse but also the emitted light from the neighboring sites.

2.8.6. Super-diffusive spin transport

Spin-dependent transport of laser-excited electrons is proposed to be another channel for the dissipation of angular momentum during the ultrafast demagnetization [141-142]. This theory takes into account multiple, spin-conserving electron (e^-) scattering events and electron cascades created by inelastic scattering. The demagnetization is described by developing transport equation for the super-diffusive flow of spin-polarized electrons. On absorbing a photon, an e^- jumps to sp -like band from the d band. As the mobility of sp -like e^- s are more than the d band e^- s, in this model, d e^- s are treated as quasilocalized. The theory assumes the optical excitation to be spin conserving. Considering that the probability of the emission direction is isotropic and integrating over all possible angles, the statistical averaged flux ϕ (number of e^- s per unit time) is calculated. For a distributed source of excited electrons, the total first-generation flux due to all e^- s with spin σ and energy E is:

$$\Phi(z, t) = \int_{-\infty}^{+\infty} dz_0 \int_{-\infty}^t dt_0 S^{ext}(z_0, t_0) \phi(z, t; z_0, t_0) \quad (2.49)$$

$S^{ext} = S^{ext}(\sigma, E, z, t)$ is the electron source term and $\hat{\phi} S^{ext} \equiv \Phi$. Similarly, the second-generation flux $S^{[2]}$ can be calculated. Finally, the equation describing the fast transport of the laser-excited e^- s can be derived:

$$\frac{\partial n^{tot}}{\partial t} + \frac{n^{tot}}{\tau} = \left(-\frac{\partial}{\partial z} \hat{\phi} + \hat{I} \right) (\hat{S} n^{tot} + S^{ext}) \quad (2.50)$$

Where \hat{I} is the identity operator and $\hat{S} n^{[1]} = S^{[2]}$, $n^{[1]}$ is the density of first-generation e^- s.

The super-diffusive transport may give rise to ultrafast demagnetization due to two reasons: 1) laser-excited e^- s in sp bands have high velocities and 2) the lifetimes of the

Chapter 2

excited spin majority and minority e 's are different. As a result of the second point, the excited majority carriers in 3d FMs are more mobile than the minority carriers which may lead to a deficit of majority carriers in the magnetic film and a transfer of magnetization away from the surface.

2.9. Ferromagnetic resonance and the macrospin model: Kittel formula

Ferromagnetic resonance (FMR) is a phenomenon in which an alternating magnetic field is applied to a FM material under a steady bias field in such a way that the ac field is perpendicular to the bias field and the angular frequency of the ac field is equal to the frequency of precession of magnetization in the FM resulting in a *resonance*. In that case, the magnetization in the FM material will precess with the resonance frequency absorbing power from the ac field. FMR was first experimentally observed by J. Griffiths [143] in a measurement analog to the Purcell-Torrey-Pound nuclear resonance experiment. Surprisingly it was found that the resonance frequency (ω_0) was quite higher than the expected Larmor frequency (ω_L), as given by the following equation, under the same effective field (H_{eff}):

$$\omega_L = \gamma H_{eff} \quad (2.51)$$

The explanation of the anomaly was given by Charles Kittel [144-145]. He found that one needs to consider the dynamical coupling caused by the demagnetizing field. All his calculations are done under the macrospin formalism where it is assumed that the magnetization is uniform throughout the sample. In this case, the magnetic moments of the entire sample can be replaced by a giant macrospin.

Chapter 2

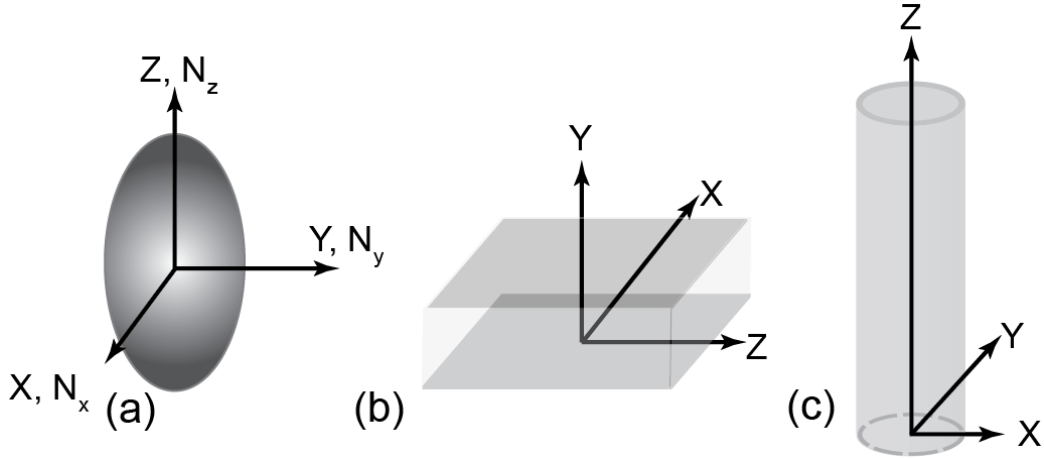


Fig. 2.11: Co-ordinate systems used for (a) an ellipsoid, (b) a plane and (c) a cylinder.

For a FM material with magnetization M under a bias field H_{eff} , the equation of motion is given by eqn. (2.43):

$$\frac{d\mathbf{M}}{dt} = -\gamma(\mathbf{M} \times \mathbf{H}_{eff})$$

For a general ellipsoid as shown in Fig. 2.11, let us assume that the demagnetizing factors along three principal axes X, Y and Z are N_x , N_y and N_z respectively. If the bias field is along Z (H_z) and the rf field is along X (H_x), then the effective values of the magnetic field components is given by [144]:

$$H_x^i = H_x - N_x M_x \quad (2.52)$$

$$H_y^i = -N_y M_y \quad (2.53)$$

$$H_z^i = H_z - N_z M_z \quad (2.54)$$

Substituting eqns (2.52) to (2.54) in eqn. (2.43):

$$\frac{dM_x}{dt} = \gamma[H_z + (N_y - N_z)M_z]M_y \quad (2.55)$$

$$\frac{dM_y}{dt} = \gamma[M_z H_x - (N_x - N_z)M_x M_z - M_x H_z] \quad (2.56)$$

Chapter 2

$$\frac{dM_y}{dt} \cong 0 \quad (2.57)$$

By considering time dependent variation of \mathbf{M} and \mathbf{H} ($\exp(j\omega t)$), the equation of resonant frequency is given by:

$$\omega_0 = \gamma \sqrt{[H_z + (N_y - N_z)M_z] \times [H_z + (N_x - N_z)M_z]} \quad (2.58)$$

The expressions for the resonance frequency for some standard shapes (under the coordinate system convention as shown in Fig. 2.11) are listed below [144, 146]:

Table 2.1: Eigen frequencies for some standard shapes.

Shape	Magnetization direction	Demagnetizing Factors			Eigen frequencies
		N_x	N_y	N_z	
Infinitely thin plane	Tangential	0	4π	0	$\omega_0 = \gamma [H_z (H_z + 4\pi M_z)]^{1/2}$
	Normal	0	0	4π	$\omega_0 = \gamma [H_z - 4\pi M_z]$
Infinitely thin cylinder	Longitudinal	2π	2π	0	$\omega_0 = \gamma (H_z + 2\pi M_z)$
	Transverse	2π	0	2π	$\omega_0 = \gamma [H_z (H_z - 2\pi M_z)]^{1/2}$
Sphere	-	$4\pi/3$	$4\pi/3$	$4\pi/3$	$\omega_0 = \gamma H_z$

2.10. Spin-waves

Spin-waves (SWs) were first introduced by Bloch as the low-lying excitations above the ground state in ordered magnetic materials [147]. If one moment is disturbed from its equilibrium position in an array of exchange and dipolar coupled spins, then by the magnetic field produced by this moment, the neighboring moments will also be disturbed. Thus the disturbance will propagate as a wave through the system. This is called the SW. In

Chapter 2

terms of quantum mechanics, SWs are actually the eigenmodes of the exchange Hamiltonian of the system [148]. The Hamiltonian is written as:

$$H' = -2J \sum_{i>j} \mathbf{S}_i \cdot \mathbf{S}_j \quad (2.59)$$

Where \mathbf{S}_i is the spin operator in units of \hbar for the i^{th} atom. The quantum equation of motion for \mathbf{S}_m is:

$$\begin{aligned} i\hbar \frac{d\mathbf{S}_m}{dt} &= [\mathbf{S}_m, H'] \\ \text{or, } i\hbar \frac{d\mathbf{S}_m}{dt} &= 2J \left[\left(\sum \mathbf{S}_i \cdot \mathbf{S}_j \right) \mathbf{S}_m - \mathbf{S}_m \left(\sum \mathbf{S}_i \cdot \mathbf{S}_j \right) \right] \\ \text{or, } i\hbar \frac{d\mathbf{S}_m}{dt} &= 2J \sum_j [(\mathbf{S}_m \cdot \mathbf{S}_j) \mathbf{S}_m - \mathbf{S}_m (\mathbf{S}_m \cdot \mathbf{S}_j)] \\ \text{or, } i\hbar \frac{d\mathbf{S}_m}{dt} &= -2J \sum_j \mathbf{S}_j \times [\mathbf{S}_m \times \mathbf{S}_m] \end{aligned} \quad (2.60)$$

Using the commutation relation $\mathbf{S} \times \mathbf{S} = i\mathbf{S}$, we obtain:

$$\hbar \frac{d\mathbf{S}_m}{dt} = 2J \mathbf{S}_m \times \sum \mathbf{S}_j \quad (2.61)$$

For small distortions, neglecting the higher order terms in the series expansion of eqn. (2.61), we have the equation of motion (in a simple cubic lattice with lattice constant a) for the spin as a classical quantity:

$$\hbar \frac{d\mathbf{S}}{dt} = 2Ja^2 [\mathbf{S} \times \nabla^2 \mathbf{S}] \quad (2.62)$$

Extending eqn. (2.62) one obtains that for any lattice of cubic symmetry having Z nearest neighbors with R_n as the separation between nearest neighbors

$$\hbar \frac{d\mathbf{S}}{dt} = J \frac{ZR_n^2}{3} (\mathbf{S} \times \nabla^2 \mathbf{S}) \quad (2.63)$$

Chapter 2

Let $\mathbf{S} = \mathbf{S}_0 + \boldsymbol{\varepsilon}$, where, \mathbf{S}_0 is the unperturbed spin vector and $\boldsymbol{\varepsilon}$ represents a SW of small amplitude. Substituting in eqn. (2.63) and assuming $\boldsymbol{\varepsilon}/\mathbf{S}_0 \ll 1$, we get:

$$\frac{d^2 \varepsilon_x}{dt^2} = -(ZR_n^2 S_0 J / 3\hbar)^2 \nabla^4 \varepsilon_x \quad (2.64)$$

The above equation is a wave equation and the solutions, *i.e.*, the SWs have the following form:

$$\varepsilon_x = \varepsilon_0 \exp[i(\omega t + \mathbf{k} \cdot \mathbf{r})]$$

Where,

$$\hbar\omega = (ZR_n^2 S_0 J / 3) k^2 \quad (2.65)$$

Hence, we arrive at the fundamental relation between the wave number and frequency of a SW. The SW is quantized and termed as “magnons” in analogy with the quantized lattice vibrations “phonons”. SWs can be used to carry information in the “magnonic crystals”. They are more compatible to the nano-technology as the wavelength of SWs is lesser than that of the light-wave of same frequency. Similar to the phonons, magnonic bands and band gaps are also observed in the magnonic crystals. The magnonic band structure can be controlled to a large extent by controlling the sample structure and the external magnetic field. The study of SWs is a very useful tool to probe the dynamic properties of magnetic materials. Classically, the spin dynamics is governed by the Landau-Lifshitz equation (without damping) under the influence of an effective magnetic field H_{eff} , which incorporates the contributions from both exchange and dipolar interactions. Depending on the wavelength range of interaction, one can have exchange dominated SWs, dipolar-exchange SWs or dipolar SWs.

2.10.1. Exchange SWs

For SWs with short wavelengths (λ) *i.e.*, with long wave-vector k , the interaction is primarily exchange dominated. Due to the strong exchange interaction, all spins are parallel in the ground state. The Heisenberg exchange interaction energy on the p^{th} spin is given by:

Chapter 2

$$-2JS_p \cdot (S_{p-1} + S_{p+1})$$

The torque on that spin is given by:

$$\frac{dS_p}{dt} = \left(\frac{2J}{\hbar}\right) (S_p \times S_{p-1} + S_p \times S_{p+1}) \quad (2.66)$$

For small amplitude of excitation, we have: $S_p^x, S_p^y \ll S$ and $S_p^z \cong S$. Considering harmonic solutions:

$$S_p^x = me^{i(pka - \omega t)}, S_p^y = ne^{i(pka - \omega t)}$$

We can derive the dispersion relation for a lattice with lattice constant a and wave-vector k :

$$\hbar\omega = 4JS(1 - ka) \quad (2.67)$$

At long wave-length limit, $ka \ll 1$ and eqn. (2.67) reduces to:

$$\hbar\omega = (2JSa^2)k^2 \quad (2.68)$$

The dispersion of exchange SW is isotropic in nature.

It can be shown easily [146, 149] that the exchange energy of a SW varies with Dk^2 ,

$$\omega_k/\gamma = H - 4\pi M_s + Dk^2 \quad (2.69)$$

where $D = 2A/M_s$, A being the exchange stiffness constant and M_s is the saturation magnetization.

2.10.2. Exchange SW in thin films - perpendicular standing spin-wave modes

Incorporating the Zeeman and volume dipolar energies, the SW dispersion relation is given by the famous Holstien-Primakoff [150] relation (and later, by Herrings and Kittel [148] in a more rigorous way):

$$\omega_k/\gamma = [(H + Dk^2)(H + Dk^2 + 4\pi M_s \sin^2 \theta_k)]^{1/2} \quad (2.70)$$

Chapter 2

Here, ω_k is the SW frequency, γ is the gyromagnetic ratio and θ_k is the polar angle between \mathbf{H} and \mathbf{k} . For SW propagation parallel to \mathbf{H} , $\theta_k = 0$ and eqn. (2.70) reduces to:

$$\omega_k = \gamma(H + Dk^2) \quad (2.71)$$

The above equation does not contain any contribution from the dipolar interactions. These types of pure exchange dominated SW modes are often observed in thin films, where they propagate perpendicular to the film surface and form standing wave pattern. They are termed as perpendicular standing SW (PSSW) modes. The wave vector k_{\perp} perpendicular to the film is quantized and assumes values $k_{\perp,l} = l\pi/d$ ($l =$ positive integer and $d =$ film thickness) for both pinned and unpinned boundary conditions. For general boundary conditions [146], the expression for $k_{\perp,l}$ is quite complicated.

2.10.3. Dipolar SWs

Referring to eqn. (2.70), for any $\theta_k \neq 0$, we have contributions from dipolar interaction along with the exchange interaction. If the wavelength of the SWs becomes long (give range of values), then we have primarily dipolar SWs. Conditions under which the exchange interaction and electromagnetic induction can be neglected were explained by Walker [151]. The magnetostatic condition assumed is valid over a considerable wavelength range. The dispersion relations for magnetostatic modes are obtained by the simultaneous solution of Maxwell's equations and the equation of motion of magnetization (the LLG equation) under proper boundary conditions [152].

In the magnetostatic limit, Maxwell's equations read:

$$\begin{aligned} \nabla \times \mathbf{H} &= 0 \\ \nabla \cdot (\mathbf{H} + 4\pi\mathbf{M}_s) &= 0 \end{aligned} \quad (2.72)$$

The magnetization may be written in the form:

$$\mathbf{M}(\mathbf{R}, t) = \mathbf{M}_s + \mathbf{m}(\mathbf{R}, t) \quad (2.73)$$

Chapter 2

Here, $\mathbf{m}(\mathbf{R}, t)$ is the variable part of the total magnetization. If the precession angle is small, the $\mathbf{m}(\mathbf{R}, t) \ll \mathbf{M}_s$, and can be expanded in a series of plane waves of magnetization, or SWs:

$$\mathbf{m}(\mathbf{R}, t) = \sum_k \mathbf{m}_k(t) e^{ik \cdot \mathbf{R}} \quad (2.74)$$

Under this approximation, the LLG equation can be linearized and solved to obtain a discrete set of dispersion curves. We define the co-ordinate system such that the X-axis is perpendicular to the film and the external field \mathbf{H} along Z-direction is in-the-plane of the film. Due to broken translational symmetry at the boundaries, the modes for a finite slab of thickness d are modified with respect to eqn. (2.70) giving rise to two sets of modes [153-154] – 1) surface modes and 2) volume modes.

Let us define:

$$\begin{aligned} \Omega_H &= H/4\pi M_s \\ \Omega_B &= \sqrt{[\Omega_H(\Omega_H + 1)]} \\ \Omega_S &= \Omega_H + 1/2 \end{aligned} \quad (2.75)$$

The component k_x no longer remains a continuous variable but takes on discrete values as determined by the boundary conditions. The series of modes, lying between Ω_H and Ω_B , are the bulk SW manifold in the low k limit. For k and M_s collinear in the film plane, a mode with negative dispersion is obtained. This is called the backward volume magnetostatic (BWVMS) mode and the corresponding dispersion relation is given by [155-156]:

$$\omega_B = \gamma \sqrt{H \left[H + 4\pi M_s \left(\frac{1 - e^{-2kd}}{kd} \right) \right]} \quad (2.76)$$

This mode becomes the usual FMR mode or the Kittel mode Ω_B for $k = 0$. Again, if k is in the plane of the sample and M_s is perpendicular to the sample, then the corresponding mode is the forward volume magnetostatic (FWVMS) mode with the dispersion relation:

Chapter 2

$$\omega_F = \gamma \sqrt{(H - 4\pi M_s) \left[H - 4\pi M_s \left(\frac{1 - e^{-2kd}}{kd} \right) \right]} \quad (2.77)$$

When both k and M_s are in-the-plane of the sample but perpendicular to each other, we get the magnetostatic surface wave (MSSW) mode or the Damon-Eshbach mode with the unique properties - 1) surface character, 2) non-reciprocal propagation, 3) disappears beyond a critical angle $\theta_c = \tan^{-1}(4\pi M_s/H)$ and 4) frequencies above the upper edge of the SW manifold. The dispersion relation is given by [155]:

$$\omega_{DE} = \gamma \sqrt{[H(H + 4\pi M_s) + (2\pi M_s)^2(1 - e^{-2kd})]} \quad (2.78)$$

The amplitude is primarily concentrated near the surface and decays exponentially away from the surface.

$$\text{For } k \rightarrow \infty, \quad (\omega_{DE})_{k=\infty} = \gamma(H + 2\pi M_s) \quad (2.79)$$

$$\text{For } k = 0, \quad (\omega_{DE})_{k=0} = \gamma \sqrt{H(H + 4\pi M_s)} \quad (2.80)$$

Observe that, as $k \rightarrow 0$, the mode reduces to the Kittel mode. Hence, the surface mode becomes a volume mode of the sample for very small values of k .

2.11. Magneto-optical Kerr effect (MOKE)

The Faraday effect [157] is the first ever observed magneto-optical effect which states that when a linearly polarized beam is transmitted through a magnetized material, the plane of polarization of the beam is rotated to give an elliptically polarized light. Later, in 1877, it was found that the same thing happens in the reflection geometry also. Upon reflection from a magnetized sample, a plane polarized light can be converted to an elliptically polarized light. This phenomenon is called the Kerr effect [158] and the corresponding rotation of the plane of polarization is called the Kerr rotation. As defined in Fig. 2.12(a), Both the Kerr rotation (θ_k) and ellipticity (ϵ_k) give a measure of the magnetization of the sample. Ever since, after its discovery, MOKE has found to be a very efficient technique to probe magnetization dynamics at various time-scales and image magnetic domains. This

Chapter 2

effect is significantly enhanced when the magnetized material is a ferromagnetic one [159]. The magneto-optical interaction introduces an orthogonal component k in the electric field vector of the reflected light both in- and out-of- phase to that of the reflected light r . The in-phase component gives rise to the Kerr rotation whereas the out-of-phase component is responsible for the Kerr ellipticity [160]. Depending on the relative orientations of the plane of incidence and magnetization (M) of the sample, there are three important geometries of MOKE as illustrated in Fig. 2.12[(b)-(d)]: i) longitudinal MOKE, ii) transverse MOKE and iii) polar MOKE. In the longitudinal case, M lies in the sample plane and parallel to the plane of incidence. In the polar geometry, M is perpendicular to the sample plane. The longitudinal and polar Kerr effects are characterized by a rotation of the plane of polarization; the amount of rotation is proportional to the component of magnetization parallel to the plane of incidence. The Kerr rotation (θ_k) and ellipticity (ε_k) can be expressed as $\theta_k + i\varepsilon_k = k/r$, when $k \gg r$ [160-161]. The longitudinal and polar MOKE occur for both p - and s -polarized lights whereas the transverse effect occurs only for p -polarized light. In the transverse geometry, M lies in the sample plane but perpendicular to the plane of incidence. This effect involves a change in the reflectivity of the light polarized parallel to the plane of incidence, not a rotation of the polarization. This change in reflectivity for the transverse effect depends upon the magnetization component perpendicular to the plane of incidence.

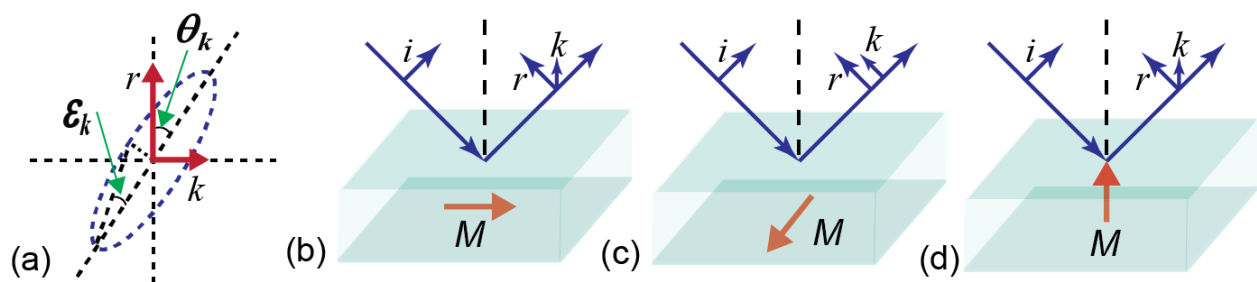


Fig. 2.12: (a) Geometry for the Kerr rotation (θ_k) and Kerr ellipticity (ε_k). (b-d) Different MOKE geometries - (b) Longitudinal MOKE, (c) Transverse MOKE and (d) Polar MOKE. i = incident electric field vector, r = reflected electric field vector, k = induced (due to MOKE effect) orthogonal component in the reflected electric field vector (both in and out of phase to r).

Chapter 2

As a powerful tool for probing the ultrafast magnetization dynamics, it caught huge attention of researcher. There are many theories which explain the origin of magneto-optical effects in FMs. This includes the band theory of metals [162] and macroscopic theory considering off-diagonal terms in the dielectric tensor [163-164].

2.11.1. Physical origin

The physical origin of magneto-optic effects may be explained by the magnetic circular dichroism effect. Consider the incident light is linearly polarized along the +X direction and is propagating along Z direction as shown in Fig. 2.13. This linearly polarized light can be expressed as a superposition of a right-circularly polarized (RCP) and left-circularly polarized (LCP) light. In absence of any external field, the expression of the linearly polarized light reads as [165]:

$$E^{inc} = \frac{E_+^{inc}}{2} (\hat{e}_x + j\hat{e}_y) e^{j(\omega t - kz)} + \frac{E_-^{inc}}{2} (\hat{e}_x - j\hat{e}_y) e^{j(\omega t - kz)} \quad (2.81)$$

With

$$RCP \text{ part amplitude } E_+^{inc} = LCP \text{ part amplitude } E_-^{inc}$$

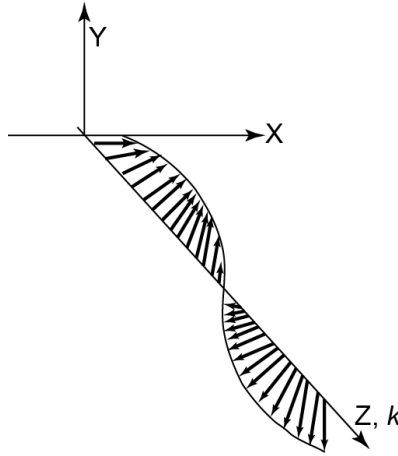


Fig. 2.13: The incident light - linearly polarized along the +X direction and propagating along Z direction.

As the light propagates through the medium, the electric field generated sets electrons into motion. The RCP electric field leads to right-circular electron motion and LCP electric field

Chapter 2

drives the electrons in left-circular electron motion. In absence of an external magnetic field, the radii of these two circular motions become equal leading to a zero difference in the dielectric constants. However, in presence of an external magnetic field, this scenario changes. The electrons will feel an additional Lorentz force due to the external magnetic field. This will in turn affect the radii of the left- and right-circular path. As a consequence, there will be a finite difference in the dielectric constants of the left- and right-circularly polarized modes [161]. The refractive indices of RCP and LCP lights also turn out to be different in the presence of the external magnetic field. The expressions for the refractive indices in presence of a field, following Larmor's theorem, are obtained as:

$$n_{\pm}(\omega) = n(\omega \pm \omega_L) \quad (2.82)$$

Where, the "+" sign refers to the RCP part and "-" refers to the LCP part. The amplitudes of the RCP and LCP reflected components are given by [166]:

$$E_+^{ref} = \frac{n_+ - 1}{n_+ + 1} E_+^{inc} \quad (2.83)$$

$$E_-^{ref} = \frac{n_- - 1}{n_- + 1} E_-^{inc}$$

Hence, the amplitude (and phase also) of each component is altered upon reflection. So, the reflected beam no longer remains a linearly polarized beam, but becomes an elliptically polarized light – hence, gives rise to the Kerr effect. The angle, by which the major axis of the polarization ellipse is rotated from the original linear polarization axis, is the Kerr angle θ_k .

2.11.2. Phenomenological origin

The dielectric tensor ϵ and optical susceptibility χ – are the two parameters, which can describe the optical response of a material completely. The dielectric tensor can be decomposed in a symmetric and an antisymmetric part. For an isotropic medium, the three eigenvalues are same and the dielectric tensor becomes a dielectric constant. The normal modes of the symmetric part, being linearly polarized lights, do not give rise to magneto-optic effects [167]. The generalized form of ϵ can be obtained using Euler's formula:

Chapter 2

$$\epsilon = \epsilon_{xx} = \begin{pmatrix} 1 & -iQm_z & iQm_y \\ iQm_z & 1 & -iQm_x \\ -iQm_y & iQm_x & 1 \end{pmatrix} \quad (2.84)$$

Where $Q = i \epsilon_{xy}/\epsilon_{xx}$ is the magneto-optic constant and $\mathbf{m} = (m_x, m_y, m_z)$ is the unit vector of magnetization. The normal modes of this antisymmetric part are the left (ϵ_L) and right (ϵ_R) circularly polarized lights, expressed as:

$$\begin{aligned} \epsilon_L &= 1 - Q\mathbf{m} \cdot \mathbf{k} \\ \epsilon_R &= 1 + Q\mathbf{m} \cdot \mathbf{k} \end{aligned} \quad (2.85)$$

The difference between these two gives rise to the magneto-optic effects. The Fresnel reflection matrix \mathbf{R} is used to derive the expression for the Kerr effect. The off-diagonal terms of this matrix originate from the SO coupling. Solving Maxwell's equations for the matrix in eqn. (2.84), \mathbf{R} , in the basis of s and p -polarized lights, is obtained as:

$$\mathbf{R} = \begin{pmatrix} r_{pp} & r_{ps} \\ r_{sp} & r_{ss} \end{pmatrix} \quad (2.86)$$

The complex Kerr angles for s - and p - polarized lights are:

$$\begin{aligned} \theta_K^s &\equiv \theta_K^s + i\epsilon_K^s = \frac{r_{ps}}{r_{ss}} \\ \theta_K^p &\equiv \theta_K^p + i\epsilon_K^p = \frac{r_{sp}}{r_{pp}} \end{aligned} \quad (2.87)$$

The expressions for Kerr rotation for different MOKE geometries can be found in [164]. We shall present here the final expressions of the Kerr angle for few cases for a thin magnetic film. For three mediums – medium 0, medium 1 and medium 2, we denote the incident and transmitted angles by $\theta_0, \theta_1, \theta_2$ and refractive indices by n_0, n_1 and n_2 .

- *Polar configuration ($m_z = 1, m_x = m_y = 0$):*

The expressions for the complex Kerr angles are:

$$\theta_{K,pol}^s = \left(\frac{r_{ps}}{r_{ss}}\right)_{pol} = \frac{-\cos \theta_0}{\cos(\theta_0 - \theta_2)} \cdot \cos \theta_2 \cdot \Phi$$

Chapter 2

$$\theta_{K,pol}^p = \left(\frac{r_{sp}}{r_{pp}}\right)_{pol} = \frac{\cos \theta_0}{\cos(\theta_0 + \theta_2)} \cdot \cos \theta_2 \cdot \Phi$$

With

$$\Phi = \frac{4\pi n_0 n_1^2 Q d}{\lambda(n_2^2 - n_0^2)}, \quad d = \text{thickness of the magnetic medium}$$

- *Longitudinal configuration* ($m_y = 1, m_x = m_z = 0$):

The expressions for the complex Kerr angles are:

$$\theta_{K,long}^s = \left(\frac{r_{ps}}{r_{ss}}\right)_{long} = \frac{\cos \theta_0}{\cos(\theta_0 - \theta_2)} \cdot \frac{\sin^2 \theta_1}{\sin \theta_2} \cdot \Phi$$

$$\theta_{K,long}^p = \left(\frac{r_{sp}}{r_{pp}}\right)_{long} = \frac{\cos \theta_0}{\cos(\theta_0 + \theta_2)} \cdot \frac{\sin^2 \theta_1}{\sin \theta_2} \cdot \Phi$$

2.10.3. Quantum mechanical origin

In quantum mechanics, the Kerr effect is explained [168] in terms of microscopic electronic structure based on the Fermi Golden rule [169] or by the Kubo formalism [170]. Simultaneous occurrence of exchange splitting and SO coupling is responsible for the Kerr effect. The MOKE is related to the off-diagonal components of the optical conductivity tensor. This tensor has the form:

$$\sigma(\omega) = \begin{bmatrix} \sigma_{xx}(\omega) & \sigma_{xy}(\omega) & 0 \\ -\sigma_{xy}(\omega) & \sigma_{xx}(\omega) & 0 \\ 0 & 0 & \sigma_{zz}(\omega) \end{bmatrix} \quad (2.88)$$

Here, the Z-axis is perpendicular to the sample. The complex Kerr angle is defined as:

$$\theta_K \equiv \theta_K + i\varepsilon_K \quad (2.89)$$

For a film of thickness d , its expression is obtained as:

$$\theta_K = \frac{i\sigma_{xy}}{\sigma_{xx}^s} \frac{4\pi d}{\lambda} \quad (2.90)$$

Chapter 2

Here, σ_{xx}^s is the optical conductivity of the substrate and λ is the wavelength of light. This expression is valid only for $\lambda \gg d$.

The real part $\sigma'(\omega)$ and the imaginary part $\sigma''(\omega)$ of the conductivity tensor are even and odd, respectively, with respect to ω and are linked by the Kramers-Kronig relations. The dissipative part of the off-diagonal component of the conductivity tensor (for $\omega > 0$), for an optical transition from the initial state i to the final state f due to the absorption of a photon, is given by:

$$\sigma_{xy}''(\omega) = \frac{\pi e^2}{4\hbar\omega m^2 \Omega} \sum_{i,f} f(\varepsilon_i)[1 - f(\varepsilon_f)] \times [\langle i|p_-|f\rangle^2 - \langle i|p_+|f\rangle^2] \delta(\omega_{fi} - \omega) \quad (2.91)$$

where $p_{\pm} \equiv p_x \pm ip_y$, $f(\varepsilon)$ is the Fermi-Dirac function, Ω is the total volume and $\hbar\omega_{fi} \equiv \varepsilon_f - \varepsilon_i$. The factor $\delta(\omega_{fi} - \omega)$ takes energy conservation into account. The matrix elements $\langle i|p_-|f\rangle$ and $\langle i|p_+|f\rangle$ correspond to dipolar electric transitions for right and left circularly polarized lights. Clearly, $\sigma_{xy}''(\omega)$ is proportional to the difference of absorption probabilities of the right and left circularly polarized lights and hence, gives rise to the Kerr effect.

3. Numerical methods

3.1. Introduction

For uniformly magnetized samples such as continuous thin films, the magnetization dynamics can be investigated under the macrospin formalism described in section 2.9. of chapter 2. The non-linear ordinary differential LLG equation is linearized under small angle approximation to extract the spin-wave (SW) frequency and other material parameters. However, for materials with finite size, the situation is significantly different. Finite boundaries result in the occurrence of uncompensated dipoles at the surface. These dipoles produce a demagnetizing field opposite to the external field. The resultant internal magnetic field becomes inhomogeneous with profile depending on the sample geometry. This demagnetizing field is primarily the origin of the dipolar anisotropy and its determination is extremely crucial for the investigation of SWs. This, in turn, affects the SW spectra significantly. Many existing literatures point at the importance of taking this demagnetizing field into account for a proper understanding of the magnetization dynamics [171-175]. Subsequently, various methods have been developed to determine the local demagnetizing field profile for samples of various shapes [64, 176-180]. One of the most popular methods is the micromagnetic simulations. The micromagnetics was developed by scientists to bridge the gap between the macrospin formalism and the discrete spin model (quantum mechanical approach). However, micromagnetic simulations are basically some sort of numerical experiments and hence, are applicable for samples with small dimensions only. On the other hand, the existing theoretical models, under some assumptions, determine the SW spectra and allow correlating the physical parameters of the modeled system with the SW spectra. Below, we shall discuss briefly about two such theoretical models, namely the Discrete Dipole Approximation (DDA) method and Plane Wave Method (PWM). We shall also discuss about two micromagnetic simulators which we have used for the analyses of the experimental results presented in this thesis.

3.2. Discrete dipole approximation (DDA) method

In this method, the system under study is considered as a set of discrete magnetic dipoles μ_r regularly arranged in sites \mathbf{r} of a crystalline structure [181-183]. Say, X-Y plane defines the base of the system and Z is the normal direction as shown in Fig. 3.1.

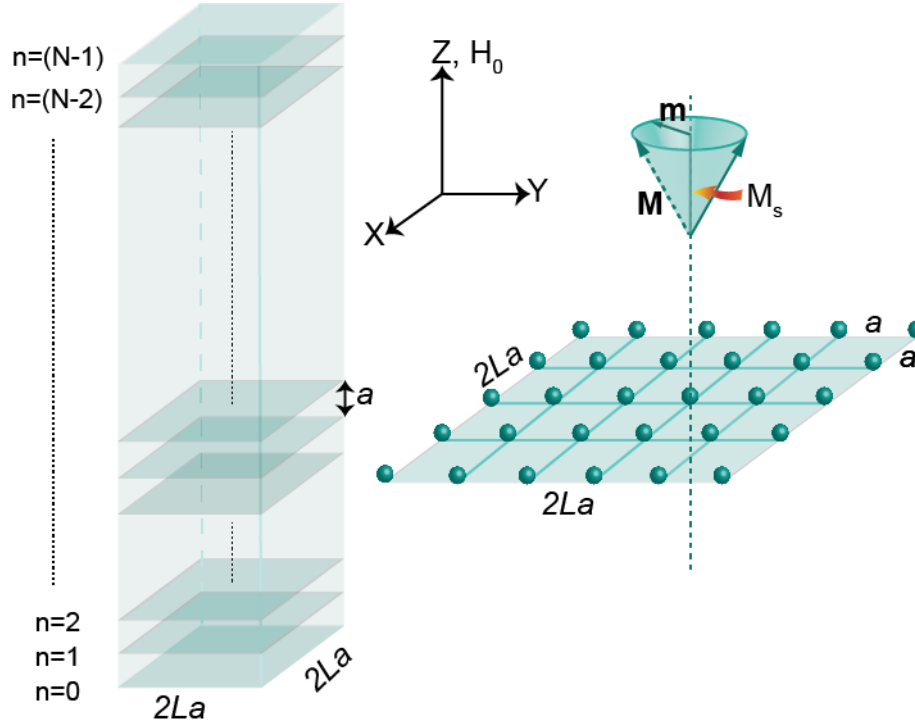


Fig. 3.1: Example of a square rod under the DDA model. The rod has a dimension $2La \times 2La \times (N-1)a$, where a is the lattice constant. All the moments in each lattice plane point to the Z direction due to the applied bias field H_0 . M_s is the static magnetization of the sample and $\mathbf{m} = \mathbf{M}/M_s$. The magnetostatic waves are assumed to propagate along the Z direction.

The dipolar energy is calculated by summing the contributions from each dipolar lattice plane parallel to the base. According to classical formula [184], the magnetic field \mathbf{h}_ρ produced by all dipoles at a site ρ is given by:

$$\mathbf{h}_\rho = \frac{1}{4\pi} \sum_{\mathbf{r} \neq \rho} \frac{3(\mathbf{r} - \rho)(\mu_r \cdot (\mathbf{r} - \rho)) - \mu_r |\mathbf{r} - \rho|^2}{|\mathbf{r} - \rho|^5} \quad (3.1)$$

Chapter 3

The lattice planes parallel to the base are numbered by $n \in \langle 0, N - 1 \rangle$. Sites within each plane are denoted by $\mathbf{r}_{\parallel} = a[p\hat{i} + q\hat{j}]$ with integers $p, q \in \langle -L, +L \rangle$. Hence, the position of a magnetic dipole in the system, with lattice constant a , is given by:

$$\mathbf{r} \equiv [\mathbf{r}_{\parallel}, an] \equiv a[p, q, n], \quad p, q \in \langle -L, +L \rangle \text{ and } n \in \langle 0, N - 1 \rangle \quad (3.2)$$

Therefore, we have $N(2L+1)^2$ number of magnetic moments in the system. It is assumed that the Z axis is the only allowed direction of propagation and magnetic field \mathbf{h} along Z is calculated. Hence, $\rho = a[0, 0, n']$ where $n' \in \langle 0, N - 1 \rangle$ and reindex the dipolar field $\mathbf{h}_{n'} \equiv \mathbf{h}_{\rho}$. Now,

$$\mathbf{r} - \rho = a(p\hat{i} + q\hat{j} + (n - n')\hat{k}) \quad (3.3)$$

It is further assumed that all the magnetic moments, within a particular plane, are identical, *i.e.*,

$$\boldsymbol{\mu}_n \equiv \boldsymbol{\mu}_{[p,q,n]}, \text{ for any } p \text{ and } q \quad (3.4)$$

This assumption also implies that magnetic excitations propagating in-plane are excluded.

In the next step, a symmetric structural matrix with elements $D_{n,n'}$ is introduced and defined as:

$$D_{n,n'} \equiv \sum'_{p,q} \frac{\frac{1}{2}(p^2 + q^2) - (n - n')^2}{[(p^2 + q^2) + (n - n')^2]^{5/2}} \quad (3.5)$$

Exclusion of the reference point $[0, 0, n']$ from the summing is indicated by the prime symbol. The magnetic field, in terms of this matrix, can be written as:

$$\mathbf{h}_{\rho} \equiv \mathbf{h}_{n'} = \frac{1}{4\pi} \sum_n \left[D_{n,n'} \frac{\hat{i}\mu_n^x + \hat{j}\mu_n^y - 2\hat{k}\mu_n^z}{a^3} \right] \quad (3.6)$$

In this model, magnetization is introduced in a phenomenological manner. For the case of a simple cubic lattice, it can be defined as $\mathbf{M}_n = \boldsymbol{\mu}_n/a^3$. Then, eqn. (3.6) becomes:

Chapter 3

$$\mathbf{h}_{n'} = \frac{1}{4\pi} \sum_n D_{n,n'} [iM_n^x + jM_n^y - 2\hat{k}M_n^z] \quad (3.7)$$

Eqn. (3.5) defines the *dipolar matrix* D with elements $D_{n,n'}$. Magnetic mode properties are deduced with the help of this matrix. This matrix is symmetric: $D_{n,n'} \equiv D_{n',n}$. Defining $\delta = n - n'$, the measure of the distance between two planes, with $0 \leq n' + \delta \leq N - 1$, equation (3.5) can be rewritten as:

$$D_\delta \equiv D_{n,n'} \equiv D_{n',n} \equiv D_{-\delta} = \sum'_{p,q} \frac{\frac{1}{2}(p^2 + q^2) - \delta^2}{[(p^2 + q^2) + \delta^2]^{5/2}} \quad (3.8)$$

Let us assume that the sample is under an external magnetic field H_0 along the Z axis. If H_0 is strong enough to orient all moments precessing about Z axis, then the magnetization vector can be decomposed into two components: i) static part M_s parallel to Z axis and ii) dynamic part \mathbf{m} lying in the X-Y plane as shown in Fig. 3.1:

$$\mathbf{M}_{n'} = M_s \hat{k} + \mathbf{m}_{n'} \quad (3.9)$$

M_s is homogeneous throughout the sample and $|\mathbf{m}| \ll M_s$. Similarly, $\mathbf{h}_{n'}$ can also be decomposed into static and dynamic parts: $\mathbf{h}_{n'} = \mathbf{h}_{n'}^s + \mathbf{h}_{n'}^d$. Using eqn. (3.7), one can deduce:

$$\begin{aligned} \mathbf{h}_{n'}^s &= -\left[\frac{1}{2\pi} \sum_n D_{n,n'}\right] M_s \hat{k} \\ \mathbf{h}_{n'}^d &= \frac{1}{4\pi} \sum_n D_{n,n'} \mathbf{m}_n \end{aligned} \quad (3.10)$$

The dynamics of a magnetic moment is governed by the Landau-Lifshitz (LL) equation (without damping, eqn. (2.43)):

$$\frac{\partial \mathbf{M}_{n'}}{\partial t} = \gamma \mu_0 \mathbf{M}_{n'} \times \mathbf{H}_{eff,n'} \quad (3.11)$$

Chapter 3

The effective magnetic field $\mathbf{H}_{eff,n'}$ acting on a magnetic moment in the plane n' is primarily a superposition of H_0 and $\mathbf{h}_{n'}$ in the magnetostatic limit.

$$\mathbf{H}_{eff,n'} = \mathbf{H}_0 + \mathbf{h}_{n'} = (H_0 + h_{n'}^s)\hat{k} + \mathbf{h}_{n'}^d \quad (3.12)$$

Combining eqns (3.9), (3.11) and (3.12), LL equation becomes:

$$\frac{\partial \mathbf{m}_{n'}}{\partial t} = \gamma \mu_0 (M_s \hat{k} + \mathbf{m}_{n'}) \times (H_0 + h_{n'}^s)\hat{k} + \mathbf{h}_{n'}^d \quad (3.13)$$

The above equation is solved under linear approximation. The problem finally reduces to an eigenvalue equation. The eigenvalues give the frequencies of the magnetostatic modes propagating along the direction of the applied field.

3.3. Plane wave method (PWM)

The PWM is an extremely useful method for determining excitation spectra in systems with discrete translational symmetry [185-189]. The conceptual simplicity and its applicability to any type of lattice, any shape of scattering centers and various dimensions of the periodicity make this method popular among researchers. Its formulation is based on the expansion of the eigenvectors in terms of superposition of plane waves.

For the calculation of SW spectra in magnonic crystals (MCs), we will start with the phenomenological LL equation as mentioned in eqn. (3.11). In this case, M and H_{eff} are functions of position vector \mathbf{r} and time t , so

$$\frac{\partial \mathbf{M}(\mathbf{r}, t)}{\partial t} = \gamma \mu_0 \mathbf{M}(\mathbf{r}, t) \times \mathbf{H}_{eff}(\mathbf{r}, t) \quad (3.14)$$

SW dispersion is calculated using the equation mentioned above. As discussed in the previous section, the effective magnetic field consists of the Zeeman field ($H_0 \hat{k}$), anisotropy field, exchange field (H_{ex}) and the magnetostatic field (H_d). Both M and H_d can be decomposed into a static and a dynamic part:

Chapter 3

$$\begin{aligned}\mathbf{M}(\mathbf{r}, t) &= M_s \hat{\mathbf{k}} + \mathbf{m}(\mathbf{r}, t) \\ H_d &= H_{ms}(r) + h_{ms}(\mathbf{r}, t)\end{aligned}\tag{3.15}$$

In the magnetostatic approximation, using Maxwell's equations, we have:

$$\begin{aligned}\nabla \times \mathbf{h}_{ms}(\mathbf{r}, t) &= 0 \\ \nabla \cdot (\mathbf{h}_{ms}(\mathbf{r}, t) + \mathbf{m}(\mathbf{r}, t)) &= 0\end{aligned}\tag{3.16}$$

The exchange contribution can be written in terms of the exchange length λ_{ex} as:

$$\begin{aligned}\mathbf{H}_{ex}(\mathbf{r}, t) &= (\nabla \cdot \lambda_{ex}^2(\mathbf{r}, t) \nabla) \mathbf{M}(\mathbf{r}, t) \\ \text{where,} \quad \lambda_{ex} &= \sqrt{\frac{2A}{\mu_0 M_s^2}}\end{aligned}\tag{3.17}$$

A is the exchange stiffness constant. Hence, neglecting anisotropy, the effective field takes the form:

$$\mathbf{H}_{eff}(\mathbf{r}, t) = H_0 \hat{\mathbf{k}} + (\nabla \cdot \lambda_{ex}^2(\mathbf{r}, t) \nabla) \mathbf{M}(\mathbf{r}, t) + \mathbf{h}_{ms}(\mathbf{r}, t)\tag{3.18}$$

Eqn. (3.14) is solved with this effective field under linear approximation. In PWM, the search is all about a solution in the form of monochromatic SW: $\mathbf{m}(\mathbf{r}, t) \sim e^{i\omega t}$, ω being the wave frequency. The dynamic component of H_d also has the same form of time dependence: $\mathbf{h}_{ms}(\mathbf{r}, t) = \mathbf{h}_{ms}(\mathbf{r}) e^{i\omega t}$.

Using linear approximation, from eqns (3.14) and (3.16), we get:

$$\begin{aligned}i\Omega m_x(\mathbf{r}) + \frac{1}{H_0} M_s [\nabla \cdot \lambda_{ex}^2 \nabla] m_y(\mathbf{r}) - m_y(\mathbf{r}) - \frac{1}{H_0} m_y(\mathbf{r}) \times [\nabla \cdot \lambda_{ex}^2 \nabla] \cdot M_s \\ + \frac{M_s}{H_0} \frac{\partial \psi(\mathbf{r})}{dy} = 0\end{aligned}\tag{3.19}$$

$$\begin{aligned}i\Omega m_y(\mathbf{r}) - \frac{1}{H_0} M_s [\nabla \cdot \lambda_{ex}^2 \nabla] m_x(\mathbf{r}) + m_x(\mathbf{r}) + \frac{1}{H_0} m_x(\mathbf{r}) \times [\nabla \cdot \lambda_{ex}^2 \nabla] \cdot M_s \\ - \frac{M_s}{H_0} \frac{\partial \psi(\mathbf{r})}{dx} = 0\end{aligned}\tag{3.20}$$

Chapter 3

$$\nabla^2 \psi(\mathbf{r}) - \left[\frac{\partial m_x(\mathbf{r})}{\partial x} + \frac{\partial m_y(\mathbf{r})}{\partial y} \right] = 0 \quad (3.21)$$

$\psi(\mathbf{r}, t)$ is the magnetostatic potential and Ω is a dimensionless parameter called as the reduced frequency defined as:

$$\Omega = \frac{\omega}{|\gamma| \mu_0 H_0} \quad (3.22)$$

In the MC, it is assumed that M_s and λ_{ex} values are periodic functions of the in-plane position vector with a period equal to “ a ”.

$$M_s(\mathbf{r} + \mathbf{a}) = M_s(\mathbf{r}), \quad \lambda_{ex}^2(\mathbf{r} + \mathbf{a}) = \lambda_{ex}^2(\mathbf{r}) \quad (3.23)$$

Eqns (3.19)-(3.21) will be solved by the PWM. Following Bloch theorem we have, the solution of a differential equation with periodic coefficients can be represented as a product of plane wave functions and a periodic Bloch function:

$$\mathbf{m}(\mathbf{r}) = \mathbf{m}_k(\mathbf{r}) e^{i\mathbf{k} \cdot \mathbf{r}} = \sum_{\mathbf{G}} \mathbf{m}_k(\mathbf{G}) e^{i(\mathbf{k} + \mathbf{G}) \cdot \mathbf{r}} \quad (3.24)$$

$$\psi(\mathbf{r}) = \psi_k(\mathbf{r}) e^{i\mathbf{k} \cdot \mathbf{r}} = \sum_{\mathbf{G}} \psi_k(\mathbf{G}) e^{i(\mathbf{k} + \mathbf{G}) \cdot \mathbf{r}}$$

where $m_k(\mathbf{r} + \mathbf{a}) = m_k(\mathbf{r})$ and $\psi_k(\mathbf{r} + \mathbf{a}) = \psi_k(\mathbf{r})$ (3.25)

\mathbf{k} is a wave-vector in the first Brillouin zone and \mathbf{G} denotes the reciprocal lattice vector. The next step is the Fourier transform to map the coefficients M_s and λ_{ex} in eqns (3.19)-(3.21) into the reciprocal space using the formula:

$$M_s(\mathbf{r}) = \sum_{\mathbf{G}} M_s(\mathbf{G}) e^{i\mathbf{G} \cdot \mathbf{r}} \quad (3.26)$$

$$\lambda_{ex}^2(\mathbf{r}) = \sum_{\mathbf{G}} \lambda_{ex}^2(\mathbf{G}) e^{i\mathbf{G} \cdot \mathbf{r}}$$

Chapter 3

When a finite no. of reciprocal lattice vectors are used in the above equations, then the problem reduces to an eigenproblem which can be expressed in a matrix form:

$$\hat{M}\mathbf{m}_k = i\Omega\mathbf{m}_k \quad (3.27)$$

The eigenvalues are Ω . Eqn. (3.27) is solved numerically. However, it is important to put the solutions, obtained by this method, to the convergence test.

3.4. Micromagnetic simulations

Micromagnetism, in a broader sense, is a tool for studying a wide variety of phenomena involving magnetization reversal and dynamics. It is a continuum theory which describes the behavior of magnetization in a significant length-scale which is large enough to replace atomistic magnetic moments by a continuous function of position and small enough to reveal the transitions between magnetic domains. A huge improvement in the availability of large-scale computer power in the mid 1980's led to a tremendous progress in the field of micromagnetic simulations. Numerical simulations based on the finite difference method (FDM) or finite element method (FEM) help to establish a correlation between the local arrangement of magnetic moments and the microstructural features on a length scale of several nanometers.

In micromagnetic simulations, the LLG equation (eqn. (2.44)) is solved assuming the magnetization to be a continuous function of position and deriving relevant expressions for different energy terms involved (section 2.4. of chapter 2). The stable equilibrium state is obtained by minimizing the total Gibb's free energy with respect to the magnetization. Apart from the magnetostatic contribution, all other energy terms depend only locally on the magnetization. Thus direct evaluation of the total Gibb's free energy is expensive in terms of both memory space and time. The magnetostatic field is a long-range interaction and hence its calculation consumes a lot of time. This long-range nature of the interaction can be eliminated by introducing a magnetic vector potential. This long-range interaction free energy functional leads to effective numerical algorithm requiring only limited memory. The expression for the total free energy of the system can be written as:

Chapter 3

$$E_T = \int \left[\frac{A}{M_s^2} (\nabla M)^2 - K_1 \left(u_c \cdot \frac{M}{M_s} \right)^2 - M \cdot H_{ext} + \frac{1}{2\mu_0} (\nabla \times A - M)^2 \right] dV \quad (3.28)$$

M_s , A and K_1 are respectively the saturation magnetization, exchange stiffness constant and anisotropy constant. The first term in eqn. (3.28) is the contribution from the exchange interaction, second term takes into account the uniaxial (along u_c) magnetocrystalline energy, the third term is the Zeeman coupling term and the last term is the magnetostatic term. As the computation of the last term consumes huge time and memory, extremely simplified and regular microstructures (whose periodicity can be used to make the calculation fast) can be used. However, this may introduce artifacts into the simulated results. The computation of the demagnetizing field from the magnetic volume and surface charges is proportional to N^2 in terms of both storage and computation time, where N is the no. of cells into which a system is discretized in FDM or FEM calculations. Fast adaptive algorithms are used in numerical micromagnetics using fast Fourier transform (FFT) or multipole expansion on regular computational grids to speed up the computation. It is evident that this method will not be applicable for finite element based codes due to irregular mesh structure.

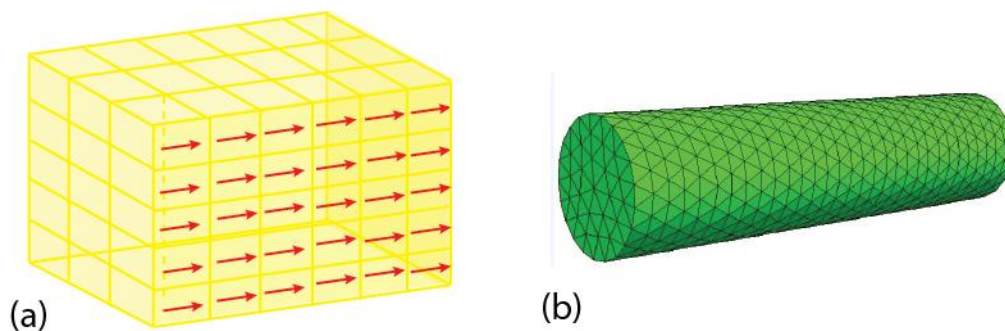


Fig. 3.2: Discretization of a sample into (a) cuboidal cells following finite difference method (FDM) and (b) tetrahedral cells following finite element method (FEM).

There are different simulator packages available as listed below [190]:

Table 3.1: Different simulator packages.

	Name of Simulation	Developer	Calculation Method	Source Websites

Chapter 3

	Code			
Free Software Packages	Object Oriented Micromagne tic Frameworks (OOMMF)	M. Donahue and D. Porter	FDM	http://math.nist.gov/ oommf/
	NMAG	H. Fangohr and T. Fischbacher	FEM	http://nmag.soton.ac. uk
	MAGPAR	Werner Scholtz	FEM	http://magnet.atp.tu wien.ac.at/scholz/ma gpar
Commercial Software Packages	LLG Simulator	M. R. Scheinefein	FDM	http://llgmicro.home. mindspring.com/
	MicroMagus	D.V. Berkov and N. L. Gorn	FDM	http://www.microma gus.de/

To solve a particular problem, one has to choose the appropriate solver to get reliable results [6, 35, 191-204]. A thumb rule is that micromagnetic simulations are valid for time scales > 1 ps and length scales > 1 nm. All the micromagnetic simulation works presented in this thesis are done by FDM by using either the OOMMF software or the LLG micromagnetic simulator software. Below, we will discuss briefly about the FDM, the general algorithm followed in numerical simulations to solve the LLG equation, and OOMF and LLG softwares.

FDM is a popular method to find approximate solutions of partial differential equations. The partial derivatives of a function $u(r, t)$ is replaced by finite difference quotients

Chapter 3

$\Delta x, \Delta y, \Delta z$ and Δt in FDM and this process is known as discretization process with the corresponding error as the discretization error.

$$u(x + \Delta x, y, z, t) = u(x, y, z, t) + \Delta x \frac{\partial u(x, y, z, t)}{\partial x} + \frac{(\Delta x)^2}{2} \frac{\partial^2 u(x, y, z, t)}{\partial x^2} + \dots \quad (3.29)$$

A set of partial differential equations are converted to a set of algebraic equations by the discretization process. The solution or derivative is specified on the boundaries. The approximate solution at any other point is obtained by solving these algebraic equations numerically by some iterative method like Euler's or Runge-Kutta methods.

In order to solve the LLG equation, first the sample is divided into a number of identical cuboidal cells with dimension $<$ the exchange length λ_{ex} of the corresponding material. Each cell is assigned a single spin. In each cell, all differential operators are replaced by FD operators.

For the calculation of the hysteresis loop: First, the sample is saturated by applying a high magnetic field H . This state corresponds to the state with minimum Gibb's free energy. A change in the external field by ΔH amount changes the energy surface by ΔE amount, hence, drives the system out of the equilibrium condition. Unless ΔH is sufficiently high to change the energy by ΔE amount, the position of the system will be close to some local minimum of energy. Once the curvature of the energy surface is altered by ΔE amount, this local minimum vanishes and the system starts to find another minimum energy state following eqn. (2.44). The hysteresis loop is calculated by the repeated minimization of energy for the increasing and decreasing applied field.

For the calculation of magnetization dynamics: To obtain the time evolution of magnetization, eqn. (2.44) is integrated for each cell. After each time step, the local field is calculated in each computational cell. To compute the contribution from the exchange interaction, the first term in eqn. (3.28) is discretized to obtain the following approximate expression:

$$H_{exch,i} = \frac{2A}{\Delta x^2 \cdot M_S^2} \sum_{i \in NN} M_i \quad (3.30)$$

Chapter 3

NN signifies nearest neighbors. The approximation of using finite difference quotients is valid only for small angle of precession. The expression for the contribution of the magnetocrystalline anisotropy is given as:

$$H_{ani} = \frac{2K_1}{M_s^2} u_c (\mathbf{M} \cdot \mathbf{u}_c) \quad (3.31)$$

To calculate the demagnetizing field, in FDM, a dipole is assumed at the center of each cell. The demagnetizing field is given by net field generated by these dipoles:

$$H_{dip} = -\frac{\Delta x^3}{\mu_0 4\pi} \sum_{j \neq i} \left(\frac{M_j}{R_{ij}^3} - 3 \frac{R_{ij} (M_j \cdot R_{ij})}{R_{ij}^5} \right) \quad (3.32)$$

With all these, the Zeeman contribution is added to calculate the local field.

The Object Oriented Micromagnetic Framework (OOMMF) software was developed by Mike Donahue and Don Porter at the National Institute of Standards and Technology, MD in 1999 [205]. All the calculations performed in OOMMF are at $T = 0$ K. This software relies on the C++ compiler. The problem is specified with all the necessary input parameters and initial conditions in a “.mif” file written in the Tcl/Tk script. During the simulation, the magnetization configurations at various steps are updated by the “evolvers”. The OOMMF has primarily two types of evolvers: 1) time evolvers (to handle the LLG equation) and 2) minimization evolvers (to find the local minimum on the energy surface through direct minimization techniques). Evolvers are paired up with corresponding “drivers” to solve a particular problem. Evolvers implement some standard methods to solve the LLG ordinary differential equation. The drivers determine the completion of a simulation stage/run using specified stopping criterion in the input MIF file. The stopping criterion is basically set on the convergence value of the maximum torque $\mathbf{m} \times \mathbf{H}$, where $\mathbf{m} = \mathbf{M}/M_s$. This is achieved by setting a stopping value for the individual stage time or $d\mathbf{m}/dt$ in such a way that the value of the maximum torque goes well below 10^{-6} A/m.

The LLG micromagnetic simulator [206] is another simulation package based on FDM but runs only on Windows operating systems. It is a full 3-D simulation tool. Unlike OOMMF it can incorporate temperature dependence in the simulations by providing an equivalent

Chapter 3

random magnetic field. This feature is extremely useful as quasistatic magnetic properties depend significantly on temperature. It can compute equilibrium magnetization distributions in small particles and in thin films, as well as fundamental properties, such as the coercive field, stray fields, switching time, interlayer coupling strength, vortex and domain-wall lengths. It can also simulate the structure and response of magnetic devices, such as magnetic random access memory, spin valves, AMR and GMR heads, and magnetic sensors. Another advantage of LLG is it can compute standard magnetic imaging contrast mechanisms realized in Lorentz microscopy, electron holography, SEMPA, and magnetic force microscopy. LLG micromagnetic simulator also provides a very easy, yet precise and detail control over the input parameters for complicated structures (*e.g.*, ML structures) unlike OOMMF or NMAG. Here also the convergence criterion is set on the maximum torque $\mathbf{m} \times \mathbf{H} \ll 10^{-6}$ A/m, where $\mathbf{m} = \mathbf{M}/M_s$, which was always reached within the allowed relaxation time. On top of all these features, LLG has various options for an attractive visualization of the simulated results.

3.5. Calculations of power and phase profiles of resonant modes

To investigate the power and phase profiles of the resonant modes, we have used the Dotmag software developed by our group [201-202]. This software uses the output files from the OOMMF software. OOMMF generates a number of “.omf” files which contain the information about the magnetization distribution at a particular time. These files can be used to plot the spatial distribution of magnetization in the sample. However, at a particular time, the profiles show a magnetization map which is a superposition of multiple resonant modes present in the system with proper powers and phases. The extraction of the power or phase profile for a particular resonant mode is a non-trivial job. To perform this job, first, one spatial co-ordinate (either x or y or z) of the time-dependent magnetization is fixed and discrete Fourier transform is performed with respect to time in the Dotmag software. The output files can be now plotted to obtain the space dependent power and phase at discrete frequencies (f). The frequency resolution depends on the total

Chapter 3

simulation time window and the spatial resolution depends on the discretization used during the micromagnetic simulations. During the fast Fourier transform (FFT), if we fix the z co-ordinate at $z = z_1$ to obtain the power and phase distribution in the X-Y plane, then we have:

$$\tilde{M}^{z_1}(f, x, y) = FFT(M^{z_1}(t, x, y)) \quad (3.33)$$

The power and phase profiles for a particular resonant mode at $f = f_r$ can then be expressed as:

$$\text{Power:} \quad P^{z_1, f_r}(x, y) = 20 \log_{10} |\tilde{M}^{z_1}(f_r, x, y)| \quad (3.34)$$

$$\text{Phase:} \quad \Phi^{z_1, f_r}(x, y) = \tan^{-1} \left[\frac{\text{Im}(\tilde{M}^{z_1}(f_r, x, y))}{\text{Re}(\tilde{M}^{z_1}(f_r, x, y))} \right] \quad (3.35)$$

4. Fabrication, synthesis, characterization and measurement techniques

4.1. Introduction

The key challenges to study the static and dynamic magnetic properties of magnetic thin films and nanostructures are the synthesis or fabrication of high quality magnetic thin films and nanostructures and their proper characterization. Technology demands fabrication of nanomagnets with narrow size dispersion and in an ordered array over a macroscopic length scale. The intrinsic static and dynamic magnetic properties depend significantly on the interface quality along with crystallinity, chemical purity and spatial and chemical uniformity of the nanostructures. The other challenge is to develop cost-effective fabrication techniques for high yield. Various fabrication/synthesis techniques have been developed to prepare high quality magnetic nanostructures. Depending upon the requirement, different techniques are used for the sample fabrication for different measurements. Also, a variety of physical properties of the nanostructures needs to be studied thoroughly before any application. Hence, different techniques were used to characterize the surface/interface properties, crystallinity or chemical purity of the samples. Only after a satisfactory characterization, the samples are used for investigating the quasistatic and/or ultrafast magnetization dynamics. In this chapter, we will discuss briefly about some state of the art fabrication and characterization techniques which were used in the works presented in this thesis. We will also discuss about the static and time-resolved magneto-optical Kerr effect microscopes which were developed during the course of this thesis and used to measure the static and dynamic magnetic properties presented in this thesis.

4.2. Fabrication

4.2.1. Sputtering

Sputtering is particularly suitable for preparing good quality magnetic thin films and multilayers (MLs). It is, basically, a multiple collision process involving a cascade of moving target atoms and is schematically shown in Fig. 4.1. It was invented more than 150 years ago [207] as “cathode sputtering”. In sputtering, high energy particles are used to supply kinetic energy to the target to eject material which is subsequently deposited on the substrate. These energized particles remain in the system as a glow diffuse plasma. The plasma is formed due to the ionization of a gas between the cathode and the anode. In terms of the power source used to generate the plasma and the way of manipulating it, the sputtering systems are categorized. We have used the magnetron sputtering. The plasma is actually partially ionized gas consisting of cations, anions and neutral atoms. The overall charge is neutral. In sputtering, the target material is the cathode and the substrate serves as the anode. The breakdown of some inert gas sustains the plasma. Argon is the most widely used working gas. There are two very advantageous properties of the argon gas – i) it has larger mass as compared to neon and helium and ii) it is less expensive as compared to xenon and krypton. The sputter yield S , *i.e.*, the efficiency of the inert gas for sputtering out materials from the target is proportional to the ratio masses of the inert gas (m_1) and the target (m_2) [208]:

$$S \propto \frac{m_1 m_2}{(m_1 + m_2)^2} \quad (4.1)$$

Several conditions have to be fulfilled to have steady plasma. At the beginning, the deposition chamber is evacuated to achieve a base pressure of about 10^{-7} - 10^{-8} Torr. This helps in reducing impurity content in the sputter deposited material. After achieving a satisfactory base pressure, the argon is introduced in the chamber to attain a deposition pressure of few mTorr. In the next step, a negative dc potential of few hundred mV is applied to the cathode. Once an electron acquires sufficient kinetic energy to travel towards the anode, it collides with the argon atoms to form argon ion which, in turn, ignites the plasma. In a magnetron sputtering system, a magnetic field is used to trap secondary

Chapter 4

electrons emitted near the surface. It helps to increase the deposition rate, decrease impurity concentration and achieve deposition at lower substrate temperature. This magnetic field causes the electrons, emitted from the cathode, to travel in a cyclic path between the cathode and the anode. As a result, the working gas, *i.e.*, argon gas undergoes a greater rate of ionization, and hence, a greater rate of sputtering is achieved as compared to the conventional (without magnetron) sputtering.

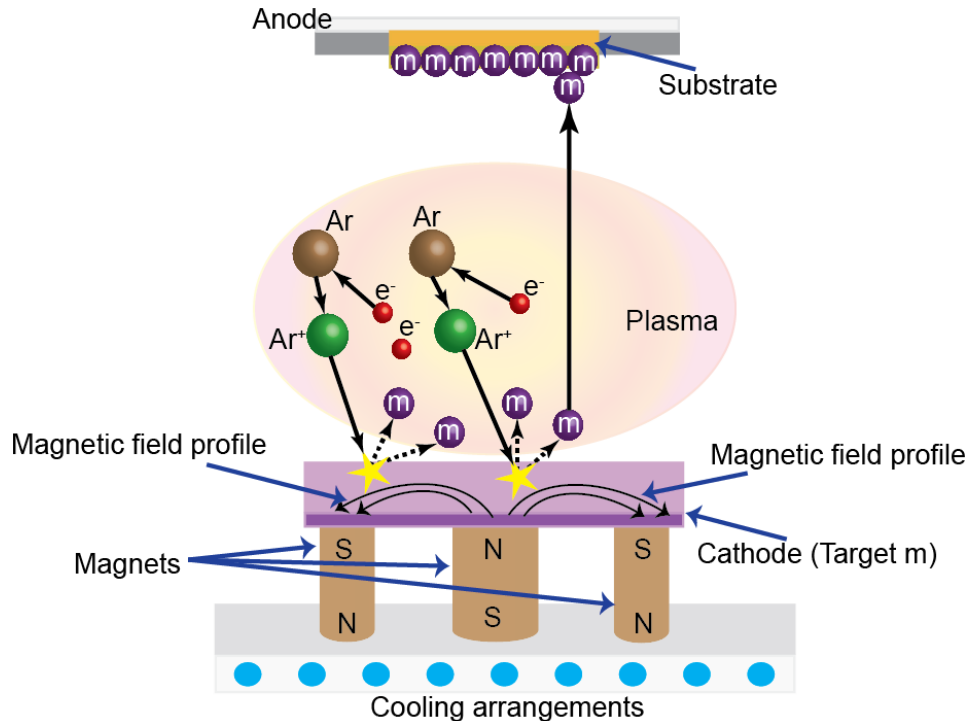


Fig. 4.1: Schematic of the sputtering technique.

4.2.2. Focused ion beam (FIB) milling

Focused ion beam (FIB) milling [209] is a popular tool for fabricating nanoscale patterned samples. We have used the FEI Helios NanoLab™ 600 Dual Beam (FIB/SEM) to fabricate patterned samples like ferromagnetic antidots in our work. This machine is equipped with an extremely high resolution Elstar™ electron column with a Field Emission Gun (FEG) electron source. The capabilities of the FIB for small probe (diameter ~ 5 nm) sputtering are achieved by the liquid metal ion source (LMIS). We have used Ga as LMIS because of the following advantages of Ga:

1. Low melting point.

Chapter 4

2. Low volatility.
3. Low vapor pressure.
4. Excellent electrical, mechanical and vacuum properties.
5. Emission characteristics enable high angular intensity with a small energy spread.

To obtain pattern, the sample is first mounted on a stage and inserted inside the chamber. The chamber is then evacuated to a pressure down to 10^{-6} Torr. The electron pole is placed exactly vertical to the chamber whereas the ion pole is tilted by 45° with respect to the electron pole/chamber [Fig. 4.2(a)]. After achieving the desired vacuum, the sample stage is tilted by 52° to reach the eucentric point as shown in Fig. 4.2(b). In the next step, the electron and ion source voltages (30 kV) are turned on. A particular portion of the sample is then identified which will be patterned and then it is scanned by the Ga ions. After that, the desired pattern is drawn by varying the X, Y and Z coordinates. Here, the Z coordinate controls the thickness. The ion beam current is then adjusted according to the requirement. It must be kept in mind that too much of ion beam current can damage the sample significantly. Finally, the ion beam mills out the material from the exposed areas according to the drawn pattern, thus creating the desired patterned sample.

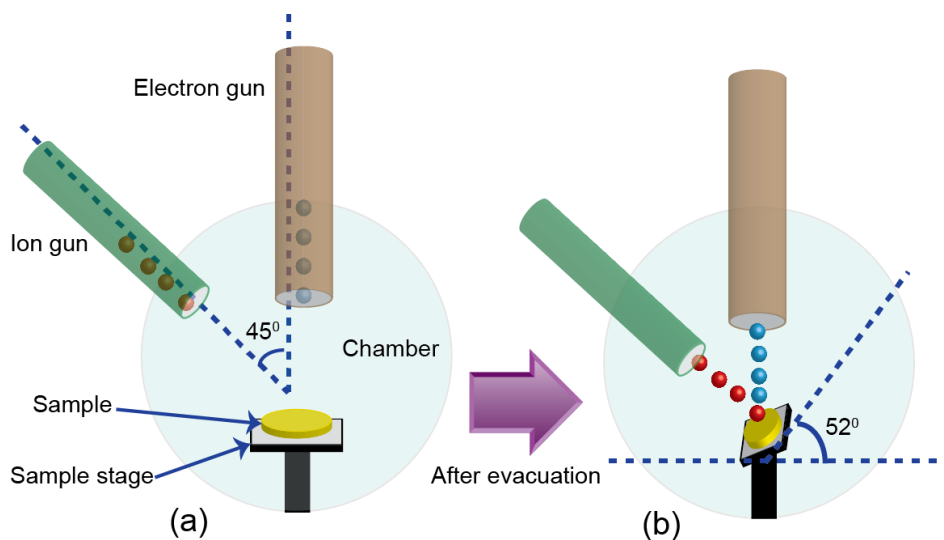


Fig. 4.2: Arrangement of the electron gun, ion gun and sample in the chamber (a) before and (b) after the evacuation.

Chapter 4

4.3. Synthesis

Magnetic nanowires (NWs), studied in the course of this thesis, were synthesized by the electrodeposition technique. Electrodeposition technique for fabrication of nanostructure uses a nanoporous membrane for deposition of material through the pores. It is a very efficient and cost-effective method [87] to produce large aspect ratio NWs at large scales with different diameters, lengths, and crystallinity.

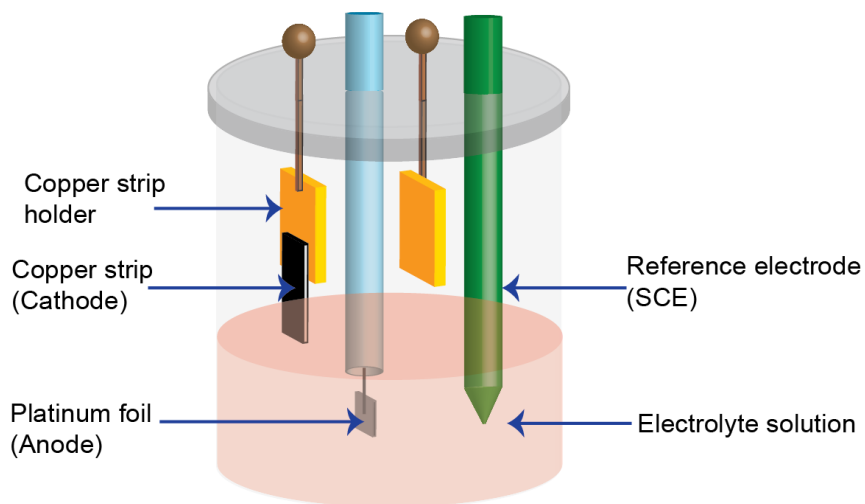


Fig. 4.3: A typical electrodeposition cell.

The limit to which a material can be used as template is defined by its reactivity with the electrolyte used for deposition. Almost any solid matter can be deposited inside the pores of a template. By depositing metals into the pores, NWs with a diameter predetermined by the template pore diameter can be formed.

Electrodeposition is the process of producing a coating, usually metallic, on a surface by the action of electric current. The deposition of a metallic coating onto an object is achieved by putting a negative charge on the object to be coated and immersing it into a solution which contains a salt of the metal to be deposited (in other words, the object to be plated is made the cathode of an electrolytic cell). A schematic of a typical electrodeposition cell is presented in Fig. 4.3. The metallic ions of the salt carry a positive charge and are thus attracted to the object. When they reach the negatively charged object (that is to be electroplated), it provides electrons to reduce the positively charged ions to metallic form.

Chapter 4

Gold coated anodic aluminium oxide (AAO) (Whatman/Synkera Technologies) [210] and polycarbonate track etched (PCTE) (Whatman) membranes attached either on gold coated glass slides or copper strips are used as the working electrode in our study. A 250ml beaker is used for containing the electrolyte solution. It is covered by a glass plate through which electrodes are inserted into the solution. Platinum foil serves as the counter electrode and saturated calomel electrode (SCE) as the reference electrode in our study. A Potentiostat (Chi600b) was used to apply constant potentials for appropriate durations for material deposition. The deposition potential is determined from the cyclic voltammetry curve. Chronoamperometry is used to perform the deposition. In chronoamperometry the potential of the working electrode is varied and the resulting faradaic current occurring at the electrode (caused by the potential step) is monitored as a function of time. Cobalt and Nickel nanowire arrays have been deposited through PCTE membranes (of average pore diameter 100 nm) and AAO templates (of average pore diameters of 35 and 55 nm). The electrolytic solution used contains Nickel or Cobalt Sulphate ($\text{NiSO}_4 \cdot 7\text{H}_2\text{O}$ or $\text{CoSO}_4 \cdot 7\text{H}_2\text{O}$) salt, Boric Acid (H_3BO_3) and Sodium Lauryl Sulphate (SLS). The details are given below:

Table 4.1: Chemical composition of the electrolytic solution.

VOLUME OF THE SOLUTION	100 ml
$\text{CoSO}_4 \cdot 7\text{H}_2\text{O}$ / $\text{NiSO}_4 \cdot 7\text{H}_2\text{O}$	0.842 g
H_3BO_3	0.742 g
SLS	1 g

SLS was used for wetting of the membrane pores. This is essential to avoid trapping of air bubbles inside the nanopores as the trapped air bubbles will prevent deposition of material through pores. Moreover these trapped bubbles disturb the optimized parameters which lead to unbalancing of electrochemical processes. At first, cyclic voltammetry was performed to select the proper deposition potential of the material concerned. The deposition potential used is -1.0V for both Co and Ni. Using this potential, Ni and Co were

Chapter 4

deposited through PCTE and AAO for different deposition times to get NWs of varying length. To release the NWs for further investigation, the PCTE membrane was soaked in dichloromethane and AAO template in different concentrations of NaOH for different times. Various methods were tried to dissolve the membrane (both AAO and PCTE) after deposition in order to get NWs free for further characterization. The schematic of the fabrication procedure is shown schematically in Fig. 4.4.

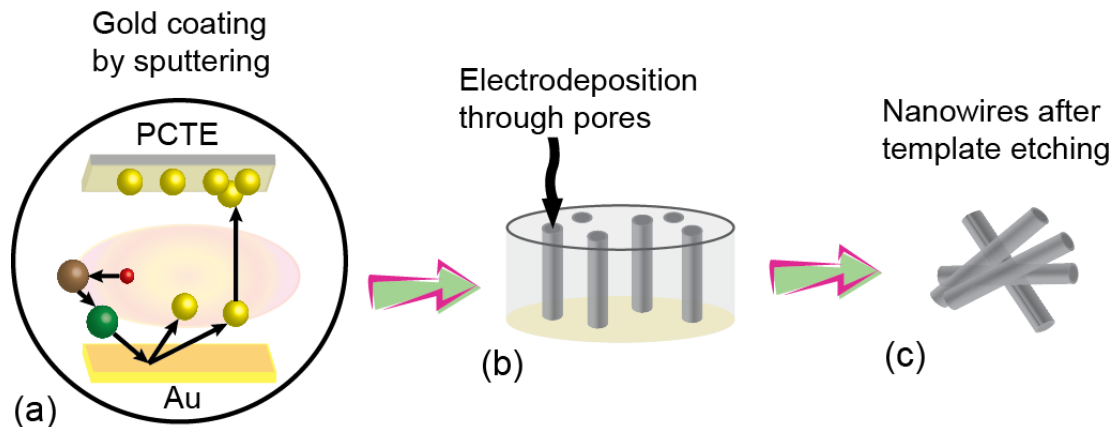


Fig. 4.4: Nanowire fabrication procedure: (a) gold coating on one face of the template by sputtering. (b) Deposition of metal ions through the pores of the template. (c) Nanowires after dissolution of templates.

4.4. Characterization techniques

4.4.1. Scanning electron microscopy (SEM)

The scanning electron microscope (SEM) is a popular tool to study surface topography and morphology of samples. In a typical SEM, the phenomenon of thermionic emission or an electric field is used to generate a stream of electrons from a cathode. We have used both types of scanning electron microscopes. For first case, the source of the electrons is an electron gun fitted with a tungsten filament cathode, whereas, the electrons are emitted from a field emission cathode in the second case. Narrower electron beam profile can be achieved with the field emission process, which results in a better spatial resolution than the thermionic emission electrons. The energy of the electrons can be varied from few

Chapter 4

hundreds eV to few tens of keV. A gradient of electric field is used to accelerate the emitted electrons.

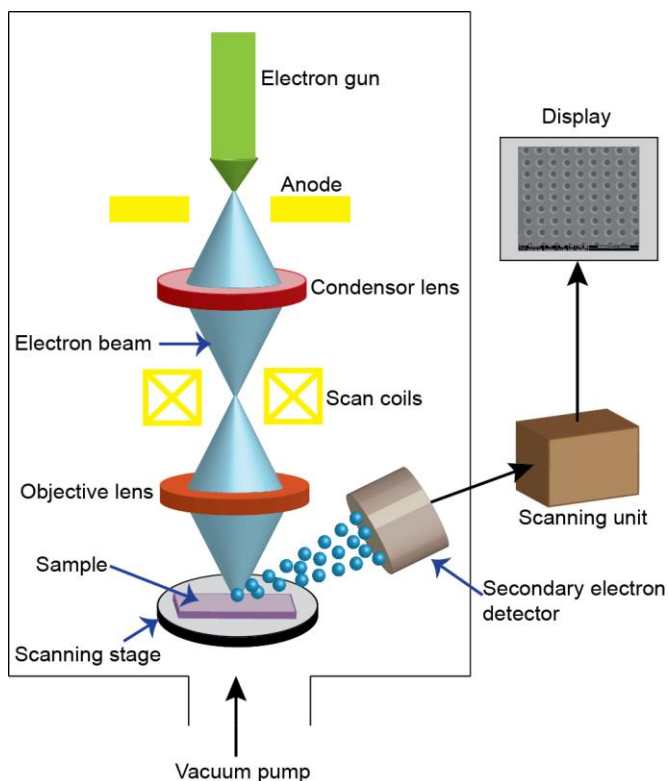


Fig. 4.5: Schematic diagram of the scanning electron microscope (SEM).

The beam first passes through two electromagnetic lenses, termed as condenser lens (Fig. 4.5) and then through an electromagnetic scanning coil and finally, is focused onto the sample [211]. When deflected by the scanning coil in the X and Y directions (*i.e.*, in the plane of the sample), the beam performs a raster scan over a rectangular area of the sample surface. Upon interaction with this highly energetic electron beam, different types of electrons including secondary electrons, backscattered electrons and Auger electrons are emitted or scattered from the sample due to the elastic and inelastic collisions. Energy is also emitted in the form of characteristic X-rays and visible light (cathodo-luminescence). The secondary electrons, produced by inelastic scattering of incident electrons with the atoms of the sample are detected by a detector. By comparing the intensity of these secondary electrons to the scanning primary electron beam, an image of the sample surface is constructed and displayed on a monitor. SEM images have large depth of field due to a

Chapter 4

very narrow electron beam. As a result, SEM has the capability of producing three-dimensional images, which are quite important for investigating the surface structure of a sample. The samples are generally mounted rigidly on a specimen stub with the help of a carbon tape. The samples should be electrically conductive at the surface and electrically grounded to prevent the accumulation of electrostatic charge at the surface. We have used “FEI QUANTA 200” and “FEI Helios NanoLab 600” SEMs to characterize our samples.

4.4.2. Energy dispersive X-ray (EDX)

A powerful tool for the elemental analysis or for investigating the chemical purity of a sample is the Energy dispersive X-ray (EDX) spectroscopy. The principle of operation of an EDX spectrometer is shown schematically in Fig. 4.6.

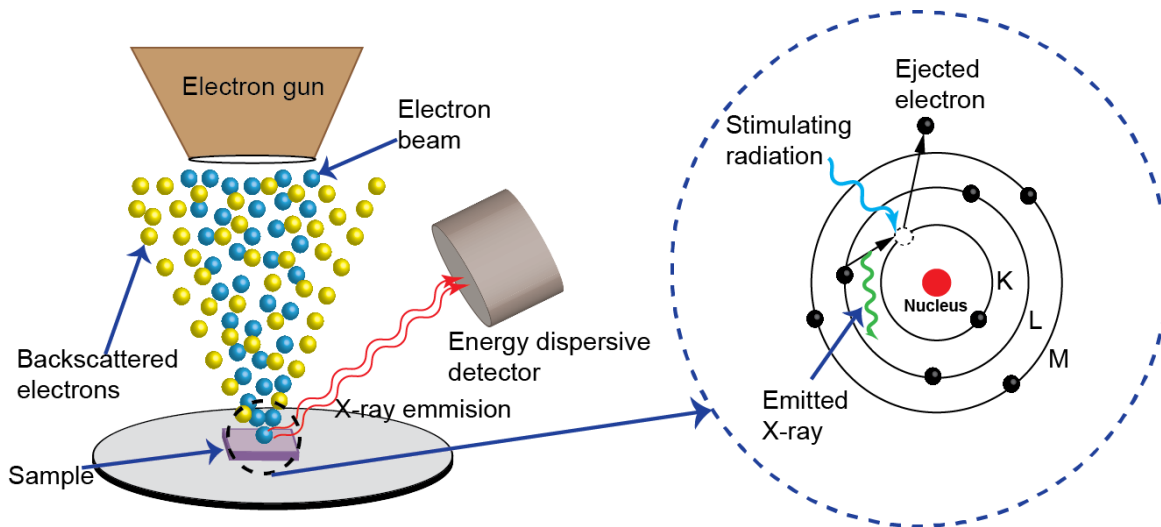


Fig. 4.6: Interaction of accelerated electrons with a sample and emission of X-rays is shown schematically.

At the ground state, every atom contains a number of electrons moving around the nuclei and arranged in different shells. In this technique, a high energy beam of charged particles, like electrons, protons or sometimes X-rays, is used to stimulate the sample and to eject out electrons from an inner shell, thus creating a hole. Electrons from outer shells with higher energies jump to the inner shell to fill up the hole. The difference of energy of these two levels is radiated in the form of an X-ray. Since the atomic structure of each element is unique, the energy of the emitted X-rays, which is basically the characteristics of an

Chapter 4

element's atomic structure, is also unique in nature. A Si (Li) detector is used as an energy dispersive spectrometer to measure the energy and number of the emitted X-rays. The element is identified from the peak energy values of the X-rays and the relative heights of the peaks give the atomic percentage of the element in the sample. In general the EDX spectrometer is attached to the SEM. We have used an EDX spectrometer from EDAX attached with "FEI QUANTA 200" SEM.

4.4.3. X-ray diffraction (XRD)

The XRD technique exploits the diffraction pattern generated from a crystal upon X-ray radiation. The diffraction pattern contains information about the crystal structure. We have used "PANALYTICAL EXPERT PRO" X-ray diffractometer for the characterization of samples used in this thesis. The $K\alpha$ radiation (X-ray) from a copper target with an average wavelength (λ) of $\sim 1.5418 \text{ \AA}$ is used in all measurements.

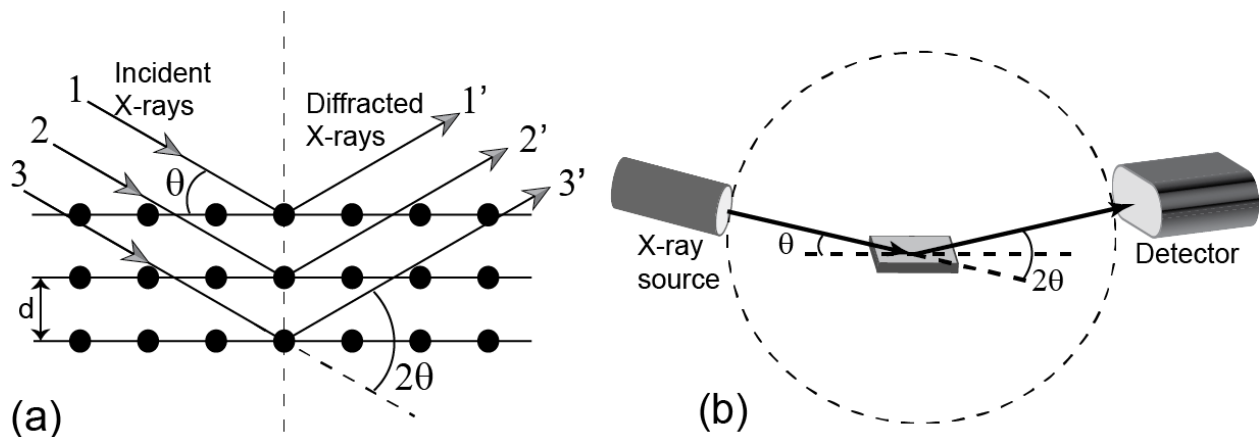


Fig. 4.7: Schematic diagrams of (a) X-ray diffraction and (b) X-ray diffractometer are shown.

The atoms, within the crystalline material under study, elastically scatter the incident X-ray. The incident angle of X-ray is varied between a range of angles in small steps and the corresponding reflected intensities are measured by a detector placed at the reflected angle. When incident angle (θ) satisfies Bragg's condition ($2d \sin\theta = \lambda$) (Fig. 4.7(a)), then X-rays are reflected from regular arrays of atoms and constructively interfere to give rise intensity peaks in the diffraction pattern [212]. The intensities of the reflected X-rays are measured as a function of the angle of the reflected beam with respect to the direction of the incident beam. In our measurements, the X-ray source is kept fixed while the sample

Chapter 4

moves at half the rate of the detector to maintain the θ - 2θ geometry (Fig. 4.7(b)). As each element has a set of unique d -spacings, conversion of the diffraction peaks to d -spacings allows identification of the elements present in the sample. Typically, this is achieved by comparison of d -spacings with standard reference patterns (*i.e.*, ICSD or Inorganic Crystal Structure Database).

4.4.4. X-ray reflectivity (XRR)

The basic principle behind the X-ray reflectivity (XRR) technique is to reflect a beam of X-rays from a flat surface and subsequently to measure the intensity of X-rays reflected in the specular direction as shown in Fig. 4.8. This effect does not depend on the periodicity of the electron density as decided by the crystal structure. However, it significantly depends upon the average electron density across the interface. Hence, this phenomenon occurs for both crystalline and non-crystalline materials. The plot of the specularly reflected X-rays versus the angle of incidence with respect to the surface is called as the reflectivity curve. Reflectometry is an X-ray technique to measure the reflectivity curve of a material. It is also called as the Grazing Incidence X-ray Reflectivity (GIXR) or reflectivity. It is a very efficient technique to measure surface layer characteristics, such as thickness, roughness and density using the reflectivity curve. During the measurements, it is assumed that the angle of incidence is equal to the angle of detection. The beam direction is fixed in the instrument and the angle of incidence is changed by rotating the sample. This is known as the ω rotation. The rotation of the detector arm away from the incident beam direction is a measure of the scattering angle and is denoted by 2θ . In this technique, a coupled $\omega/2\theta$ scan is performed from an angle nearly zero degree to a few degrees. Until the critical angle for the total external reflection is reached, the X-ray barely penetrates into the material. This critical angle depends on the electron density of the surface layer. As soon as the angle of incidence exceeds the critical angle, X-ray starts to penetrate into the material and this penetration depth increases rapidly with angle. Consequently, absorption of X-ray also increases and the intensity of the specularly reflected radiation decreases. The critical angle is the starting point of the rapid fall of intensity observed in the reflectivity curve. The profile of the curve immediately before the critical angle is ideally a plateau and determined by the size and flatness of the sample and measurement parameters. If the

Chapter 4

electron density is inhomogeneous at the surface, then the intensity drop at the critical angle may become less than the ideal case. Some instrumental parameters such as the wavelength spread and the divergence of the incident beam also affects the sharpness of the critical edge. As the incident beam penetrates into the sample, a proportion of the incident beam is specularly reflected at every interface, within the penetration depth, in which the electron density of the material changes. Waves reflected back outwards towards the surface the material may be re-reflected towards the bulk. Oscillations in the reflected amplitudes are created. They interfere to give rise to complicated interference patterns. These patterns are related to the angle of incidence, and the depths of the interfaces with respect to each other and the surface. As the angle of incidence increases further, the absorption increases and the specularly reflected intensity is eventually reduced below the background and no useful reflectivity information can be obtained beyond this point.

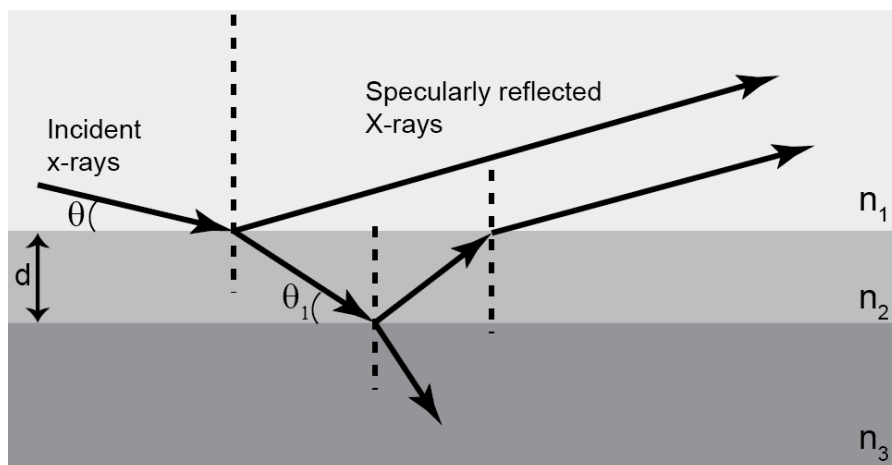


Fig. 4.8: The principle of X-ray reflectivity (XRR).

4.4.5. Vibrating sample magnetometer (VSM)

The variation of magnetic moment (magnetization, M) as a function of applied magnetic field (H) or temperature (T) [213] can be measured quite efficiently by a Vibrating Sample Magnetometer (VSM). The schematic diagram of a VSM is shown in Fig. 4.9. The working principle of VSM is based on the Faraday's law, which states that whenever there is a change in magnetic flux through a coil, an electromotive force (emf) is induced in the coil. Mathematically,

Chapter 4

$$E_{in} = -na \frac{dB}{dt} \quad (4.2)$$

where E_{in} is the induced *emf*, a is the area of coil and n is the number of turns in the coil. Using $\mathbf{B} = \mathbf{H} + 4\pi\mathbf{M}$, we get:

$$E_{in} = -na \left(4\pi \frac{dM}{dt} \right) \quad (4.3)$$

if \mathbf{H} remains unchanged.

Now, if the initial M is negligible compared to the induced magnetization, then we have the induced *emf* proportional to the magnetization of the sample:

$$E_{in} dt = -na(4\pi M) \quad (4.4)$$

For the measurement of the static magnetic properties, the sample is placed inside a uniform magnetic field produced by two pole pieces of an electromagnet (Fig. 4.9).

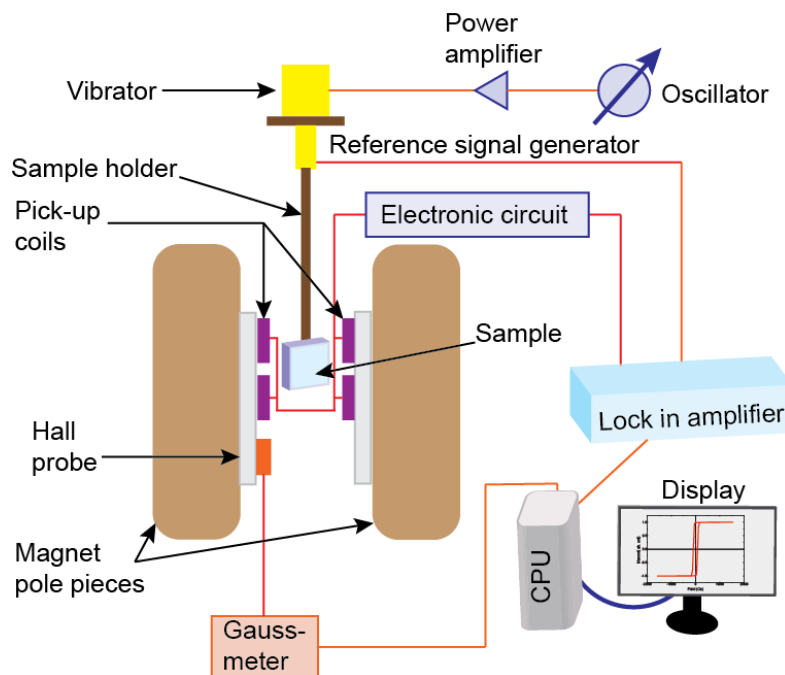


Fig. 4.9: Schematic diagram of Vibrating Sample Magnetometer (VSM).

The sample is mounted on a vertical nonmagnetic plastic/quartz rod connected to a piezoelectric transducer assembly located above the magnet. The transducer converts a

Chapter 4

sinusoidal electric signal (generated by an oscillator/amplifier) into a sinusoidal vertical vibration of the sample rod which results in a sinusoidal oscillation of the sample in presence of the magnetic field. Hence, a voltage, proportional to the sample's magnetic moment, is induced in the stationary pickup coils located in between the pole pieces. However, this voltage does not depend on the strength of the applied magnetic field as the magnetic field is stationary. Typically, the induced voltage is measured through the use of a lock-in amplifier using the output of the piezoelectric signal as its reference signal. The $M-H$ or $M-T$ curves of a ferromagnetic material can be obtained by measuring induced voltage as a function of magnetic field (H) of an external electromagnet or temperature (T) of the sample.

4.5. Measurement techniques

4.5.1. Introduction

Initially, after its discovery, MOKE [158] found its application primarily in the investigation of hysteresis loops. Ever since the first implementation of the time-resolved magneto-optical Kerr effect to probe the dynamics of magnetic thin films in 1991 [214], this technique has evolved as a very powerful means of studying the magnetization dynamics [35, 96, 160, 191-194, 196-197, 200, 203, 215-219]. There are a number of variants of the TR-MOKE technique, out of them the all-optical TR-MOKE has several advantages including the absence of special and complicated sample fabrication process and a very high temporal resolution limited only by the pulse-width of the laser. The temporal resolution enabled the measurement of ultrafast demagnetization [120], various relaxation processes [220] and coherent precession of magnetization in a single measurement. The simultaneous spatio-temporal resolution enabled the measurement of dynamics of single nanomagnets well beyond the diffraction limit [192, 221]. All the experimental results on the magnetization dynamics presented in this thesis were obtained by using an all-optical TR-MOKE microscope.

Chapter 4

4.5.2. Time resolved magneto-optical Kerr effect (TR-MOKE) microscope

4.5.2.1. Components required for the construction of the TR-MOKE microscope

Two photographs of the all-optical TR-MOKE microscope, in our lab in the S. N. Bose National Centre of Basic Sciences, Kolkata, India, are presented in Fig. 4.10.

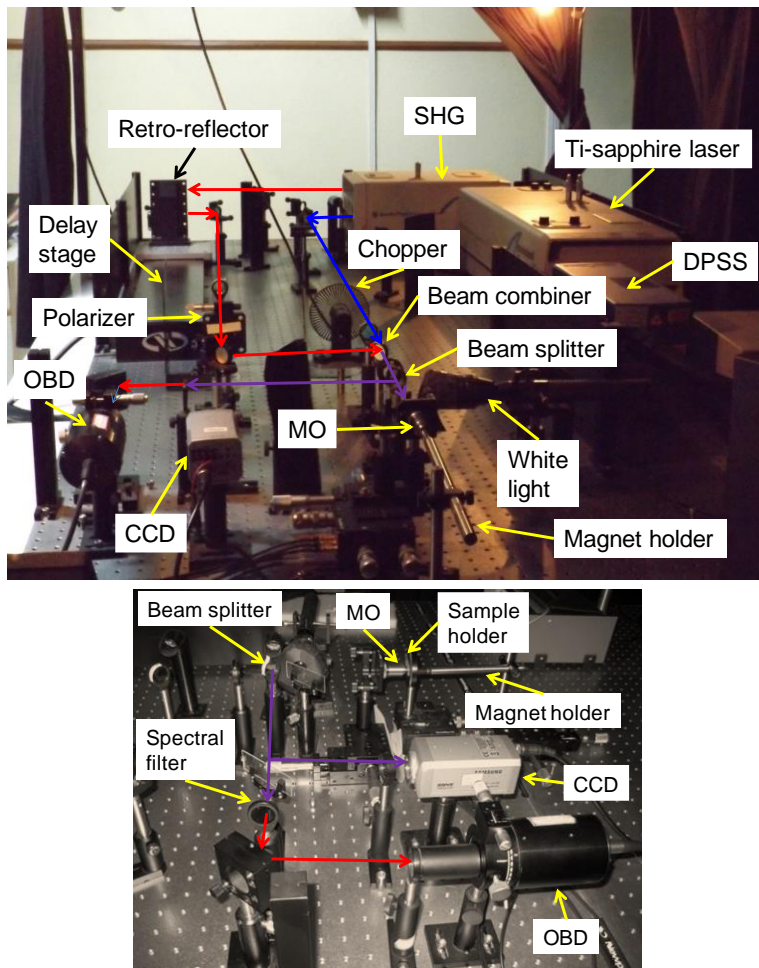


Fig. 4.10: (Upper panel) A photograph of the all optical time-resolved magneto-optical Kerr effect (TR-MOKE) microscope in our laboratory in the S. N. Bose national Centre for Basic Sciences. (Lower panel) An enlarged view of the detection procedure. The important components in the set up are labeled in the figures.

This is an all-optical measurement in a sense that both the excitation and detection of the magnetization dynamics in the samples are done optically. The TR-MOKE set up was developed during the course of this thesis. Few important components are labeled in the

Chapter 4

photograph. Although there are few components which are always kept unaltered, some components are regularly changed/modified according to the experimental requirement. Below, we list the essential components required to set up the TR-MOKE microscope.

Table 4.2: Components of the TR-MOKE magnetometer.

Sl. No.	Name	Company	Model
1	Optical Table	Newport	RS 4000™
2	Optical Table Enclosure	Custom Made	-
3	Diode Pumped Solid State (DPSS) Laser	Spectra Physics	Millenia Pro 10s (with diode laser: model J80)
4	Ti-sapphire Laser	Spectra Physics	Tsunami
5	Second Harmonic Generator	Spectra Physics	3980
6	Retro-reflector	Newport	UBBR1-2S
7	Delay Stage	Newport	(M-)IMS series
8	Delay Stage Motion Controller	Newport	EPS301
9	Optical chopper and its Controller	Thorlabs	MC1F60, MC2000
10	Polarizer	Thorlabs	GTH5M
11	Microscope Objective (MO)	Newport	M-10X, M-40X, M-60X
12	Piezo Electric x-y-z stage and its Controller	Thorlabs	BPC203, NanoMax-TS
13	CCD Camera & Monitor	Samsung	SDC-313B

Chapter 4

14	Optical Bridge Detector (OBD)	Neoark Corporation	NDT-40110GTP
15	Dielectric Mirrors	Thorlabs	BB1-E02 BB1-E03
16	Spectral Filters	Thorlabs	FGB37 FGL610
17	Attenuators, Neutral Density Filters	Thorlabs	NE40B NDL-10C-4
18	Beam Splitters (Non-polarized)	Thorlabs and Newport	EBS1 (50:50) EBP1 (70:30)
19	Lenses	Thorlabs	LA1608 LA1708
20	Lock-in Amplifiers	Stanford Research Laboratory	SR830
21	Mirror Mounts	Thorlabs	KS1, KM100
22	Lens Mounts	Thorlabs	LMR1/M
23	Polarizer Mounts	Holmarc	PMC-25
24	Linear Stage	Holmarc	TS-90-Mu10-01
25	Manual X-Y Stages	Holmarc	TS-90-Mu10-02
26	Oscilloscope	Agilent	DS05032A
27	Digital Multimeter	Rishabh	RISH Multi 15S
28	Spectrometer	Ocean Optics	USB4000
29	IR Viewer	Newport	IRV2-1700
30	Beam Height	Home Made	-

Chapter 4

31	Beam Block	Home Made	-
32	Power Meter	Newport, Coherent	407A, FieldMate

4.5.2.2. Description of lasers

The entire set-up involves three lasers. A diode pumped solid state laser (DPSS) with maximum power 10 W (adjustable) and wavelength $\lambda = 532$ nm is used to pump a Ti-sapphire oscillator. Regenerative acousto-optic mode locking mechanism is used inside the Ti-sapphire oscillator or the “Tsunami” to produce the output laser pulses of ~ 70 fs pulse width at 80 MHz repetition rate. The wavelength of the oscillator is tunable from 700 – 1080 nm, however, we kept it fixed at around 800 nm during our experiment as our Si-based detectors are most sensitive near that wavelength. The fundamental beam is divided into two parts. The intense part goes through a second harmonic generator (type-I BBO crystal) to produce the second harmonic ($\lambda = 400$ nm), which is used to pump the sample. The time-delayed fundamental is used to probe the dynamics. Below we will briefly discuss the components and working principles of these lasers [222-226].

❖ DIODE LASERS

The CW output of the diode laser bars, consisting of twenty diode lasers, is collimated with a cylindrical microlens of high numerical aperture (N.A.) and the highly asymmetric output beam is coupled into a fiber bundle by the so called FCbar technology, which is a highly efficient method of coupling the output of diode laser in fiber. Typically 85-90% light of diode laser is coupled into the fiber bundle. This output is directly fed to the Millenia through the fiber [224].

❖ DIODE PUMPED SOLID STATE (DPSS) LASER OR MILLENIA

- *Working principle*

Nd^{3+} ions doped in a Yttrium Vanadate crystalline matrix (Nd:YVO_4) serves as the gain medium in the Millenia. The monochromatic output of the diode laser overlaps with the absorption spectra of the Nd^{3+} ion. Consequently, the diode laser pumps the Millenia with

Chapter 4

high efficiency. The efficiency of the Millennia is further improved by focusing the diode laser output on a volume in the active medium of the Millennia in such a way that it matches with the radius of TEM₀₀ mode of the Millennia (mode matching) [Fig. 4.11(a)]. The Nd³⁺ is a four level system where a photon of wavelength (λ) = 1064 nm is emitted due to the transition of an electron from 4F_{3/2} level to 4I_{1/2} level. There are also transitions at 1319, 1338 and 946 nm. However, at room temperature they have lower gain along with a higher threshold value than the 1064 nm transition and the wavelength selection optics limit the oscillation to 1064 nm [224]. A part of the output is fed back to the pump laser driver to provide a constant output in power mode operation. A shutter placed outside the cavity acts as a beam blocker [Fig. 4.11(b)] which can be opened by the controller. The 90° polarization rotation aligns the polarization axis of the output beam vertically.

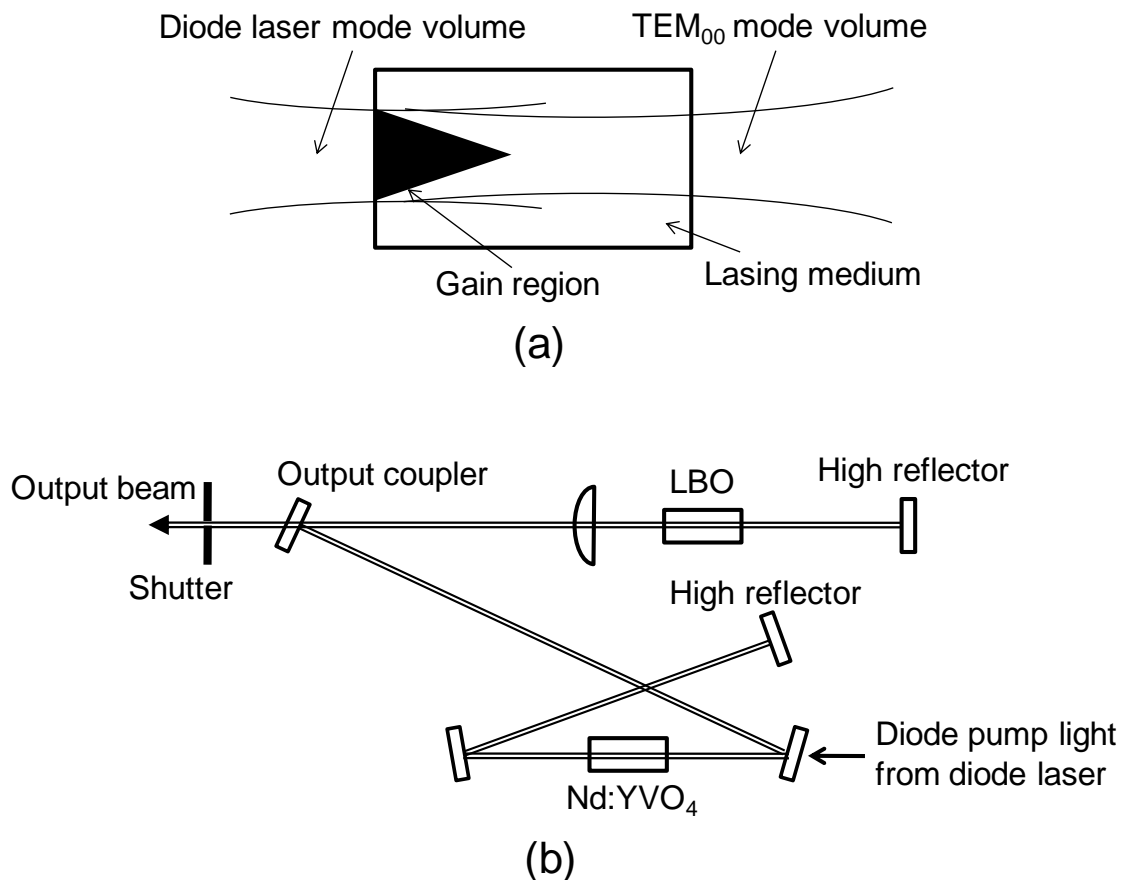


Fig. 4.11: (a) Schematic diagram of mode matching between diode laser mode volume and TEM₀₀ mode volume of Millennia. (b) Schematic diagram of Millennia laser head. The figures are reproduced from Ref. [224].

Chapter 4

- *Frequency doubling*

A lithium triborate (LBO) nonlinear crystal is used to convert the infrared output with $\lambda = 1064$ nm to visible light with $\lambda = 532$ nm. As the efficiency of the LBO crystal is sensitive to temperature, it is important to maintain the crystal at the appropriate phase-matching temperature to optimize its efficiency and to keep the output fixed at $\lambda = 532$ nm. This is achieved by using a temperature regulating oven. As the crystal itself keeps the fundamental and the second harmonic beams collinear (noncritically phase-matched), a rigorous alignment of the Millenia cavity is not required. Again a large acceptance angle makes it insensitive to any slight misalignment within the Millenia. Though the LBO crystal has lower nonlinear coefficient than other materials, these advantages make it very useful for frequency doubling in the Millenia.

The expression for the second harmonic power is given by [224] :

$$P_{2\omega} \propto \frac{d_{eff}^2 P_{\omega}^2 l^2 [\phi]}{A} \quad (4.5)$$

where d_{eff} is the effective nonlinear coefficient, P_{ω} is the fundamental input power, l is the effective crystal length, $[\phi]$ is the phase matching factor and A is the cross sectional area of the beam in the crystal.

- ❖ **MODE LOCKED TI-SAPPHIRE LASER OR TSUNAMI**

- *Working principle*

Ti-sapphire is a lasing medium that is obtained by doping the sapphire crystal (Al_2O_3) with titanium ions (Ti^{3+}). The absorption transitions occur over a broad range of wavelengths from 400 nm to 600 nm. Hence, this system is efficiently pumped by the output of the Millenia. The fluorescence band also extends over a broad range from 600 nm to 1000 nm. However, the short wavelength end of fluorescence and long wavelength end of the absorption spectrum overlap with each other [Fig. 4.12] making lasing action possible only for $\lambda > 670$ nm.

Chapter 4

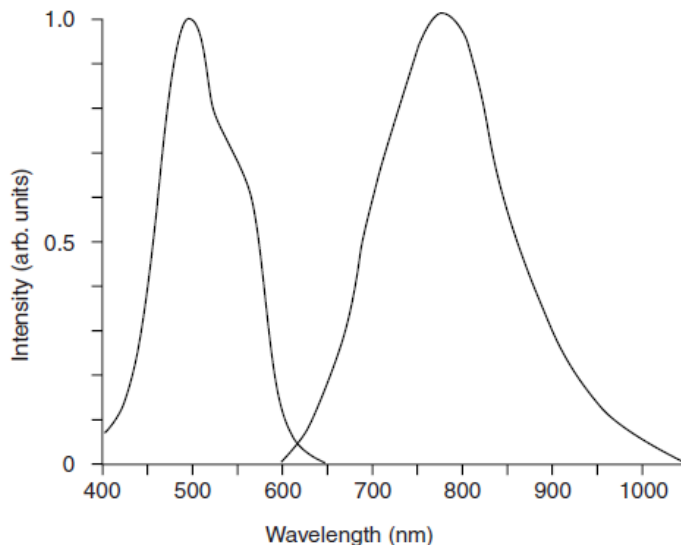


Fig. 4.12: Absorption and emission spectra of Ti-sapphire crystal. The figure is reproduced from Ref. [222].

- *Ten-fold mirror cavity*

In a mode-locked laser like Tsunami, to achieve a repetition frequency of ~ 80 MHz, it is essential to have a cavity longer than that in a CW laser. The longer cavity length is realized by a ten-mirror folded arrangement in the Tsunami as presented in Fig. 4.13.

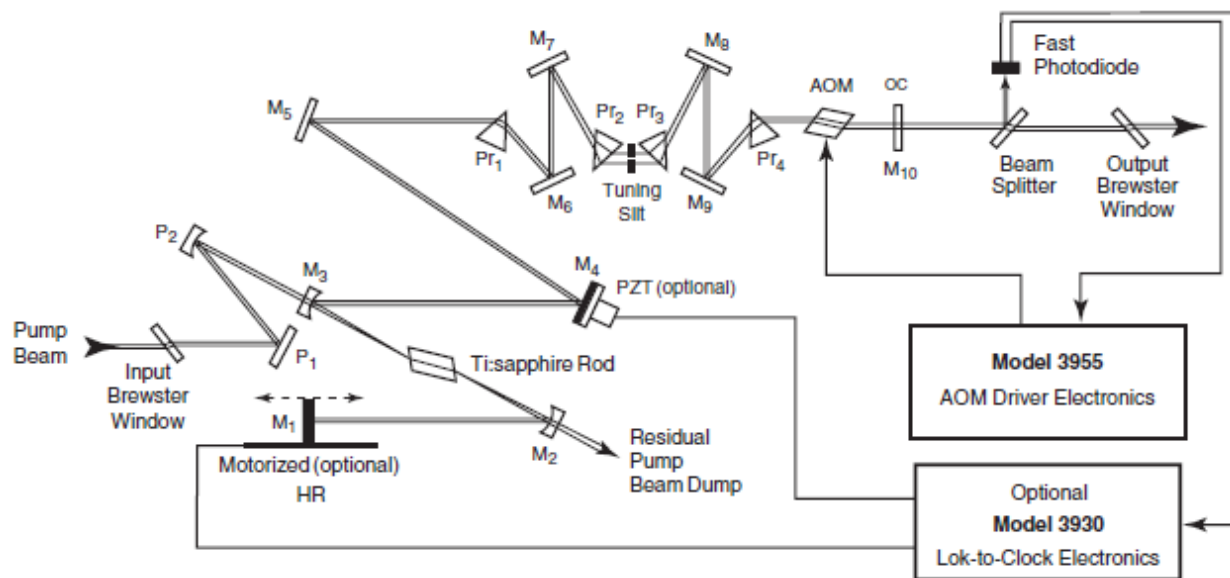


Fig. 4.13: A schematic of the beam path inside the folded cavity of Tsunami. The figure is reproduced from Ref. [222].

Chapter 4

However, though this arrangement optimizes the space available, it makes pumping more complex. It may even introduce astigmatism in the beam if the focusing mirror is used at an angle other than the normal incidence. But this can be virtually eliminated by a proper selection of angles of the cavity focus mirrors and the rod-length.

For further stability of the cavity, clean and dry nitrogen gas (purity = 99.999%) is constantly purged to the laser head to remove dust and water vapor. A chiller unit is also provided to keep the Ti-sapphire rod at constant temperature for long term stable performance.

- *Group velocity dispersion and wavelength selection*

Following the Heisenberg uncertainty principle (time-bandwidth product of a Gaussian pulse is 0.44), we know, shorter the pulse, greater the difference between lowest to highest frequencies within a pulse. As the refractive index (n) is a function of frequency, there is a distribution of n in a pulse and hence a distribution of velocities. This variation of transit time as a function of the frequency, *i.e.*, the wavelength is called as the group velocity dispersion (GVD). If lower frequencies travel faster than the higher frequencies, then that is called positive GVD and the corresponding pulse is said to be positively chirped and *vice versa*. Also, nonlinear n introduces an intensity dependent index at high intensities.

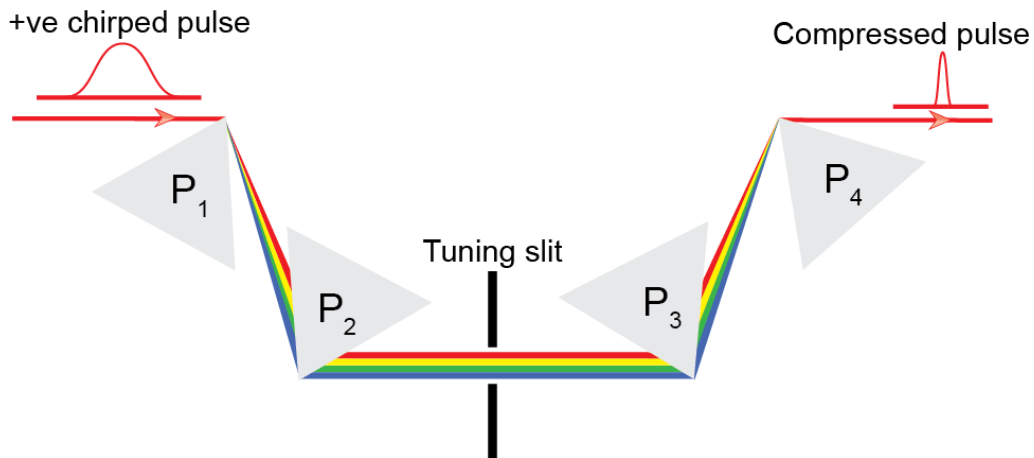


Fig. 4.14: The four prism arrangement used for dispersion compensation in Tsunami laser.

Chapter 4

In Tsunami laser, positive GVD is compensated by a four prism arrangement as shown in Fig. 4.14. The net intracavity GVD is tuned by translating prisms P_2 and P_3 perpendicular to their bases. More optical material can be inserted into the cavity by translating P_2 and P_3 further into the intracavity beam and net intracavity GVD becomes less negative. The different spectral components of the pulse are spatially spread between prisms P_2 and P_3 . This results in a convenient wavelength selection by moving a slit between these two prisms in the direction of the spectral spread. The output bandwidth and hence the pulse width can be controlled by varying the slit width.

❖ SECOND HARMONIC GENERATOR (SHG)

A barium beta borate (BBO) crystal is used to double the frequency of the output of the Tsunami in a second harmonic generator (SHG). A BBO crystal also has higher conversion efficiency than an LBO crystal. This crystal does not require any heater. A schematic diagram of SHG and the optical path inside are shown in Fig. 4.15 [223].

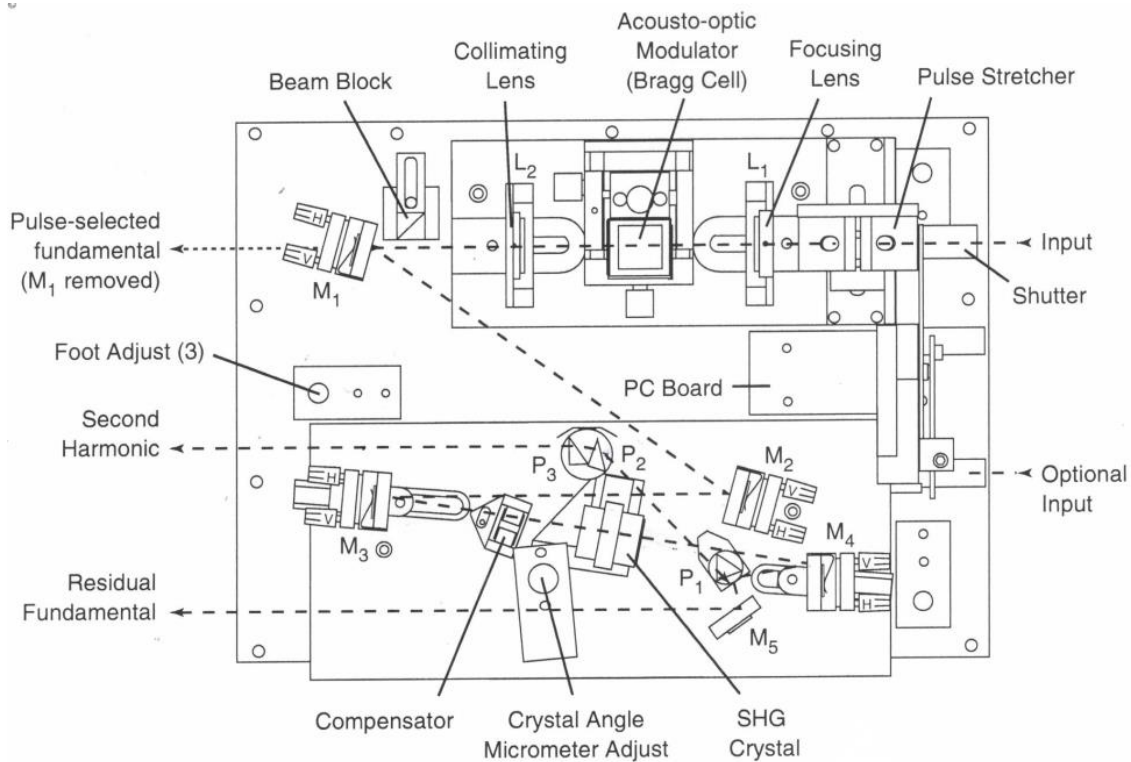


Fig. 4.15: A schematic diagram of the SHG unit and the optical path inside it are shown. The figure is reproduced from Ref. [223].

Chapter 4

The mirrors M_1 and M_2 direct the output beam, while mirror M_3 focuses the beam to a small waist into a critically phase matched (angle tuned) type I second harmonic generator. The BBO crystal produces horizontally polarized second harmonic beam, whereas the residual fundamental beam remains vertically polarized. The prism P_1 separates out the second harmonic and residual fundamental beams. Because of the highly reflective coating on P_1 at residual fundamental IR wavelength, the fundamental beam is reflected, whereas the second harmonic beam is diffracted to prisms P_2 and P_3 . These prisms have anti-reflection (AR) coating at second harmonic wavelength. This prism pair redirects the second harmonic beam roughly parallel to the fundamental beam along with compensating the beam ellipticity.

A thin BBO crystal is used for the following advantages:

1. Minimizes the pulse broadening problem due to group velocity dispersion (GVD).
2. No compensating crystal is required.
3. Only a single SHG crystal is required to match the phase over the entire tuning range (690 nm to 1090 nm).

As it can be observed from eqn. (4.5) that the conversion efficiencies of SHG crystal is inversely proportional to the cross sectional area of beam in the crystal, the conversion efficiency can be further increased by minimizing the beam waist. The pair of lenses (L_1 and L_2), with telescopic configuration, helps to achieve an optimum beam waist. However, the BBO crystal is slightly hygroscopic. Hence, it is sealed in a small cylinder with AR-coated windows and filled with an index matching fluid.

4.5.2.3. Description of the set up

As seen from the photograph in Fig. 4.10, the entire set up is developed on an L-shaped optical table (two Newport *RS4000 series* tables are joined) with vibration isolation. The optical table is an essential part of any highly sensitive optical experiment like TR-MOKE microscopy. The optical table used in our set up is made of vertically bonded closed cell honeycomb core sandwiched in between two sheets of ferromagnetic material (4.8 mm thick). This helps to increase the stiffness constant of the table and decrease the mass to increase the resonant frequency of the table well above the external mechanical and

Chapter 4

acoustic vibration frequency. Therefore, the external vibrations cannot resonate the table easily. To damp out the vibrations and acoustic modes of the table fast, the core of the table is filled up by broadband and tuned hydraulic dampers. The mechanical vibrations originating from the ground is eliminated by placing the table on top of vibration isolation in floating condition. The flatness of the table surface is ± 0.1 mm over 600×600 mm² area. There is a square grid of circular holes with 25 mm pitch for mounting of the lasers, optics and detectors.

A schematic diagram of the TR-MOKE microscope is shown in Fig. 4.16. The solid state laser (Millenia) is pumped by an array of diode lasers to produce a maximum output power 10 W (adjustable) and wavelength $\lambda = 532$ nm. The output of the DPSS pumps the Ti-sapphire laser (Tsunami). As mentioned earlier, regenerative mode locking mechanism produces a train of laser pulses with ~ 70 fs pulse width and maximum average power of 2 W at a repetition rate of 80 MHz (25 nJ/pulse). Though, the output wavelength can be tuned from 690 nm to 1080 nm, the output is kept fixed at around 800 nm in our experiments for stable operation and for better spectral response of the Si based detectors at that wavelength.

The output red beam from the Ti-sapphire oscillator has a spot size of ~ 2 mm and is vertically polarized. This beam is split into two parts (70:30) by a beam splitter (B_1). The intense part goes through the second harmonic generator (type-I BBO crystal) to produce the second harmonic ($\lambda = 400$ nm), which is used to pump the sample. The linearly polarized time-delayed fundamental is used to probe the dynamics. A broadband mirror M_{b1} is placed outside the SHG which reflects a beam within the wavelength range 400 – 750 nm, to filter out the residual fundamental beam. A spectral filter (F_b) is placed in the path of the pump beam to further reduce any residual fundamental beam present in the pump beam, because a slight amount of the fundamental beam mixed with the pump beam can produce a very noisy signal. After getting reflected from two more highly reflecting mirrors (M_{b2} and M_{b3}), the pump beam travels through a variable neutral density filter also called an attenuator (A_2). The attenuator is coated with a reflecting material such that the reflectivity of the material changes gradually from one end to other end causing a gradual

Chapter 4

The pump beam goes through a fixed optical path and is modulated by a mechanical chopper at a frequency of 2 kHz. The chopper frequency is used as the reference signal for the lock-in-amplifiers for a phase sensitive detection. Initially, the probe beam is guided through a fixed optical path by using a set of highly reflecting mirrors (M_{r1} , M_{r2} , M_{r3} and M_{r4}). Here also, we have a variable attenuator (A_1) to adjust the fluence of the probe beam. The probe beam goes through a variable delay line fitted with a retro-reflector, which is used to vary the optical path of probe beam. The broadband hollow retro-reflector is placed on the delay line which reflects the incident beam in such a way that the reflected beam becomes antiparallel to the incident beam. The probe path can be varied by moving the retro-reflector back and forth on the delay stage. This is generally done by a motion controller and a PC interfaced with the delay stage through GPIB connection. The difference between the optical paths of the pump and probe beams corresponds to the time-delay in this experiment. In the next step, a pair of lenses L_1 ($f_1 = 75$ mm) and L_2 ($f_2 = 200$ mm) arranged in a telescopic arrangement is used to collimate the beam and increase its diameter to ~ 5 mm so that it fills the back-aperture of the microscope objective. The beam is then passed through a Glan-Thompson polarizer with extinction coefficient of 100,000:1, which refines the polarization state of the probe beam to a very high quality.

Subsequently, the modulated pump beam and linearly polarized probe beam are spatially combined with the help of a 50:50 non-polarized beam splitter B_2 set at 45° to the optical path of the probe beam, which acts as a beam combiner. The beams are collinearly focused onto the sample under study using a single microscope objective (MO: M-40X, N.A. = 0.65). The collinearity is optimized with the help of steering mirrors (particularly M_{r6} , M_{r7} , M_{b1} , M_{b2} and M_{b3}). The combined beams pass through a 50:50 non-polarized beam splitter B_3 and a glass slide (G_1) both set at 45° to the optical path before entering into the MO at normal incidence. It is essential to ensure that the sample is precisely normal to the axis of the microscope objective and also to the directions of the pump and probe beams. This is achieved by adjusting the tilt of the MO. The sample is generally held by using a suitable sample holder, which is mounted on a computer controlled piezo-electric scanning X-Y-Z stage. The probe beam is focused to a diffraction limited spot size (~ 800 nm) at the sample surface with the help of the MO and the Z-travel of the piezoelectric stage. The pump beam

Chapter 4

is spatially overlapped with the probe beam after passing through the same MO and is carefully placed at the centre of the pump beam, where the later is slightly defocused with a spot size of $\sim 1 \mu\text{m}$ due to the chromatic aberration as shown in Fig. 4.17(a).

The back-reflected beams from the samples are collected and collimated by the same microscope objective (MO) and are reflected by the beam splitter B_3 towards the detector. In this path, small parts of the back-reflected pump and probe beams are sent to a CCD camera (after reflection from a glass slide G_2) for viewing the spatial overlaps of the pump and probe onto the sample. The remaining part is sent to an optical bridge detector (OBD) after filtering out the pump beam by a spectral filter (F_r). The optical bridge detector measures the Kerr rotation under a balanced condition and separates it from the total reflectivity signal. Consequently, the spin (Kerr rotation) and the charge and phonon (reflectivity) dynamics are isolated from each other. A white light is reflected by a glass slide (G_1) placed in between B_3 and MO and is focused onto the sample surface through the MO to view the sample structure with sub- μm spatial resolution such that we can locate the exact position where the pump and probe beams are focused onto the sample.

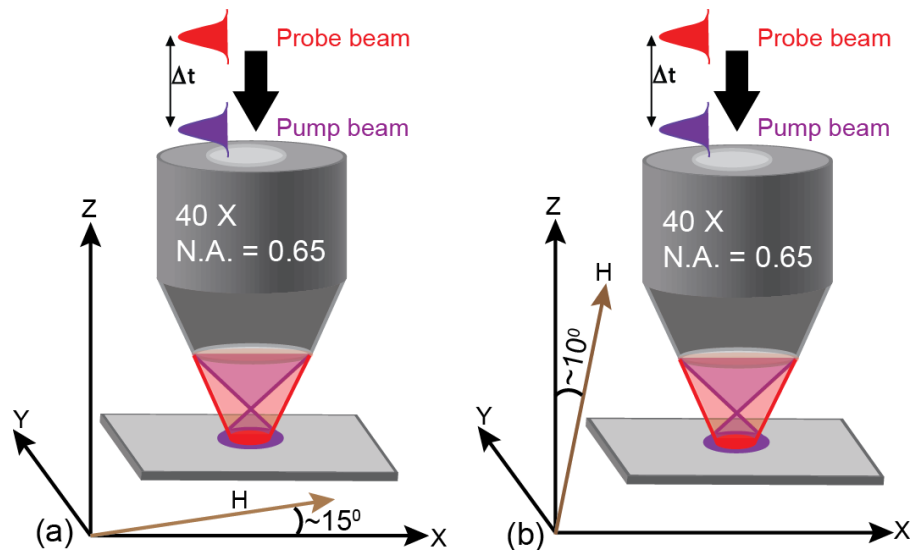


Fig. 4.17: Schematic diagram of the collinear geometry of pump and probe beams focused by a microscope objective (MO) on the sample surface with (a) in-plane and (b) out-of-plane bias field (H) geometry.

Chapter 4

Any ray with non-zero angles of incidence carries information about the longitudinal Kerr rotations, if any, present in the magnetization dynamics. However, in our measurements we have not used split photodiodes and hence, the longitudinal Kerr effect gets averaged out to negligible net value and we primarily measure the polar Kerr rotation. Still, there can be a finite longitudinal Kerr rotation component mixed with polar Kerr rotation if the incident beam is not perfectly normal to the sample/MO or the beam does not travel along the axis of the MO.

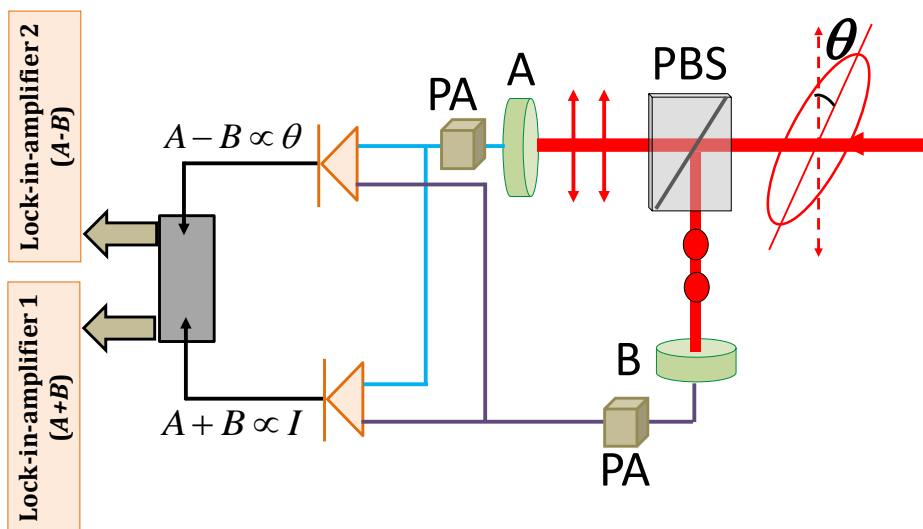


Fig. 4.18: Schematic diagram of the optical bridge detector unit is shown.

The geometries of dc bias magnetic fields for different samples are shown in Fig. 4.17. For samples with high perpendicular magnetic anisotropy (PMA) and nanowires, the bias field is applied at a small angle ($\sim 10^\circ$) to the surface normal of the samples whereas for the rest of the samples, it is applied at a small angle ($\sim 15^\circ$) to the sample plane. Initially, a high field is applied along the normal to the sample (for high PMA samples and nanowires) or in the sample plane (for the rest of the samples) to saturate the magnetization. The magnetic field strength is then reduced to the bias field value to ensure that the magnetization remains saturated along the bias field direction. The bias field is tilted to have a finite demagnetizing field. This demagnetizing field is eventually modified by the pump pulse to induce the magnetization precession within the sample and we measure the corresponding

Chapter 4

polar Kerr rotation for the out-of-plane component of the precession orbit of the tip of the magnetization vector.

Fig. 4.18 presents the schematic diagram of the OBD used in the TR-MOKE measurements. There is a polarized beam splitter (PBS) at the entrance of the OBD, which splits the beam into two orthogonal polarization components. These two parts with intensities I_A and I_B are then detected by two photodiodes A and B, respectively. The outputs of these two photodiodes are then preamplified (by pre-amplifiers PAs) and used as inputs for two operational amplifiers (Op-Amps) to measure the total signal $A+B$ (*i.e.*, $I_A + I_B$) and the difference signal $A-B$ (*i.e.* $I_A - I_B$). The outputs of these two Op-Amps are measured by the lock-in-amplifiers (SR830) in a phase sensitive manner with the chopper frequency as the reference frequency. Initially, in the absence of the pump beam, the optical axis of this PBS is set at 45° to the plane of polarization of the probe beam. Under this condition $I_A = I_B$, *i.e.*, $A-B = 0$ and the detector is said to be in a “balanced” condition. In the next step, when the pump beam excites the sample, the plane of polarization of the probe beam is rotated due to the magneto-optical Kerr effect. Consequently, the optical axis of the PBS is no longer at 45° to the plane of polarization of the probe beam. As a result $I_A \neq I_B$ and $A-B \neq 0$. The linear magneto-optical Kerr rotation is proportional to the sample magnetization and hence the signal $A-B$ gives a non-invasive way of measuring the magnetization of the sample. Thus, by measuring $A-B$ as a function of time, magnetization dynamics over different time-scales are observed. This magnetization dynamics can be used to extract various material parameters including Gilbert damping, magnetic anisotropy, saturation magnetization, gyromagnetic ratio of ferromagnetic thin films, multilayers and confined structures. On the other hand, the time-resolved reflectivity of the sample gives us the charge and phonon dynamics. The schematic diagram is shown in Fig. 4.18. The outputs ($A-B$ and $A+B$) are regularly checked while aligning and optimizing the function of the OBD. In our set up the PBS and the two photodiodes A and B are mounted on a stage attached with a precision rotation mount, while the electronic signal processing is done in the circuit placed in a separate box using low noise amplifiers and connected by low noise cables and connectors. This improves the stability of the signal and the ease of optical alignment.

Chapter 4

The collinear pump-probe geometry enables us to achieve a diffraction limited spatial resolution of about 800 nm along with a temporal resolution of about 100 fs limited by the cross-correlation between the pump and probe pulses. The balanced photodetector or OBD helps to achieve a very high measurement sensitivity of Kerr signal ($\sim \mu\text{deg}$) because a small variation of the Kerr rotation or ellipticity can be measured on top of a zero or negligible background.

4.5.2.4. Development of TR-MOKE microscope and its alignment procedures

The all-optical TR-MOKE microscope in our laboratory offers an excellent spatio-temporal resolution [217]. However, this requires very thorough and methodical high precision optical alignments of the set up. During the construction of the set up, a complete thorough alignment was performed. The TR-MOKE set up consists of highly sensitive lasers, a number of linear and non-linear optics, precision mounts and motion controlled stages. Hence, the entire set up is extremely sensitive to the vibration, temperature, humidity and dust level in the laboratory. Hence, a careful control of the lab conditions is necessary to avoid large long-term drift of the alignment. However, even with all precautions, small amount of misalignment of the laser and the optical components occur which leads to a degraded spatial resolution and reduced signal-to-noise ratio. As a result, systematic minor alignments are often required to achieve good quality signal from the set up before each measurement. Below, we discuss step by step systematic alignment procedure performed for the development and maintenance of the set up during the course of this thesis.

At the very beginning, the optical tables with vibration isolations are installed on the ground floor of the laboratory. The flat surface of the table has to be exactly parallel to the horizontal base of the ground. The heights of the vibration isolation legs could be adjusted to make the flat surface horizontal. This is confirmed by a spirit level. The table is kept under floating condition with a low noise air compressor attached to the air line manifold feeding air to each of the isolator legs. It uses a laminar flow damping, which employs many tiny orifices, resulting in greater damping efficiency. The air volume between piston motion and damper airflow is minimized by the hybrid chamber design. Moreover, it has built in leveling indicators, which provide visual feedbacks ensuring the table is properly floating at the correct level. The combination of broadband and tuned damping provided an

Chapter 4

outstanding stability to the laser and the optical setup against the ground vibration as well as the acoustic noise.

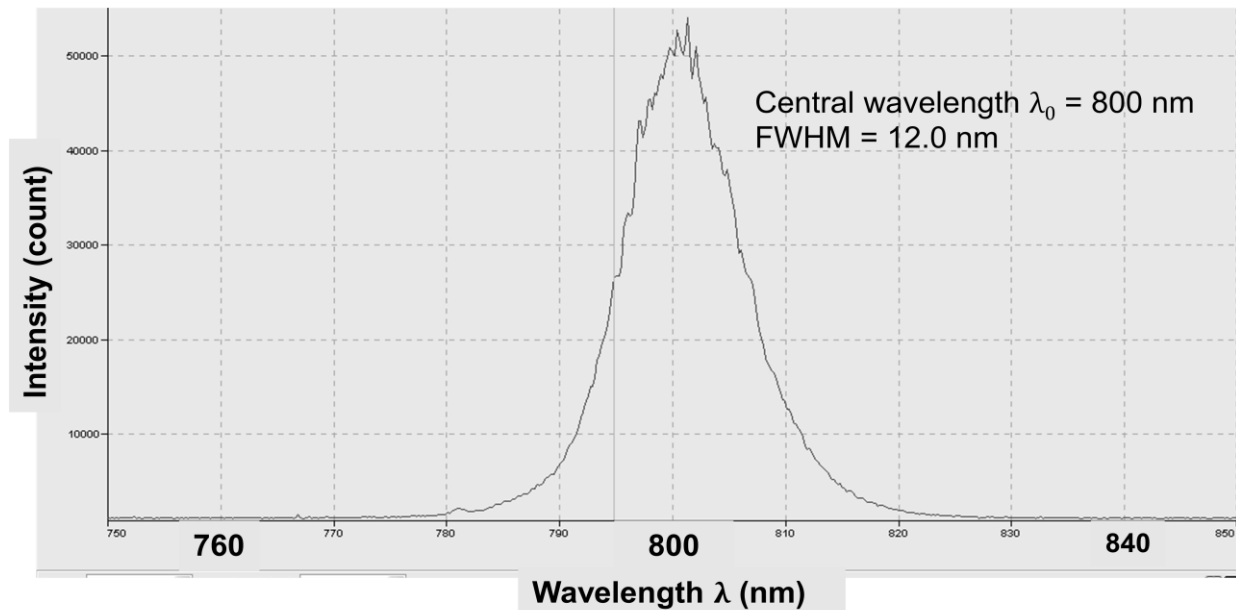


Fig. 4.19: A typical mode-locked power spectrum of the output beam from Tsunami.

In the next stage, the lasers (Millenia, Tsunami) and SHG are installed on the optical table. An optimized diode current and temperatures of the diode laser are set first at which the performance of the Millenia is most stable. In the next step, the laser is switched on. From this time onwards, the cavity of the Tsunami is continuously purged with ultra high pure (99.999%) dry N₂ gas till the completion of the experiment. It takes about 60-75 minutes (warm up time) for the laser to achieve a stable mode locking. All the routine alignments are done only after this warm up. The power spectrum of the output beam from the Tsunami is monitored first by a fiber optic spectrometer (Ocean Optics model no. USB4000). The central wavelength (λ_0) of the spectrum is set close to 800 nm (Fig. 4.19) and the full width at half maxima (FWHM) is adjusted to greater than 12 nm by iteratively adjusting the micrometer drives of the slit for wavelength selection and the prisms for dispersion control in the Tsunami. The laser output power is routinely optimized primarily by adjusting the cavity end mirrors and occasionally by the output couplers and GVD micrometer drive. The part of the fundamental beam, which is sent into the SHG for frequency doubling, is guided by the beam splitter B₁ (Fig. 4.16). The beam path inside the

Chapter 4

SHG is controlled externally by aligning the beam splitter B_1 with the horizontal and vertical screws attached to its mount and by adjusting the phase matching angle of the BBO crystal inside the SHG through the external micrometer screw. The output of the SHG serves as the pump beam in our experiment. A circular beam profile with uniform intensity distribution within the beam profile (*i.e.*, close to TEM_{00} mode) is essential for both pump and probe beams. Care has been taken in the alignment of the SHG to obtain this desirable pump beam profile. However, for the probe beam, a TEM_{00} mode is essentially observed.

❖ ALIGNMENT OF THE BEAM BEFORE THE RETRO-REFLECTOR

The weaker part of the fundamental beam serves as the probe beam. For the height adjustment (14.4 cm, from the top surface of the optical table) of both the pump and probe beams, we use a reference called as the 'beam height'. Up to the retro-reflector, the probe beam is guided by four mirrors M_{r1} , M_{r2} , M_{r3} and M_{r4} (Fig. 4.16). The beam is always aligned in a rectangular path cutting across a set of holes on the optical table for the convenience of alignment. At first, the retro-reflector is removed and the beam is made parallel to a set of holes up to the other end of the optical table. The height of the beam, throughout the whole path, is confirmed by using the reference 'beam height'. Only after that, the retro-reflector is mounted on the delay stage.

❖ ALIGNMENT OF THE RETRO-REFLECTOR

The motivation behind the alignment of the retro-reflector is to align the axis of retro-reflector and the axis of motion of the delay stage exactly parallel to the incident beam path. The procedure is schematically shown in Fig. 4.20(a)-(d). At first the delay stage is placed on the optical table in such a way that its axis becomes parallel to an imaginary line going through the set of holes. The 'beam height' is placed after M_{r5} . The beam is supposed to pass through the middle of the hole in the 'beam height'. When the retro-reflector is moved to the extreme left side (L) of the stage and the height (14.4 cm) and horizontal positions of the beam are adjusted by M_{r3} with the help of screws, S1, S2 and S3, attached to its mount as shown in Fig. 4.20(b).

Chapter 4

Next, the retro-reflector is moved to the extreme right side (R). The position of the beam on 'beam height' will be shifted from the hole as the incident beam and the axis of the delay stage may not be exactly parallel and the position of the beam is adjusted to its previous position (hole on the 'beam height') with the help of M_{r4} .

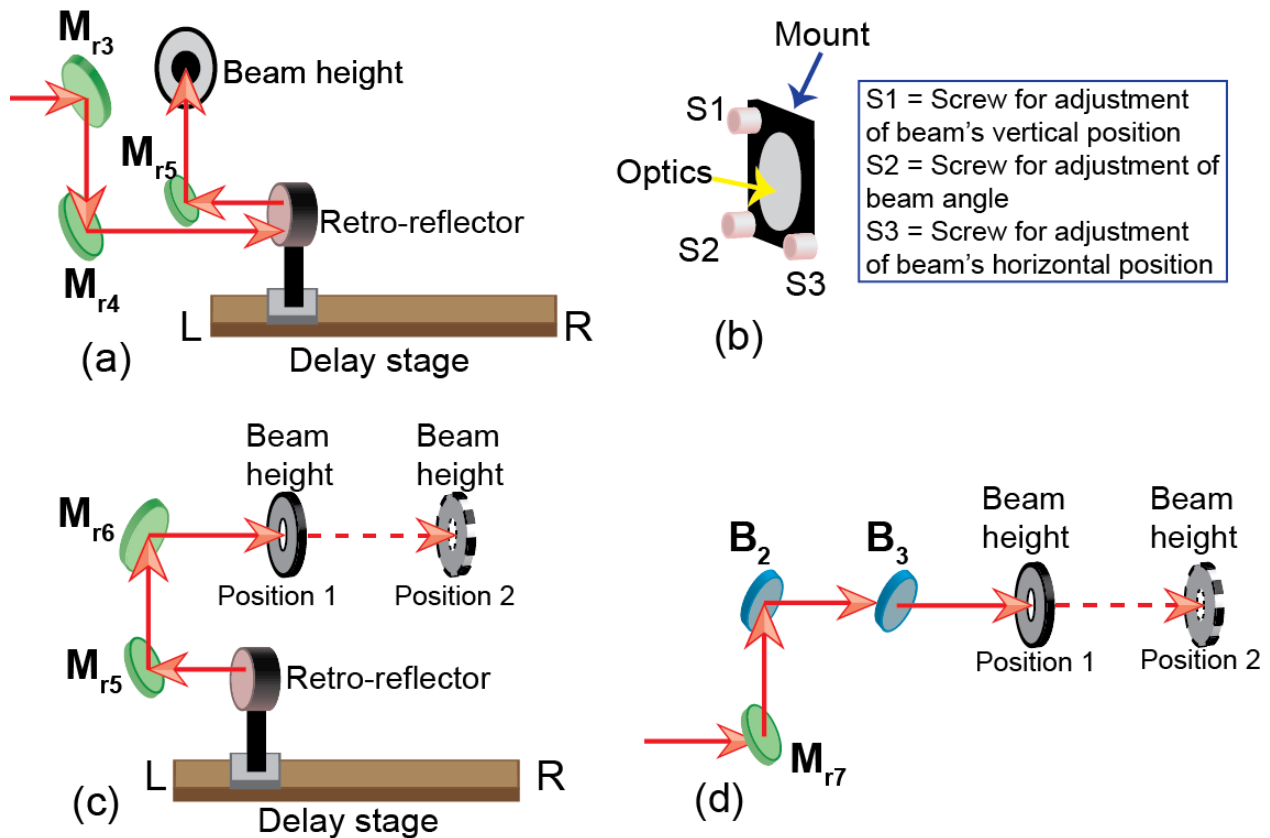


Fig. 4.20: Schematic diagrams of (a) alignment procedure of the retro-reflector, (b) a kinematic mirror mount along with the screws on it and (c-d) alignment procedure of probe beam (c) just after the retro-reflector and (d) after the polarizer.

The retro-reflector is again moved to L position and the beam position is adjusted by mirror M_{r3} . This procedure is continued iteratively till the beam position remains unchanged when the retro-reflector is placed at two extreme ends of the delay stage. After that the 'beam height' is shifted to a much far away position from the retro-reflector (typically 3-4 m) and the above procedure is again performed for further improvement of the alignment of the retro-reflector. Once this is done, we may conclude that the incident

Chapter 4

beam has become precisely parallel to the motion axis of delay stage and the alignment of the retro-reflector is considered to be complete.

❖ ALIGNMENT AFTER THE RETRO-REFLECTOR

After the retro-reflector the probe beam travels through a long path as shown in Fig. 4.16. Two mirrors M_{r5} and M_{r6} are placed right after the retro-reflector for the alignment of the probe beam. The probe beam is reflected to M_{r6} by M_{r5} and is approximately made parallel to the line of holes on the optical table by M_{r6} . The 'beam height' is placed after the mirror M_{r6} at two positions (Fig. 4.20(c)) on the optical table marked as 'position 1', which is close to M_{r6} , and 'position 2', which is close to the other end of the table, so that an imaginary line joining the two positions should be exactly parallel to the line of holes on the optical table. The 'beam height' is first placed at 'position 1' and the mirror M_{r5} is adjusted to make the beam pass through the middle of the hole in the 'beam height'. The 'beam height' is then shifted to 'position 2' and the beam is aligned by using M_{r6} . The 'beam height' is again moved back to 'position 1' and the entire process is repeated until the beam is fully aligned at the two positions of the 'beam height'. After that the beam is collimated and magnified by two convex lenses (L_1 and L_2) placed in a telescopic arrangement in the beam path. It should be ensured that the beam is passing through the centre of the lenses at normal incidence to avoid spatial chirping.

The beam is then passed through the centre of a Glan-Thompson polarizer. The spatial profile (shape and intensity) of the transmitted beam is symmetric on both sides of the centre. The transmitted intensity from the polarizer is made maximum by setting the optical axis of the polarizer parallel to the polarization axis of the beam. The beam then reaches the MO along the path shown in Fig. 4.16 with the help of the mirror M_{r7} , the beam combiner B_2 (50:50 beam splitter) and another beam splitter B_3 (50:50). The dielectric coating of B_2 faces the probe beam. The reflected beam from B_2 is made exactly parallel to the array of holes on the optical table and the height is adjusted to 14.4 cm. For this alignment, again two positions on the optical table are marked (in the absence of the MO) as shown schematically in Fig. 4.20(d) and the alignment is achieved with the aid of M_{r6} , M_{r7} and the 'beam height' in a similar fashion as mentioned previously.

Chapter 4

❖ ALIGNMENT OF THE PUMP BEAM

The pump beam is guided to B_2 with the help of three mirrors M_{b1} , M_{b2} and M_{b3} as shown in Fig. 4.16. At zero delay, the optical path lengths of pump and probe beams should be equal. The desirable position of the zero delay is close to L (Fig. 4.16 and Fig. 4.20) so that we can have a maximum utilization of the length of delay stage as the time delay between the pump and probe beams. Before alignment of the pump beam, we calculated the optical path length of the pump and probe beams starting from the beam splitter B_1 and ending at the beam combiner B_2 . For calculating the optical path of the pump beam the optical path inside SHG, shown in Fig. 4.15, should also be taken into account accurately. The optical path of probe was calculated by keeping the retro-reflector at L . The path length of pump beam is kept slightly longer (10-15 mm) than the path length of the probe beam when the retro-reflector is at L in order to get a negative delay (probe beam reaches the sample before the pump) between pump and probe beams. The difference between path lengths of pump and probe beams are adjusted by re-positioning the mirrors M_{b1} , M_{b2} and M_{b3} . Once the positions of the mirrors are fixed, the alignment of the pump beam is initiated. Since we are working with collinear pump-probe geometry, the pump beam has to be made precisely collinear with the probe beam after B_2 . Consequently, with the help of M_{b1} , M_{b2} and M_{b3} , the pump beam after B_2 is aligned in a similar manner as the probe beam as discussed in the last section.

❖ ALIGNMENT OF THE MICROSCOPE OBJECTIVE (MO)

The alignment of the MO is one of the most crucial steps which ensure a good spatial overlap of the pump and the probe beams. To align the MO, first, a white screen is placed perpendicular to the beam path (Fig. 4.21) and the incident position of aligned probe beam is marked on the screen in the absence of the MO. Then the MO is mounted in such a way that the incident beam almost fills the back aperture of the MO as shown in Fig. 4.21. The output beam from MO is made to incident on the white screen in a defocused condition. If the beam is incident exactly on the centre of the back aperture and passes through the axis of the MO, then the defocused beam on the white screen should be exactly circular with equal intensity and the marked position of incident beam without the MO should be at the

Chapter 4

centre of the defocused beam. Any discrepancy implies that the incident beam on MO is not exactly centered. In that case the MO is moved either horizontally (for adjusting horizontal shift) or vertically (for adjusting vertical shift) to correct this misalignment. The intensity profile of the defocused spot is adjusted with the tilt of the axis of the MO till a symmetric intensity profile is achieved.

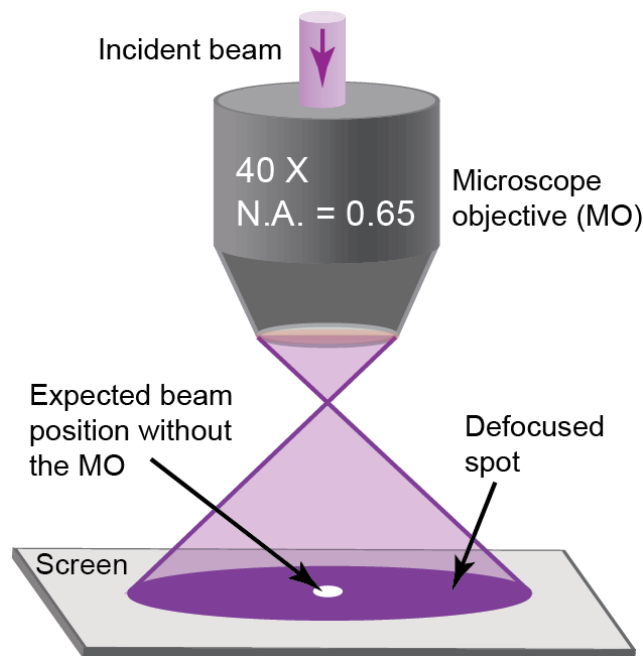


Fig. 4.21: A schematic diagram showing the alignment procedure of the microscope objective.

❖ ALIGNMENT OF THE OPTICAL BRIDGE DETECTOR (OBD)

First, the probe beam is made parallel to the array of hole on the optical table with the help of mirror Mr_8 without the OBD. The OBD is then placed in such a way that the beam is incident on the centre of the front aperture of the OBD. The beam then falls on the two photodiodes and reflects back through the front aperture of the OBD. To ensure that the incident beam and the axis of the detector are collinear, the back-reflected beams are made collinear to the incident beam. This is achieved by placing an aperture in the incident beam path little before the OBD and rotating the OBD around its horizontal and vertical axes to bring the back-reflected beams back to the aperture. The output voltages A , B , $A + B$ and $A - B$ are also monitored for finer alignment of the detector.

Chapter 4

4.5.2.5. *Some Routine Alignments*

Generally, all the alignments mentioned above are not required to be performed daily. They are required during the construction of the set up. However, performances of the lasers generally degrade after few months (4-6 months) due the change in the environment. Hence, a routine alignment of the laser cavity has to be done and this may result into a significant walking of the output beam from the Tsunami. In case there occurs a significant walking of the output of the Tsunami, the alignment procedures mentioned in the previous section (except the alignment of optical table) are required. In general, few steps as mentioned below are always followed, before starting daily experiments, to ensure a good alignment.

- At first, the output power and spectra of Tsunami are maximized after adjusting the central wavelength ($\lambda_0 = 800 \text{ nm}$) and FWHM ($\sim 12 \text{ nm}$ or more) with the help of external micrometer controllers of Tsunami.
- The alignment of the retro-reflector is checked by placing the 'beam height' after B₂ and by moving the retro-reflector from L position to the R position of the delay stage. If there is a shift of the probe beam with the movement of the retro-reflector, then the alignment procedure explained in section 4.5.2.4. is performed.
- The collinearity of the pump and probe beams is checked by placing the 'beam height' after the beam combiner (B₂). Both beams should go through the hole on the beam height. The overlap is further confirmed by observing their images in CCD camera. Any misalignment is fixed with the help of mirrors M_{b1}, M_{b3} and M_{r6}, M_{r7}.
- Next job is to check whether the pump and probe beams are co-axial with the MO or not. For that purpose, the MO is moved back and forth with the help of micrometer screw attached to the stage on which it is mounted. The pump and probe beams are focused and defocused with the movement of the MO, which can be monitored in the TV screen attached to the CCD camera. A movement of the centre(s) of the pump and/or probe spot(s) in the TV screen either along the horizontal direction or the vertical direction implies that the beam(s) is (are) not co-axial with the MO. In that case, the pump and/or probe beams are made collinear with the help of the mirrors M_{b1}, M_{b3} and M_{r6}, M_{r7}.

Chapter 4

- Finally, the alignment of the OBD is confirmed by aligning the back reflected beam from OBD with the incident beam.

On top of all these routine alignments, a fine tuning is required before starting the measurement. This is usually done by optimizing the reflectivity signal from some standard sample. We use a small piece of Si(100) wafer as the change in the reflectivity signal is significant in this sample. It is mounted on a sample holder with its polished surface facing the incident beams. The pump and probe fluences are chosen to be about 10 mJ/cm^2 and 2 mJ/cm^2 by adjusting attenuators A_1 and A_2 . The total reflectivity in the presence of the pump beam, just after the zero delay (by moving the stage to the position just after the zero delay), is checked. For a reasonably good alignment, this value should be above $600 \mu\text{V}$ in our set up. Otherwise, the overlap of pump and probe beams on the sample surface is improved by adjusting the mirrors M_{b1} , M_{b3} and M_{r6} , M_{r7} . After achieving the desired alignment, the time-resolved reflectivity data from the Si wafer is measured for about $\sim 2000 \text{ ps}$. The cross-correlation of pump and probe is obtained to be around 100 fs by fitting a Gaussian function to the reflectivity signal at the zero delay.

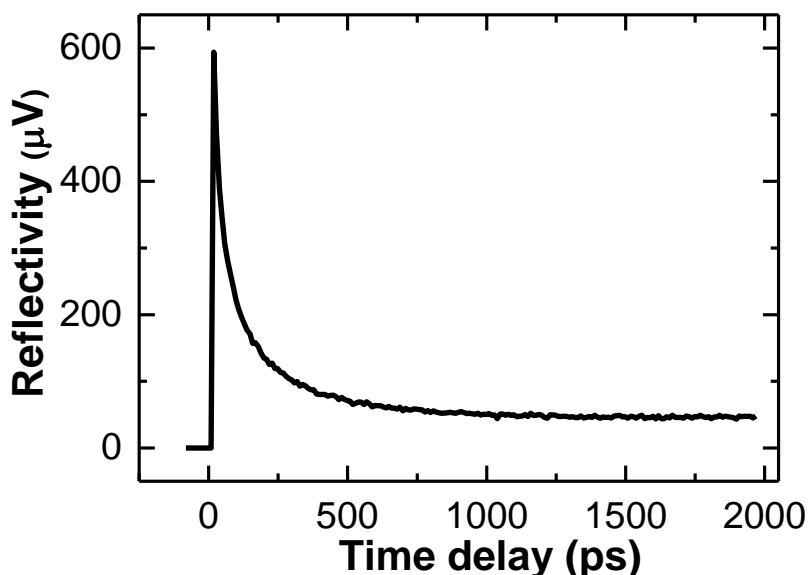


Fig. 4.22: The reflectivity signal obtained from a Si(100) wafer as a function of the time delay between the pump and the probe beams. The decay of the reflectivity signal after the zero delay can be fitted with a double exponential decay function to obtain the time constant of the longer decay which is about 220 ps in our case.

Chapter 4

A typical reflectivity signal from the Si wafer is shown as a function of the time delay between the pump and the probe in Fig. 4.22. The reflectivity increases to a maximum value right after the zero delay and then decays exponentially as the time delay increases. The reflectivity for the standard Si sample used in our set up is found to decay with a time constant of about 220 ps for a good alignment of the retro-reflector and the pump and probe beams. A faster decay indicates poor spatial overlap of the pump and probe beams for longer time delay. In that case, the retro reflector is moved to longer time delays from the zero delay in steps and the reflectivity signal is optimized at each time delay with the help of the steering mirrors. In this way, the delay stage is aligned for longer time delays. After optimizing the reflectivity signal for 3 - 4 different time delays, the full time-resolved reflectivity signal is measured again to check the decay constant. The entire process is repeated unless the desired decay constant is obtained. Once the whole alignment is finished, the set up becomes ready for measurements.

4.5.3. Static magneto-optical Kerr effect microscope (Static MOKE)

The static magneto-optical Kerr effect (Static MOKE) microscope was used to measure the magnetic hysteresis loops from some arrays of magnetic dots. The schematic diagram of the set up is shown in Fig. 4.23.

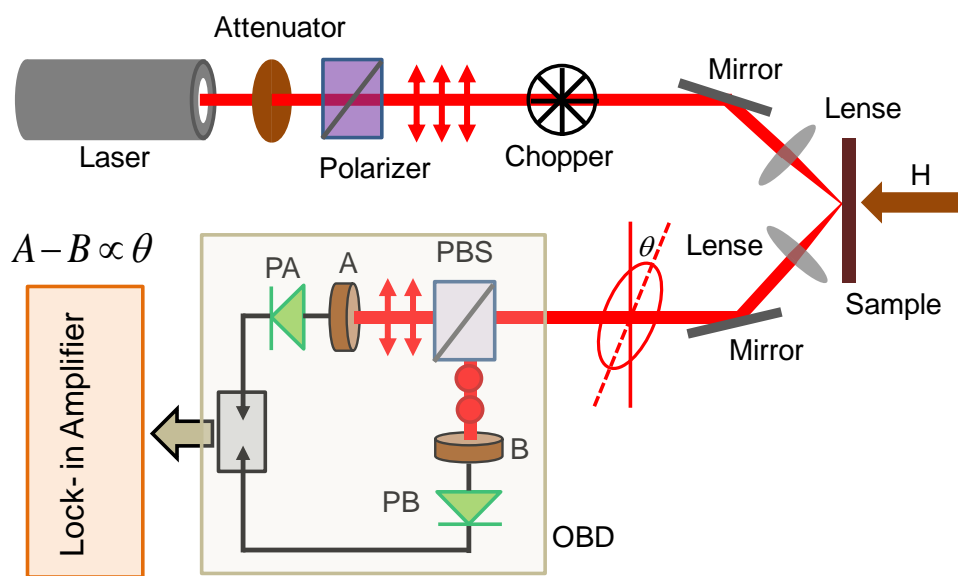


Fig. 4.23: A schematic diagram of static magneto-optical Kerr effect (Static MOKE) microscope along with the direction of the applied bias field H .

Chapter 4

A He–Ne laser of wavelength (λ) = 632 nm was used for this measurement. The laser beam passes through a variable attenuator for controlling the intensity of the incident beam on the sample. The intensity of the transmitted beam is controlled by moving the attenuator perpendicular to the beam with the help of a moving stage. The beam is polarized linearly by passing it through a Glan-Thompson polarizer with *s*-polarization. This polarized beam is then chopped at 2 kHz frequency by a chopper controlled by a controller unit. A lens is used to focus the beam on the sample. The reflected beam is collected by another lens and directed towards an optical bridge detector (OBD) as described in section 4.5.2. with the help of a mirror. The magnetic field is applied in the normal direction to the plane of the sample. In this geometry the polar Kerr rotation is measured. In absence of any magnetic field, first the balanced condition of the detector is obtained by rotating the axis of the polarized beam splitter (PBS) slightly away from 45°. To calibrate the OBD, the PBS is rotated by 1° on both sides of the balanced condition and the dc output of the detector is recorded. When the magnetic field is applied, the detector will no longer be in the balanced condition (*i.e.*, $A \neq B$). The difference signal ($A - B$), which is proportional to the magnetization of the sample, is measured as a function of the bias magnetic field to obtain the hysteresis loop and is converted to Kerr rotation by multiplying it with the calibration factor. The output signal is measured in a phase sensitive manner by using a lock-in amplifier with the reference signal from the chopper.

5. Literature survey

5.1. Introduction

Investigation of high frequency (ultrafast) magnetization dynamics in ferromagnetic thin films and confined structures, such as magnetic multilayers (MLs), antidot lattices (ADLs), nanodots, nanostrips, nanoparticles and nanowires (NWs) are interesting for both fundamental research and technological applications. Since the time-scale of the dynamical processes involved in various applications is in the sub-nanosecond regime, it is essential to understand the ultrafast magnetization dynamics in these structures down to sub-nanosecond scale in order to optimize the operational speeds.

The interface effects between layers in a periodically layered ultrathin magnetic and non-magnetic structures give rise to some novel properties which are highly desirable in present and future technology. However, the dynamics depends significantly on the layer thicknesses. Depending upon the spacer layer thickness, one can have dipolar or dipole-exchange or exchange dominated spin-wave (SW) modes in these systems. As a result, these structures offer rich magnetization dynamics, which is important to understand and needs to be controlled for various applications including data storage, spin transfer torque-magnetoresistive random access memory (STT-MRAM), magnonic crystals and in magnetic meta-materials with a negative refractive index in the high GHz frequency regime [227]. Consequently, a large amount of studies are being performed on the magnetization dynamics on magnetic MLs by various methods. In this thesis, we will concentrate on Co/Pd and Co/Pt MLs which are considered to be strong candidates for these studies due to their large perpendicular magnetic anisotropy (PMA) and strong spin-orbit coupling, and hence large magneto-optic Kerr effect. Consequently, patterning these MLs to nanoscales has also created large interest. Exchange-spring (ES) bilayers also emerged as promising candidates for storage and permanent magnet applications. The exchange coupling between soft and hard layers gives an option to modify its properties for different applications. The spin-twist structure introduced in the soft layer, due to the presence of the hard layer, affects the propagation of SWs. As a result, new SW modes are observed in

Chapter 5

the ES regime as opposed to the rigid magnet regime and they depend strongly on the soft layer thickness [194]. These features have triggered considerable interest in the ES samples. On the other hand, ferromagnetic (FM) nanowires (NWs) have attracted significant attention due to its high and tunable shape anisotropy. Their dynamic properties significantly depend on the material as well as their diameter and aspect ratio. The finite width and packing density of the NWs play crucial role in determining their magnetization dynamics [228]. The shape anisotropy competes with the magnetocrystalline anisotropy of the material and the anisotropy due to the inter-wire magnetostatic interactions to modify the SW modes in the system. A mode localized in one particular region of the NW can be transferred to some other region by simply applying a dc spin-polarized current. Hence, these magnetic NWs offer a vast field of study. Below, we will briefly discuss about some previous studies of magnetization dynamics in these structures.

5.2. Magnetic multilayers

Initially, studies were performed on MLs with thick spacer layer so that the constituent layers are not exchange coupled. Hence, in these structures purely dipolar collective modes were observed. A dipolar surface wave mode exists in each magnetic layer [229-231] and due to the dipolar stray fields, these modes may get coupled via the spacer layers and form collective excitations. The exchange interaction and surface anisotropies can significantly affect the SW modes. In ML, due to the presence of many interfaces, this effect is strongly enhanced. So, if the spacer layer is thin enough to allow coupling between the magnetic layers, then the SW spectra change significantly. In magnetic ML with ultrathin layers, the dipolar collective modes (except the stack surface mode) gets converted to exchange dominated modes (PSSW modes) in the full coupling limit. In case of Co/Pd MLs, theoretical calculations show that the effect of interlayer exchange coupling comes into play only when the layer thicknesses are $< 50 \text{ \AA}$. BLS experiments performed on $[\text{Co/Pd}]_{30}$ ML with varying Co layer thickness [232] show that when the individual Co layers are 32 atomic layers thick, collective dipolar SW excitations are observed. With decreasing thickness, the band-

Chapter 5

width of the collective excitations decreases upto a thickness of 4 atomic layers. Beyond this thickness, the surface mode frequency remains fixed, however, the frequency of the bulk mode increases. For in-plane magnetized Co(25Å)/Pt ML with varying Pt layer thickness also, studies confirm the presence of multimode spectra due to the coupling of the Co layers [233]. Theoretical calculations performed with a semi-classical model in the magnetostatic limit [234] show surface SW modes in ultrathin films can be extremely sensitive to PMA at interfaces. For a stack of six 8.8 Å Co films separated by some non-magnetic spacer layer of thickness 7.6 Å, when the surface anisotropy $K_s < -0.4 \text{ erg.cm}^{-2}$, the magnetization prefers an out-of-plane orientation. For this configuration, the surface mode merges into the bulk band whereas the lowest order bulk mode becomes strongly localized to the sample and becomes soft [235]. This rich SW spectra in MLs hence contain information on interlayer coupling, magnetic properties including saturation magnetization, g -factor, volume and interface anisotropies and spatial variation of magnetic parameters [231-232, 234-235]. For example, epitaxial (100) textured Co(3-5Å)/Pt(17Å) MLs show a broad band of collective SWs. The extracted volume (K_v) and interface (K_s) anisotropy values show that in these MLs $K_v > K_s$, and the SW spectra is determined by the in-plane anisotropy. On the other hand, in polycrystalline (111) textured Co(3-5Å)/Pt(17Å) MLs $K_v < K_s$, and hence these MLs show high PMA. In both cases, the broadening of SW spectra is found to be due to the variation of interlayer exchange coupling constant and local variation of Co layer thickness (which means local variation of effective anisotropy in presence of a strong interface anisotropy) [236-237]. Following these findings, several works on magnetization dynamics in magnetic MLs by various measurement techniques were started [22, 238-251]. Study of magnetization reversal of PMA Co/Pt ML in ultrashort time scale establishes the crucial role of anisotropy in determining the reversal behaviour [22, 245]. At the time of the magnetic field excitation, the lattice may freeze into phonon distorted state. This causes some local changes in the electronic band structure, which in turn modifies the anisotropy due to the spin-orbit coupling. As a result, instead of having a sharp region, a broad transition region between two magnetization states is observed. Broadband extraordinary Hall effect (EHE) microcircuits were also used to measure the high frequency magnetization dynamics of PMA MLs [246]. However, the breakthrough in this research area is the all-optical

Chapter 5

excitation and probing of magnetization dynamics in PMA Co/Pt MLs by TR-MOKE technique in 2007 [216]. A systematic study is performed with $[\text{Co}(4\text{\AA})/\text{Pt}(8\text{\AA})]_n$ MLs with varying no. of bilayer repeats (n). Due to high PMA, very fast precession frequency is observed for all samples. The PMA values decrease with increasing n whereas the damping parameter α increases with increasing n . The enhanced interaction between magnons and conduction electrons was suggested as a possible mechanism for the enhancement of α with n . On the other hand, when the α values were calculated from domain wall motion in Pt/Co/Pt films, they were found to be independent of Co layer thickness although PMA increases with decreasing thickness [249]. TR-MOKE measurements on Pt/Co/Pt films show that the PMA is inversely proportional to the Co layer thickness [250]. The α values were also found to be dependent on Co layer thickness, but they do not follow any particular trend. On the other hand, in CoFeB buffered $[\text{Co}(0.3\text{ nm})/\text{Pd}]_6$ MLs with varying Pd layer thickness, it is found that the α value depends on the Pd layer thickness also. The CoFeB buffer layer significantly affects both the precession frequency and α of the films due to its in-plane anisotropy [252].

Not only the SW spectra, α or PMA, in MLs one can even control the speed and efficiency of ultrafast demagnetization [253]. By using the spin-pumping mechanism [254-256], it has been found that it is possible to control the efficiency of spin-angular-momentum transfer by introducing a spacer between two ferromagnetic (FM) layers. If the magnetizations in FM layers are parallel (P configuration), then there will be no spin current. But if the magnetizations are antiparallel (AP configuration), then there will be some non zero spin current. In Co/Pt MLs, by introducing different spacer layers (NiO or Ru), significant changes in the ultrafast demagnetization were observed. In case of Ru spacer layer, in AP configuration, larger magnetization loss along with $\sim 25\%$ faster demagnetization was observed as compared to the P configuration. This difference in the demagnetization times between the P and AP configurations was not observed when NiO spacer layer was used however, there was still a difference in the amount of demagnetization for P and AP configurations. The $\sim 25\%$ decrease in demagnetization time in AP state for Ru spacer layer was attributed to the direct spin-momentum transfer between two Co-Pt layers.

5.3. Exchange-spring magnets

Though there are several studies of magnetization dynamics on magnetic MLs with PMA, there are only limited numbers of reports in the literatures on the magnetization dynamics of ES magnets and there have been no report on time-domain measurements on ES systems at all. Dynamical measurements on the Sm-Co/Fe ES bi-layers by BLS technique [57, 257] show interesting dependence of magnon frequency on the applied field. The Sm-Co layer thickness was fixed at 200 Å and the Fe layer thickness was varied from 25 to 200 Å and field dependence of the magnon frequency was measured. The cleanest spectra were obtained for Fe layer with thickness of 100 Å. The spectra were obtained for two configurations: applied field (H) along i) hard axis and ii) easy axis of the system. For fields along hard axis, the results were same for positive or negative fields, which can be justified by symmetry arguments. However, for fields applied along easy axis, the results for positive and negative fields were significantly different. The frequency first decreases with decreasing H upto $H = -2.5$ kOe where it attains a minimum value indicating the onset of the reorientation of the Fe film into a spiral structure. Beyond this if H is decreased further, the frequency starts to increase and shows a jump at $H = -5$ kOe due to the reversal of magnetization in the Sm-Co layer. Below this field, the frequency values are similar to those for the positive fields. The experimental results were qualitatively described by a simple theoretical model employing layer-by-layer permeability calculations [258]. An interfacial exchange field of 2.4 kOe in 100 Å Fe layer was obtained from the calculation. The presence of the hard layer also affects the in-plane anisotropy of the soft layer. To find the functional dependence of the in-plane anisotropy [259], the FMR spectra of Sm-Co(x)/Fe(y) ES bi-layers with (x,y)= (20,20) and (35,30) nm were recorded as a function of the in-plane angle. The spectra were characterized by symmetric line shapes. Sm-Co(20nm)/Fe(20nm) sample was measured at room temperature but Sm-Co(35nm)/Fe(30nm) was measured at 150 K to prevent Sm-Co from switching during the measurements. Measurements show the presence of three anisotropy contributions: i) an out-of-plane anisotropy dominated by shape effects, ii) a unidirectional exchange anisotropy originating from the strong interface interactions between Sm-Co and Fe layers and iii) a crystal field anisotropy consistent with that of epitaxial (211) Fe. By similar measurements in Sm-Co(20nm)/Fe(20nm) samples,

Chapter 5

three SW modes were observed: one bulk and two surface modes [260] in both in-plane (IPG) and out-of-plane (OPG) geometry. For IPG, the bulk mode was found to shift to lower field values and disappear at an angle of 40° .

Another very important candidate for the hard magnetic layer in an ES bi-layer is FePt. Its high thermal stability [261] and large uniaxial magnetic anisotropy originate from the spin-orbit coupling of the Pt and the hybridization between Pt $5d$ and Fe $3d$ states [262-263]. This high anisotropy and broad relaxation channel originating from the spin-orbit coupling results in high precession frequency and small relaxation time in FePt which is extremely desirable for technological applications. There are two very important studies on the ultrafast magnetization dynamics of $L1_0$ -ordered FePt films [264-265]. In case of 6.5 nm thick FePt film, it was observed that the precession frequency did not show any monotonic dependence on the applied field H . However, the relaxation time increases slowly and α decreases steadily with increasing H [264]. As one of the possible reasons of this dependence, inhomogeneity of the effective anisotropy in the sample was suggested. Whereas in the other study [265], the precession frequency was found to increase systematically with increasing H , however, a slight decrease in the relaxation time with increasing H was observed. Another important finding of this work was that both the first and second order anisotropies in the FePt layer contribute in determining its magnetic behavior. However, later it was found that in $L1_0$ -ordered FePt films, only first order anisotropy is important [266]. The presence of a small hard-axis hysteresis causes local fluctuations of the internal fields that influences the shape of the hard-axis hysteresis loop and often misinterpreted as a second order anisotropy. FMR measurements on FePt(10nm)/Fe(2 and 3.5nm) show how the magnetization dynamics depends on the soft layer thickness in an ES magnet [267]. For 2 nm thick Fe layer, the bi-layer behaves as a rigid magnet. However, when the Fe layer thickness is increased to 3.5 nm, the bi-layer behaves as an ES magnet and in addition to the rigid magnet mode; two additional SW modes are observed. Similar results were also obtained by micromagnetic simulations [268].

5.4. Magnetic nanowires

The study of SWs in magnetic NWs dates back to the 1991 when discrete modes in the SW spectrum of permalloy (Py) NW array were observed at a single value of wave-vector k . However, the origin of the modes was not identified at that time. The origin of this quantization was discovered later in 1998 [269]. BLS measurements on Py NWs revealed the existence of discrete SW modes in the low k region. Interestingly, these modes did not show any noticeable dispersion and behave like standing wave modes. They were observed over a continuous range of k for a wire of finite width. These modes were not much affected by the separation between the wires. Hence, it can be believed that these modes originate purely due to the finite width of the wires. More than one set of discrete modes were observed in the experiment. The lowest frequency modes appeared near zero k whereas higher frequency modes appeared at higher k values with an increase in the corresponding cut-off k . The frequency splitting of the discrete modes was found to decrease with increasing wave number. Beyond a certain value of k , continuous film like dispersion is obtained. It was proposed that each wire acts as an independent scattering centre. The SW modes, in that case, were described by truncated plane waves and hence, k was no more conserved. As the dynamic component of the magnetization was no longer a periodic function, the Fourier transform was non-zero over a continuous range of k and hence, the discrete modes were observed over a finite range of k . No clue of the zone folding effect due to the periodic nature of the NW arrangements was found.

The quantization of modes were also supported by theoretical studies [270]. From FMR studies [271] on Ni, Co and Py NWs, it was found that the resonance frequencies depend strongly on the material. The frequencies of Co were higher than that of Ni for all bias field values whereas the frequencies values of Py were in the intermediate range. It was found that above a certain critical field H_s , the frequency varied linearly with the applied field for all samples, whereas below H_s , there is a deviation from the linear relationship. In the linear regime, the samples were in saturated state and the dependence was well explained by the Kittel [144] formula. On the other hand, the behavior below H_s was attributed to the unsaturated state of the NWs. The effect of dipolar coupling between the NWs was also characterized by the FMR technique [272-274]. The dipolar coupling acts as an additional

Chapter 5

anisotropy which acts in a direction perpendicular to the wire axis. For an array of Py or Ni NWs, we have only the shape anisotropy along the wire axis. In that case, if the wire density is increased, the effective anisotropy will decrease. Eventually, the dipolar interaction may overcome the shape anisotropy and a cross-over between easy and hard directions of magnetization can be observed.

To understand the results obtained experimentally, theoretical models were developed for the SW modes in circular NWs under the application of uniform microwave field [275-277]. Later, this theory was generalized for NWs with arbitrary cross sections [278]. Integral equations were developed using the extinction theorem to obtain both eigenvectors and eigenvalues. This theory also provided an insight to the effect of roughness on the SW modes [279]. It was found that to the first order, the roughness could cause a shift in the frequencies of the SWs in the magnetostatic limit. Theoretical calculations were performed to calculate the differential cross-section for inelastic magnon scattering of non-polarized neutrons [280]. The cross-sections for SWs of different forms, due to the delta-function dependence, were found to be strongly dependent on the direction of the wave-vector k . Further, studies on Py NWs by BLS showed that under the application of a small transverse field, a branch of low frequency SW modes appeared [281]. However, this branch did not exist for fields applied along the longitudinal direction. With increasing transverse field, a SW hybridization was observed in the vicinity of the switching field. A Hamiltonian-based microscopic theory for NWs with inhomogeneous magnetization showed that the appearance of this low frequency mode was a consequence of small easy-plane single-ion anisotropy at the NW surface. TR-MOKE microscopy was also used to measure the magnetization dynamics in electro-deposited Py NWs with high packing density and wire diameter much greater than the exchange length of Py [228]. The experimental data were supported reasonably well by the micromagnetic simulations. The competition between shape anisotropy and the anisotropy associated with the inter-wire magnetostatic interaction in the array was investigated. Simulations of the remanent state revealed the presence of antiferromagnetic alignment of magnetization in adjacent NWs and formation of vortex flux closure structures at the ends of each NW. As the applied bias field was increased from the remanent state, the ground state changes and accordingly, the profile of

Chapter 5

the resonant mode changes from nonuniform to uniform nature within the plane of the wire. As a result, the frequency of the mode was found to decrease initially with increasing bias field. Resonant modes were also studied for fields applied in the direction perpendicular to the wire axis. The dependence of the SW spectra on the packing density and the dispersion relations for the modes propagating through the array for field parallel to the wire axis were also investigated. Finally, a tunneling of the end modes through the middle of the wire was observed due to the extended penetration of the dynamic demagnetizing fields into the middle of the wires and also due to the lowering of the tunnel barrier by the static demagnetizing field in the array.

BLS spectra obtained from low aspect ratio Ni nanorods [282] possessed two important features: 1) two-peak structure of BLS lines due to the presence of zones with high density of states in the spectrum of SW resonant modes localized in the nanorods and 2) high asymmetry between Stokes and anti-Stokes lines. To study the effective anisotropy field H_{ani} in an array of FM NWs, anisotropy field distribution (AFD) method was implemented [283]. The resonant SW modes in arrays of Ni, Co and Py NWs were measured by FMR technique first. It was found that if the magnetocrystalline anisotropy of the system is negligible, then the AFD method provided an accurate estimation of H_{ani} . Determination of H_{ani} by AFD method included the interwire dipolar interactions also. However, if the magnetocrystalline anisotropy of the system was high, then complex magnetization processes other than the coherent rotation was observed when the magnetization was relaxed from its saturation state and the accuracy of the results obtained from the AFD method was found to decrease accordingly. FMR measurements along with first order reversal curve (FORC) analysis were performed to explore the anisotropy in $\text{Co}_{94}\text{Fe}_5\text{B}_1$ NW arrays in which Co had two types of crystallinity – 1) c-axis oriented parallel to the wire axis and 2) c-axis oriented perpendicular to the wire axis [284]. An apparent positive first order anisotropy constant was observed for case 1, whereas case 2 showed the presence of a negative uniaxial anisotropy. On the other hand, FMR studies on CoFeB NWs under the application of transverse magnetic field revealed the presence of two distinct modes [285]. These two modes were observed below saturation field and modeled as the response from two interacting populations of the wires, magnetized mirror-symmetrically to each other

Chapter 5

relative to the plane of the array. Spatial profiles of the SW modes in cylindrical NWs were investigated by micromagnetic simulations [286-287]. Under the application of a spin-polarized dc current, it was observed that apart from the edge mode, other SW modes disappeared from the system. Surprisingly, when the current exceeded a certain critical value, an edge mode transformed to the uniform mode of the NWs. As the edge mode varies linearly with bias field, a particular frequency can thus be chosen and transferred through the NW which is extremely desirable phenomenon in some present technological applications.

Current and Oersted field induced domain wall dynamics in FM NWs have been a research field of intense interest due to their potential applications in race track memory [288-289]. However, this is beyond the scope of this thesis and hence is not introduced in details.

6. Correlation between perpendicular magnetic anisotropy and Gilbert damping in [Co/Pd]₈ multilayers with variable Co layer thickness

6.1. Introduction

Magnetic multilayers (MLs) with perpendicular magnetic anisotropy (PMA) have attracted attention due to their potential applications in patterned magnetic media [14], spin transfer torque magnetic random access memory (STT-MRAM) [290-291] and magnonic crystals [3, 292]. For applications in magnetic media and STT-MRAM devices, large precession frequency associated with the large PMA and a reliable and low damping constant α are desirable. On the other hand, for applications in magnonic crystals, broadly tunable magnonic frequencies, and α with physical and material parameters are essential. All potential applications demand large and broadly tunable precession frequencies, small α values and a correlation between the PMA and α . PMA is believed to originate from the interface anisotropy due to the broken symmetry and d - d hybridization [107] at the Co/Pd and Co/Pt interfaces. The competition between interface and volume anisotropies results in a variation in PMA with the thickness of the Co layer (t_{Co}) as has been reported in continuous [293] and patterned [294] magnetic MLs. Consequently, a large variation in the precession frequency in the picosecond magnetization dynamics of these MLs is expected. On the other hand, it has been predicted recently [250] that there may be a linear correlation between PMA and damping based on existing theoretical works [104, 295]. The intrinsic Gilbert damping α and PMA both have their origins in the spin-orbit interaction and are approximately proportional to ξ^2/W , where ξ is the spin-orbit interaction energy and W is the d -band width. However, no clear correlation between the PMA and α has been observed so far [216, 249-250]. Mizukami *et al.* [250] observed an increase in α with decrease in t_{Co} but it was not inversely proportional to t_{Co} . In this work, we studied the picosecond magnetization dynamics in [Co(t_{Co})/Pd(0.9 nm)]₈ MLs with t_{Co} varying between 1.0 and 0.22 nm. We observed a systematic increase in the precession frequency and α with

Chapter 6

the decrease in t_{co} . The extracted PMA, from the macrospin modeling of the precession frequency, shows a linear correlation with α .

6.2. Sample fabrication

The $[\text{Co}(t_{co})/\text{Pd}(0.9\text{nm})]_8$ MLs were fabricated on (100) oriented Si wafer with a native SiO_2 surface layer by dc UHV magnetron sputtering with confocal sputter up geometry [294]. The Co target was tilted and arranged in a circle around the central Pd target. The substrate was rotated at 3 Hz during the deposition and placed at the focal point of the targets. The base pressure of the deposition chamber was 2×10^{-8} mbar and magnetron sputtering was performed at 3 mTorr Ar pressure. $\text{Ta}(1.5\text{nm})/\text{Pd}(3.0\text{nm})$ seed layer was used to confirm the (111) texture with a mosaic spread of 7° full width at half maximum (FWHM). The samples were taken out of the chamber after the deposition of the Pd cap layer.

6.3. Characterization and measurement of quasistatic and ultrafast magnetization dynamics

The interface qualities of the MLs were investigated by X-ray reflectivity (XRR) technique as described in section 4.4.4. of chapter 4. In this method, X-ray reflection intensity curves from grazing incident X-ray beam are collected to extract i) individual layer thickness in the ML and ii) surface and interface roughness. The electron density profile (EDP) can also be determined in different layers. However, this is beyond the scope of our study. We have used the Cu K_α X-ray beam of wavelength 1.54 \AA for the XRR measurements. The static magnetic properties were investigated by both polar magneto-optical Kerr effect (P-MOKE) and vibrating sample magnetometry (VSM) at room temperature. In VSM, the magnetic field up to 16 kOe is applied in steps of 100 Oe in two different orientations during the measurements – 1) along the normal to the ML and 2) in the plane of the ML.

Chapter 6

The ultrafast magnetization dynamics was probed by time-resolved magneto-optical Kerr effect (TR-MOKE) measurements in a two-color pump-probe set up. The second harmonic ($\lambda = 400$ nm) of a Ti-sapphire laser (Tsunami, SpectraPhysics, pulse-width < 70 fs) was used to pump the samples, while the time-delayed fundamental ($\lambda = 800$ nm) laser beam was used to probe the dynamics by measuring the Kerr rotation by means of a balanced photo-diode detector, which completely isolates the Kerr rotation and the total reflectivity signals. The pump and the probe beams were focused and spatially overlapped onto the sample surface by a microscope objective with numerical aperture N. A. = 0.65 in a collinear geometry. A bias field (H) of variable amplitude is applied at a small angle ($\sim 10^\circ$) to the surface normal of the sample. The pump beam was chopped at 2 kHz frequency and a phase sensitive detection of the Kerr rotation was made by using a lock-in amplifier with a reference signal taken from the chopper. The optical bridge detector completely isolated the time-resolved Kerr rotation and the reflectivity data and there is no breakthrough of one signal into another.

6.4. Results and discussions

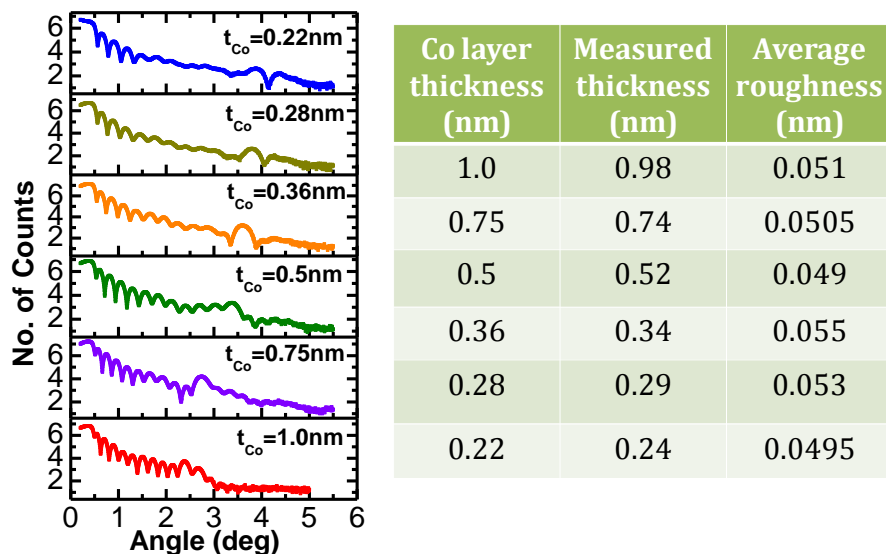


Fig. 6.1: X-Ray reflectivity data and the extracted thickness and interface roughness values for $[\text{Co}(t_{Co})/\text{Pd}(0.9\text{nm})]_8$ MLs.

Chapter 6

The average interface roughness and thickness values obtained after comparing simulated and experimental results of the XRR data are presented in Fig. 6.1 along with the corresponding XRR spectra. The average roughness value at the Co/Pd interface is about 0.05 nm. However, there is a slight variation (although, not a systematic one) in the roughness values. Generally, in MLs, the magnetization dynamics gets affected by the interface roughness. Hence, here also we may see some effect of this variation in the roughness values on the magnetization dynamics. The measured thickness values, however, are close to the nominal values.

Fig. 6.2(a) shows the results obtained from VSM measurements on the series of ML samples. The extracted magnetic anisotropy field (H_k) increases systematically with the decrease in t_{Co} and exhibits a maximum at 0.22 nm, beyond which it decreases sharply. The saturation magnetization (M_s), on the other hand, decreases monotonically with the decrease in t_{Co} over the entire range.

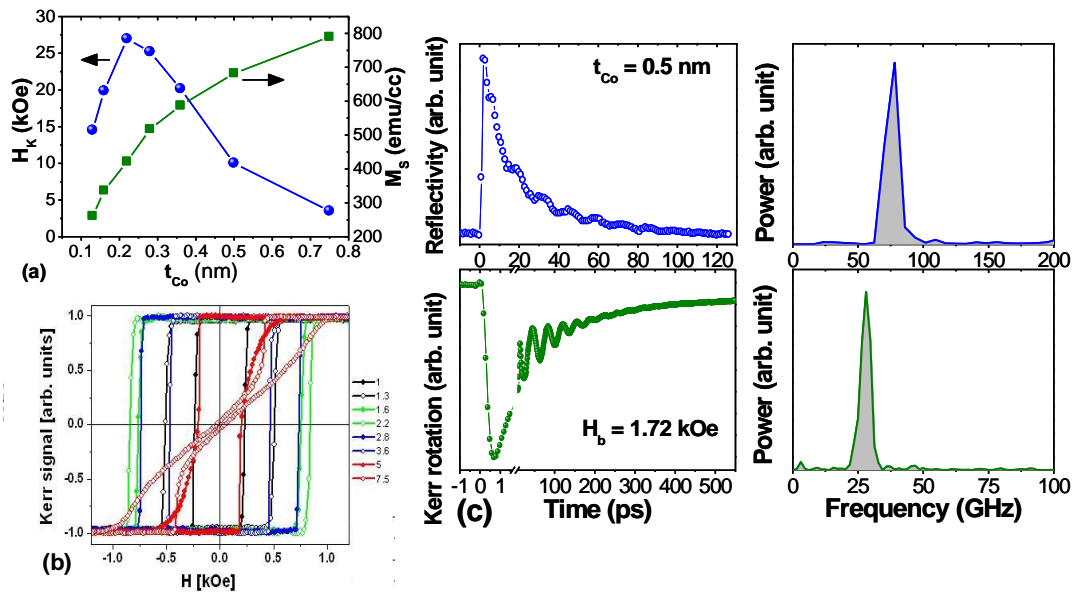


Fig. 6.2: (a) Dependence of magnetic anisotropy field and the saturation magnetization on the Co layer thickness t_{Co} in $[\text{Co}/\text{Pd}]_8$ multilayer films, as measured by static magnetometry. (b) Hysteresis loops from the multilayer samples obtained from polar MOKE measurement. (c) The time-resolved reflectivity and Kerr rotation signals and the corresponding FFT spectra from the multilayer sample with $t_{Co} = 0.5$ nm, showing the frequencies of phonon and the precession of magnetization, respectively.

Chapter 6

Fig. 6.2(b) shows the magnetic hysteresis loops as measured by the PMOKE. Although the saturation magnetization cannot be characterized by using PMOKE but the anisotropy field obtained from the VSM data are confirmed by the PMOKE loops.

Fig. 6.2(c) shows typical time-resolved reflectivity and the Kerr rotation data and the corresponding fast Fourier transform (FFT) spectra using a Welch window function from the ML with $t_{Co} = 0.5$ nm at $H = 1.72$ kOe. The precessional dynamics appears as an oscillatory signal above the slowly decaying part of the time-resolved Kerr rotation after an ultrafast demagnetization within 600 fs, and a fast remagnetization within 10 ps. The time-resolved reflectivity also shows an oscillation with about 77 GHz frequency, originating from thermally excited strain waves [296], which is well above the frequency of precession of 28 GHz for this sample, confirming that there is no cross-talk between these two signals. In addition, the precessional frequency shows a clear variation with the bias magnetic fields as opposed to the frequency of oscillation observed in the reflectivity signal.

Table 6.1: Variation of demagnetization, slow and fast remagnetization times with t_{Co} .

Co layer thickness (t_{Co}) (nm)	Demagnetization time (fs)	Fast remagnetization times (ps)	Slow remagnetization times (ps)
1.0	500	5.8	225
0.75	500	6.2	350
0.5	600	6.0	400
0.36	600	5.5	280
0.28	700	6.1	550
0.22	700	4.8	490

Chapter 6

Although, a slow increase of the demagnetization time, as shown in Table 6.1, is observed with decreasing t_{Co} , there is no such trend for fast and slow remagnetization times for these MLs. However, the different values of these times for different samples can be attributed to the spins at different surface of the layers [297-298] and a variation of the spin-orbit coupling in these samples [299-301].

Fig. 6.3(a)-(b) show the time-resolved Kerr rotations and the corresponding FFT spectra for samples with different t_{Co} . All samples show a single precession frequency due to the collective precession of the whole stack, which allows us to use the macrospin modeling of their frequency and damping.

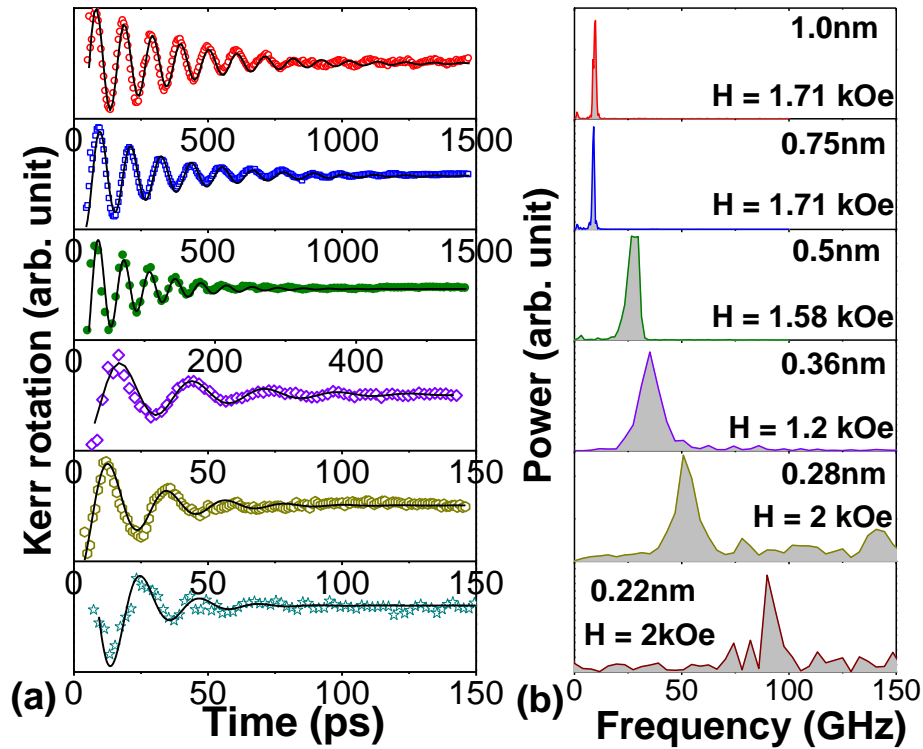


Fig. 6.3: (a) The time-resolved Kerr rotation data after background subtraction and (b) the corresponding FFT spectra are shown for $[Co/Pd]_8$ films with different Co layer thickness t_{Co} . The solid lines in Fig. 6.3(a) correspond to the fit with eqn. (6.2). The applied bias fields are also shown in the figure.

The variation of precession frequency with the bias magnetic field is plotted in Fig. 6.4(a) for various values of t_{Co} . The precession frequency increases sharply for $t_{Co} \leq 0.75$ nm

Chapter 6

indicating the sharp increase in the PMA in this range. The variation of the precession frequency with bias field is analyzed by the solution of the Landau-Lifshitz-Gilbert (LLG) equation [132, 302] (eqn. (2.44)) under macrospin model.

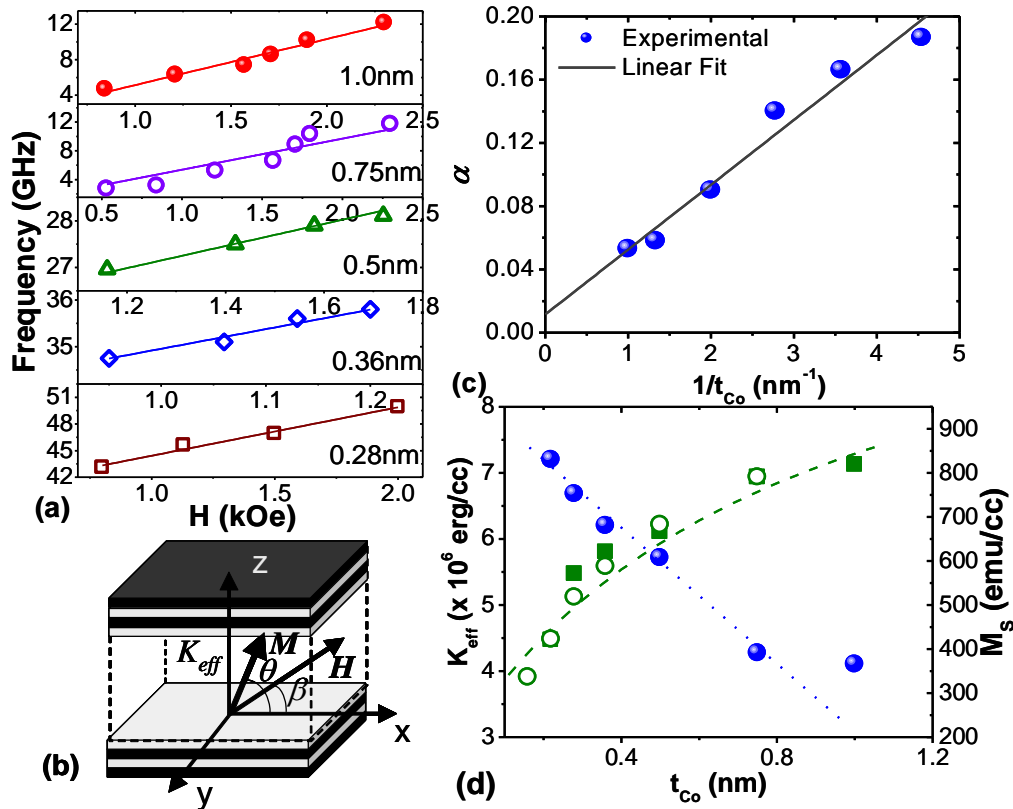


Fig. 6.4: (a) The bias field dependence of experimental precession frequency (symbols) and the calculated frequencies (solid line) with eqn. (6.1) are shown for multilayers with different Co layer thickness. (b) The geometry for the macrospin model is shown. (c) The damping coefficient α (symbols: experimental data, solid line: linear fit) is plotted as a function of $1/t_{Co}$. The extracted perpendicular magnetic anisotropy (K_{eff}) and the saturation magnetization M_s (filled squares: from TR-MOKE, open circles: from static magnetometry) are plotted as a function of t_{Co} . The dashed line shows the calculated M_s values, while the dotted line corresponds to the linear fit to K_{eff} vs t_{Co} .

For the experimental geometry as shown in Fig. 6.4(b), the expression for precession frequency obtained after linearizing LLG equation under small angle approximation is given by

Chapter 6

$$f = \frac{\gamma\mu_0}{(1 + \alpha^2)} \left[H \frac{\sin \beta}{\sin \theta} + 2 \frac{K_{eff}}{\mu_0 M_s} - M_s \right] \quad (6.1)$$

where γ is the gyromagnetic ratio, α is the damping coefficient, θ and β are the angles made by the equilibrium magnetization (M) and the bias field with X-axis, K_{eff} is the effective magnetic anisotropy and M_s is the saturation magnetization. θ is obtained by minimizing the total energy of the system, while β is known from the experimental geometry. α is determined by fitting the time-resolved magnetization with a damped sine function

$$M(t) = M(0)e^{-\frac{t}{\tau}} \sin(\omega t - \phi) \quad (6.2)$$

where $\tau = \frac{1}{2\pi f\alpha}$, f is the experimentally obtained precession frequency and ϕ is the initial phase of oscillation [303].

The calculated frequencies are plotted as solid lines in Fig. 6.4(a) and are in good agreement with the experimental data. α is found to be inversely proportional to t_{Co} over the entire range, as shown in Fig. 6.4(c). The extrapolation of the linear fit to α vs. $1/t_{Co}$ data upto $1/t_{Co} = 0$ gives $\alpha = 0.011$, which is very close to the value for bulk Cobalt (0.01). In Fig. 6.4(d) we plot K_{eff} and M_s as a function of t_{Co} , as extracted from the macrospin modeling. K_{eff} is also found to be inversely proportional to t_{Co} similar to α , indicating a clear linear correlation between α and K_{eff} . For a comparison the M_s values, as obtained independently from the static magnetometry, are also plotted as open circles in Fig. 6.4(d). The values of M_s obtained from the TR-MOKE measurements almost coincide with those obtained from the VSM loops. We have also calculated the variation of M_s with t_{Co} and found that consideration of slight induced magnetization (15% of the Cobalt layer) of the Pd layers [16, 303] is essential for a good agreement between the experimental and the theoretical data (dotted line in Fig. 6.4(d)).

Chapter 6

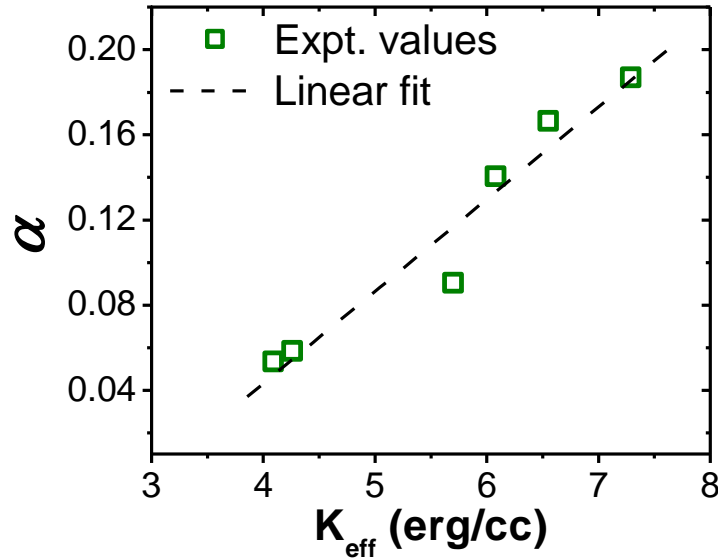


Fig. 6.5: The damping coefficient α is plotted as a function of K_{eff} (symbols) and the dotted line corresponds to the linear fit.

In Fig. 6.5, we plot α as a function of K_{eff} , which clearly shows that α is directly proportional to K_{eff} with a slope of 4.33×10^{-8} cc/erg. The values of α obtained for $[\text{Co}/\text{Pd}]_8$ MLs in this experiment are much lower than the previously published works [216, 250, 304-305]. One common channel of dissipation of energy is by scattering of the uniform precession with short wavelength magnons due to the presence of inhomogeneities including defects, which should increase as the thickness reduces. However, it has been reported that for perpendicularly magnetized samples magnon scattering is less effective [306] and hence is ruled out in materials with high PMA. The second possibility is spin pumping [254], caused by the spin current generated by the precession of magnetization entering into the Pd layer and getting absorbed due to its small spin diffusion length, thereby enhancing α . This is usually accounted for by considering the variation of the relaxation frequency $G = \alpha\gamma Ms$ with $1/t_{co}$ ^{12,22} but its value is much lower in our case than the previously reported values. The third possibility is the decrease in bandwidth W for the Co atomic layer in contact with the Pd due to the Co 3d-Pd 4d hybridization [107]. The intrinsic Gilbert damping α and PMA both have their origins in the spin-orbit interaction and are approximately proportional to ξ^2/W , where ξ is the spin-orbit interaction energy and W is the d -band width. This is primarily an interface effect and effectively increases both α and K_{eff} . The

Chapter 6

observation of direct proportionality between α and K_{eff} strongly indicates that this may be the primary mechanism of enhancement of α in our experiment. The fourth possibility is the roughness and alloying effects at the interface [250]. However, while interface roughness and alloying would increase α , it would also decrease K_{eff} , which is opposite to our observation and hence this possibility is also ruled out. Other possibilities such as dephasing of multiple spin-wave modes due to incoherent precession of the constituent layers and formation of perpendicular standing waves are negligible because of the observation of a collective precession of all the layers in the stack and uniform excitation of the whole stack, respectively.

6.5. Conclusions

In summary, we have studied the time-resolved magnetization dynamics in a series of $[\text{Co}(t_{Co})/\text{Pd}(0.9 \text{ nm})]_8$ multilayers with variable Co layer thickness t_{Co} . The decrease in t_{Co} increases the perpendicular magnetic anisotropy K_{eff} , which effectively increases the precession frequency and a broadly tunable precession frequency between about 5 GHz and 90 GHz is observed. The precession frequency was analyzed by macrospin modeling of LLG equation due to the appearance of a single collective mode in these samples and the saturation magnetization M_s , α , and K_{eff} were independently obtained from the dynamics. Both α and K_{eff} are inversely proportional to t_{Co} and hence they are found to be directly proportional for the first time as opposed to the previous reports [15, 18]. The enhancement of α is possibly due to both spin pumping and the $d-d$ hybridization at the Co/Pd interfaces as both effects are inversely proportional to $1/t_{Co}$. However, only the later is directly correlated to the enhancement of K_{eff} due to the decrease in bandwidth W of the Co atomic layer at the interface, while the former has no contribution to K_{eff} . Hence, we tend to believe that in our case the enhancement of α is caused primarily due to the $d-d$ hybridization effect. The observations of relatively low value of α associated with large K_{eff} and their linear correlation are significant for their applications in the STT-MRAM devices and magnonic crystals.

7. Time-resolved measurement of spin-wave spectra in CoO capped $[\text{Co}(t_{\text{Co}})/\text{Pt}(7\text{\AA})]_{n-1}\text{Co}(t_{\text{Co}})$ multilayer systems

7.1. Introduction

Magnetic multilayers (MLs) with perpendicular magnetic anisotropy (PMA) have inspired technological progress within magnetic data storage [14, 307], spin transfer torque magnetic tunnel junctions [291] and magnonic crystals [292, 308]. New applications such as in magnetic metamaterials with negative refractive index in the high GHz frequency regimes using magnetic MLs have been predicted theoretically [227]. For many of these applications exploration of rich spin-wave (SW) bands in such MLs are desirable. There have been very few experimental efforts of measuring SW spectra in MLs with PMA by frequency and wave-vector domain techniques. Exchange dominated collective SW excitations have been observed in Co/Pd MLs by Brillouin light scattering [232]. On the other hand spectra of standing SWs have been detected by ferromagnetic resonance [309]. Theoretical investigations of SWs in such MLs have been investigated by various methods including effective medium formulation [310], analytical method including RKKY interaction [311] and discrete dipole approximation [312].

Time-resolved measurements of magnetization dynamics of Co/Pd and Co/Pt MLs with PMA have become a subject of recent interest. Tunability of precession frequency and damping coefficient with the variation of Co layer thickness and number of bi-layer repeats have been reported [216, 218, 250, 313]. More recently, a correlation between the PMA and the damping coefficient, both originating from the interfacial $d-d$ hybridization [107], have also been demonstrated [218]. However, the above works focused mainly upon the excitation and detection of the fundamental SW mode of the whole ML stacks and the time-domain excitation and detection of the SW manifold remained unexplored. In this chapter, we investigate an all-optical excitations and detection of dipole-exchange SWs in a series of CoO capped $[\text{Co}(t_{\text{Co}})/\text{Pt}(7\text{\AA})]_{n-1}\text{Co}(t_{\text{Co}})$ ML systems. The observed SWs modes are

Chapter 7

reproduced by theoretical calculations based upon discrete dipole approximation (DDA) as discussed in section 3.2. of chapter 3. We have further calculated the spatial distribution of the observed modes to understand their origin.

7.2. Sample fabrication and characterization

A series of $[\text{Co}(t_{\text{Co}})/\text{Pt}(7 \text{ \AA})]_{n-1} \text{Co}(t_{\text{Co}})$ MLs with variable Co layer thickness (t_{Co}) and number of bi-layer repeats (n) were deposited by dc magnetron sputtering [314]. For the whole series the product $n \times t_{\text{Co}} = 80 \text{ \AA}$ was kept constant, *i.e.*, the total amount of Co in the ML is the same for all samples. The base pressure of the deposition chamber was 2×10^{-8} mbar and magnetron sputtering was performed at 3 mTorr Ar pressure. The thickness of the top Co-layer was increased from t_{Co} to $t_{\text{Co}} + 12 \text{ \AA}$ and then exposed to ambient air, thus yielding oxidation of the top $\sim 12 \text{ \AA}$ of Co into $\sim 15\text{-}20 \text{ \AA}$ of CoO for optional exchange biasing at lower temperatures (with Neel temperature $T_N = 250 \text{ K}$ and blocking temperature $T_B = 220 \text{ K}$) [23, 315]. All experiments reported here are performed at room temperature and the CoO layer can be considered as being paramagnetic with no exchange bias effect. However the CoO layer still introduces an asymmetry between top and bottom Co-layers of the Co/Pt ML. While the bottom Co layer is seeded with a Ta(1.5 nm)/Pt(20.0 nm) underlayer structure, the top Co layer is partially oxidized into CoO and then subsequently covered by additional 3 nm of Pt for long term stability of the samples. The Co layer thickness within the ML is varied from 0.2 nm ($n = 40$) to 0.8 nm ($n = 10$) in this experiment.

The interface qualities of the MLs were investigated by X-ray reflectivity (XRR) technique as described in section 4.4.4. of chapter 4. X-ray reflection intensity curves from grazing incident X-ray beam are collected to extract i) individual layer thickness in the ML and ii) surface and interface roughness. One can also study the electron density profile (EDP) in different layer. However, this is beyond the scope of our study. We have used the Cu K_α X-ray beam of wavelength 1.54 \AA for the XRR measurements.

7.3. Measurements of the quasistatic and ultrafast magnetization dynamics

The magnetic hysteresis loops were measured by polar magneto-optical Kerr effect (P-MOKE). The time-resolved magnetization dynamics were measured by a home built all-optical time-resolved magneto-optical Kerr effect (TR-MOKE) magnetometer as described in detail in section 4.5.2. of chapter 4. About 10 mJ.cm^{-2} of 400 nm laser pulses (pulse-width $\sim 100 \text{ fs}$) was used to pump the samples, while time-delayed 2.5 mJ.cm^{-2} of 800 nm laser pulses was used to probe the dynamics by measuring the Kerr rotation with a balanced photo-diode detector. The pump and the probe beams were focused and spatially overlapped onto the sample surface by a microscope objective with numerical aperture $N.A. = 0.65$ in a collinear geometry. A bias magnetic field (H) is applied at a small angle ($\sim 10^\circ$) to the surface normal of the sample during the dynamical measurements. The pump beam was chopped at 2 kHz frequency and a phase sensitive detection of the Kerr rotation was used.

7.4. Results and discussions

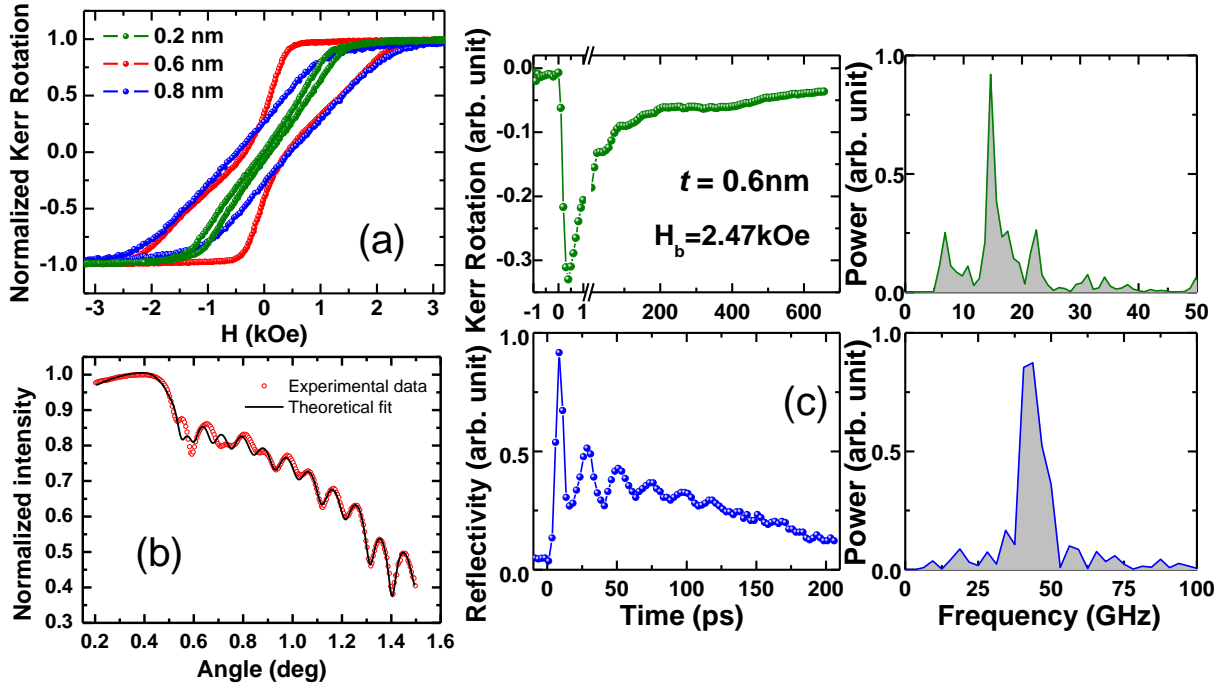


Fig. 7.1: (a) P-MOKE loops for a series of $[\text{Co}(t_{Co})/\text{Pt}(7\text{\AA})]_{n-1} \text{Co}(t_{Co})$ samples. (b) The experimental and fitted X-ray reflectivity results from the multilayer sample with $t_{Co} = 0.8$ nm. (c) The time-resolved reflectivity and Kerr rotation data and the corresponding FFT spectra are shown for the multilayer with $t_{Co} = 0.6$ nm at a bias field of 2.47 kOe.

Fig. 7.1(a) shows the P-MOKE loops for samples with $n \times t_{Co} = 40 \times 0.2$ nm, 13×0.6 nm, and 10×0.8 nm. It is clear from the data that the perpendicular anisotropy field increases (saturation field decreases) as t_{Co} reduces from 0.8 nm to 0.6 nm and decreases (saturation field increases) again as t_{Co} reduces further to 0.2 nm. Fig. 7.1(b) shows the experimental XRR data and the theoretical fit for the sample with $t_{Co} = 0.8$ nm, which shows reasonably good agreement with the data. The extracted values of the layer thickness are very close to the nominal thickness and average interface roughness is of the order of 0.05 nm, confirming a sharp interface. Fig. 7.1(c) shows typical time-resolved reflectivity and Kerr rotation data and the corresponding fast Fourier transform (FFT) spectra from the ML with $t_{Co} = 0.6$ nm at $H = 2.47$ kOe. The precessional dynamics appear as an oscillatory signal above the slowly decaying part of the time-resolved Kerr rotation after a fast

Chapter 7

demagnetization within the first 400 fs, and a two step remagnetization with relaxation time $\tau_1 = 7$ ps and $\tau_2 = 391$ ps. A bi-exponential background is subtracted from the time-resolved data before performing the FFT to obtain the corresponding power spectra.

Fig. 7.2 shows the precessional part of the time-resolved Kerr rotation data after subtracting the bi-exponential decay and the corresponding FFT spectra for the three MLs. The time-resolved dynamics for all three samples show large amplitude precession for the initial one or two cycles followed by a heavy decay of the amplitude of precession and further an incoherent small amplitude oscillation.

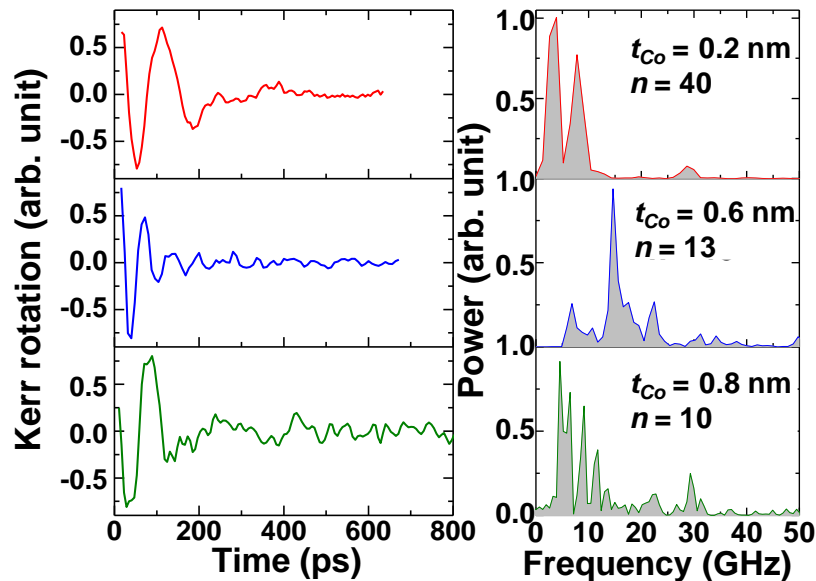


Fig. 7.2: Time-resolved Kerr rotation data and the corresponding FFT spectra for $[\text{Co}(t_{\text{Co}})/\text{Pt}(7\text{\AA})]_{n-1}\text{Co}(t_{\text{Co}})$ multilayers with $n \times t_{\text{Co}} = 40 \times 0.2$ nm, 13×0.6 nm and 10×0.8 nm at bias magnetic field $H = 2.47$ kOe.

This indicates the presence of a number of SW modes in the time-resolved dynamics, as revealed by the FFT spectra. For $t_{\text{Co}} = 0.2$ nm, we observe two intense peaks below 10 GHz and small amplitude peaks above 20 GHz. For $t_{\text{Co}} = 0.6$ nm, we observe a prominent peak followed by a shoulder below 10 GHz, a band of modes between 10 and 20 GHz and a small amplitude band at around 30 GHz. For $t_{\text{Co}} = 0.8$ nm, we observe large amplitude split modes below 10 GHz, a large amplitude broad band between 10 and 15 GHz and two small amplitude narrow bands at around 20 GHz and 30 GHz. The magnetic origin of the modes

Chapter 7

was verified by the bias magnetic field dependence of the observed modes (not shown). The physical origin of the modes was investigated further by theoretical modeling as described below.

The aim of the theoretical modeling is twofold: 1) the verification of the hypothesis that standing waves formed across the $[\text{Co}(t_{\text{Co}})/\text{Pt}(7\text{\AA})]_{n-1} \text{Co}(t_{\text{Co}})$ ML can explain the multi-peak spectra observed in TR-MOKE measurements and 2) to establish the spin pinning at the surface of the ML introduced by the paramagnetic CoO layer on top of the ML. In order to do that we considered a system of magnetic moments μ_r regularly disposed in sites r of a sample consisting of stacks of planes with magnetic moments arranged on the two-dimensional crystallographic lattice points of a simple hexagonal crystal lattice. Solely Co or Pt magnetic moments (μ_{Co} or μ_{Pt}) are present on each single plane, *i.e.*, we assume sharp interfaces in our model, which was also confirmed by the XRR measurements. The system has the shape of a thin film (see Fig. 7.3(a)) of total thickness $(n \times t_{\text{Co}} + n \times 7) \text{\AA}$ with a square base of dimensions $2000a \times 2000a$ ($a = 2.29 \text{\AA}$ is the distance between nearest magnetic moments in the hexagonal plane). The 7 \AA thick Pt layers are modeled by 3 Pt monolayers in all studied samples.

The harmonic dynamics of the magnetization, *i.e.*, SW spectra, were calculated in a linear approximation, without damping by numerically solving Landau-Lifshitz equation on the discrete lattice – DDA method as described in section 3.2. of chapter 3. The analysis was limited only to the standing waves formed across the ML. The magnetostatic, exchange and uniaxial anisotropy fields were included in calculations. The magnetostatic field was calculated in the dipolar approximation by direct summation over all magnetic moments. The exchange interactions between nearest neighbors were included in the Heisenberg form. We considered the sample in a saturated state along the direction of the effective field, *i.e.*, a superposition of the anisotropy and bias magnetic field. The approximate direction of the static magnetization was found from the standard equation with the assumption of a uniform thin film [146]. The magnetic moment in the saturated state can be regarded as a superposition of two components: the static (parallel to \mathbf{H}) and the dynamic (perpendicular to \mathbf{H}). In the Co planes we assumed a magnetic moment of $1.8\mu_B$.

Chapter 7

(or $1.9\mu_B$ for one sample), which is characteristic for the bulk Co, while for the Pt planes a smaller magnetic moment (μ_{Pt}) was used, which according to ab-initio simulations can be induced in Pt due to the close proximity to the Co atoms [316]. The approximate values of the exchange integral were chosen as follows: J_{Co-Co} and J_{Co-Pt} : 24×10^{-22} J and a much smaller value for J_{Pt-Pt} [317]. All parameters used in the calculations are summarized in Table 7.1.

Harmonic dynamics modeling as described above was performed for three different MLs with Co thicknesses of $t_{Co} = 0.2, 0.6$ and 0.8 nm (*i.e.*, with 1, 3 and 4 monolayers of Co in each unit cell of the considered ML). The intensities of the SW lines measured in TR-MOKE were compared with the relative intensities calculated according to the procedure described in [22]. The out-of-plane component of the dynamical magnetization is primarily measured and the theoretical intensities are calculated from the projected component of the dynamical magnetic moment on the film normal. The refractive indices of Co and Pt used in the intensity calculations are, $3.65 + i 4.73$ and $2.87 + i 4.99$, respectively [318].

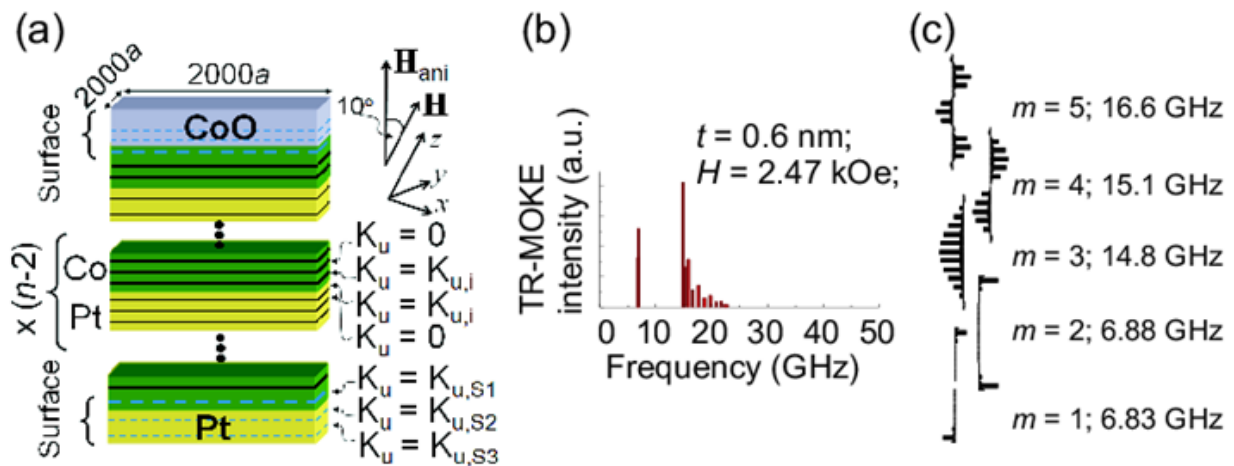


Fig. 7.3: (a) Model structure of the Co/Pt ML film with PMA used in the calculations. The lateral sizes of the ML film are $2000a \times 2000a$, where a is the in-plane lattice constant. Bias magnetic field \mathbf{H} is rotated 10° from the surface normal of the film. The anisotropy constants on surface layers ($K_{u,S1}, K_{u,S2}, K_{u,S3}$) and at the interfaces ($K_{u,i}$) are different from zero. (b) TR-MOKE relative intensities calculated with the DDA method for the ML with $t_{Co} = 0.6$ nm at $H = 2.47$ kOe. (c) The profiles of SWs with lower frequencies from the spectra shown in (b). Mode number m and corresponding frequency of the mode are listed on the right.

Chapter 7

The anisotropy constant, magnetic moment induced on Pt, and exchange integral between Pt-Pt planes were changed to obtain agreement between experimental and theoretical results, see Table 7.1. Fig. 7.3(b) shows the spectrum calculated for the ML with $n \times t_{Co} = 13 \times 0.6$ nm at $H = 2.47$ kOe.

We found good qualitative agreement with experimental FFT spectrum as shown in Fig. 7.2. A non-zero anisotropy equal to $3.9E5$ J/m³ limited to planes at interfaces (see Fig. 7.3(a)) was used in the calculation.

In order to separate the first mode from the frequency band we had to assume different anisotropy values at the external surfaces of the ML. By surface layers we mean the last (first) layers with a non-zero magnetic moment, *i.e.*, last (first) Co plane (S1) and two neighbor planes S2 and S3 (in Fig. 7.3(a) marked by dashed lines). It is a reasonable assumption that the electronic configuration of the two surface Pt layers that have only Co atoms on one side differs from the electronic configuration of Pt planes inside the ML that have Co atoms on both sides. This difference in symmetry with respect to the outermost Pt planes can explain the different anisotropy constant values assumed for these surface layers, *i.e.*, on the last (and first) cobalt layer S1, and on the Pt layers S2 and S3 layers.

Table 7.1: Exchange integrals ($J_{Co-Co}, J_{Co-Pt}, J_{Pt-Pt}$), magnetic moments (μ_{Co}, μ_{Pt}), anisotropy constants at interfaces ($K_{u,i}$) and average anisotropy fields (H_{ani}) used for calculations of SW spectra in $[Co(t_{Co})/Pt(7\text{\AA})]_{n-1}Co(t_{Co})$ MLs.

	J_{Co-Co} [10 ⁻²¹ J]	J_{Pt-Pt} [10 ⁻²¹ J]	J_{Co-Pt} [10 ⁻²¹ J]	μ_{Co} [μ_B]	μ_{Pt} [μ_B]	$K_{u,i}$ [10 ⁵ J/m ³]	H_{ani} [T]
$[Co(2\text{\AA})/Pt(7\text{\AA})]_{40}Co(2\text{\AA})$	-	0.086	2.4	1.9	0.18	1.78	0.71
$[Co(6\text{\AA})/Pt(7\text{\AA})]_{13}Co(6\text{\AA})$	2.4	0.200	2.4	1.8	0.27	3.9	0.36
$[Co(8\text{\AA})/Pt(7\text{\AA})]_{10}Co(8\text{\AA})$	2.4	0.140	2.4	1.8	0.25	4.0	0.28

Chapter 7

The corresponding values of surface anisotropy constants are summarized in Table 7.2. Here we assumed the same anisotropy on bottom and top surfaces of the ML.

Table 7.2: Anisotropy constants at external surfaces ($K_{u,S1}$, $K_{u,S2}$, $K_{u,S3}$) used for calculations of the SW spectra in $[\text{Co}(t_{Co})/\text{Pt}(7\text{\AA})]_n\text{Co}(t_{Co})$ MLs by assuming the same values on both surfaces.

	$K_{u,S1}$	$K_{u,S2}$	$K_{u,S3}$
	$[10^5]/\text{m}^3$	$[10^5]/\text{m}^3$	$[10^5]/\text{m}^3$
$[\text{Co}(2\text{\AA})/\text{Pt}(7\text{\AA})]_{40}\text{Co}(2\text{\AA})$	1.78	0.712	0.0
$[\text{Co}(6\text{\AA})/\text{Pt}(7\text{\AA})]_{13}\text{Co}(6\text{\AA})$	1.86	1.86	-0.78
$[\text{Co}(8\text{\AA})/\text{Pt}(7\text{\AA})]_{10}\text{Co}(8\text{\AA})$	3.33	3.33	-0.80

The spectrum in Fig. 7.3(b) can be split into two groups of modes according to profiles of SWs presented in Fig. 7.3(c): 1) low frequency surface waves (antisymmetric and symmetric, at 6.83 and 6.88 GHz, respectively) and 2) the band of the bulk SWs (starting at 14.8 GHz). Changes of the anisotropy on the external surfaces results only in a shift of the surface modes, the band of the bulk modes changes only when the parameters in the internal layers are modified. The complete SW spectrum also consists of other bands, with much higher frequencies. All SW modes from the 1st band (shown in Fig. 7.3(b)) are connected with in-phase precession in Co (Pt) planes only [10].

We further performed calculations of the SW spectra for the ML with $t_{Co} = 0.8$ nm ($n = 10$) at $H = 2.47$ kOe and with the same parameters as in Fig. 7.3(b). The qualitative changes resulting from increasing thicknesses of the Co layers found experimentally are reproduced quite well in our model as shown in Fig. 7.4(a)-(b). It is: the shift of the main band of SW spectra to the lower frequencies, the comparable intensity of the first peaks and appearance of an additional peak at high frequencies (in TR-MOKE measurements at ~ 30 GHz, in calculations not shown here at ~ 40 GHz).

Chapter 7

To obtain better agreement minor changes of parameters were necessary (*i.e.*, a decrease of the magnetic moment in Pt to $\mu_{\text{Co}}/7.2$, a decrease of $J_{\text{Pt-Pt}}$, an increase in the anisotropy constants at interfaces to $K_{u,i} = 4.0 \times 10^5 \text{ J/m}^3$, and changes of the anisotropy constants at surface layers: $K_{u,S1} = K_{u,S2} = 3.33 \times 10^5 \text{ J/m}^3$, and $K_{u,S3} = -0.8 \times 10^5 \text{ J/m}^3$).

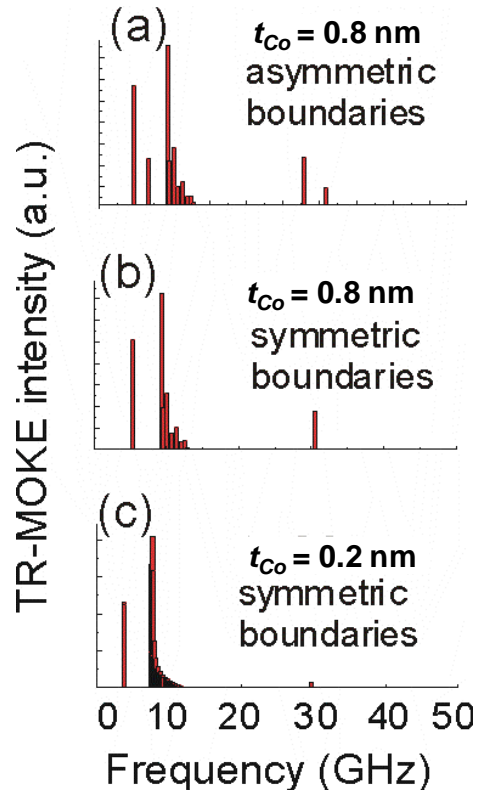


Fig. 7.4: Relative intensities calculated with the DDA method for $[\text{Co}(t_{\text{Co}})/\text{Pt}(7\text{\AA})]_{n-1} \text{Co}(t_{\text{Co}})$ ML with (a) $t_{\text{Co}} = 0.8 \text{ nm}$ ($n = 10$) and asymmetric magnetic anisotropies at surfaces, (b) $t_{\text{Co}} = 0.8 \text{ nm}$ with symmetric magnetic anisotropies at surfaces and (c) $t_{\text{Co}} = 0.2 \text{ nm}$ ($n = 40$) with symmetric surfaces. The magnetic field assumed in calculations was $H = 2.47 \text{ kOe}$.

Fig. 7.4(b) shows the calculated spectra for the ML with $t_{\text{Co}} = 0.8 \text{ nm}$ with those fitted parameters. The two low frequency modes have almost degenerate frequencies in the calculations (5.36 GHz), while in the experiment two modes, at 4.6 and 6.5 GHz are found. This is a result of the ideal symmetry assumed in the calculations, while in the real structure asymmetry between top and bottom surfaces of the ML is present due to the presence of different materials, Pt on the bottom and CoO on the top. The introduction of the asymmetry will result in the splitting of the symmetric and antisymmetric modes. This

Chapter 7

is confirmed in Fig. 7.4(a) where results of the calculations with different anisotropies on the top and bottom surfaces are shown. We assumed $K_{u,S1} = K_{u,S2}$ ($K_{u,S3}$) equal 4.0×10^5 (-0.8×10^5) and 3.33×10^5 (-0.89×10^5) J/m³ on the top and bottom surfaces of the ML structure, respectively.

Finally, we calculated the SW spectrum for the [Co(2Å)/Pt(7Å)]_{n-1} Co(2Å) ML at the same bias magnetic field. The result is shown in Fig. 7.4(c). We assumed that each Co layer consists of only one monolayer of Co atoms. From the experiment we found two broad peaks, centered at 3.9 and 7.8 GHz and another low intensity peak at 29 GHz. For such small thickness of the Co layers (less than 1 monolayer of the full fcc Co) it is expected to have cluster formation at the interfaces. Non-uniform interfaces will change significantly the electron configuration of atoms, magnetocrystalline anisotropy, magnetic moments induced on Pt atoms and exchange interaction between different planes.

In order to match our calculations with the experimental results we had to increase slightly $\mu_{Co} = 1.9 \mu_B$, decrease the magnetic moment induced on Pt layers to the value $\mu_{Pt} = \mu_{Co}/10.5$ and change the exchange integral between Pt-Pt planes to $J_{Pt-Pt} = 0.86 \times 10^{-22}$ J. The uniaxial anisotropy (still present only at interfaces) was reduced to the value 1.78×10^5 J/m³. Additionally, small changes of the anisotropies at the surfaces (we assumed the same value on both surfaces) had to be introduced, $K_{u,S1} = 0.8 \times 10^5$ J/m³ and $K_{u,S2} = 0.712 \times 10^5$ J/m³. In Fig. 7.4(c) the SW spectra calculated with these parameters are shown. The first two peaks (with degenerate frequencies) are connected with surface excitations as observed previously. The second broad peak consists of many modes, *i.e.*, 38 modes, with frequencies lying in the range between 7.6 and 11.8 GHz. In this range all modes belong to the first band of the ML structure. The width of the band indicates the strength of interaction, *i.e.*, narrowing of the band points at a decrease of the interaction between magnetic moments in ML structure. This explains the lower value of the exchange integral assumed in calculations, $J_{Pt-Pt} = 0.086 \times 10^{-21}$ J.

We estimate the average perpendicular magnetic anisotropy field of the whole ML stack, H_{ani} from anisotropy constants and magnetic moments assumed in calculations [319]. Calculated values of H_{ani} are collected in Table 7.1. As the Co layer thickness decreases

Chapter 7

from $t_{Co} = 0.6$ nm to 0.2 nm average PMA field increases even if the anisotropy constant at interfaces decreases. On the other hand, when t_{Co} increases from 0.6 nm to 0.8 nm a decrease of PMA occurs. We compared estimated PMA values for Co/Pt MLs with published data for Co/Pd MLs [16]: values for Co/Pt are lower by a factor of about 3-4, especially for sample $n \times t_{Co} = 40 \times 0.2$ nm since the $t_{Co} = 0.2$ nm sample of Co/Pd has an anisotropy field of about 23 kOe [16]. This is possibly because of the deviation of Co layer thickness from nominal thickness and increased fraction of roughness at the Co/Pt interface for this sample.

7.5. Conclusions

To conclude, we found good agreement between TR-MOKE measurements of MLs with PMA and a simple theoretical model used to calculate standing SW spectra in such PMA-MLs. The PMA field found is lower compared to those in Co/Pd MLs. The important aspect for modeling the low frequency part of the spectra is the external surfaces of the ML. It means that this part of the spectra is affected by the substrate or the overlayer, roughness, cluster formation or anisotropy distribution on the surfaces. The lines with higher frequencies are created by bulk excitations in the multilayered structure.

8. Optically induced spin-wave dynamics in [Co/Pd]₈ antidot lattices with perpendicular magnetic anisotropy

8.1. Introduction

The perpendicular percolated media (PPM) has been proposed, as an alternative to the bit patterned media (BPM), towards achieving higher storage density in magnetic recording and as a potential candidate for magnonic devices [320]. Although BPM emerged as a promising candidate for extending the areal storage density beyond 1Tbit/in², there are primarily two severe challenges inherent in BPM: 1) requirement of extremely sophisticated sample fabrication technique and 2) synchronisation of the write-field pulse with the bit location. The PPM is basically a system of exchange coupled magnetic films with densely distributed holes which act as pinning sites for magnetic domain-walls. In contrast to the BPM, PPM does not require a uniform distribution of pinning centres. However, a uniform distribution of pinning sites improves the performance of a PPM further. The study of PPM was started since 2006 [36-37]. Several routes were attempted for the fabrication of PPM: co-deposition of magnetic materials and non-magnetic oxides [38-39], magnetic thin films on anodized alumina templates [40-41], deposition of hard magnetic materials on arrays of non-magnetic nanoparticles [42], deposition of hard magnetic thin films on nanoporated membranes fabricated by an organic/inorganic self-assembly process [43-44] and sputtering [45], to name a few. A micromagnetic study of the hysteresis properties of PPM structures shows that with increasing areal density of pinning sites, the medium coercivity increases [36]. Also, the hysteresis loop has a very steep slope due to the high degree of intergranular exchange coupling. It was also found that a uniform separation of pinning sites leads to zero transition position jitter. While investigating the stability of written bits in a PPM [37], it was observed that if the defect diameters are smaller than the domain wall (DW) width, then no pinning occurs. The exchange coupling constant of the medium significantly influences the medium coercivity [46]. The

Chapter 8

mechanism of the reversal process transforms from magnetization rotation to domain nucleation and further to wall motion with increasing exchange coupling constant. Interestingly, the switching time is independent of the damping constant of the PPM. Calculation of the energy barrier was also performed to estimate the thermal stability [37, 47]. The Co/Pd and Co/Pt continuous multilayers (MLs) with high perpendicular magnetic anisotropy (PMA) are already well studied for their possible applications in present day technology [218-219]. Patterning such MLs to nanoscale for fabricating PPM with novel properties has recently triggered tremendous research. Study of magnetic properties on antidots based on Co/Pd MLs with varying Co layer thicknesses claims antiferromagnetic coupling to be responsible for the PMA in these structures [48]. For Co/Pt PMA antidot lattices (ADLs) the magnetic properties depend strongly on the AD size and separation [41]. With increasing pore diameter, the domain-wall energy changes and the pinning field increases. Due to this increase in the DW pinning, the coercive field of the system also increases. However, the anisotropy near the rim of the pores, instead of being exactly perpendicular, gets a little bit tilted. With the increase in pore diameter, the perimeter increases and consequently, the tilting becomes more severe and degrades the PMA. Beyond a critical hole diameter, the PMA is sufficiently reduced to reduce both pinning and coercive fields. Similar phenomenon of increase of coercive field in PMA Co/Pd ADLs (with larger diameter) compared to continuous ML was observed [320] due to the DW-pinning controlled magnetization reversal mechanism. The presence of strong PMA and DW-pinning controlled magnetization reversal mechanism in these antidots were also confirmed by out-of-plane magnetoresistance measurements as a function of temperature. Magnetic recording property studies on $[\text{Co/Pt}]_8$ ML antidots deposited on nanoporated ZrO_2 templates [321] also show that, the hindered DW movements due to holes controls the magnetization reversal process.

On the other hand, for applications in magnonics [292, 322], the understanding of the magnetization dynamics is important. So far, there have been a significant amount studies on propagation, damping and dispersion [203, 323-327] of spin-waves (SWs) in ferromagnetic (FM) ADLs with in-plane anisotropy. However, a detailed study of the magnetization dynamics in ADLs with high PMA is still absent in the literature. Here, we

Chapter 8

present an all-optical time-resolved measurement of SW spectra in a series of ADLs based on $[\text{Co}(0.75 \text{ nm})/\text{Pd}(0.9 \text{ nm})]_8$ ML systems with PMA by using a time-resolved magneto-optical Kerr effect (TR-MOKE) microscope. A systematic study of the dependence of the SW spectrum on the areal density of the antidots is performed. The observed SW modes are modeled by the plane wave method (PWM).

8.2. Sample fabrication

The $[\text{Co}(0.75\text{nm})/\text{Pd}(0.9)]_8$ ML structures are deposited by dc magnetron sputtering using a confocal sputter up geometry with the targets tilted and arranged in a circle around a center target (Pd) [218, 294]. The substrate, which rotates during deposition at 3 Hz, is at the focal point of the targets. The base pressure of the deposition chamber was 2×10^{-8} mbar and the deposition was performed at 3 mTorr of Ar pressure.

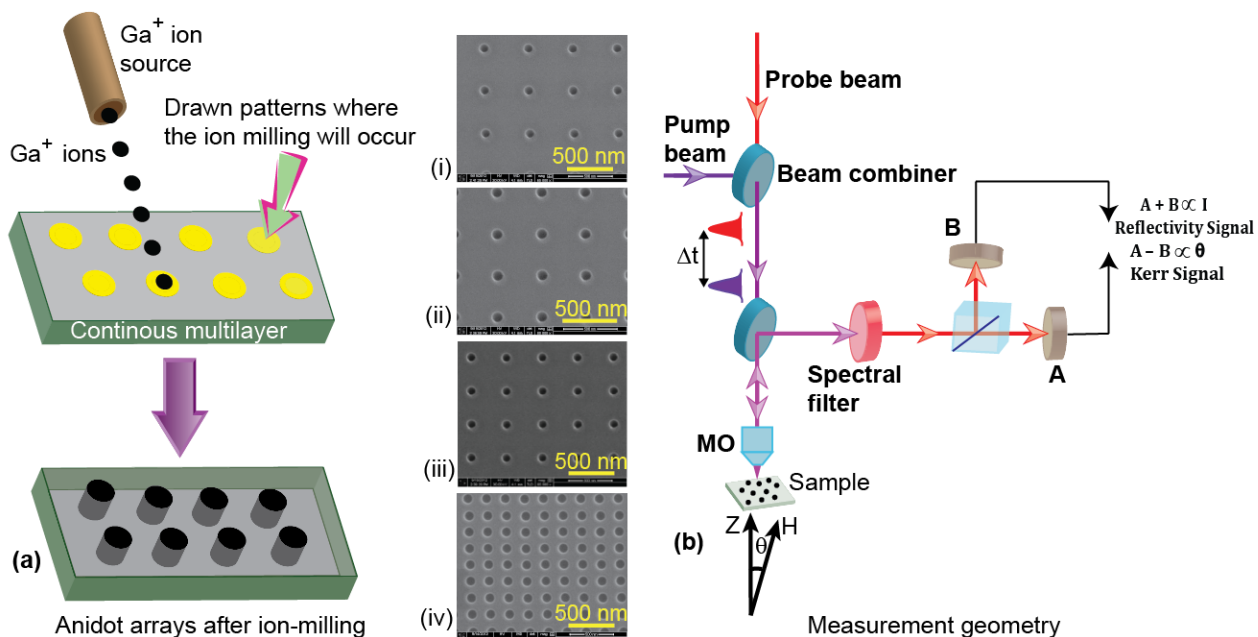


Fig. 8.1: (a) ADL fabrication procedure and typical scanning electron micrographs of ADLs with lattice constant $a =$ (i) 500 nm, (ii) 400 nm, (iii) 300 nm and (iv) 200 nm. (b) Measurement geometry.

Chapter 8

The ADLs are fabricated by focused ion beam (FIB) milling of the Co/Pd ML using liquid Ga⁺ ion at 30 kV voltage and 20 pA beam current, which produces a spot size of about 8 nm. For creating the ADLs, first we create a pattern of ADLs having desired diameter (d) and edge to edge separation (s) on the ML sample. In our case, the d value is fixed at 100 nm and s varies from 100 to 400 nm and hence the lattice constant $a = d + s$ varies from 200 to 500 nm. Subsequently, the material is sputtered out by exposing the patterned part to the Ga⁺ ion beam source. Each pattern covers an area of $8 \times 8 \mu\text{m}^2$. The initial milling is done by using a raster scan of the focused ion beam in a single pass, which is followed by cleaning the residual materials from the ADLs in multipass (about 200 passes). Fig. 8.1(a) presents a schematic of the sample fabrication along with the scanning electron micrographs of the ADLs. The measured a and d values are close to the nominal values.

8.3. Measurement of ultrafast magnetization dynamics

The ultrafast magnetization dynamics is measured by a custom-built TR-MOKE microscope in a two-color optical pump-probe set up as described in details in section 4.5.2. of chapter 4. The second harmonic ($\lambda = 400$ nm, spot size $\sim 1 \mu\text{m}$, fluence = 18 mJ.cm^{-2}) of a Ti-sapphire oscillator was used to pump the dynamics whereas the time delayed fundamental ($\lambda = 800$ nm, spot size ~ 800 nm, fluence = 2.5 mJ.cm^{-2}) was used to probe the dynamics. The two beams are made collinear before falling on the sample through a microscope objective with numerical aperture of 0.65. The back-reflected probe beam is collected by the same microscope objective and is used to measure the Kerr rotation by an optical bridge detector as a function of the time delay between the pump and probe beams. The external magnetic field (H) is tilted at a small angle ($\sim 10^\circ$) to the surface normal of the sample. The schematic of the measurement technique is presented in Fig. 8.1(b).

8.4. Results and discussions

Fig. 8.2(a) presents typical TR-MOKE data obtained from the ADL with $a = 400$ nm at $\mu_0 H = 0.084$ T. The data shows characteristic ultrafast demagnetization (within 400-500 fs from

Chapter 8

the zero-delay) and fast (within 9 ps) and slow remagnetization signals (within 410 ps). The precessional dynamics appears as an oscillatory signal on top of the decaying part of the TR-MOKE signal. A bi-exponential background is subtracted from the time-resolved data before performing the fast Fourier transform (FFT) to obtain the corresponding SW spectrum.

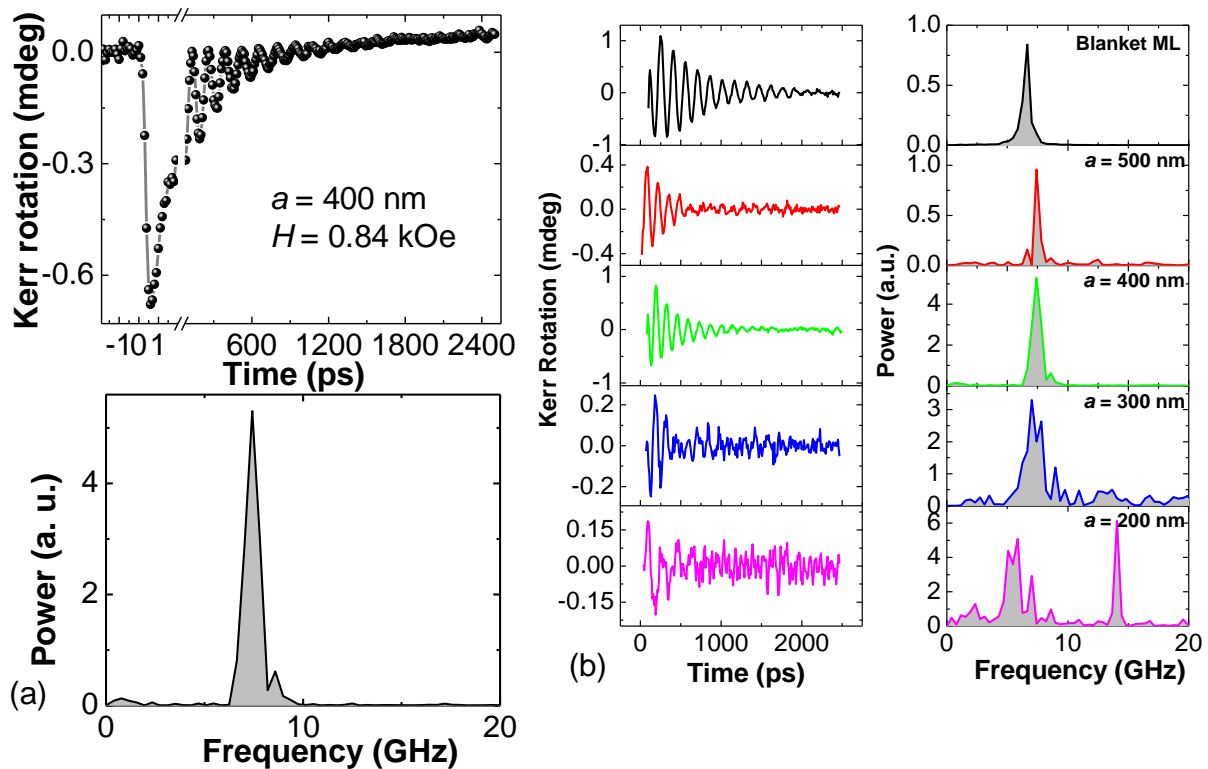


Fig. 8.2: (a) Typical TR-MOKE signal and corresponding SW spectra for ADL with $a = 400$ nm. (b) Areal density dependence of the TR-MOKE signal with the bi-exponential background subtracted and the SW spectra of the ADLs at $\mu_0 H = 0.084$ T.

Fig. 8.2(b) shows that the SW spectrum depends significantly on the areal density of the ADLs. For $a = 500$ nm, an intense peak at frequency (f) 7.4 GHz with small side lobes on both sides of the peak are found. The frequency of the intense peak is slightly greater than the frequency of the uniform mode of the continuous ML ($f = 6.64$ GHz). For $a = 400$ nm, this peak remains almost in the same position ($f = 7.42$ GHz) as for $a = 500$ nm. Interestingly, as a is reduced further, multiple SW modes start to appear. For $a = 300$ nm, there is a broad band of modes centred at around $f = 7.05$ GHz with a number of low

Chapter 8

intensity modes in the higher frequency regime. A further drastic change is observed for the ADL with the smallest period, *i.e.*, $a = 200$ nm. In this sample there are two distinct bands - a broad band centred around $f = 5.64$ GHz and a narrow band centred at around $f = 14.11$ GHz. The lower band experienced a significant red-shift as opposed to the other ADLs. In Fig. 8.3(a) we plot the f vs. H result of the continuous ML. The data was fitted to the Kittel formula [218] (details in section 2.8. in chapter 2) to extract material parameters which will be used later in this article for theoretical calculations. As a uniform collective precession of the whole ML stack is observed for all field values, we assume the ML structure as an effective magnetic medium with parameters: saturation magnetization $M_S = 0.78 \times 10^6$ A/m, gyromagnetic ratio $\gamma = 187$ GHz/T, and PMA field $\mu_0 H_{\text{ani}} = 1.119$ T. These values are in accordance with parameters found in previous measurements [14].

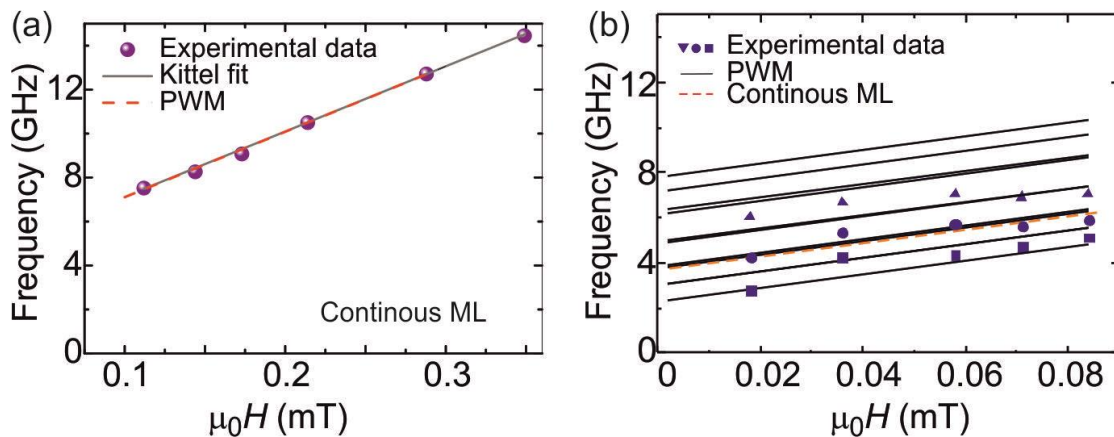


Fig. 8.3: (a) Dependence of frequency of SW mode on H for continuous Co/Pd ML. The TR-MOKE data (symbol), fit to the Kittel formula (solid line) and the PWM results (dashed line) using the same parameters are shown. (b) Dependence of frequencies of SW modes on H for ADLs with $a = 200$ nm (dots) along with the results from PWM calculations (solid lines) and continuous ML (dashed line).

The bias field dependence of f in ADLs with $a = 200$ nm is presented in Fig. 8.3(b). Occurrence of multiple SWs at all H values is observed. The frequencies of the lower frequency modes decrease with decreasing H , whereas the highest frequency mode does not show any discernible dependence on H .

Chapter 8

For interpretation of these intriguing experimental results we have used PWM which is a suitable method for calculations of spectra of collective dynamics in periodic structures. The PWM is described in detail in section 3.3. of chapter 3. This method has already been used for the studies of SW spectra in various kinds of magnonic crystals (MCs), *e.g.*, thin films of ADL [326, 328], bi-component two-dimensional MCs [189, 329] and three-dimensional MCs [330]. It was shown that the PWM applied to ADL structures works well under the following assumptions: i) the sample is magnetically saturated along the direction of the external magnetic field, ii) the crystalline magnetic anisotropy, if present, is parallel to the external magnetic field and the saturation magnetization, iii) the internal magnetic field is uniform across the ADL thickness, iv) the SW dynamics are described well by the linearized Landau-Lifshitz (LL) equation and finally, v) the magnetization dynamics is pinned at the antidots edges [331]. Regarding the measurements presented in the previous section, the assumption i) is satisfied as was confirmed by the hysteresis loop measurements performed along the normal to the film plane. In TR-MOKE measurements, the bias magnetic field was tilted from the normal direction (*i.e.*, direction of the uniaxial magnetic anisotropy) by about 10° . This small angle should not violate assumptions i) and ii) due to the presence of the anisotropy field normal to the film plane, which exceeds the demagnetizing field significantly. Regarding the assumption iii) we can distinguish between two sources of inhomogeneity across the ADL thickness: the inhomogeneity of the static demagnetizing field and inhomogeneity in SWs dynamics (introduced by the formation of the standing SW modes confined between the top and bottom faces of ADL). The total ML film thickness is ~ 14 nm (when the Pd layers at the bottom and the top of the ADL are taken into account), thus the SWs eigenmodes with amplitudes oscillating in space across the film thickness will have large frequency due to the contribution from the exchange energy (the exchange contribution to the frequency of SW can be estimated with the expression: $\gamma 2Ak^2/(2\pi M_s)$, which for the first perpendicular standing wave gives ~ 50 GHz). Moreover, the TR-MOKE signal from the nonuniform SW amplitude across the thickness is much smaller as compared to the uniform excitation, thus the contribution from these modes to the measured signal is negligible. The pattern of antidots also introduces a small inhomogeneity in the out-of-plane component of demagnetizing field

Chapter 8

near the antidots edges. This component of the magnetic field is tangent to the edges of the antidots and thus continuous. The out-of-plane component of demagnetizing field is then significantly increased above the value $-M_s$ in the vicinity of the edges of the antidots. In our model this contribution will be taken into account indirectly by the effective parameters of the shells introduced later in this article. The assumption iv) of the linearization is fulfilled to large extent for the measured SWs because coherent SW precession contributes in harmonic oscillations of the magnetization which are significantly smaller than its saturation value. The influence of the magnetization pinning at the edges of the antidots (assumption v) will also be discussed later. From the discussion presented above, it follows that PWM should give good insight into the mechanism responsible for the effects observed in the TR-MOKE measurements.

In PWM calculations we have used material parameters (M_s , H_{ani} and γ) obtained from the fitting of the continuous ML's TR-MOKE data to the Kittel formula [218] as described in detail in section 2.8 of chapter 2 and additionally the effective exchange constant of the ML film, $A = 1.3 \times 10^{-11}$ J/m was assumed [309]. The PWM results with this set of parameters match very well with the experimental data shown in Fig. 8.3(a). The calculated spectra of SWs extending along the lateral dimensions of the ADLs and uniform across the ADL thickness as a function of the lattice constant is shown in Fig. 8.4.¹ For ADL calculations we took nominal value of the radius of antidots $R = 50$ nm (Fig. 8.4(b)). In Fig. 8.4(a), the frequencies of SWs as a function of lattice constant a are shown. We can see a monotonous increase of the frequencies of SWs with decreasing a . The frequency of the first mode in ADL with $a = 500$ nm is close to the FMR frequency (6.63 GHz) of the continuous ML but shifts up to 14 GHz for $a = 150$ nm. In Fig. 8.4(c), the maps of amplitude (the in-plane component of the magnetization vector) for SWs modes in ADL with $a = 200$ nm are shown. We can see that the pinning at the edges of the antidots introduces a quantization of SW and leads to the formation of the lateral standing SW modes in the spaces between antidots. In this case, the decrease of separation between nearest antidots results in an

¹ In all calculations with PWM presented in this paper with have used 2061 and 8281 plane waves to obtain good convergence of the results in ADL and ADLS, respectively. The significant increase of the number of plane waves for ADLS was necessary to take into account dynamics in small (as compared to the lattice constant) shells.

Chapter 8

increase of the wavenumbers of the modes confined between antidots and is followed by the increase in their frequencies.

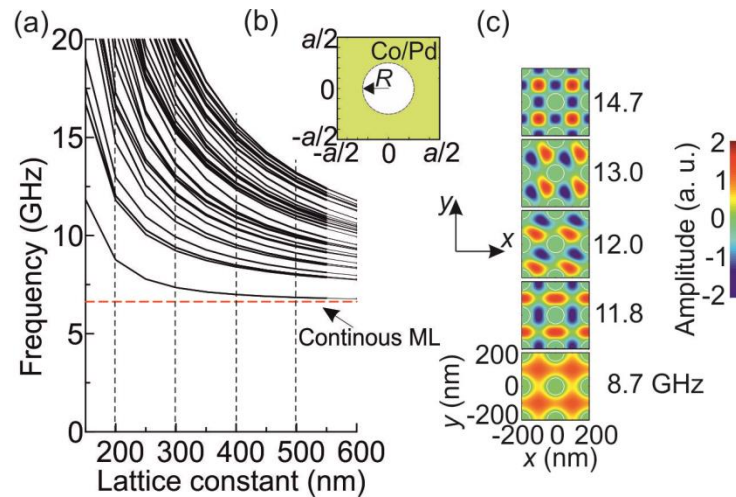


Fig. 8.4: (a) Dependence of the frequency of SWs in ADL on the lattice constant at $\mu_0 H = 0.084$ T for the bunch of the lowest modes. The horizontal dashed line marks the FMR frequency of the continuous ML. Vertical dashed lines marks the periods investigated experimentally in this chapter. (b) The unit cell of the ADL used in the PWM calculations. (c) Amplitude of the dynamical component of the magnetization vector in ADL for five modes with the lowest frequencies for $a = 200$ nm.

However, this scenario (*i.e.*, monotonous change in SW's frequencies with changes in a) does not agree with the TR-MOKE results (Fig. 8.2(b)). This means that in the calculations presented in Fig. 8.4 we did not take into account an important factor which affects the measurements, and this factor is especially strong in ADLs with high density of antidots. Calculations presented above show, that this is not a result of a periodicity or quantization of SW excitations. Thus, the observed effect can be related to the impact of the edges of antidots. If some SW excitations are localized at the edges of the antidots, then those modes will contribute in very small amount to the TR-MOKE signal for the samples with large a , because in this case the area of the edge regions is relatively small as compared to the ML area of the ADL (in measurements this area is limited by the spot size of the probe beam). The edge effects will increase with decreasing a . To understand this observation, we assume the formation of shell like structures at the edges of the antidots. These shells are

Chapter 8

formed by bombardment of the Ga ions onto the ML film during FIB milling and the structural and magnetic properties within those shells may get significantly modified to the extent that a regular structure of $[\text{Co}(0.75\text{nm})/\text{Pd}(0.9)]_8$ ML may get destroyed. Therefore, a decrease of the effective magnetization, exchange interactions and especially the PMA field in the shell regions around antidots is expected [332]. We are unable to extract a detailed profile of the magnetic properties near the edges of antidots. One may expect a gradual variation in magnetic properties from the outermost edge to radially inwards of the shell and also a possible reorientation of magnetization due to degradation of PMA. However, PWM does not offer such a possibility for modeling precise changes in the magnetic properties near the edges of the antidots. Instead, we propose a simplified model, which (as we will show later) reproduces the main features of the measured spectra. We consider an ADL consists of two magnetic materials: one, with the properties of the continuous ML (used above) and the second the material of the shells (of the width ΔR) around the antidots. The results of the corresponding calculations are shown in Fig. 8.5(a).

The unit cell of an antidot lattice with shell (ADLS) structure is shown in Fig. 8.5(b). The pinning of SW dynamics at the antidot edges can additionally influence the SW spectra in ADLS, thus to mimic the various pinning conditions in the theoretical model we also extended the shell into the hole interior. Such approach is known from the study of SW dynamics in stripes where the pinning strength at the border of the stripe is exchanged with an effective stripe width [27, 28]. The antidot size is decreased from $R = 50$ nm by putting the circular shell centred at $R = 50$ nm (extended from $R - \Delta R / 2$ to $R + \Delta R / 2$). As it is very difficult to measure the precise values of M_s and A characteristic for the shell region of the ADLS, these parameters were used as fitting parameters to obtain an agreement with the TR-MOKE data. We have chosen here shells of width $\Delta R = 17$ nm, $M_s = 0.3 \times 10^6$ A/m, $A = 0.2 \times 10^{-11}$ J/m, and $\mu_0 H_{\text{ani}} = 0.03$ T. To obtain convergence of PWM in the case of ADLS we have to solve a larger eigen-problem than in the ADL case. This originates from the small size of the shells as compared to the lattice constant, which requires us to add shorter wavelength plane waves (*i.e.*, with a wavelength smaller than the shell width) to properly represent the excitations in the shells of ADLS using the PWM. Thus, we had to

Chapter 8

incorporate a larger number of reciprocal lattice vectors into the basis that we use for our ADLS plane wave expansion.

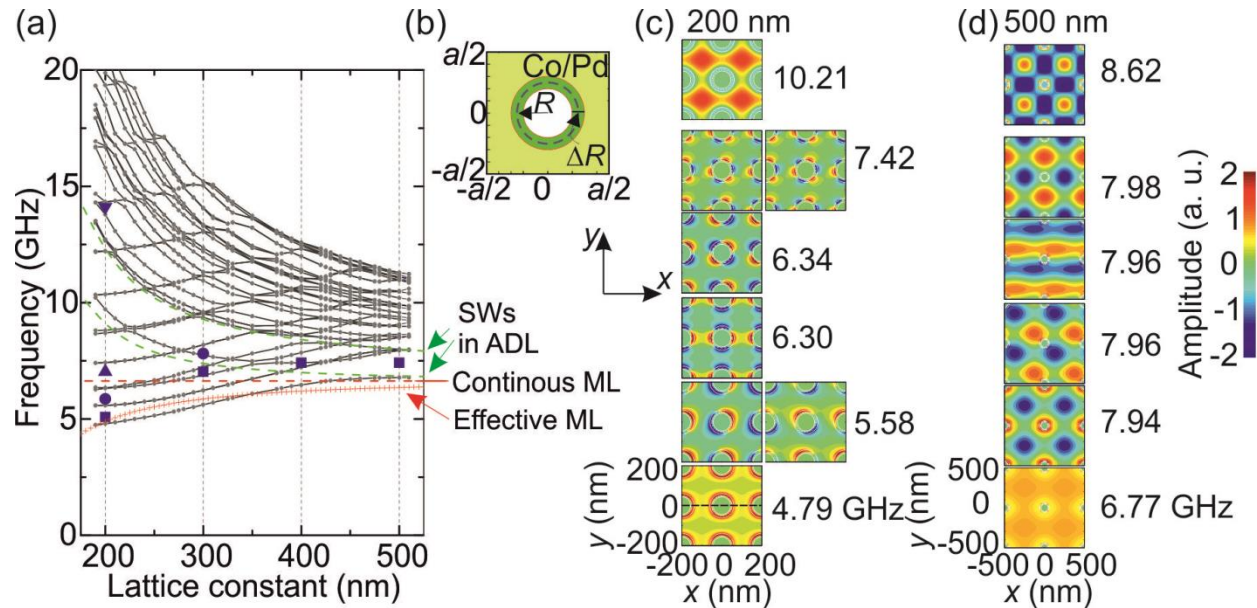


Fig. 8.5. (a) Dependence of the frequency of SW excitations in ADL with shells (ADLS) on the lattice constant at $\mu_0 H = 0.084$ T. The horizontal dashed line marks the FMR frequency of the continuous ML, the dashed green lines point the two frequencies of the ADL taken from Fig. 8.4(a). The symbols represent frequencies extracted from the TR-MOKE data (Fig. 8.2(b)). Vertical dotted lines marks the periods investigated experimentally in this chapter. (b) The unit cell of the ADLS. (c) and (d) Amplitude of the dynamical component of the magnetization vector in ADLS. The profiles of the few modes with lowest frequencies for $a = 200$ nm and 500 nm are shown.

From Fig. 8.5(a), we can distinguish two families of modes: one with decreasing frequency with increasing a (they follow the dependence found for ADL without the shells in Fig. 8.4(a) and are marked also in Fig. 8.5(a) by the green dashed lines) and the second with increasing frequency with increasing a , present at lower frequencies for small lattice constants. Based on the analysis of the profiles of SWs shown in Fig. 8.5(c) and Fig. 8.5(d), we can attribute these two groups of modes to the bulk modes and modes localized in the shells, respectively. For $a = 200$ nm the nine modes (seven of them are shown in Fig. 8.5(c)) in the lower frequency regime (from 4.79 to 8.8 GHz) are the modes with amplitude localized mainly in the shell (which we will refer to as shell modes). The first bulk mode

Chapter 8

(with a quasiuniform distribution of the SW amplitude between the antidots, *i.e.*, fundamental mode) is located at 10.21 GHz frequency, similar to the first mode in ADL in Fig. 8.4(a). With increasing a the frequency of the first bulk mode decreases and at some values of a , it crosses or anti-crosses with the family of shell modes. For $a = 500$ nm the first mode (at 6.77 GHz) is a fundamental mode with visible contribution from the shell mode, similar as the second mode. The other modes shown in Fig. 8.5(d) are purely bulk modes or bulk modes mixed with shell modes. At $a = 400$ nm the first mode is at 6.47 GHz while at $a = 200$ nm its frequency drops to 4.79 GHz, *i.e.*, both below FMR frequency of the continuous ML. The interesting question is why the frequency of shell modes decreases with decreasing a , even below the FMR frequency of the continuous ML (6.63 GHz, marked with the horizontal red dashed line in Fig. 8.5(a))? As there is no changes in the material parameters with a , we believe that one of the reasons for this behavior is the impact of collective dynamics of shell modes.

The decrease of the SW frequency with decreasing lattice constant was already reported [326] for the SW mode in the ADL based on Py thin film with in-plane magnetization and in the Damon-Eshbach configuration. In that paper, the decrease of the frequency of the SW mode was associated with the increase of the group velocity. This mode was found to be the edge mode localized in the wells of the internal magnetic field – the wells created by the static demagnetizing field near the edges of the antidots. The decrease of the frequency and the increase of its group velocity were attributed to the local decrease of the internal magnetic field and tunnelling mediated coupling between modes in neighboring areas of localization. We can also attribute the dependence found in our measurement and calculations to the increase of interactions between the shell modes. However, in our case the static demagnetizing field does not play a significant role for the strength of the coupling of the shell modes, because its changes are small and this field does not form potential wells. Thus, we can conclude that at a small lattice constant, ($a < 300$ nm) in the ADLS, the dynamic coupling between the SW shell modes is efficient to decrease the coupled mode frequency below the FMR frequency of the continuous ML.

Chapter 8

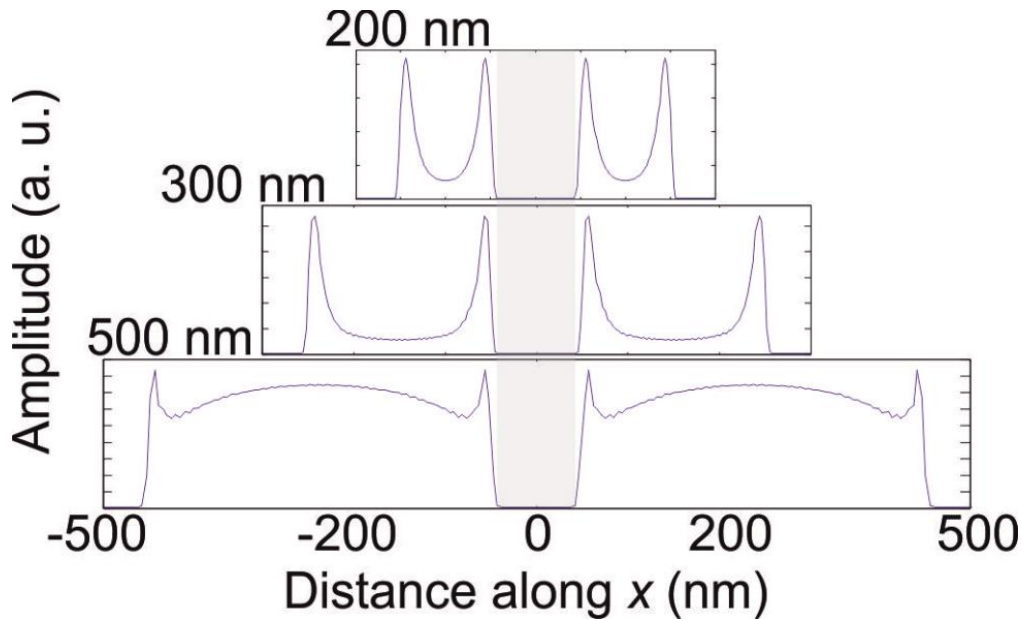


Fig. 8.6: The amplitude of the SW with the lowest frequency (the first mode) in ADLS across the center of the unit cell along x axis for $a = 200, 300$ and 500 nm. The grey area marks the antidot position within the unit cell.

To have deeper insight into the type of interactions between shell modes we plotted (in Fig. 8.6) the amplitudes of the first mode along the x -axis crossing the center of antidots [*i.e.*, along the line marked on the profile of the first mode in Fig. 8.5(c)] for ADLS with lattice constant $a = 200, 300$ and 500 nm. For $a = 200$ nm and 300 nm we can see that the amplitude is dominated by SWs localized in the shells, while for 500 nm a broad fundamental mode (bulk mode) is observed in between antidots with strong contributions from the shell modes localized at the antidot edges. Note that the SW amplitude between the neighbouring shells (in the bulk of ADLS) is different from zero. Therefore, we can expect to have a coupling, due to the overlap of SW amplitudes localized in neighbouring shells. In Fig. 8.5(a) we have also plotted (red crosses line) the FMR frequency of the effective ML film with the M_s and H_{ani} being weighted average of the $[\text{Co}(0.75 \text{ nm})/\text{Pd}(0.9 \text{ nm})]_8$ ML and the material of the shell in dependence on a . This dependence describes the decrease of the fundamental mode frequency with the decrease in a but does not explain the localization of the SW amplitude and broad band of modes found in the TR-MOKE measurements (Fig. 8.2(b)).

Chapter 8

The coupling between the shell modes may also be due to the dynamic dipolar coupling. In fact the decrease of frequency of SW modes with decreasing lattice constant was observed for the fundamental mode in a chain of FM dots (or in an array of FM stripes) when the magnetic field was perpendicular to the axis of the chain (or along the stripe) [333-335]. However, in our study, the distance between peaks of the shell modes even for $a = 200$ nm (which is ~ 100 nm) significantly exceeds the ML thickness. Moreover, a similar decrease of higher mode frequencies (*i.e.*, modes with their phases changing around the shells, in Fig. 8.5(c) are modes from 5.58 to 7.42 GHz) with decreasing a is also found in calculations. These properties indicate that the dipolar coupling may not play an important role here. The presence of magnetic material can additionally create exchange coupling between SW excitations, but the elucidation of the role of various possible couplings between the shell modes in ADLS with PMA is out of the scope of this paper and needs further experimental and theoretical investigations.

The bias field dependence of the SW modes for $a = 200$ nm was also reproduced reasonably well by the calculations as shown in Fig. 8.3(b), and confirmed the proposed model. The deviations at lower field values (< 0.04 T) can be attributed to the reorientation of magnetization at the edges of the antidots due to a degraded PMA which results in mode softening and non-linear dependences of frequencies on the bias field which is impossible to incorporate in the PWM calculations rigorously.

8.5. Conclusions

In summary, we have investigated the collective SW dynamics in ADLs in thin [Co(0.75 nm)/Pd(0.9 nm)]₈ ML with PMA. With TR-MOKE microscopy, we have measured the SW excitations in a series of ADLs with different lattice constants and with fixed antidot radius. We have found a decrease of the frequency of SW with increasing density of antidots, down to values well below the FMR frequency of the continuous ML. Based on the PWM calculations, we have found that these excitations are connected with the SW modes localized in the shells around the antidots. The shells were unintentionally created during

Chapter 8

fabrication of the antidots by Ga ion bombardment, and are characterized by degraded magnetic properties as compared to the bulk areas of magnetic material in ADL. Moreover, we have shown that this decrease of SW frequencies is driven by a dynamical coupling between the localized modes within the shells. Even though the exact nature of the coupling is debatable we propose that tunnelling and exchange interactions play important roles. We have demonstrated that in ADL based upon magnetic MLs with PMA, localized and collective SW excitations are possible. This new collective behavior is important for exploiting the magnonic field of research and to explore the properties of perpendicular percolated media for various technological applications.

9. Effect of the spin-twist structure on the spin-wave dynamics in $\text{Fe}_{55}\text{Pt}_{45}/\text{Ni}_{80}\text{Fe}_{20}$ exchange coupled bi-layers with varying $\text{Ni}_{80}\text{Fe}_{20}$ thickness

9.1. Introduction

Over the last few decades, there has been a rapidly increasing interest in magnetic multilayers due to their novel properties like perpendicular magnetic anisotropy, giant magnetoresistance, tunnel magnetoresistance, spin-valve and spin-torque effects. After the discovery of exchange bias [110, 336], it was found that systems based on the interfacial exchange-coupling of soft and hard ferromagnetic thin films can be exploited to tune the materials properties for a broad range of applications [50-51]. These are called exchange spring (ES) magnets [337]. For permanent magnet applications, the hard magnetic phase provides a high nucleation field for irreversible magnetization reversal and at the same time, the soft magnet is used to attain a high saturation magnetization (M_s). In addition, the soft magnetic phase may protect the hard phase against corrosion. Care is needed to design the composite material system in order to avoid the soft phase lowering the coercive field too much to adversely affect the composite energy product. Conversely for magnetic recording applications, the soft phase is used to improve the writability of magnetic media without compromising thermal stability. The exchange coupling of the soft layer to the hard layer is also being pursued as the pathway to raising the operating frequencies of planar microwave devices [338]. When the soft layer is pinned at the interface of the hard layer there are significant shifts in the resonance frequency, with only a small reduction in the strength of the resonance. Since the early development of the ES systems [49, 339], extensive efforts have been made to explore their basic magnetic properties, such as the giant magnetoresistance [58], magnetization switching behavior [59-62, 340], coercivity reduction [64-65] and spin configurations [54-56, 341-342]. Micromagnetic simulations

Chapter 9

show that the application of spin polarized currents causes a stationary rotation of magnetization of the ES systems [343]. Dynamical measurements using Brillouin light scattering on SmCo/Fe bi-layer [57, 257] reveal the presence of a well-defined minimum in the frequency-field characteristics due to the alignment of hard and soft phases and the absence of a spiral or domain wall state in these samples. On the other hand, ferromagnetic resonance (FMR) measurements [259-260] on the same system reveal the presence of surface spin-wave (SW) modes in addition to the bulk resonance modes.

L1₀ Fe-Pt has emerged as an attractive material for the hard magnetic phase of an ES system, particularly for magnetic recording applications. Its high thermal stability [261] and large uniaxial magnetic anisotropy originate from the spin orbit coupling of the Pt and the hybridization between Pt 5*d* and Fe 3*d* states [262-263]. Ultrafast magnetization dynamics studies of L1₀-ordered Fe-Pt thin film [264-265] show that both the first and the second order uniaxial anisotropy terms contribute to the total anisotropy. In contrary, some recent works show only the first order anisotropy term plays significant role in determining the total anisotropy [266]. FMR measurements [267] and micromagnetic simulations [268] on Fe-Pt/Fe bi-layers, with spiral spin structure, reveal the existence of new modes in the ES regime as opposed to the rigid magnet regime. However, time domain measurements of the magnetization dynamics of ES magnets are absent in the literature. Here, we present a systematic study of the ultrafast magnetization dynamics in a series of Fe₅₅Pt₄₅(20 nm)/Ni₈₀Fe₂₀(*t* nm) ES bi-layers with varying thickness *t* from 10 to 80 nm. We have observed a strong dependence of the SW spectra on *t*. The experimental data is explained via micromagnetic simulations by taking into account an effective magnetic field gradient in the Ni₈₀Fe₂₀ layer.

9.2. Sample fabrication

The ES bi-layers Fe₅₅Pt₄₅(20nm)/Ni₈₀Fe₂₀(*t*) with varying Ni₈₀Fe₂₀ thickness *t* were grown on glass substrate by magnetron sputtering with an Ar pressure of 10 mTorr [59]. A 1.5 nm Pt seed layer was deposited prior to the deposition of the hard magnetic phase by cosputtering from elemental targets. This cosputtering process enabled controlling of the

Chapter 9

composition of the hard layer. The substrate temperature was fixed at 420°C. The L1₀ phase of Fe₅₅Pt₄₅ layer had (111) texture with a high anisotropy along (001) direction. At high temperatures, there can be chemical reaction between the soft and hard magnets. Hence, before depositing the Ni₈₀Fe₂₀ layers from an alloy target, the substrate was cooled down to 150°C. During the deposition of the soft magnet, the Ar pressure was reduced to 3 mTorr. The Fe₅₅Pt₄₅ layer has a constant thickness of 20 nm. The Ni₈₀Fe₂₀ layer thickness t is chosen as 0, 10, 20, 50 and 80 nm for samples *S0*, *S10*, *S20*, *S50* and *S80* in this work. The magnetic hysteresis loops measured by the static magneto-optical Kerr effect (MOKE) microscope and SQUID magnetometry show that the coercivity decreases systematically with increasing t value [59].

9.3. Measurement of ultrafast magnetization dynamics

The ultrafast magnetization dynamics were measured by a time-resolved MOKE (TR-MOKE) magnetometer based upon a two-color all-optical collinear pump-probe geometry as described in detail in section 4.5.2 of chapter 4. The second harmonic ($\lambda = 400$ nm) of a Ti-sapphire laser, chopped at 2 kHz frequency, (Tsunami, SpectraPhysics, pulse-width < 70 fs) was used to pump the samples, while the time-delayed fundamental ($\lambda = 800$ nm) laser beam was used to probe the dynamics by measuring the Kerr rotation by means of a balanced photo-diode detector (via a lock-in amplifier with a reference signal taken from the chopper), which completely isolates the Kerr rotation and the total reflectivity signals. The probe beam fluence was chosen as about 2.5 mJ.cm⁻² whereas the pump beam fluence was chosen as about 15 mJ.cm⁻². The pump and the probe beams were focused and spatially overlapped onto the sample surface by a microscope objective with numerical aperture N. A. = 0.65 in a collinear geometry. The applied bias field was tilted to about 15° angle from the plane of the sample, the in-plane component of which is referred to as H in this article.

9.4. Results and discussions

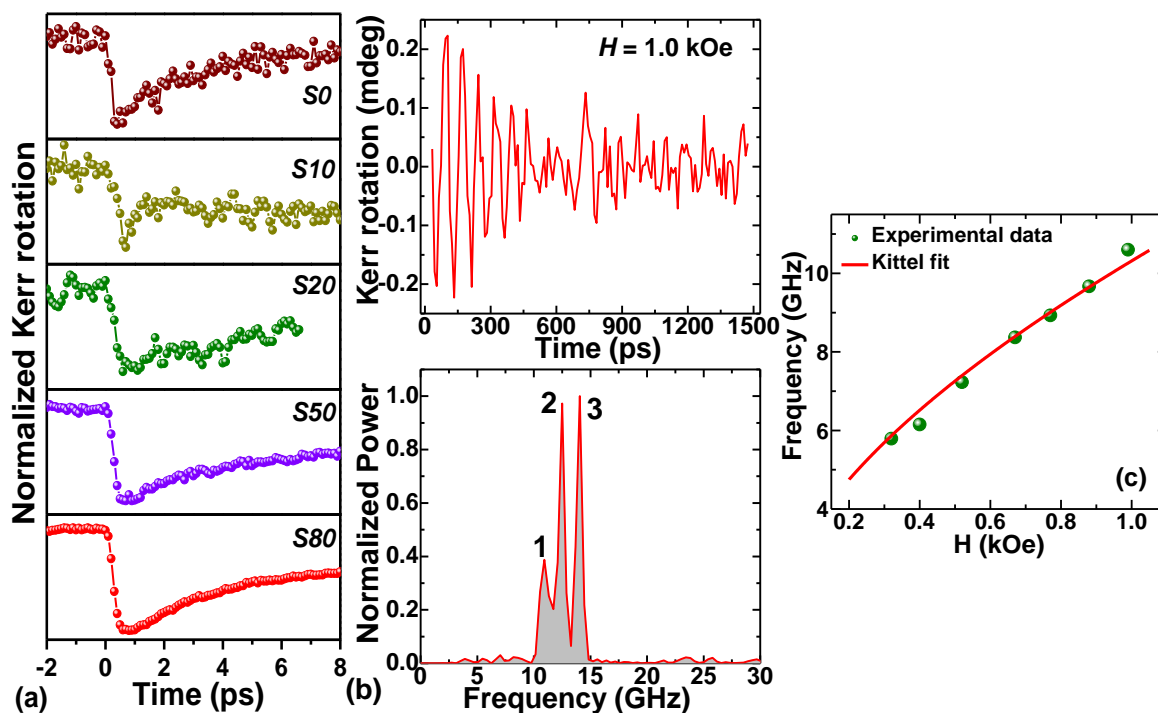


Fig. 9.1: Time-resolved Kerr rotation data showing (a) the ultrafast demagnetization for all samples and (b) magnetization precession and corresponding FFT power spectra at a bias field of 1.0 kOe for *S80*. (c) Bias field dependence of mode 1 and the corresponding Kittel fit for *S80*.

Fig. 9.1(a) to (c) present typical experimental data obtained from our measurements. The time-resolved Kerr rotation data shows an ultrafast demagnetization within about 500 fs for all samples as shown in Fig. 9.1(a). Subsequently, there is a fast recovery of magnetization within 5 ps followed by a slower recovery within 500 ps, on top of which precession of magnetization is observed as an oscillatory signal. The demagnetization and remagnetization times are tabulated in Table 9.1.

The demagnetization time, being a characteristic of the material, is constant for all the bi-layers, but slightly different for the bare $\text{Fe}_{55}\text{Pt}_{45}$ layer. The fast remagnetization time, on the other hand, changes significantly as we move from bare $\text{Fe}_{55}\text{Pt}_{45}$ layer to the bi-layers. However, for the bi-layers, it does not exhibit any significant variation. The fast relaxation occurs due to the distribution of energy between electron, spin and lattice baths. Hence this

Chapter 9

gets significantly affected by the spin-orbit (SO) interaction. Now, this SO interaction is modified in the bi-layers as compared to the bare Fe₅₅Pt₄₅ layer due to the presence of two materials and the interface.

Table 9.1: Demagnetizaion, fast and slow remagnetization times for different samples.

Sample	Demagnetization time (fs)	Fast remagnetization time (ps)	Slow remagnetization time (ps)
<i>S0</i>	400	3.2	400
<i>S10</i>	500	4.8	325
<i>S20</i>	500	5.3	212
<i>S50</i>	500	5.1	438
<i>S80</i>	500	5.0	515

This justifies the different values of fast remagnetization time (τ_1) in Fe₅₅Pt₄₅ layer and bi-layers. The intensity of the pump beam and magnetocrystalline anisotropy also have some effect on τ_1 . These parameters do not vary significantly for the samples studied. However, the SO interaction gets affected by the local lattice structure and symmetry along with the intrinsic SO coupling [298, 301]. For the four bi-layers, the Fe₅₅Pt₄₅/Ni₈₀Fe₂₀ interfaces are not identical. Hence this and the different t values introduce a variation in the distribution of surface, interface and interior spins in these bi-layers. As the rate of energy and momentum transfer from spins to lattice is different for surface, interface and interior spins, a variation in τ_1 values is obtained for the bi-layers. However, as there is no systematic change in the interfaces with the thickness of the bi-layers, the variation in τ_1 values is also random.

A bi-exponential background is subtracted from the time-resolved data before performing the fast Fourier transform (FFT) to extract the SW spectra from the samples. The upper

Chapter 9

panel of Fig. 9.1(b) presents the time-resolved precessional dynamics for $S80$ at a bias field $H = 1.0$ kOe, while the lower panel presents the corresponding FFT spectra showing the presence of a number of SW modes for this sample. The variation of the frequency of mode 1 with the bias field is plotted in Fig. 9.1(c) along with a fit to Kittel's formula (eqn. (2.58) in chapter 2) [144] confirming the magnetic origin of the modes. The SW modes as obtained from the TR-MOKE measurements on samples of different t values are presented in Fig. 9.2(a).

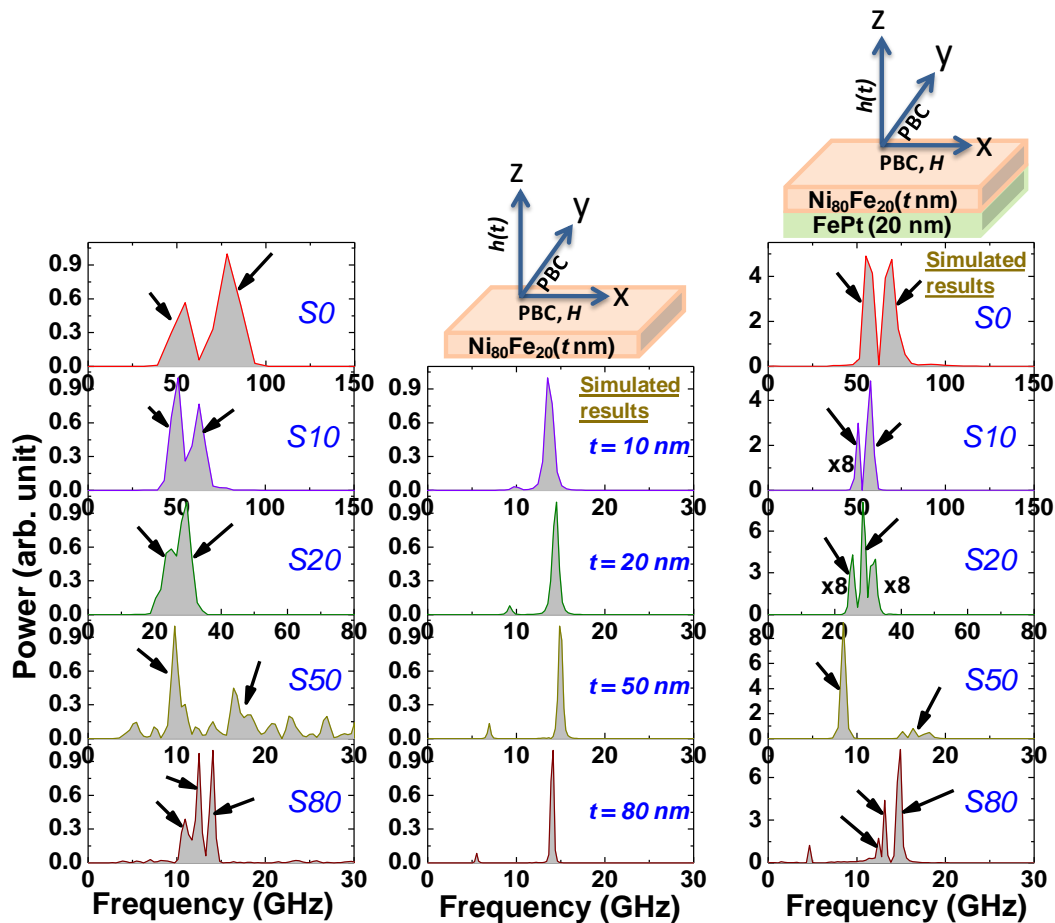


Fig. 9.2: (a) Experimentally obtained SW spectra for samples with varying $\text{Ni}_{80}\text{Fe}_{20}$ layer thickness t for $H = 1$ kOe, (b) simulated SW modes for bare $\text{Ni}_{80}\text{Fe}_{20}$ films with varying thickness and (c) simulated SW frequencies for $\text{Fe}_{55}\text{Pt}_{45}/\text{Ni}_{80}\text{Fe}_{20}$ bi-layers. Schematics show the directions of the applied bias field (H) and the pulsed field ($h(t)$) as used in the simulations. The intensities of the lower frequency mode in $S10$, lowest and highest frequency modes in $S20$ were magnified 8 times as shown next to those peaks for visual clarity.

Chapter 9

We observe that the mode frequencies of these bi-layers are higher than that of the bare $\text{Ni}_{80}\text{Fe}_{20}$ layers of comparable thickness. A number of modes are observed for all samples studied here. For *S0*, two peaks at about 52 and 77 GHz with a clear splitting are observed. The entire spectrum shifts to lower frequency regime as we keep on increasing the $\text{Ni}_{80}\text{Fe}_{20}$ layer thickness. For *S10*, the peak frequencies are about 49.64 and 62.48 GHz and the splitting gets weaker. In the case of *S20*, the peaks are very weakly split and the frequencies are also reduced to about 24.8 and 28.9 GHz. The spectrum changes suddenly for *S50* and we get two distinct bands of modes at about 10.07 and 17.46 GHz. Finally, for *S80*, only a single band of modes around 12.45 GHz is observed. In some cases a lower frequency mode (< 5 GHz) is observed, which does not vary significantly with the bias field or t , and therefore are not shown in Fig. 9.2(a).

To understand the dynamic magnetic behavior in more details, we performed micromagnetic simulations and the simulated results are presented in Fig. 9.2 (b) & Fig. 9.2(c). We first simulated the static magnetic configurations of all the samples by using the LLG Micromagnetic Simulator [206] as described in section 3.4. of chapter 3. Calculations were done by dividing the samples in arrays of cuboidal cells with two-dimensional periodic boundary conditions applied within the plane of the samples. The $\text{Fe}_{55}\text{Pt}_{45}$ layer is discretized into cells of dimension $5 \times 5 \times 2 \text{ nm}^3$. On the other hand, $\text{Ni}_{80}\text{Fe}_{20}$ layers were divided into arrays of cells with dimensions $5 \times 5 \times 5 \text{ nm}^3$. The simulations assume typical material parameters for $\text{Fe}_{55}\text{Pt}_{45}$ as saturation magnetization $M_s = 1140 \text{ emu/cc}$, exchange stiffness constant $A = 1.05 \text{ } \mu\text{erg/cm}$, first order anisotropy constant $K_{u1} = 15.5 \text{ Merg/cc}$ along (001) direction and for $\text{Ni}_{80}\text{Fe}_{20}$ as $M_s = 820 \text{ emu/cc}$, $K_{u1} = 0$ and $A = 1.3 \text{ } \mu\text{erg/cm}$. The interlayer exchange stiffness constant is set to $1.3 \text{ } \mu\text{erg/cm}$. The gyromagnetic ratio $\gamma = 18.1 \text{ MHz Oe}^{-1}$ is used for both layers. In the real system the $\text{Fe}_{55}\text{Pt}_{45}$ layer has (111) texture with a high magnetic anisotropy along the (001) direction [59]. This corresponds to (001) directions that have $L1_0$ order, *i.e.*, alternating Fe and Pt planes are the uniaxial easy axis anisotropy directions. These easy axes all lie at an angle of about 55° from the surface normal with the in-plane component having random orientation for the different crystallographic grains. Modeling such a complex spin configuration is beyond the scope of the micromagnetic simulations and hence we considered a simpler model system with an

Chapter 9

effective anisotropy along the (001) direction, assuming that due to the (111) out-of-plane and random in-plane orientation of the crystallites on the macroscopic length scale, the in-plane modulation of the spins in the $\text{Fe}_{55}\text{Pt}_{45}$ layer cancels out.

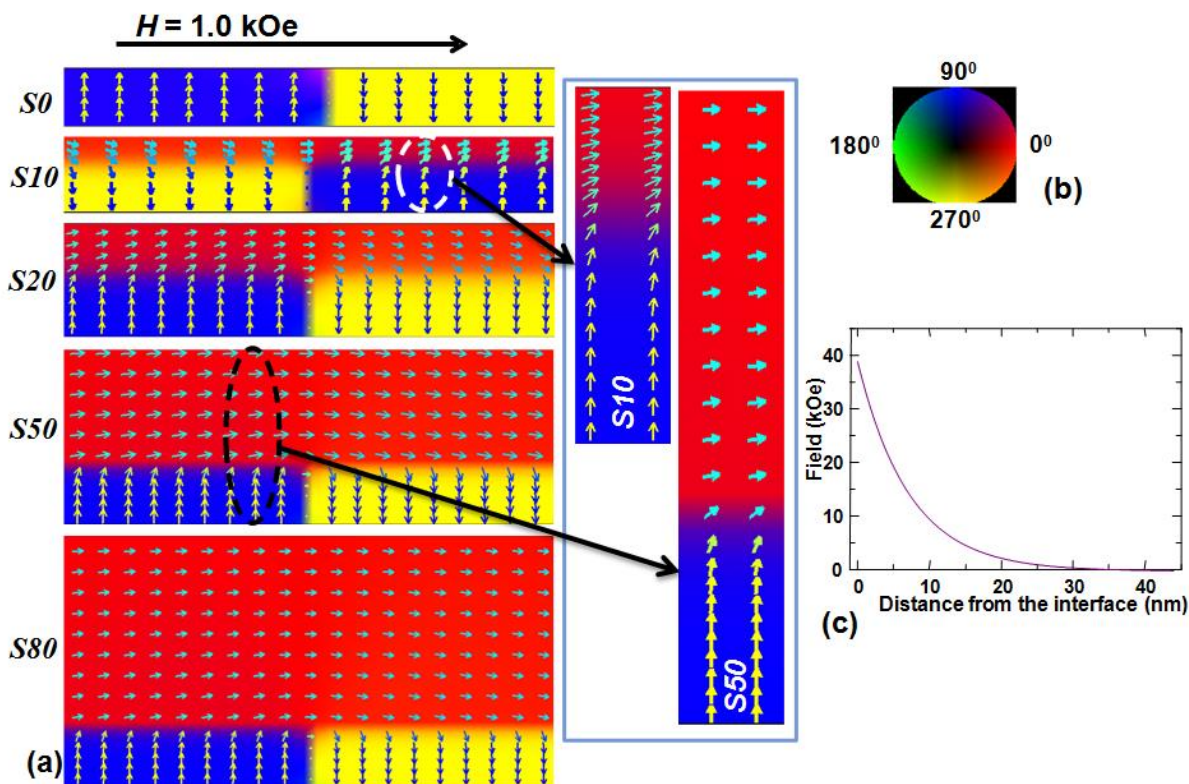


Fig. 9.3: (a) Simulated static magnetic configurations of bare $\text{Fe}_{55}\text{Pt}_{45}$ thin film ($S0$) and $\text{Fe}_{55}\text{Pt}_{45}/\text{Ni}_{80}\text{Fe}_{20}$ bi-layers with varying $\text{Ni}_{80}\text{Fe}_{20}$ layer thickness ($S10$, $S20$, $S50$ and $S80$). Magnified views of parts of $S10$ and $S50$ are shown to elaborate the spin-twist structure inside the $\text{Ni}_{80}\text{Fe}_{20}$ layer. (b) The color map used for Fig. 9.3(a). (c) The effective magnetic field used inside the $\text{Ni}_{80}\text{Fe}_{20}$ layer (as a function of the distance from the $\text{Fe}_{55}\text{Pt}_{45}/\text{Ni}_{80}\text{Fe}_{20}$ interface) in the simulations.

Due to the very high anisotropy of the $\text{Fe}_{55}\text{Pt}_{45}$ layer along the (001) direction, the spins at $\text{Fe}_{55}\text{Pt}_{45}/\text{Ni}_{80}\text{Fe}_{20}$ interface are considered as pinned along (001) direction by assigning same anisotropy as $\text{Fe}_{55}\text{Pt}_{45}$ on the $\text{Ni}_{80}\text{Fe}_{20}$ cells at the interface. These parameters were optimized by calculating the hysteresis loops of the samples and by comparing the results with the experimental loops as reported previously [59]. The static magnetic configurations were calculated by applying a 1 T bias field in the plane of the sample (along the x-direction) to fully magnetize the sample and allowing the magnetization to relax for 5

Chapter 9

ns. The applied field was then reduced to the desired H value and the magnetization was further allowed to relax for another 10 ns. During this process, α was set at 0.99 so that the precession dies down quickly and the magnetization fully relaxes within 15 ns. The convergence criteria was set on the maximum torque $\mathbf{m} \times \mathbf{H} \ll 10^{-6}$ A/m, where $\mathbf{m} = \mathbf{M}/M_s$, which was always reached within the allowed relaxation time. Fig. 9.3(a) presents the simulated static magnetic states of all the samples and the color map used is shown in Fig. 9.3(b). The color map shows the orientation of the magnetization with respect to the applied field direction. Due to the application of very high field for the first 5 ns, the sample becomes fully saturated during that time. However, when the field is reduced to the bias field value $H = 1.0$ kOe, all spins get aligned either to the bias field or to the anisotropy field, whichever is higher. Prominent domain formations are observed in the hard magnetic layer ($\text{Fe}_{55}\text{Pt}_{45}$) for all samples. The spins in the $\text{Fe}_{55}\text{Pt}_{45}$ layer are aligned parallel (antiparallel) to its anisotropy direction (001) whereas the spins in the $\text{Ni}_{80}\text{Fe}_{20}$ layer rearrange themselves to minimize the energy of the system during the calculation of static magnetic configuration and finally end up with the twisted spin orientation in the $\text{Ni}_{80}\text{Fe}_{20}$ layer as elaborated in the inset of Fig. 9.3(a) for two different samples $S10$ and $S50$. These static configurations were used to simulate the dynamics of these samples after applying a pulsed magnetic field $h(t)$ with rise-time of 50 ps and peak amplitude 30 Oe perpendicular to the plane of the samples. In the dynamic simulations, we have introduced an effective magnetic field in the $\text{Ni}_{80}\text{Fe}_{20}$ layer as shown in Fig. 9.3(c). To justify the use of the spatially varying field in the $\text{Ni}_{80}\text{Fe}_{20}$ layer, we calculate the internal field distribution in the samples under three different conditions: i) without any additional field in the $\text{Ni}_{80}\text{Fe}_{20}$ layer, ii) with an additional field confined only at the $\text{Ni}_{80}\text{Fe}_{20}$ layer at the $\text{Fe}_{55}\text{Pt}_{45}/\text{Ni}_{80}\text{Fe}_{20}$ interface and iii) with the additional spatially varying (exponentially varying) field in the $\text{Ni}_{80}\text{Fe}_{20}$ layer as presented in Fig. 9.3(c).

Chapter 9

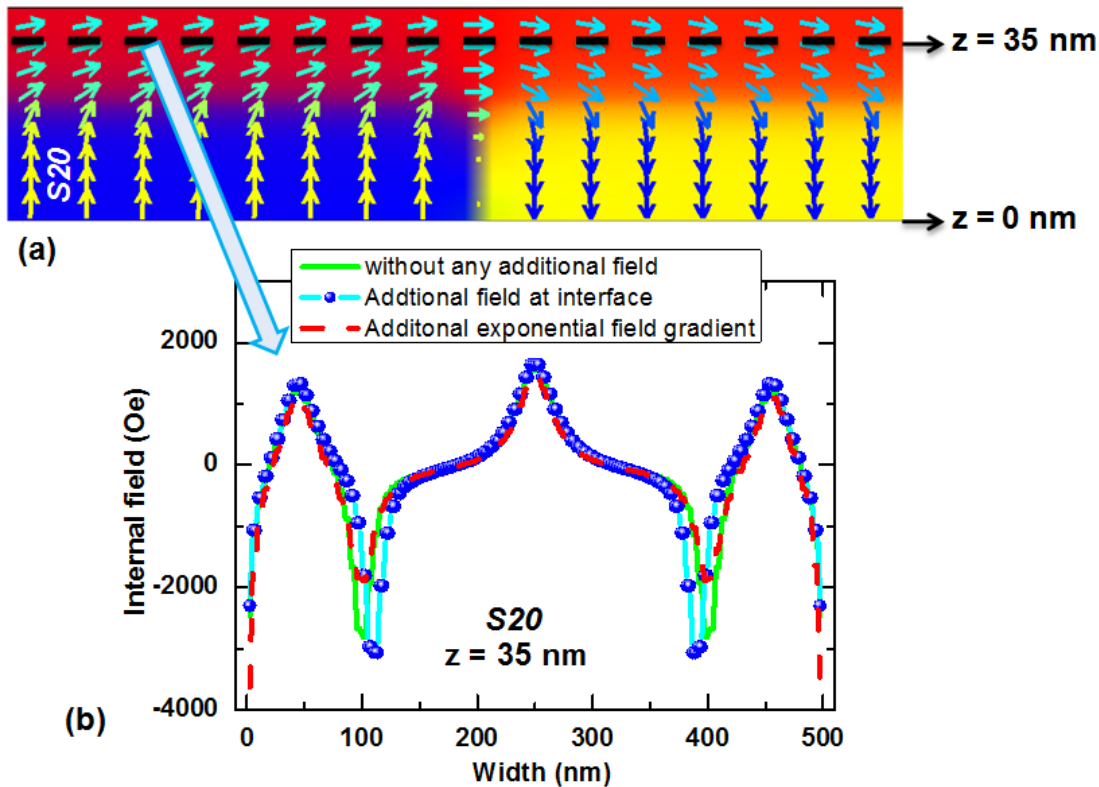


Fig. 9.4: (a) Static magnetic state of the sample *S20* with the black dashed line, along which the internal field distribution is calculated and (b) Internal field distribution at $z = 35$ nm for the sample *S20* under different configurations.

The internal field within the $\text{Ni}_{80}\text{Fe}_{20}$ layer is then calculated at different distances (z) from the interface. A typical result for *S20* at $z = 35$ nm is shown in Fig. 9.4. This shows that the internal field distribution is similar for the first two cases indicating that the exchange bias field applied at the interface layer does not penetrate into the $\text{Ni}_{80}\text{Fe}_{20}$ layer automatically due to the exchange interaction in the micromagnetic simulation [344] and an additional field gradient in the $\text{Ni}_{80}\text{Fe}_{20}$ layer is indeed required to reproduce the experimental frequency values. This discrepancy is probably because in the modeling we assume sharp interface between the $\text{Fe}_{55}\text{Pt}_{45}$ and $\text{Ni}_{80}\text{Fe}_{20}$ layers, which may have oversimplified the experimental systems. The interface quality significantly depends upon the deposition process and the subsequent post-deposition treatments. Also, the degree of atomic coherency and chemical and atomic roughness at the interface affect the interphase exchange coupling in the exchange spring magnets [345]. However, quantification of these parameters and incorporation of those in micromagnetic simulations are beyond the scope

Chapter 9

of this paper. Hence, we have instead approximated those possible effects as an additional magnetic field in our calculation. The field values were adjusted extensively to obtain a qualitative agreement with the experimental mode frequencies. As the spins of the $\text{Ni}_{80}\text{Fe}_{20}$ layer are pinned at the interface, the effective magnetic field is assumed maximum at the interface and decays exponentially as we move from the interface inside the $\text{Ni}_{80}\text{Fe}_{20}$ layer, due to its origin in the exchange interaction. The dynamic magnetization was averaged over the entire sample volume and images of the same were saved until the precession died down. We have also simulated the dynamics of only $\text{Ni}_{80}\text{Fe}_{20}$ films with thickness ranging from 10 to 80 nm under identical conditions as above for a comparison and the results are presented in Fig. 9.2(b). Two resonant modes are observed in this case, out of which the lower frequency mode reduces from 10 GHz to nearly 5 GHz with increasing t but the higher frequency mode increases slightly from 13.73 to 15.0 GHz upto $t = 50$ nm and then decreases slightly to 14.15 GHz for $t = 80$ nm. This shows that the presence of the adjacent $\text{Fe}_{55}\text{Pt}_{45}$ layer and the resulting pinning at the interface and an effective magnetic field gradient within the $\text{Ni}_{80}\text{Fe}_{20}$ layer play important roles in determining the frequency and nature of the SW spectra in the bi-layer systems. Fig. 9.2(c) presents the simulated spectra of the $\text{Fe}_{55}\text{Pt}_{45}/\text{Ni}_{80}\text{Fe}_{20}$ bi-layers with the static magnetic configurations as shown in Fig. 9.3(a). The simulations reproduced the important features in the experimental spectra qualitatively. The domains in the hard layer affect the non-linear spin orientation in the $\text{Ni}_{80}\text{Fe}_{20}$ layer significantly, which in turn affects the SW modes of the bi-layers. For $S0$, $S10$ and $S20$, experimentally observed peaks are reproduced at nearly same frequencies in the simulations. In all cases the experimentally observed mode splitting is reproduced although the relative mode intensities are not exactly reproduced. For some samples, additional modes are observed in the simulations, which were not detected experimentally. Also, the experimental peaks are broader due to shorter time window of about 1.5 ns as opposed to the simulation window of about 4.0 ns. For $S50$, the simulation qualitatively reproduced the experimental modes at similar frequencies, with the band of modes near 17 GHz. Finally, for $S80$, three modes observed experimentally are reproduced in the simulation with an additional mode at around 5 GHz, which was not observed experimentally. This mode is probably a backward volume magnetostatic mode, which propagates out of the probe spot volume after excitation and do not get detected with

Chapter 9

reasonable intensity. It is also found from the simulation that this low frequency mode grows significantly in intensity only after about 1.5 ns. Since in the experiment the time-resolved data was acquired for 1.5 ns, the intensity of the detected mode is further reduced and almost becomes invisible in the experiment. In Fig. 9.2(c), we have shown FFT spectra of the simulated time-resolved magnetization for the first 1.5 ns for $S80$, which significantly reduced the intensity of the mode at around 5 GHz.

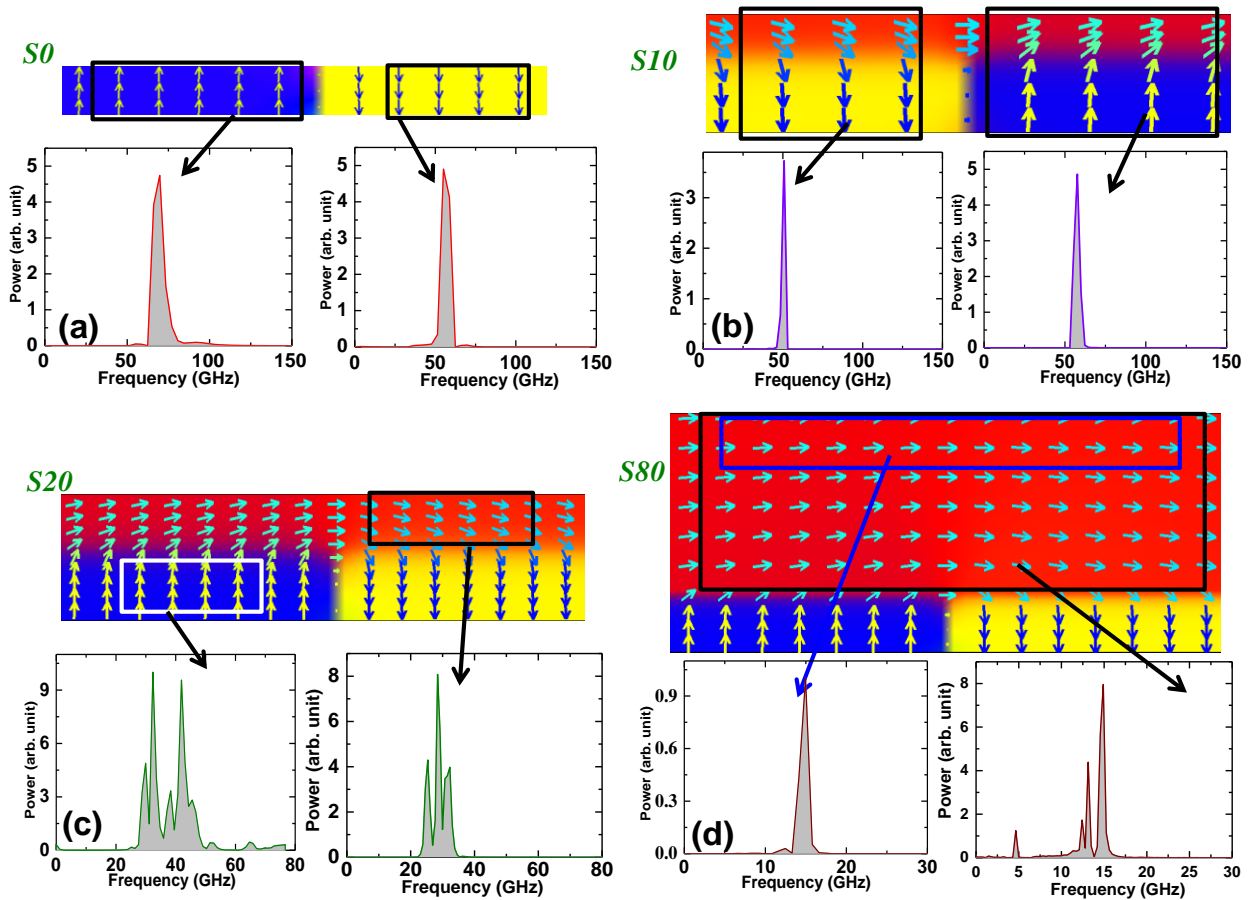


Fig. 9.5: Region-wise extraction of precession frequencies from (a) $S0$, (b) $S10$, (c) $S20$ and (d) $S80$. The static magnetic states are not in scale for better visual clarity.

In order to understand the origin of the observed SW modes, we extracted the dynamics locally from different regions of the simulated samples as shown in Fig. 9.5. For $S0$, the origin of the observed modes lies within the formation of the domains in the static configuration and the frequency of precession of magnetization within the yellow (blue) domain is found to be 56.8 (69.6) GHz, as shown in Fig. 9.5(a). For $S10$, the modes originate

Chapter 9

from the precession of magnetization of two different domains where the $\text{Fe}_{55}\text{Pt}_{45}$ and the $\text{Ni}_{80}\text{Fe}_{20}$ layers are strongly coupled as presented in Fig. 9.5(b). In contrary, for $t \geq 20$ nm, the spins in the $\text{Ni}_{80}\text{Fe}_{20}$ layer are slightly modulated due to the presence of the domains in the $\text{Fe}_{55}\text{Pt}_{45}$ layer and the observed modes primarily originate from the spin-twist structure inside the $\text{Ni}_{80}\text{Fe}_{20}$ layer. For $S20$, a clear mode splitting is observed from the dynamics extracted from the $\text{Ni}_{80}\text{Fe}_{20}$ layer as shown in Fig. 9.5(c), whereas dynamics extracted from the $\text{Fe}_{55}\text{Pt}_{45}$ layer gives only a band of modes, which are not observed in the experiment. Similar pattern is also observed for $S50$. As we move to $S80$, from Fig. 9.5(d), we observe that the major contribution to the modes comes from the $\text{Ni}_{80}\text{Fe}_{20}$ layer. The extracted modes from the top 10 nm of the $\text{Ni}_{80}\text{Fe}_{20}$ layer reproduces two higher frequency modes but the third mode with lower frequency is reproduced only after considering the non-uniform spin structure up to about 20 nm from the $\text{Fe}_{55}\text{Pt}_{45}/\text{Ni}_{80}\text{Fe}_{20}$ interface. There is also an effective field gradient present up to about 28 nm within the $\text{Ni}_{80}\text{Fe}_{20}$ layer from the interface for this sample but that does not significantly modify the values of the mode frequencies compared to that of a bare 80 nm $\text{Ni}_{80}\text{Fe}_{20}$ film. However, the presence of the spin-twist structure modifies the mode profiles giving rise to a band of modes for this bi-layer structure instead of a single mode for a $\text{Ni}_{80}\text{Fe}_{20}$ film.

9.5. Conclusions

In summary, we have studied the ultrafast magnetization dynamics of a series of exchange coupled $\text{Fe}_{55}\text{Pt}_{45}/\text{Ni}_{80}\text{Fe}_{20}$ bi-layers with varying $\text{Ni}_{80}\text{Fe}_{20}$ thickness by an all-optical TR-MOKE measurement and micromagnetic simulations based on a simplified sample microstructure. Even though the simulations are simplified they are sufficient to capture the important features observed in our experiments. Rich SW spectra are observed in these samples, which depend strongly on the $\text{Ni}_{80}\text{Fe}_{20}$ thickness. The mode frequencies obtained for the bi-layers differ significantly from those of a single $\text{Ni}_{80}\text{Fe}_{20}$ layer with comparable thickness and new modes are also observed. For thinner samples, the magnetization dynamics are found to be primarily governed by the formation of stripe domain and with increasing thickness of the $\text{Ni}_{80}\text{Fe}_{20}$ layer, the effect of the spin-twist structure within this

Chapter 9

layer comes into play. As the thickness of Ni₈₀Fe₂₀ increases further, the effect of the spin-twist structure in determining the dynamic mode profile decreases. The observed dynamics will be important for understanding and future applications of exchange spring magnets in high speed storage and memory devices and for microwave applications.

10. Magnetization reversal dynamics in Co nanowires with competing magnetic anisotropies

10.1. Introduction

Ordered arrays of magnetic nanowires (NWs) have tremendous potential in technological applications including magnetic storage [1], field sensors [346], logic devices [347], and magnonic crystals [3]. Measurements and understanding of magnetization reversal [69, 76, 348], domain wall movements [349-350] and spin wave dynamics [221, 351] in magnetic NWs and nanopillars have emerged as important problems from the viewpoints of both fundamental science and for the above applications. The ever increasing demand for storage density leads towards the reduction of bit size, but an upper limit to the storage density occurs due to the superparamagnetism. Densely packed ordered arrays of magnetic NWs with large aspect ratios (R) may overcome this problem due to the large volumes of the individual NW and its large shape anisotropy along the wires axis, associated with larger areal density. On the other hand, in NWs formed of magnetic materials with high magnetocrystalline anisotropy, a competition between the two anisotropies may arise if the anisotropy directions are different. Electrodeposition through nanoporous templates [87] is a very efficient and cost-effective method to produce large aspect ratio NWs at large scales with different diameters, lengths, and crystallinity. Previous reports on electrodeposited Co NWs have shown that the high melting point and high binding energy of Co with hexagonal close-packed (hcp) crystalline structure favors aggregation of atoms into small three-dimensional (3D) clusters, which form Co NWs with their c-axis orientated either parallel [352] or perpendicular [352-353] to the long-axis of the NW depending on the pH of the electrolyte used during electrodeposition. On the other hand, the shape anisotropy naturally occurs along the long-axis of the wire, and competing magnetic anisotropy has become an important topic due the possibility of tuning of the magnetic anisotropy energy barrier in these NWs simply by tuning their aspect ratio. The competing

Chapter 10

magnetic anisotropies and the consequent cross-over of the magnetic easy and hard axes that depends the aspect ratio have been studied in ferromagnetic (FM) NWs and nanotubes with large magnetocrystalline anisotropy [354-357]. The cross-over has been observed both by varying the diameter and length of the NWs and from the measurements of magnetization as a function of the amplitude and orientation of the applied magnetic field. However, the detailed magnetization reversal mechanisms associated with the cross-over of the magnetic easy and hard axes have not been studied in detail. In this chapter, we present a systematic study of the magnetization reversal mechanisms in Co NWs, where the competing magnetic anisotropies are observed. In order to minimize the further complications arising from magnetostatic interactions between the NWs, we have grown them in track-etched polycarbonate membranes (PCTE) with very low pore density. We have performed 3-D micromagnetic simulations to obtain an extensive understanding of the magnetization reversal processes in the NWs.

10.2. Sample preparation

The Co NWs were prepared by a standard three-electrode electrodeposition process (as described in detail in section 4.3. of chapter 4) through commercially available polycarbonate track etched (PCTE) templates (Whatman) with a fixed nominal diameter of about 100 nm. The deposition was carried out by the application of a pulsed potential with voltage levels at 0.1 and -1.0 V and with uniform pulse width = 10 s. The electrolyte used is a 100 ml solution of 30 mM $\text{CoSO}_4 \cdot 7\text{H}_2\text{O}$ and 120 mM H_3BO_3 in distilled water [358]. The templates were left into a solution of sodium lauryl sulphate prior to deposition to allow wetting and opening up of the pores and to have smooth and uniform deposition. The backside of the PCTE membrane was coated with a 100 nm thick Au layer by thermal evaporation, which served as the cathode. The lengths of the NWs were varied by varying the electrodeposition time between 2000 and 80 s.

10.3. Characterization and measurement of the quasistatic magnetic properties

For structural and compositional analyses, the templates were dissolved in dichloromethane and washed several times with ethanol and distilled water to clean the Co NWs. The surface morphology and the dimensions of the NWs were studied with field emission scanning electron microscopy (FESEM; Helios NanoLab, FEI). The compositional analysis was made by using energy dispersive X-ray spectroscopy (EDX; Helios NanoLab, FEI). The crystal structure of the NWs was studied from as-deposited templates by using X-ray diffraction using Cu K α radiation of wavelength 1.54 Å (XRD; PANalytical X'Pert PRO). Finally, the quasistatic magnetization reversal properties of the NWs embedded inside the templates and lying vertically on the substrate plane were studied by vibrating sample magnetometry (VSM; Lakeshore model 7407) at room temperature. The magnetic field up to 16 kOe is applied in steps of 50 Oe in two different orientations during the measurements – 1) parallel to the long axes of the NWs and 2) perpendicular to the long axes of the NWs.

10.4. Results and discussions

The scanning electron micrographs of Co NWs with different aspect ratios are shown in Fig. 10.1(a)–(d), after dissolving the templates. The diameters of the NWs are found to be about 95 nm \pm 5 nm. By varying the deposition time between 2000 and 80 s, the lengths of the NWs are controlled between 5.75 μ m and 240 nm, which correspond to a variation of aspect ratio between about 60 and 2.5. The EDX spectrum (Fig. 10.1(e)) shows little traces of Oxygen apart from Co which confirms the chemical purity of the NWs with slight oxidation of the surface layer. The XRD data (Fig. 10.1(f)) confirms an *hcp* crystal structure. However, the crystallinity is not very high, which may result in a reduction of magnetocrystalline anisotropy compared to the value for single crystal Co.

Chapter 10

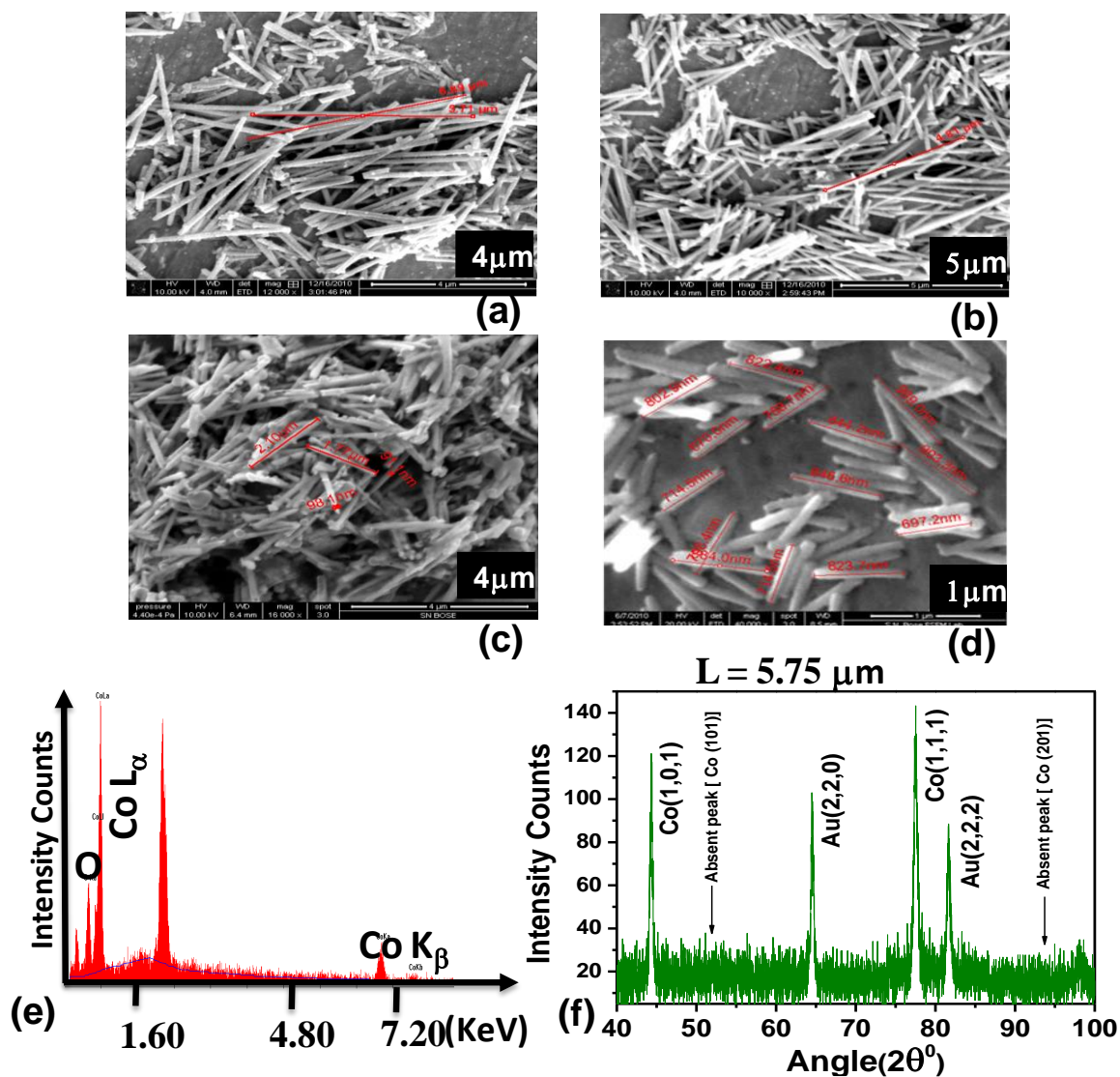


Fig. 10.1: Scanning electron micrographs of Co NWs with different aspect ratios: (a) 60, (b) 49.5, (c) 18.1, and (d) 6.8. (e) The EDX spectrum and (f) the XRD data obtained from the electrodeposited Co NWs.

The magnetization (M) as a function of the applied magnetic field (H) for three different samples, measured by VSM at $T = 300$ K, are shown in Fig. 10.2(a). For NWs with $R > 10$, we clearly observe that the long-axis loop (magnetic field applied parallel to NWs axes) has higher coercive field and remanence and lower saturation field than those obtained from the short-axis loop (magnetic field applied perpendicular to NWs axes). As the aspect ratio is decreased, the differences between the loops are reduced. For $3 < R < 10$, the two loops

Chapter 10

are close to each other. In Fig. 10.2(a), we show that for $R = 6.8$ the two loops are almost identical, defining the cross-over region between the easy axis and the hard axis. With further reduction in aspect ratio ($R < 3$), the short-axis loop starts to show higher coercivity and remanence and lower saturation field than those for the long-axis loop. For NWs with large aspect ratio ($R > 10$), the shape anisotropy, parallel to the axis of the NWs, dominates, which causes higher coercive field and remanence and lower saturation field for the long-axis loop. For intermediate values of R ($10 < R < 3$), the contributions from the shape and magnetocrystalline anisotropies are comparable and it is difficult to distinguish the differences between the loops along the long and short axes. For $R < 3$, the magnetocrystalline anisotropy starts to clearly dominate, and the short-axis loop shows higher coercivity and remanence and lower saturation field. According to the macrospin model [359], the cross-over should ideally occur sharply at $R \sim 7.0$ (for saturation magnetization $M_s = 1400$ emu/cc, magnetocrystalline anisotropy $K = 5 \times 10^6$ erg/cc along the [100] direction). However, the smearing of the cross-over region, as observed in our experiment, is possibly due to a distribution of magnetocrystalline anisotropy over the NWs and due to the complicated magnetization reversal processes that is not considered in the macrospin model.

Chapter 10

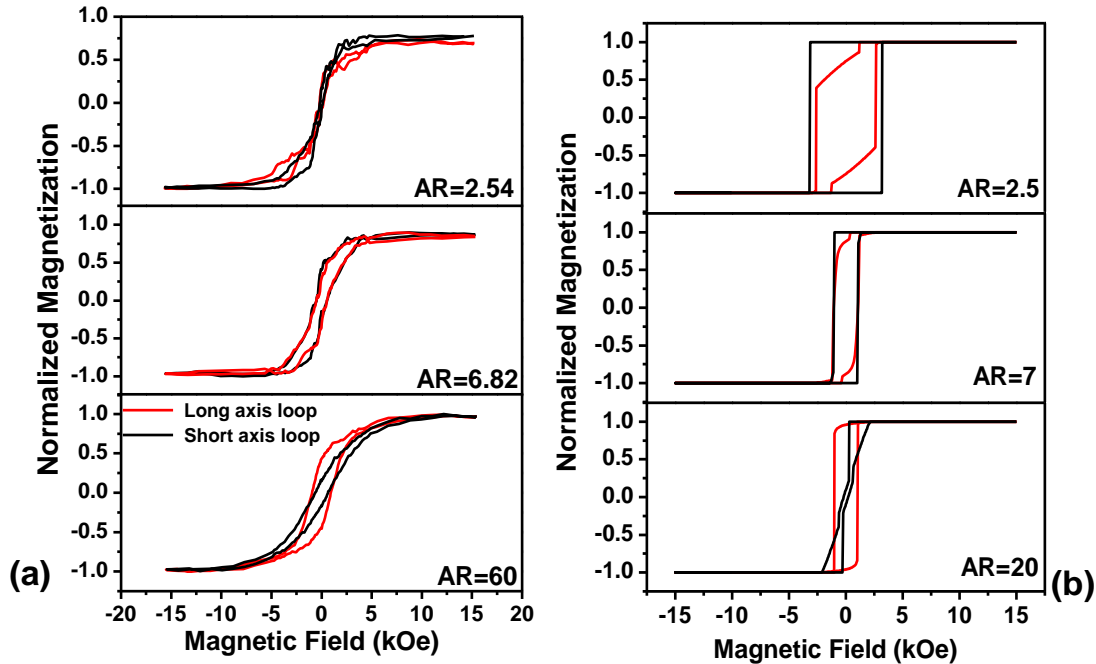


Fig. 10.2: (a) Experimental and (b) simulated M - H curves of Co NWs with different aspect ratio (R). The red lines correspond to the M - H curves with H applied parallel to the long-axis of the NW and the black lines correspond to the M - H curves with H applied perpendicular to the long-axis of the NW.

To understand the details of the magnetization reversal mechanisms associated with the cross-over, we performed micromagnetic simulations to numerically solve the Landau-Lifshitz-Gilbert equation [eqn. (2.44) in chapter 2] by using the public domain software object oriented micromagnetic framework (OOMMF), from the NIST website [205]. A description of the working principle for this software is given in section 3.4 of chapter 3. We have simulated the magnetization (M) as a function of the applied magnetic field (H) for Co NWs with aspect ratio varying between 2.5 and 60. Calculations were performed by dividing the samples into 3D arrays of cuboidal cells with dimensions $2 \times 2 \times 5 \text{ nm}^3$. The linear dimensions of the cells are comparable to the exchange length of Co, which is defined as $\sqrt{A/2\pi M_s^2}$, where A is the exchange constant and M_s is the saturation magnetization, respectively. The simulations assume the following material parameters for Co: $4\pi M_s = 17.59 \text{ kOe}$, exchange stiffness constant $A = 30 \times 10^{-7} \text{ erg/cm}$, magnetocrystalline anisotropy $K = 4.5 \times 10^6 \text{ erg/cc}$ along the $[100]$ direction, and gyromagnetic ratio $\gamma = 17.6 \text{ MHz/Oe}$.

Chapter 10

Shape anisotropy is already included in the calculation of the demagnetizing field of the system. The applied magnetic field was varied between +15 to -15 kOe in steps of 50 Oe. In some cases, when required, a field step of 5 Oe was also used to observe finer details. The stopping criterion is given on the change in magnetization with time. A damping coefficient $\alpha = 0.9$ was used to ensure that the system finds equilibrium within the allowed simulation time between two consecutive steps of the applied magnetic field.

Some typical simulated M - H loops are shown in Fig. 10.2(b). Since the measured samples were deposited inside PCTE templates, the NWs embedded inside the pores are separated by large distance, and we may neglect the dipolar interaction between the NWs. Hence, the simulations were performed in single NWs without losing any important information. The M - H loops obtained for $R = 60$ and $R = 20$ are almost identical, and hence for visual clarity of the magnetization reversal modes (as presented in Fig. 10.3) we have shown the results for $R = 20$ only. The simulated data qualitatively agree with the experimental data. However, detailed quantitative agreement is not expected, as the simulations were performed at $T = 0$ K and the experiment was at $T = 300$ K.

In general, for small nanomagnets with dimensions ≤ 100 nm, the magnetization reversal is primarily dominated by coherent (quasi-coherent) rotation, although the enhancement of dimensions along one or more axes may lead to various other reversal modes [118], including curling, fanning, buckling, and generation of local magnetic domains such as vortex and Bloch domains. This depends upon the competition between various magnetic energies, which, in turn, depends strongly upon the parameters of the system and external fields. Here, we study how the competing magnetic anisotropy energies influence the reversal modes in Co NWs. For large aspect ratio ($R = 20$, shown in Fig. 10.3) and H applied parallel to the long-axis, the reversal starts at the two ends (Fig. 10.3(a)), but before the end regions reverse, the magnetization in the central region of the NW reverses drastically and nearly coherently at about $H = -1.05$ kOe. The two ends reverse gradually and completely reverse at a larger magnetic field. When the field is applied along the short-axis, the reversal occurs by nucleation of reversed domains at $H = -0.65$ kOe at the two ends of

Chapter 10

the NWs and slow propagation of the reversed domains towards the centre of the NWs (Fig. 10.3(b)).

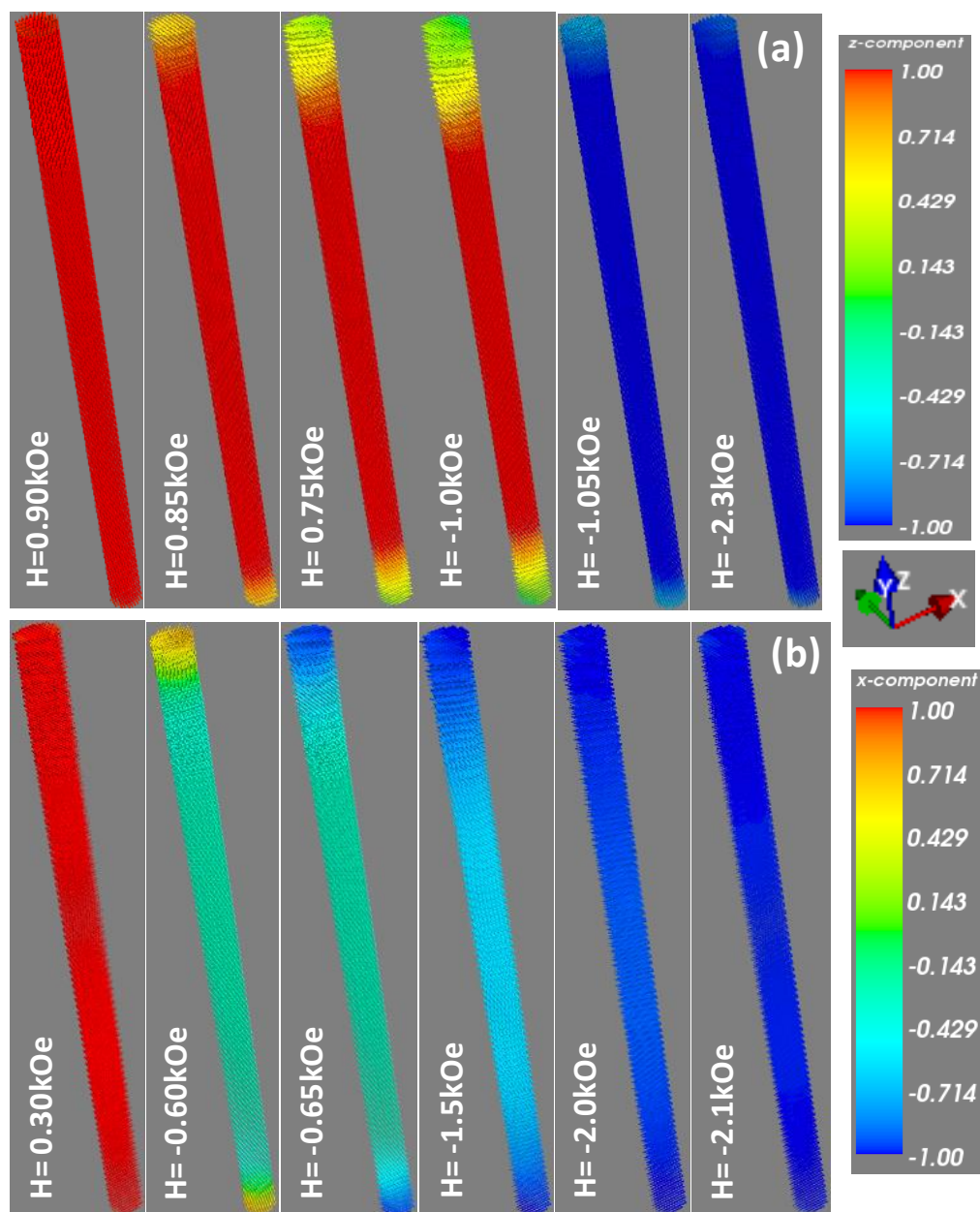


Fig. 10.3: Vector maps of magnetization reversal in a Co NW with $R = 20$. The magnetic field is applied along (a) the long-axis and (b) the short-axis of the NW. The coordinate system and the color map indicating the direction of the magnetization are shown next to the images.

At $R = 7$, when the field is applied parallel to the long-axis, the reversal occurs via formation of a Bloch domain along the length of the NW (Fig. 10.4(a)). With decreasing field, the

Chapter 10

width of the domain shrinks towards the centre of the NW. At $H = -1.1$ kOe, the central region drastically reverses, triggering further reversal of the spins from the centre towards the end regions along the length of the NW. The ends gradually reverse with further increase in the reverse field. The reversal mechanism is similar for this sample when the field is applied along the short-axis of the NW (Fig. 10.4(b)).

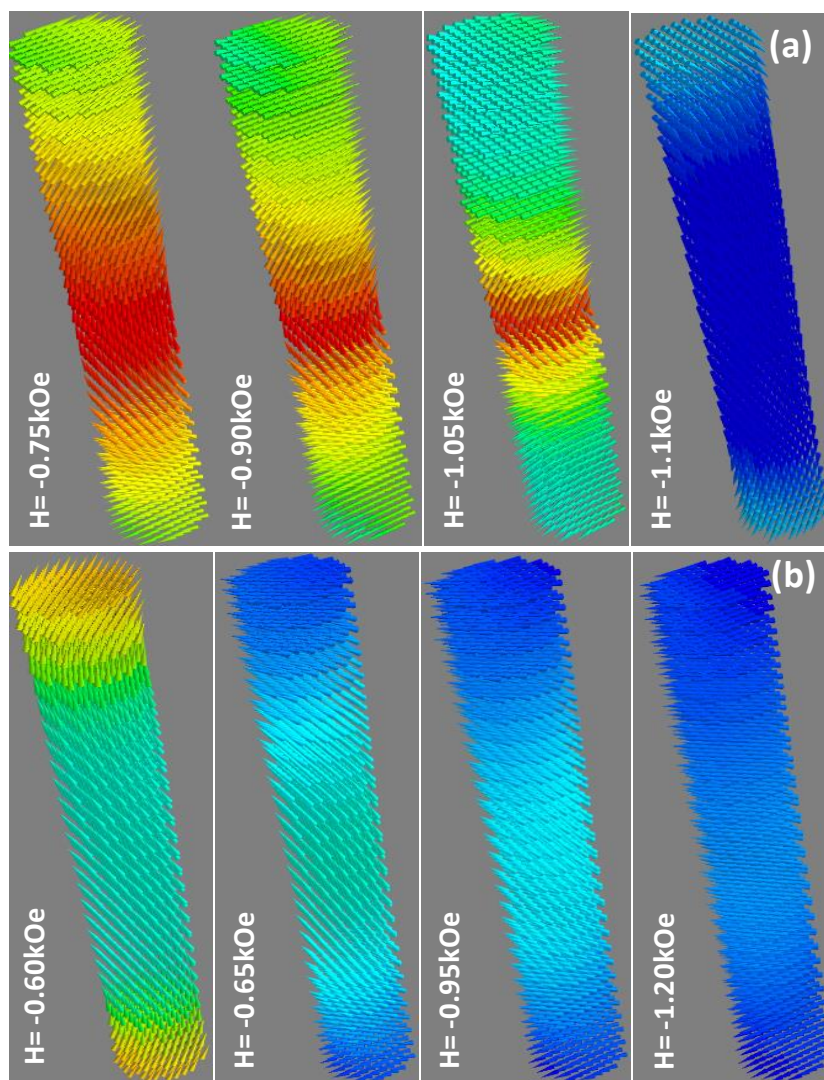


Fig. 10.4: Vector maps of magnetization reversal in a Co NW with $R = 7$. The magnetic field is applied along (a) the long-axis and (b) the short-axis of the NW. The coordinate system and the color map indicating the direction of the magnetization are as shown in Fig. 10.3.

With further reduction in aspect ratio below the cross-over ($R = 2.5$), when the field is applied along the wire axis, the reversal again occurs through the formation of Bloch

Chapter 10

domains, however, a corkscrew-like mode [116] is observed within the individual domains (Fig. 10.5(a)). At this aspect ratio, since the magnetocrystalline anisotropy is dominant over the shape anisotropy, we see that the reversal occurs by quasi-coherent rotation, when the field is applied along the short-axis of the wire (Fig. 10.5(b)).

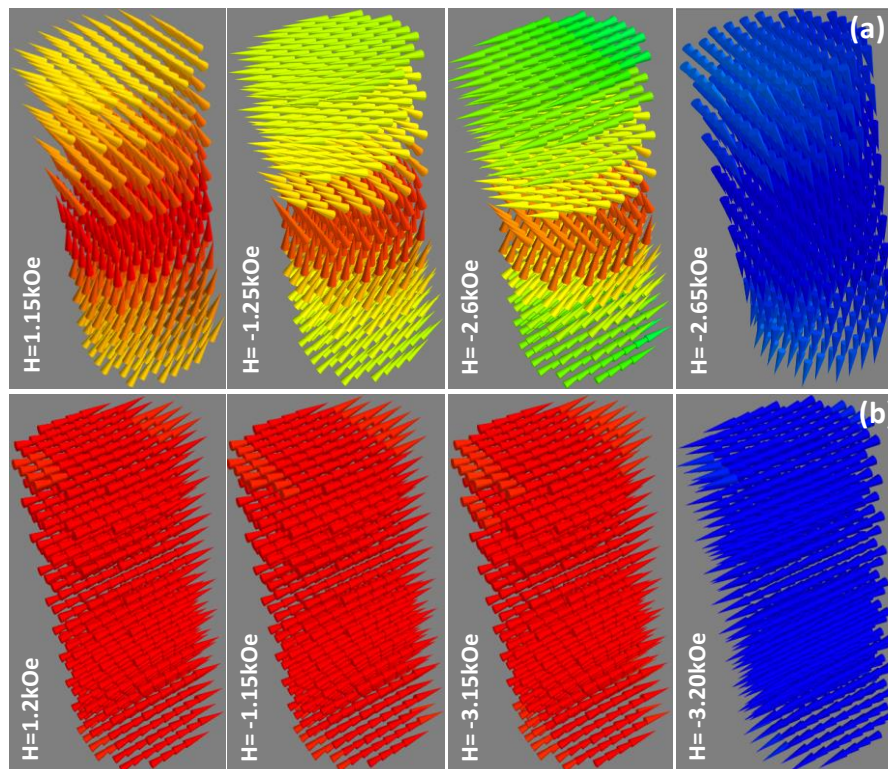


Fig. 10.5: Vector maps of magnetization reversal in a Co NW with $R = 2.5$. The magnetic field is applied along (a) the long-axis and (b) the short-axis of the NW. The coordinate system and the color map indicating the direction of the magnetization are as shown in Fig. 10.3.

10.5. Conclusions

In summary, we experimentally observed tunable magnetic easy and hard axes and a cross-over between the two from the magnetic hysteresis loops of Co NWs by varying their aspect ratio. This is primarily due to the competition between the shape and magnetocrystalline anisotropies in the NWs. From the micromagnetic simulations of a single NW, it is observed that the magnetization reversal mechanism changes from quasi-

Chapter 10

coherent rotation to the formation of Bloch domains to the corkscrew-like reversal mode for the long-axis loop with the decrease in the aspect ratio and the corresponding shape anisotropy. At the cross-over of the magnetic easy axis from the long-axis to the short-axis of the NWs, a transformation of the reversal mechanism from quasi-coherent rotation of magnetization to Bloch domain formation occurs. On the other hand, for aspect ratios below the cross-over region, the reversal mode in the short-axis loop transformed from nucleation and propagation of reversed domains to quasi-coherent rotation. These observations are important both from the viewpoints of fundamental science and for applications of magnetic NWs in various devices.

11. All optical excitation and detection of spin-waves in high aspect ratio ferromagnetic nanowires

11.1. Introduction

In the previous chapter, we investigated about the quasistatic magnetic properties of ferromagnetic (FM) nanowires (NWs). In this chapter, we shall concentrate on the magnetization dynamics of FM NW arrays. Understanding of magnetization dynamics in FM NWs is important in terms of its application in high density storage and microwave devices [284]. NWs possess high anisotropies due to their shapes. The magnetic properties are modified when they are placed in an array due to the interwire magnetostatic interactions [273]. Along with these, if the material of the NW possesses magnetocrystalline anisotropy, then the magnetic properties are further influenced. Hence, the study of magnetization dynamics in FM NWs is also interesting in terms of fundamental science. The magnetization dynamics of FM NWs was studied by various methods. By BLS measurements, discrete modes were observed in the spin-wave (SW) spectrum of permalloy (Py) NW array over a continuous range of wave-vector (k) for wires of finite width. [269]. These modes did not show any noticeable dispersion and were not much affected by the separation between the wires. The frequency splitting of the discrete modes was found to decrease with increasing wave number. Hence, it may be considered that each wire acts as an independent scattering centre and these modes originate purely due to the finite width of the wires. No zone folding effect due to the periodic nature of the NW arrangements was found. The quantization of modes were also found by theoretical studies [270]. From FMR studies [271], it was found that the resonance frequencies of Co NWs were higher than that of Ni for all bias field values whereas the frequencies values of Py were in the intermediate range. Above a certain critical field H_s , the frequency varied linearly with the applied field for all samples and the behavior could be explained by the Kittel [144] formula, whereas below H_s , there is a deviation from the linear relationship due to the unsaturated states of

Chapter 11

the wires. The dipolar coupling between the NWs was found to act as an additional anisotropy which acts in a direction perpendicular to the wire axis by the FMR technique [272-273, 360]. A number of theoretical studies have been made to understand the SW modes in NWs under the application of uniform microwave field [275-280]. It was found that to the first order, the roughness also may cause a shift in the frequencies of the SWs in the magnetostatic limit. BLS showed that under the application of a small transverse field, a branch of low frequency SW modes appeared [281]. The competition between shape anisotropy and the anisotropy associated with the inter-wire magnetostatic interactions in the array were investigated by the time-resolved magneto-optical Kerr effect (TR-MOKE) microscopy measurements along with micromagnetic simulations, in electro-deposited Py NWs with high packing density [228]. Antiferromagnetic alignment of magnetization in adjacent NWs and formation of vortex flux closure structures at the ends of each NW was observed by simulations. With increasing bias field, the ground state changes and accordingly, the profile of the resonant mode changes from nonuniform to uniform nature within the plane of the wire. Resonant modes for fields applied in the direction perpendicular to the wire axis and the dependence of the SW spectra on the packing density and the dispersion relations for the modes propagating through the array for field parallel to the wire axis were also investigated. Due to the extended penetration of the dynamic demagnetizing fields into the middle of the wires and also due to the lowering of the tunnel barrier by the static demagnetizing field in the array, a tunneling of the end modes through the middle of the wire was observed. Two-peak structure of BLS lines due to the presence of zones with high density of states in the spectrum of SW resonant modes localized in the nanorods and high asymmetry between Stokes and anti-Stokes lines were observed in BLS spectra obtained from low aspect ratio Ni nanorods [282]. Anisotropy field distribution (AFD) method was implemented to study the effective anisotropy field H_{ani} in an array of FM NWs [283]. FMR measurements along with first order reversal curve (FORC) analysis were performed to explore the anisotropy in $\text{Co}_{94}\text{Fe}_5\text{B}_1$ NW arrays [284]. Two distinct SW modes were observed by FMR studies on CoFeB NWs under the application of transverse magnetic field [285]. Study of spatial profiles of the SW modes in cylindrical NWs by micromagnetic simulations under the application of spin-polarized dc current reveals the existence of edge and uniform modes [286-287].

Chapter 11

In this chapter, our aim is to study the magnetization dynamics in an array of Ni NWs and to explore the origin of the observed SW modes. For this study we choose Ni NW arrays instead of Co NWs as Co has a high magnetocrystalline anisotropy which introduces additional complications in the study as observed in the previous chapter. In contrary, Ni has negligible magnetocrystalline anisotropy and offers a perfect test bed for studying the SW modes in arrays of large aspect ratio NWs.

11.2. Sample preparation

The Ni NWs were prepared by pulsed electrodeposition through commercially available nanoporous anodic alumina (AAO) templates [210] in a way similar to described in Refs. [361-362]. The templates have fixed thickness $l = 50 \mu\text{m}$ and diameter $d = 35 \text{ nm}$. One side of the template was coated with 200 nm thick silver layer by evaporation and it served as the working electrode. A platinum foil was used as the counter electrode and saturated calomel electrode was used as the reference electrode. The detail of the electrodeposition process is described in section 4.3. of chapter 4. The electrolytic solution contains 300 g/l $\text{NiSO}_4 \cdot 6\text{H}_2\text{O}$, 45 g/l $\text{NiCl}_2 \cdot 6\text{H}_2\text{O}$ and 45 g/l H_3BO_3 . The pulse potential of the working electrode was maintained at -1 V (with respect to the reference electrode) with 80% duty cycle and pulse period of 1s [361].

11.3. Measurement of quasistatic and ultrafast magnetization dynamics

The easy axis and magnetocrystalline anisotropy of the NWs embedded inside the templates and lying vertically on the substrate plane were studied by vibrating sample magnetometry (VSM; Lakeshore model 7407) at room temperature. The magnetic field up to 16 kOe is applied in steps of 50 Oe in two different orientations during the measurements – 1) parallel to the long axes of the NWs and 2) perpendicular to the long axes of the NWs.

Chapter 11

The magnetization dynamics of the array of Ni NWs was measured by a home-built all optical time-resolved magneto-optical Kerr effect (TR-MOKE) microscope as described in detail in section 4.5.2. of chapter 4. The samples were pumped by 400 nm laser pulses (pulse width = 100 fs, repetition rate = 80 MHz, spot size = 1 μm) of about 16 mJ/cm^2 fluence and the magnetization dynamics was probed by 800 nm laser pulses (pulse width = 70 fs, repetition rate = 80 MHz, spot size = 800 nm) of about 2 mJ/cm^2 fluence. The bias field (H) was tilted at $\sim 15^\circ$ from the normal to the sample. The Kerr signal was measured with a balanced photo-diode detector. The Kerr ellipticity of Ni is larger than Kerr rotation. Hence, it is convenient to measure the Kerr ellipticity as it will give higher signal to noise ratio. From section 2.11. of chapter 2, we see that the Kerr rotation is the real part while the Kerr ellipticity is the imaginary part of the complex Kerr rotation. Now, if we introduce a quarter wave plate in the path of the probe beam in front of the optical bridge detector, it will introduce a $\pi/2$ phase shift. As a result, the Kerr rotation and ellipticity will be interchanged. Hence, by measuring the ($A - B$) signal from the optical bridge detector as a function of the time-delay between the pump and the probe beams, we, actually, measure the time-resolved Kerr ellipticity when a quarter wave plate is placed in front of the detector.

11.4. Results and discussions

From the VSM results, as presented in Fig. 11.1(a), we observe that the long-axis is the easy axis of magnetization. To check if there is any magnetocrystalline anisotropy present, hysteresis loops are measured in different direction normal to the wire axis as shown by black arrows in Fig. 11.1(b). Two typical short-axis loops are presented in Fig. 11.1(a). The loops are identical implying the presence of zero or negligible magnetocrystalline anisotropy in the NW array. During the dynamical measurements, the bias field H was tilted to 15° with respect to the wire axis and the geometry is shown in Fig. 11.1(b). The precessional dynamics appears as an oscillatory signal above the slowly decaying part of the time-resolved Kerr ellipticity signal after a fast demagnetization within 400 fs, and a fast remagnetization within 8 ps followed by a slow remagnetization within 500 ps. The

Chapter 11

precessional dynamics is extracted and fast Fourier transform (FFT) was performed to obtain the SW modes of the sample. A typical result showing the ultrafast demagnetization from the Ni NW array with individual wire diameter $d = 35$ nm at $H = 1.5$ kOe is shown in Fig. 11.1(c).

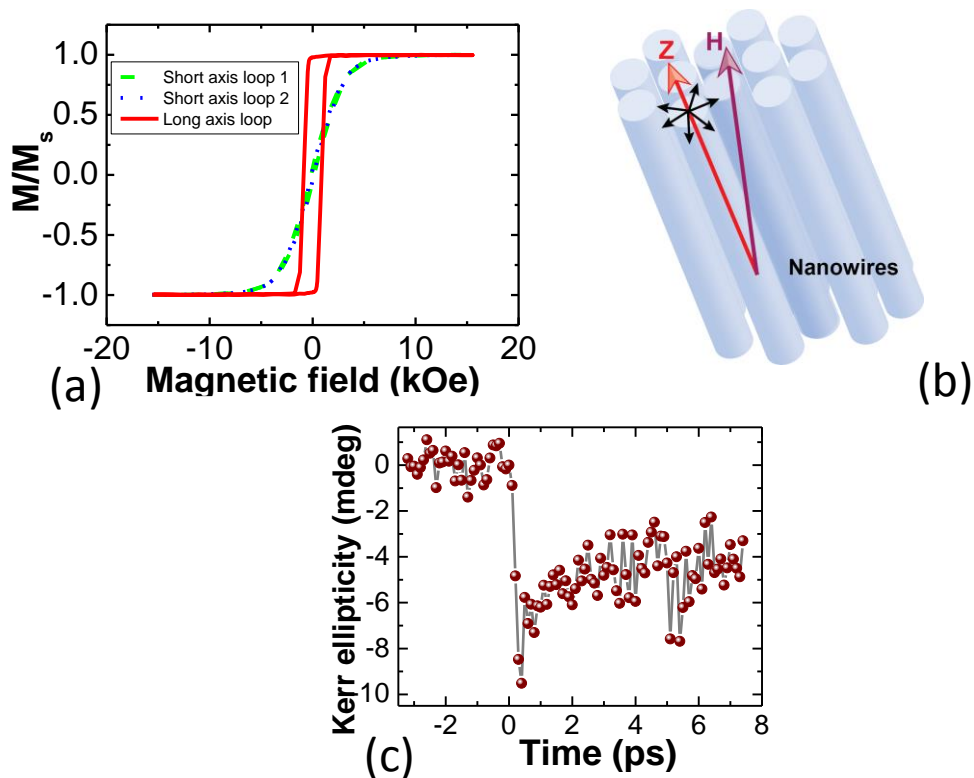


Fig. 11.1: (a) Hysteresis loops for the Ni nanowire (NW) array along the long and two typical short axes directions. (b) Schematic showing the NW array. The wire axis is along the Z axis and the black arrows show different directions along which the short-axis loops were measured. The direction of the applied bias field H during the TR-MOKE measurements is also shown. (c) Typical time-resolved Kerr ellipticity data from the sample showing ultrafast demagnetization and fast remagnetization at $H = 1.5$ kOe.

The bias field dependence of the precessional frequency is investigated and the results are shown in Fig. 11.2(a)-(b). Rich SW spectra are obtained for all bias field values. Down to $H = 0.7$ kOe, four distinct modes are observed. However, as H is reduced below 0.7 kOe, mode 1 and mode 2 can still be identified clearly whereas modes 3 and 4 are not discernible and instead a broad peak appears. The frequencies of all these modes decrease with decreasing

Chapter 11

H. To understand the origin of these modes, we performed extensive 3-D micromagnetic simulations.

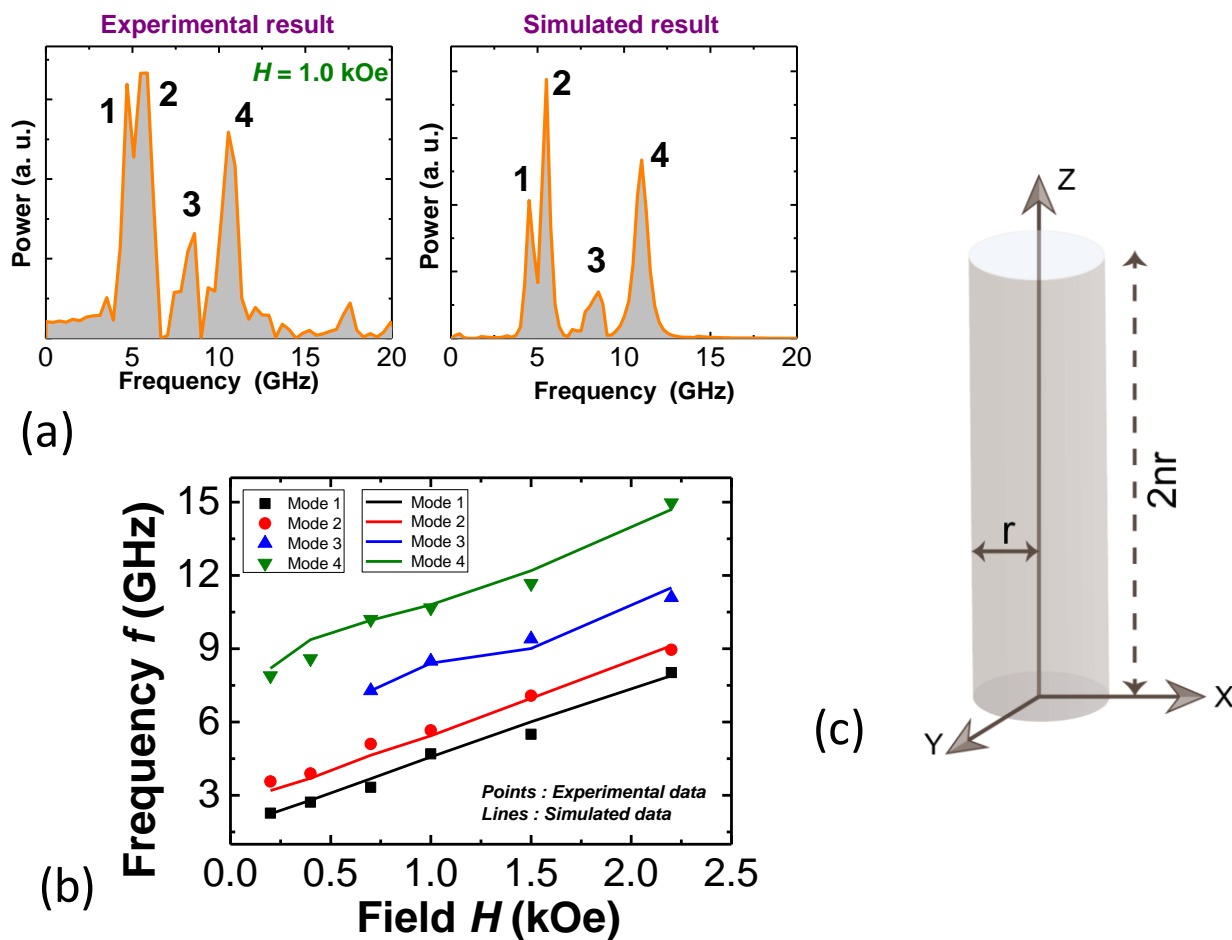


Fig. 11.2: (a) Typical experimental and simulated spin-wave (SW) spectra for NWs with $d = 35$ nm at $H = 1.0$ kOe. (b) Dependence of the experimental (points) and simulated (lines) SW modes on the bias field H . (c) A right circular cylinder of radius r and length $2nr$.

The simulations are performed by the OOMMF software [205] as described in section 3.4. of chapter 3 using typical material parameters for Ni: $4\pi M_s = 6.034$ kOe with M_s as the saturation magnetization, exchange stiffness constant $A = 9 \times 10^{-7}$ erg/cm, magnetocrystalline anisotropy $K = 0$ as obtained from the VSM measurements and gyromagnetic ratio $\gamma = 17.6$ MHz/Oe. Shape anisotropy is already included in the calculation of the demagnetizing field of the system. The simulations are performed on a hexagonal array of NWs. Initially, the cell size was chosen as $5 \times 5 \times 500$ nm³ which implied that the

Chapter 11

exchange interaction along the Z axis, *i.e.*, the wire axis is neglected. The simulated spectra could not reproduce the multimode spectra in this case.

To investigate the possible reasons for this disagreement, it was suspected that, in the simulation, the exchange interaction along the Z-direction was not considered and this may influence the SW spectra. To confirm, the simulations are reperformed for a single NW with a cell size of $5 \times 5 \times 5 \text{ nm}^3$ to include the exchange interaction along the wire axis, which shows a multimode spectrum. However, the length of the measured sample is $50 \text{ }\mu\text{m}$ and it is beyond our computational resource to discretize the Z axis in 5 nm cells if an array of NWs is considered.

The possible solution is to reduce the length (also the aspect ratio) of the NWs without sacrificing the shape anisotropy of the NWs. The NWs, under investigation, are of very high aspect ratio. If we reduce the length of NWs to say, $1 \text{ }\mu\text{m}$ while maintaining the aspect ratio, then the diameter reduces to 0.7 nm . Reducing the diameter to such a small value may give erroneous results in the simulations.

To overcome this difficulty, we made one approximation. We reduced the length to $1 \text{ }\mu\text{m}$ from $50 \text{ }\mu\text{m}$ keeping the diameter unchanged. In the following we calculate the change in the shape anisotropy field due to this approximation by calculating the difference in the corresponding demagnetizing factors.

For a finite right cylinder of aspect ratio n , as shown in Fig. 11.2(c), the expressions for demagnetizing factors are [363]:

$$N_x = N_y = \frac{\frac{2n}{\sqrt{\pi}}}{\left[\frac{2 \times 2n}{\sqrt{\pi}} + 1\right]} \quad (11.1)$$

and

$$N_z = \frac{1}{\left[\frac{2 \times 2n}{\sqrt{\pi}} + 1\right]} \quad (11.2)$$

Chapter 11

Where N_x , N_y and N_z are the demagnetizing factors in the directions of the X, Y and Z axes respectively with

$$N_x + N_y + N_z = 1 \quad (11.3)$$

Calculations for demagnetizing factors for sample under study:

When the bias field is applied along Z axis and the perturbation is along X axis, from Kittel formula as described in section 2.9. of chapter 2, we have the expression for the resonance frequency [144]:

$$f = \frac{\gamma}{2\pi} \sqrt{[H_z + (N_y - N_z)M_S][H_z + (N_x - N_z)M_S]} \quad (11.4)$$

Where H_z is the bias field and M_S is the saturation magnetization.

Below we calculate the $N_x - N_z$ values for our sample.

Calculations for the demagnetizing factors for a nanowire with $2r = 35$ nm and $l = 50$ μ m:

For $l = 50$ μ m, $n = 1428.57$

From eqns (11.1) and (11.2), we get:

$$N_{x1} = N_{y1} = 0.4998$$

$$N_{z1} = 0.0003$$

$$N_{x1} - N_{z1} = N_{y1} - N_{z1} = 0.4995 \quad (11.5)$$

Calculations for the demagnetizing factors for a nanowire with $2r = 35$ nm and $l = 1$ μ m:

For $l = 1$ μ m, $n = 28.57$

From eqns (11.1) and (11.2), we get:

$$N_{x2} = N_{y2} = 0.4924$$

$$N_{z2} = 0.0153$$

$$N_{x2} - N_{z2} = N_{y2} - N_{z2} = 0.4771 \quad (11.6)$$

Chapter 11

The difference:

Hence, comparing eqns (11.5) and (11.6), we see that the difference in the contributions from the demagnetizing factors is only $\approx 4.5\%$ and we can safely use this approximation to analyze our results under micromagnetic simulations.

Fig. 11.2(a)-(b) show the new simulated results along with the experimental results for various bias fields for NW array with $d = 35$ nm. By simulations, we can fairly reproduce the experimental modes at similar frequencies, although the relative mode intensities are not exactly reproduced.

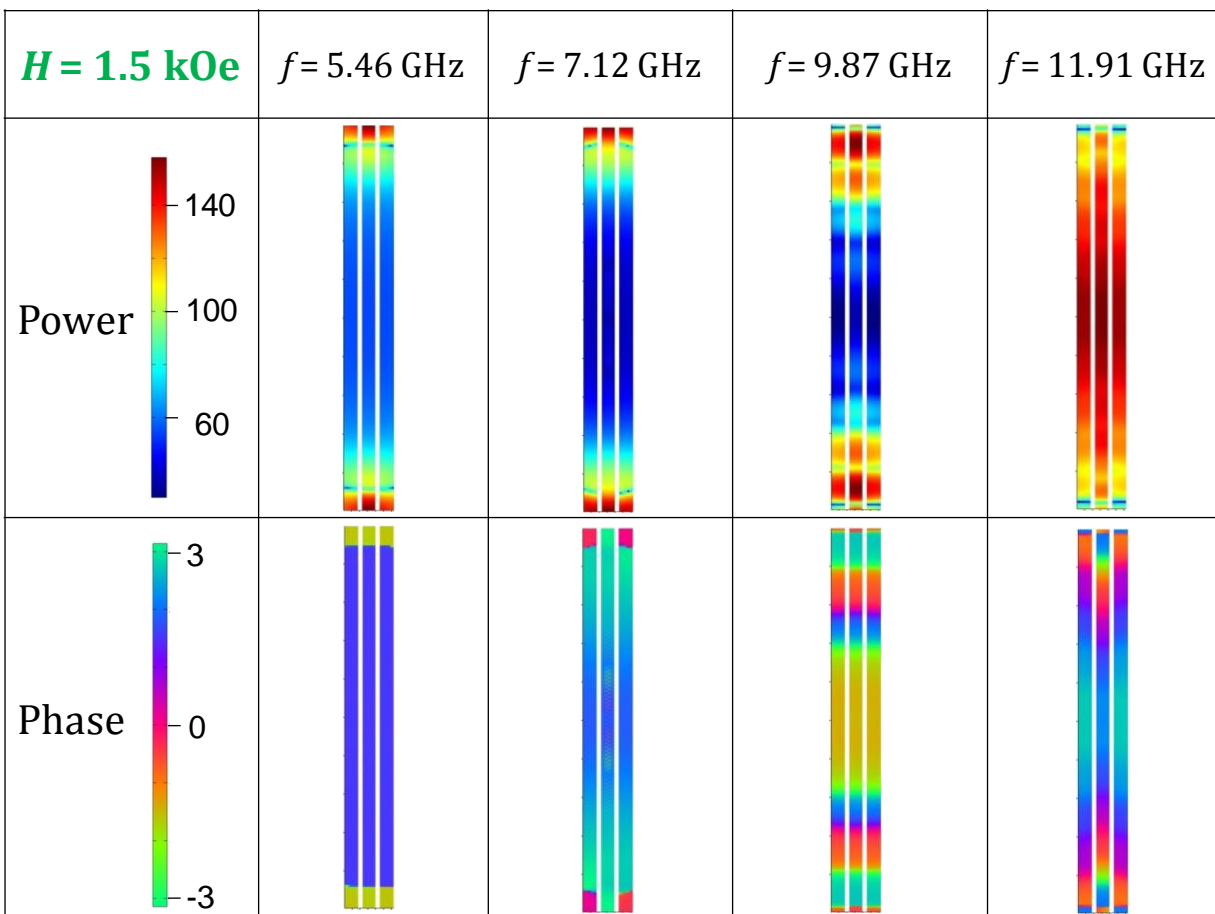


Fig. 11.3: Power and phase distributions of different modes with the view plane in Z vs. X-Y plane for $H = 1.5$ kOe. The color scales for power and phase distributions are shown in the first column of the table.

Chapter 11

The spatial profiles of the amplitude and phases of the modes were investigated by numerically calculating [201-202] the spatial distributions of the amplitudes and phases corresponding to the SW modes. The results for $H = 1.5$ kOe (with the view plane in Z vs X-Y plane) are presented in Fig. 11.3. The lowest frequency mode, *i.e.*, mode1 is primarily the edge mode of the NWs. The spins are in phase at the edges whereas the spins in the central part are 180° out-of-phase. Mode 2 is of same nature as of mode 1 but it penetrates a little deeper into the wires than mode 1. The nature of mode 3, on the other hand, is completely different. It basically forms a standing wave pattern at the ends of the NWs although the pattern does not reach the middle of the wire.

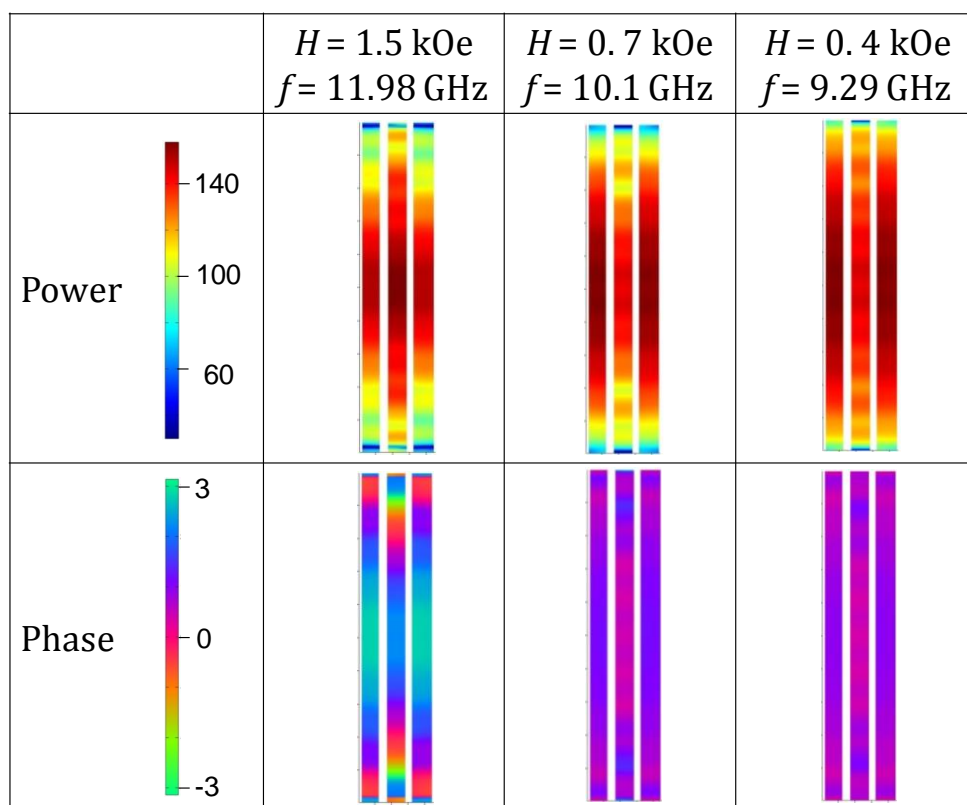


Fig. 11.4: Power and phase distributions of the highest frequency mode for different bias field values. The color scales for power and phase distributions are shown in the first column of the table.

However, mode 4 varies significantly with H . For $H \geq 0.7$ kOe, it shows a uniform precession at the central parts of the NWs with standing wave formation at the ends. As H decreases,

Chapter 11

modes 4 and 3 become very close and they eventually merge together to form a single mode with standing wave formation over the entire NW (Fig. 11.4).

11.5. Conclusions

In summary, we have excited and measured SWs in high aspect ratio Ni NWs by an all optical time-resolved magneto-optical Kerr effect microscopy. An ultrafast demagnetization within 400fs is observed. The bias field dependence of the SW modes are investigated and rich SW spectra are observed for all bias field values. The experimental results are modeled numerically by micromagnetic simulations and the results are reasonably reproduced. The mode origins are investigated. Presence of four distinct SW modes – two edge modes, a standing wave mode and a uniform mode is observed at high bias field values. However, with decreasing bias field, the number of modes reduces to three. It is found that by tuning the bias field amplitude, an overlap between the standing wave mode and the uniform mode can be accomplished.

12. Summary and future perspective

12.1. Summary

In this thesis, we have investigated the quasistatic and ultrafast magnetization processes of magnetic materials with high magnetic anisotropy at different time-scales. The samples are prepared by different techniques including ultra high vacuum magnetron sputtering, focused ion beam lithography and electrodeposition. The initial characterizations of the samples are done by the X-ray diffraction (XRD), scanning electron microscopy (SEM) and energy dispersive X-ray (EDX) spectroscopy techniques. The interface roughness and thickness of individual layer in the multilayers are studied by X-ray reflectivity (XRR) technique. The static magnetic properties are measured by the vibrating sample magnetometer (VSM) and static magneto-optical Kerr effect (static MOKE) magnetometer. The time domain magnetization dynamics in the femtosecond to nanosecond time-scales are measured by a home-built time-resolved magneto-optical Kerr effect (TR-MOKE) microscope. The experimental results are modeled by the solution of the Landau-Lifshitz-Gilbert (LLG) equation under the frameworks of the macrospin formalism, discrete dipole approximation method, plane wave method and micromagnetic simulations.

We have studied the ultrafast magnetization dynamics of $[\text{Co}(t_{\text{Co}}\text{nm})/\text{Pd}(0.9\text{nm})]_8$ multilayers (MLs) with varying Co layer thickness t_{Co} . The XRR measurement confirms that the interface roughness is about 0.05 nm. The magnetic origin of the observed modes is confirmed by the bias field (H) dependence of the precession frequency. For all samples studied here, a collective precession of the whole stack is observed so that the variations of the precession frequency with bias field and damping coefficient α are analyzed by the solution of the LLG equation under macrospin model. Due to the sharp increase in PMA with the decrease in t_{Co} , a broadly tunable precession frequency is observed. It is found that α is inversely proportional to t_{Co} over the entire range. We plot K_{eff} and M_s as a function of t_{Co} , as extracted from the macrospin modeling of the dynamics along with the saturation magnetization (M_s) values as obtained from the static measurements. The values of α obtained for $[\text{Co}(t_{\text{Co}}\text{nm})/\text{Pd}(0.9\text{nm})]_8$ MLs in this experiment are much lower than the

Chapter 12

previously published works. Analysis for the reasons for the enhancement of α over its bulk value shows that magnon-magnon scattering is not responsible as for perpendicularly magnetized samples it is less effective. The other possibility is the roughness and alloying effects at the interface. However, while interface roughness and alloying would increase α , it would also decrease K_{eff} , which contradicts our observation and hence this possibility is also ruled out. So, the enhancement of α is possibly due to spin pumping and the $d-d$ hybridization at the Co/Pd interfaces as both effects are inversely proportional to $1/t_{Co}$. However, only the later is directly correlated to the enhancement of K_{eff} due to the decrease in bandwidth W of the Co atomic layer at the interface, while the former has no contribution to K_{eff} . Hence, we believe that in our case the enhancement of α is caused primarily due to the $d-d$ hybridization effect at the Co/Pd interface.

The study of dipole-exchange spin-wave (SW) spectra in a series of CoO capped $[\text{Co}(t_{Co})/\text{Pt}(0.7 \text{ nm})]_{n-1} \text{Co}(t_{Co})$ MLs with varying t_{Co} and n show large amplitude precession for the initial one or two cycles of oscillation followed by a heavy decay and an incoherent small amplitude oscillation. This indicates the presence of a number of SW modes, as revealed by the fast Fourier transform (FFT) spectra. The SW spectra are also calculated by numerically solving linearized Landau-Lifshitz equation under the discrete dipole approximation (DDA) method. The analysis is limited only to the standing waves formed across the ML. The magnetostatic, exchange and uniaxial anisotropy fields are included in calculations. We found good qualitative agreement with experimental FFT spectrum. In order to separate the first mode from the frequency band we had to assume different anisotropy values at the external surfaces of the ML. It is a reasonable assumption because the electronic configuration of the two surface Pt layers that have only Co atoms on one side differs from the electronic configuration of Pt planes inside the ML that have Co atoms on both sides. This difference in symmetry with respect to the outermost Pt planes explains the different anisotropy constant values assumed for these surface layers. Both low frequency surface waves and higher frequency bulk SW modes are observed in the samples. It is also found that the presence of different external surface layers (*i.e.*, CoO at the top and Pt at the bottom surfaces) affects the SW spectra significantly by offering

Chapter 12

different anisotropy values. For Co layer thickness lesser than the thickness of one monolayer of Co, cluster formations at the interfaces are found to influence SW spectra.

As we fabricate antidot lattices (ADLs) of fixed diameter (d) and with different edge to edge separation (s) on the $[\text{Co}(0.75\text{nm})/\text{Pd}(0.9\text{nm})]_8$ ML, the SW spectra becomes considerably different from that of the unpatterned ML. The spectra consist of single intense peak for ADLs with lattice constant $a (= d+s) > 300$ nm and additional higher frequency peaks for $a \leq 300$ nm. The frequency of the single intense peak for $a = 500$ nm is higher than that of the continuous ML. It systematically decreases with the decrease in a and goes well below that of the continuous ML. In contrary the line width of this mode increases with the decrease in a . The observed SW modes are modeled by the plane wave method (PWM), in which the sample is considered as ADL homogeneous across the thickness. To reproduce experimental data we considered that the ADL consists of two materials: 1) with the bulk properties of the continuous Co/Pd ML with effective parameters extracted from the Kittel fit to the bias field dependence of frequency of the continuous ML and 2) created in the thin shells around the antidots due to modification of the regular Co/Pd structure by Ga ion bombardment during the fabrication. Calculations show that there are two families of lines: one with increasing frequency with increasing a , and the second with decreasing frequency with increasing a . Based on the spatial profiles of SW modes, we can identify these families as the modes localized in the shells and bulk modes of the ADL, respectively. These interesting results can be attributed to the increase of areal density of the shells and to the increase of interactions between localized modes. For small a , the shell modes get coupled through the barrier and decrease the coupled mode frequency. We propose and discuss the possible mechanisms for this coupling - which can be exchange interaction, tunneling or dipolar interaction.

For $\text{Fe}_{55}\text{Pt}_{45}/\text{Ni}_{80}\text{Fe}_{20}$ exchange spring (ES) magnets also a broadly tunable SW spectra is achieved by simply controlling the thickness of the $\text{Ni}_{80}\text{Fe}_{20}$ layer. The spin-twist structure introduced in the $\text{Ni}_{80}\text{Fe}_{20}$ layer due to the exchange coupling with the $\text{Fe}_{55}\text{Pt}_{45}$ layer modifies the SW modes significantly in the composite system as opposed to the bare $\text{Ni}_{80}\text{Fe}_{20}$ films of same thickness. To understand the origin of the modes, we extracted the dynamics locally from different regions of the simulated samples. From micromagnetic

Chapter 12

simulations, it is found that for thinner samples, the magnetization dynamics is primarily governed by the formation of stripe domain. However, with increasing thickness of the Ni₈₀Fe₂₀ layer, the effect of the spin-twist structure within this layer comes into play. As the thickness of Ni₈₀Fe₂₀ increases further, the effect of the spin-twist structure in determining the mode profile decreases.

In Co nanowires (NWs) of different aspect ratios (R), we have observed a cross-over of magnetic easy and hard axes due to the competition between shape and magnetocrystalline anisotropies. We have also studied various magnetization reversal modes associated with the cross-over. At the cross-over, the reversal occurs via the formation of Bloch domains along the length of the nanowires for both short and long axes loops. For NWs with higher R , for the field applied along the long-axis, the reversal occurs through quasi-coherent rotation of magnetization while for the field applied along the short-axis, reversal occurs by the nucleation and propagation of the reversed domains. For R below the cross-over, for the field applied along the long-axis, the reversal occurs again via the formation of Bloch domains but a corkscrew like mode is observed while for the field applied along the short-axis, a quasi-coherent rotation of magnetization is observed.

We have also studied the ultrafast magnetization dynamics in Ni NWs. The bias field dependence of the SW modes is studied. For $H \geq 0.7$ kOe, four modes appear in the spectra which reduce to three modes for H below 0.7 kOe. Frequencies of all modes decrease systematically with decreasing H . The experimental modes are reproduced by micromagnetic simulations. Calculation of spatial profiles of the modes shows that the two lower frequency modes are edge modes while the third mode shows standing wave patterns near the ends of the NWs. However, the highest frequency mode varies significantly with H . For $H \geq 0.7$ kOe, it shows a uniform precession at the central parts of the NWs with standing wave formation at the ends. As H decreases, the third and fourth modes become very close and they eventually merge together to form a single mode with standing wave formation over the entire NW.

12.2. Future perspectives

We have already discussed the importance of magnetic materials with high anisotropy in present and future technologies and investigated some of the important static and dynamical properties of such materials. However, there are still lots to be explored.

Consideration of future prospects starts with the time-resolved magneto-optical Kerr effect (TR-MOKE) magnetometer itself. The set up is combined with a scanning facility along with its very high spatio-temporal resolution. The spatial map of the magnetization at a particular instant can be experimentally obtained by this scanning programme. This may even provide information on spatial uniformity of damping behavior. The set up can even be extended to perform all-optical pump-probe measurements at low temperatures and to study how temperature dependent anisotropy plays a role in determining the SW dynamics.

Study and control of damping and anisotropy constants are now a crucial problem. It has been shown that damping constant, anisotropy and SW spectra can be tuned by tuning the thickness of the ferromagnetic (FM) layer and the number of repeats in a ML. These can be further manipulated by using a graded thickness for the FM layers in a ML. The graded thickness introduces graded anisotropy in the system which affects the static properties. This will also affect the dynamic properties and may give rise to some novel properties. Patterning these MLs to form dot (antidot) lattice structures can also be very interesting in terms of manipulation of propagation velocity and band structures of SWs, its damping and the anisotropy in SW propagation. With the change in Co layer thickness, the magnetic parameters will be modified and influence the SW dynamics. To add another degree of freedom, one can even fabricate dot (antidot) of different shapes. Different shapes give rise to different stray (internal) field distributions and complicated inter-element interactions. Specific shapes introduce specific symmetries in the sample which is an efficient tool to control the SW band structure. Arrangement of these dots (antidots) over different lattice structures (for example: square, triangular hexagonal etc.) is another effective way to influence the stray (internal) fields and corresponding inter-element interactions.

Chapter 12

In the case of the ES magnets, one can play with the soft and hard magnetic materials to manipulate the spin-twist structure, which will in turn affect the magnetization dynamics. In future, patterning may be done in ES magnets also to have finer control on the magnetization dynamics. Other possibility of manipulation of magnetization dynamics involves the study of FM nanowires (NWs) with varying aspect ratio. Especially, FM NWs having high magnetocrystalline anisotropy can offer rich SW modes in the system due to the interplay between magnetocrystalline anisotropy, shape anisotropy and dipolar energies. The study of magnetization dynamics in FM NWs can be further extended for multilayer (ML) NWs. In case of ML NWs, each individual wire has a periodic structure. This periodicity will influence the propagation of SWs. This becomes more complicated for an array of NWs as the periodicity of individual wires varies within the same specimen and will result in the variation of magnetic parameters.

In summary an extensive area of investigation of magnetization dynamics over various time-scales and length-scales in various tailored magnetic materials remained unexplored and will be subject of future investigation both from fundamental interest as well as applications in spin based technologies.

Bibliography

- [1] B. D. Terris and T. Thomson, "Nanofabricated and Self-assembled Magnetic Structures as Data Storage Media," *J. Phys. D: Appl. Phys.* **38**, R199 (2005).
- [2] S. A. Wolf, D. D. Awschalom, R. A. Buhrman, J. M. Daughton, S. von Molnár, M. L. Roukes, A. Y. Chtchelkanova, and D. M. Treger, "Spintronics: A Spin-Based Electronics Vision for the Future," *Science* **294**, 1488 (2001).
- [3] S. Neusser and D. Grundler, "Magnonics: Spin Waves on the Nanoscale," *Adv. Mater.* **21**, 2927 (2009).
- [4] E. N. Abarra, A. Inomata, H. Sato, I. Okamoto, and Y. Mizoshita, "Longitudinal Magnetic Recording Media with Thermal Stabilization Layers," *Appl. Phys. Lett.* **77**, 2581 (2000).
- [5] E. E. Fullerton, D. T. Margulies, M. E. Schabes, M. Carey, B. Gurney, A. Moser, M. Best, G. Zeltzer, K. Rubin, H. Rosen, and M. Doerner, "Antiferromagnetically Coupled Magnetic Media Layers for Thermally Stable High-density Recording," *Appl. Phys. Lett.* **77**, 3806 (2000).
- [6] S. Pal, S. Saha, D. Polley, and A. Barman, "Magnetization Reversal Dynamics in Co Nanowires with Competing Magnetic Anisotropies," *Solid State Commun.* **151**, 1994 (2011).
- [7] S.-I. Iwasaki, "Discoveries that Guided the Beginning of Perpendicular Magnetic Recording," *J. Magn. Magn. Mater.* **235**, 227 (2001).
- [8] A. Moser, K. Takano, D. T. Margulies, M. Albrecht, Y. Sonobe, Y. Ikeda, S. Sun, and E. E. Fullerton, "Magnetic Recording: Advancing into the Future," *J. Phys. D: Appl. Phys.* **35**, R157 (2002).
- [9] T. Yogi, T. A. Nguyen, S. E. Lambert, G. L. Gorman, and G. Castillo, "Role of Atomic Mobility in the Transition Noise of Longitudinal Media," *IEEE Trans. Magn.* **26**, 1578 (1990).
- [10] H. Hata, T. Hyohno, T. Fukuichi, K. Yabushita, M. Umesaki, and H. Shibata, "Magnetic and Recording Characteristics of Multilayer CoNiCr Thin Film Media," *IEEE Trans. Magn.* **26**, 2709 (1990).
- [11] E. S. Murdock, B. R. Natarajan, and R. G. Walmsley, "Noise Properties of Multilayered Co-Alloy Magnetic Recording Media," *IEEE Trans. Magn.* **26**, 2700 (1990).
- [12] Y. C. Feng, D. E. Laughlin, and D. N. Lambeth, "Magnetic Properties and Crystallography of Double-Layer CoCrTa Thin Films with Various Interlayers," *IEEE Trans. Magn.* **30**, 3960 (1994).
- [13] Hitachi Global Storage Technology, A Western Digital Company. Available: <http://www.hgst.com>

Bibliography

- [14] T. Thomson, G. Hu, and B. D. Terris, "*Intrinsic Distribution of Magnetic Anisotropy in Thin Films Probed by Patterned Nanostructures*," Phys. Rev. Lett. **96**, 257204 (2006).
- [15] L. Néel, "*Anisotropie Magnétique Superficielle et Surstructures D'orientation*," J. Phys. Radium **15**, 225 (1954).
- [16] P. F. Carcia and A. Suna, "*Structural, Magnetic and Electric Properties of Thin Film Pd/Co Layered Structures*," J. Superlattices and Microstruct. **1**, 101 (1985).
- [17] P. F. Carcia, A. D. Meinhardt, and A. Suna, "*Perpendicular Magnetic Anisotropy in Pd/Co Thin Film Layerd Structures*," Appl. Phys. Lett. **47**, 178 (1985).
- [18] K. Kobayashi and G. Ishida, "*Magnetic and Structural Properties of Rh Substituted CoCr Alloy Films with Perpendicular Magnetic Anisotropy*," J. Appl. Phys. **52**, 2453 (1981).
- [19] H. J. G. Draaisma, W. J. M. d. Jonge, and F. J. A. d. Broeder, "*Magnetic Interface Anisotropy in Pd/Co and Pd/Fe Multilayers*," J. Magn. Magn. Mater. **66**, 351 (1987).
- [20] N. Nakajima, T. Koide, T. Shidara, H. Miyauchi, H. Fukutani, A. Fujimori, K. Iio, T. Katayama, M. Nývlt, and Y. Suzuki, "*Perpendicular Magnetic Anisotropy Caused by Interfacial Hybridization via Enhanced Orbital Moment in Co/Pt Multilayers: Magnetic Circular X-Ray Dichroism Study*," Phys. Rev. Lett. **81**, 5229 (1998).
- [21] S. Choe and S. Shin, "*Magnetization Reversal in Nanostructured Co/Pd Multilayers*," Phys. Rev. B **57**, 1085 (1998).
- [22] C. H. Back and H. C. Siegmann, "*Ultrashort Magnetic Field Pulses and the Elementary Process of Magnetization Reversal*," J. Magn. Magn. Mater. **200**, 774 (1999).
- [23] O. Hellwig, S. Maat, J. B. Kortright, and E. E. Fullerton, "*Magnetic Reversal of Perpendicular-biased Co/Pt Multilayers*," Phys. Rev. B **65**, 144418 (2002).
- [24] P. Grünberg, R. Schreiber, Y. Pang, M. B. Brodsky, and H. Sowers, "*Layered Magnetic Structures: Evidence for Antiferromagnetic Coupling of Fe Layers across Cr Interlayers*," Phys. Rev. Lett. **57**, 2442 (1986).
- [25] M. N. Baibich, J. M. Broto, A. Fert, F. N. Van Dau, F. Petroff, P. Etienne, G. Creuzet, A. Friederich, and J. Chazelas, "*Giant Magnetoresistance of (001)Fe/(001)Cr Magnetic Superlattices*," Phys. Rev. Lett. **61**, 2472 (1988).
- [26] G. Binasch, P. Grünberg, F. Saurenbach, and W. Zinn, "*Enhanced Magnetoresistance in Layered Magnetic Structures with Antiferromagnetic Interlayer Exchange*," Phys. Rev. B **39**, 4828 (1989).
- [27] M. Julliere, "*Tunneling Between Ferromagnetic Films*," Phys. Lett. **54A**, 225 (1975).

Bibliography

- [28] D. Wang, C. Nordman, J. M. Daughton, Z. Qian, and J. Fink, "70% TMR at Room Temperature for SDT Sandwich Junctions With CoFeB as Free and Reference Layers," *IEEE Trans. Magn.* **40**, 2269 (2004).
- [29] T. R. McGuire and R. I. Potter, "Anisotropic Magnetoresistance in Ferromagnetic 3d Alloys " *IEEE Trans. Magn.* **11**, 1018 (1975).
- [30] W. Thomson, "On the Electro-Dynamic Qualities of Metals: Effects of Magnatization on the Electric Conductivity of Nickel and Iron," *Proc. Roy. Soc.* **8**, 546 (1857).
- [31] F. Lesmes, A. Salcedo, J. J. Freijo, D. Garcia, A. Hernando, and C. Prados, "Influence of the Interfaces on the Anisotropic Magnetoresistance of Ni/Co Multilayers," *Appl. Phys. Lett.* **69**, 2596 (1996).
- [32] J. M. Gallego, D. Lederman, T. J. Moran, and I. K. Schuller "Large Magnetoresistance with Low Saturation Fields in Magnetic/Magnetic Superlattices," *Appl. Phys. Lett.* **64**, 2590 (1994).
- [33] C. Prados, D. García, F. Lesmes, J. J. Freijo, and A. Hernando, "Extraordinary Anisotropic Magnetoresistance Effect under 35 Oe Field at Room Temperature in Co/Ni Multilayers," *Appl. Phys. Lett.* **67**, 718 (1995).
- [34] X. M. Cheng, S. Urazhdin, O. Tchernyshyov, and C. L. Chien, "Antisymmetric Magnetoresistance in Magnetic Multilayers with Perpendicular Anisotropy," *Phys. Rev. Lett.* **94**, 017203 (2005).
- [35] R. Mandal, S. Saha, D. Kumar, S. Barman, S. Pal, K. Das, A. K. Raychaudhury, Y. Fukuma, Y. Otani, and A. Barman, "Optically Induced Tunable Magnetization Dynamics in Nanoscale Co Antidot Lattices," *ACS Nano* **6**, 3397 (2012).
- [36] J.-G. Zhu and Y. Tang, "A Medium Microstructure for High Area Density Perpendicular Recording," *J. Appl. Phys.* **99**, 08Q903 (2006).
- [37] D. Suess, J. Fidler, K. Porath, T. Schrefl, and D. Weller, "Micromagnetic Study of Pinning Behavior in Percolated Media," *J. Appl. Phys.* **99**, 08CG905 (2006).
- [38] D. E. Laughlin, Y. Peng, Y. Qin, M. Lin, and J. Zhu, "Fabrication, Microstructure, Magnetic, and Recording Properties of Percolated Perpendicular Media," *IEEE Trans. Magn.* **43**, 693 (2007).
- [39] A. Sun, J. Hsu, P. Kuo, and H. Huang, "Magnetic Properties of Percolated Perpendicular FePt-MgO Films," *IEEE Trans. Magn.* **43**, 2130 (2007).
- [40] M. T. Rahman, N. N. Shams, Y. Wu, C. Lai, and D. Suess, "Magnetic Multilayers on Porous Anodized Alumina for Percolated Perpendicular Media," *Appl. Phys. Lett.* **91**, 132505 (2007).

Bibliography

- [41] M. T. Rahman, N. N. Shams, C. H. Lai, J. Fidler, and D. Suess, "*Co/Pt Perpendicular Antidot Arrays with Engineered Feature Size and Magnetic Properties Fabricated on Anodic Aluminum Oxide Templates*," *Phys. Rev. B* **81**, 014418 (2010).
- [42] D. Makarov, E. Bermúdez-Ureña, O. G. Schmidt, F. Liscio, M. Maret, C. Brombacher, S. Schulze, M. Hietschold, and M. Albrecht, "*Nanopatterned CoPt Alloys with Perpendicular Magnetic Anisotropy*," *Appl. Phys. Lett.* **93**, 153112 (2008).
- [43] A. Fisher, M. Kuemmel, M. Järn, M. Linden, C. Boissière, L. Nicole, C. Sanchez, and D. Grosso, "*Surface Nanopatterning by Organic/Inorganic Self-assembly and Selective Local Functionalization*," *Small* **2**, 569 (2006).
- [44] M. Grobis, C. Schulze, M. Faustini, D. Grosso, O. Hellwig, D. Makarov, and M. Albrecht, "*Recording Study of Percolated Perpendicular Media*," *Appl. Phys. Lett.* **98**, 192504 (2011).
- [45] S. Oikawa, T. Onitsuka, A. Takeo, and M. Takagishi, "*Flat Surface Percolated Perpendicular Media with Metal Pinning Sites*" *IEEE Trans. Magn.* **48**, 3192 (2012).
- [46] Y. Tang and J. Zhu, "*Micromagnetics of Percolated Perpendicular Medium for 1 Tb/in² and Beyond*," *IEEE Trans. Magn.* **42**, 2360 (2006).
- [47] Y. Tang and J. Zhu, "*Domain Wall Pinning and Corresponding Energy Barrier in Percolated Perpendicular Medium*," *IEEE Trans. Magn.* **43**, 2139 (2007).
- [48] S. N. Piramanayagam, M. Ranjbar, H. K. Tan, W. C. Allen Poh, R. Sbiaa, and T. C. Chong, "*Magnetic Properties of Antiferromagnetically Coupled Antidots of Co/Pd Multilayers*," *J. Appl. Phys.* **111**, 07B916 (2012).
- [49] E. F. Kneller and R. Hawig, "*The Exchange-spring Magnet: A New Material Principle for Permanent Magnets*," *IEEE Trans. Magn.* **27**, 3588 (1991).
- [50] A. Scholl, M. Liberati, E. Arenholz, H. Ohldag, and J. Stöhr, "*Creation of an Antiferromagnetic Exchange Spring*," *Phys. Rev. Lett.* **92**, 247201 (2004).
- [51] Y. Y. Wang, C. Song, B. Cui, G. Y. Wang, F. Zeng, and F. Pan, "*Room-temperature Perpendicular Exchange Coupling and Tunneling Anisotropic Magnetoresistance in an Antiferromagnet-based Tunnel Junction*," *Phys. Rev. Lett.* **109**, 137201 (2012).
- [52] T. Ando and T. Nishihara, "*Triple-Layer Perpendicular Recording Media for High SN Ratio and Signal Stability*," *IEEE Trans. Magn.* **33**, 2983 (1997).
- [53] G. Asti, M. Ghidini, R. Pellicelli, C. Pernechele, and M. Solzi, "*Magnetic Phase Diagram and Demagnetization Processes in Perpendicular Exchange-Spring Multilayers*," *Phys. Rev. B* **73**, 094406 (2006).

Bibliography

- [54] K. V. O'Donovan, J. A. Borchers, C. F. Majkrzak, O. Hellwig, and E. E. Fullerton, "*Pinpointing Chiral Structures with Front-Back Polarized Neutron Reflectometry*," Phys. Rev. Lett. **88**, 067201 (2002).
- [55] N. d. Sousa, A. Apolinario, F. Vernay, P. M. S. Monteiro, F. Albertini, F. Casoli, H. Kachkachi, and D. S. Schmool, "*Spin Configurations in Hard/Soft Coupled Bilayer Systems: Transitions From Rigid Magnet to Exchange-spring*," Phys. Rev. B **82**, 104433 (2010).
- [56] R. Röhlsberger, H. Thomas, K. Schlage, E. Burkel, O. Leupold, and R. Rüffer, "*Imaging the Magnetic Spin Structure of Exchange-Coupled Thin Films*," Phys. Rev. B **89**, 237201 (2002).
- [57] E. E. Fullerton, J. S. Jiang, M. Grimsditch, C. H. Sowers, and S. D. Bader, "*Exchange-spring Behavior in Epitaxial Hard/Soft Magnetic Bilayers*," Phys. Rev. B **58**, 12193 (1998).
- [58] S. N. Gordeev, J. M. L. Beaujour, G. J. Bowden, B. D. Rainford, P. A. J. d. Groot, R. C. C. Ward, M. R. Wells, and A. G. M. Jensen, "*Giant Magnetoresistance by Exchange Springs in DyFe₂/YFe₂ Superlattices*," Phys. Rev. Lett. **87**, 186808 (2001).
- [59] O. Hellwig, J. B. Kortright, K. Takano, and E. E. Fullerton, "*Switching Behavior of Fe-Pt/Ni-Fe Exchange-spring Films Studied by Resonant Soft-X-ray Magneto-optical Kerr Effect*," Phys. Rev. B **62**, 11694 (2000).
- [60] H. Hou, D. Suess, J. Liao, M. Lin, H. Lin, F. Chang, and C. Lai, "*Direct Probing Magnetization Reversal of Exchange-coupled-composite Media by X-Ray Magnetic Circular Dichroism*," Appl. Phys. Lett. **98**, 262507 (2011).
- [61] T. J. Fal, K. L. Livesey, and R. E. Camley, "*Domain Wall and Microwave assisted Switching in an Exchange Spring Bilayer*," J. Appl. Phys. **109**, 093911 (2011).
- [62] G. B. G. Stenning, A. R. Buckingham, G. J. Bowden, R. C. C. Ward, G. v. d. Laan, L. R. Shelford, F. Maccherozzi, S. S. Dhesi, and P. A. J. d. Groot, "*Exchange-spring Driven Spin Flop in an ErFe₂/YFe₂ Multilayer Studied by X-Ray Magnetic Circular Dichroism*," Phys. Rev. B **84**, 104428 (2011).
- [63] Y. Choi, J. S. Jiang, J. E. Pearson, S. D. Bader, J. J. Kavich, J. W. Freeland, and J. P. Liu, "*Controlled Interface Profile in Sm-Co/Fe Exchange-spring Magnets*," Appl. Phys. Lett. **91**, 072509 (2007).
- [64] L. S. Huang, J. F. Hu, and J. S. Chen, "*Critical Fe Thickness for Effective Coercivity Reduction in FePt/Fe Exchange-coupled Bilayer*," J. Magn. Magn. Mater. **324**, 1242 (2012).
- [65] M. Carbucicchio and R. Ciprian, "*Influence of the Phenomena Occurring at the Soft/Hard Interface on the Coercivity Behavior in Exchange-spring Magnets*," Solid State commun. **152**, 189 (2012).

Bibliography

- [66] J. L. Costa-Krämer, "Conductance Quantization at Room Temperature in Magnetic and Nonmagnetic Metallic Nanowires," *Phys. Rev. B* **55**, R4875 (1997).
- [67] C. Beeli, B. Doudin, and P. Stadelmann, "Flux Quantization in Magnetic Nanowires Imaged by Electron Holography," *Phys. Rev. Lett.* **75**, 4630 (1995).
- [68] K. Liu, K. Nagodawithana, P. C. Searson, and C. L. Chien, "Perpendicular Giant Magnetoresistance of Multilayered Co/Cu Nanowires," *Phys. Rev. B* **51**, 7381 (1995).
- [69] D. J. Sellmyer, M. Zheng, and R. Skomski, "Magnetism of Fe, Co and Ni Nanowires in Self-assembled Arrays," *J. Phys.: Condens. Matter.* **13**, R433 (2001).
- [70] X. Y. Zhang, G. H. Wen, Y. F. Chan, R. K. Zheng, X. X. Zhang, and N. Wang, "Fabrication and Magnetic Properties of Ultrathin Fe Nanowire Arrays," *Appl. Phys. Lett.* **83**, 3341 (2003).
- [71] H. Zeng, R. Skomski, L. Menon, Y. Liu, S. Bandyopadhyay, and D. J. Sellmyer, "Structure and Magnetic Properties of Ferromagnetic Nanowires in Self-assembled Arrays," *Phys. Rev. B* **65**, 134426 (2002).
- [72] W. Wernsdorfer, E. B. Orozco, K. Hasselbach, A. Benoit, B. Barbara, N. Demoncy, A. Loiseau, H. Pascard, and D. Maily, "Experimental Evidence of the Néel-Brown Model of Magnetization Reversal," *Phys. Rev. Lett.* **78**, 1791 (1997).
- [73] W. Wernsdorfer, K. Hasselbach, A. Benoit, B. Barbara, B. Doudin, J. Meier, J. P. Ansermet, and D. Maily, "Measurements of Magnetization Switching in Individual Nickel Nanowires," *Phys. Rev. B* **55**, 11552 (1997).
- [74] W. Wernsdorfer, B. Doudin, D. Maily, K. Hasselbach, A. Benoit, J. Meier, J. P. Ansermet, and B. Barbara, "Nucleation of Magnetization Reversal in Individual Nanosized Nickel Wires," *Phys. Rev. Lett.* **77**, 1873 (1996).
- [75] R. Ferré, K. Ounadjela, J. M. George, L. Piraux, and S. Dubois, "Magnetization Processes in Nickel and Cobalt Electrodeposited Nanowires," *Phys. Rev. B* **56**, 14066 (1997).
- [76] P. M. Paulus, F. Luis, M. Kröll, G. Schmid, and L. J. de Jongh, "Low-temperature Study of the Magnetization Reversal and Magnetic Anisotropy of Fe, Ni, and Co Nanowires," *J. Magn. Magn. Mater.* **224**, 180 (2001).
- [77] M. Lederman, S. Schultz, and M. Ozaki, "Measurement of the Dynamics of the Magnetization Reversal in Individual Single-domain Ferromagnetic Particles," *Phys. Rev. Lett.* **73**, 1986 (1994).
- [78] A. D. Kent, S. v. Molnár, S. Gider, and D. D. Awschalom, "Properties and Measurement of Scanning Tunneling Microscope Fabricated Ferromagnetic Particle Arrays (invited)," *J. Appl. Phys.* **76**, 6656 (1994).

Bibliography

- [79] S. Wirth, M. Field, D. D. Awschalom, and S. von Molnár, "Magnetization Behavior of Nanometer-scale Iron Particles," *Phys. Rev. B* **57**, R14028 (1998).
- [80] H.-B. Braun, "Thermally Activated Magnetization Reversal in Elongated Ferromagnetic Particles," *Phys. Rev. Lett.* **71**, 3557 (1993).
- [81] H.-B. Braun, "Nucleation in Ferromagnetic Nanowires—Magnetostatics and Topology," *J. Appl. Phys.* **85**, 6172 (1999).
- [82] T. G. Sorop, C. Untiedt, F. Luis, M. Kröll, M. Raşa, and L. J. de Jongh, "Magnetization Reversal of Ferromagnetic Nanowires Studied by Magnetic Force Microscopy," *Phys. Rev. B* **67**, 014402 (2003).
- [83] C. A. Ross, M. Hwang, M. Shima, J. Y. Cheng, M. Farhoud, T. A. Savas, H. I. Smith, W. Schwarzacher, F. M. Ross, M. Redjald, and F. B. Humphrey, "Micromagnetic Behavior of Electrodeposited Cylinder Arrays," *Phys. Rev. B* **65**, 144417 (2002).
- [84] F. J. Himpsel, J. E. Ortega, G. J. Mankey, and R. F. Willis, "Magnetic Nanostructures," *Adv. Phys.* **47**, 511 (1998).
- [85] C. B. Roxlo, H. W. Deckman, J. Gland, S. D. Cameron, and R. R. Chianelli, "Edge Surfaces in Lithographically Textured Molybdenum Disulfide," *Science* **235**, 1629 (1987).
- [86] A. Sugawara, D. Streblichenko, M. McCartney, and M. R. Scheinfein, "Magnetic Coupling in Self-organized Narrow-spaced Fe Nanowire Arrays," *IEEE Trans. Magn.* **34**, 1081 (1998).
- [87] A. Fert and L. Piraux, "Magnetic Nanowires," *J. Magn. Magn. Mater.* **200**, 338 (1999).
- [88] B. Heinrich and J. A. C. Bland, "Ultrathin Magnetic Structures II," Springer, Berlin (1994).
- [89] M. Bailleul, D. Olligs, and C. Fermon, "Micromagnetic Phase Transitions and Spin Wave Excitations in a Ferromagnetic Stripe," *Phys. Rev. Lett.* **91**, 137204 (2003).
- [90] V. P. Denysenkov and A. M. Grishin, "Broadband Ferromagnetic Resonance Spectrometer," *Rev. Sci. Instrum.* **74**, 3400 (2003).
- [91] S. Tamaru, J. A. Bain, R. J. M. van de Veerdonk, T. M. Crawford, M. Covington, and M. H. Kryder, "Imaging of Quantized Magnetostatic Modes using Spatially Resolved Ferromagnetic Resonance," *J. Appl. Phys.* **91**, 8034 (2002).
- [92] J. V. Harzer, B. Hillebrands, R. L. Stamps, G. Güntherodt, D. Weller, C. Lee, R. F. C. Farror, and E. E. Marinero, "Characterization of Large Magnetic Anisotropies in (100)- and (111)-Oriented Co/Pt Multilayers by Brillouin Light Scattering," *J. Magn. Magn. Mater.* **104**, 1863 (1992).
- [93] A. Barman and A. Haldar, "Time-domain Study of Magnetization Dynamics in Magnetic Thin Films and Micro- and Nanostructures," in *Solid State Phys.* **65**, 108 Academic Press (2014).

Bibliography

- [94] W. K. Hiebert, A. Stankiewicz, and M. R. Freeman, "*Direct Observation of Magnetic Relaxation in a Small Permalloy Disk by Time-resolved Scanning Kerr Microscopy*," Phys. Rev. Lett. **79**, 1134 (1997).
- [95] Y. Acremann, C. H. Back, M. Buess, O. Portmann, A. Vaterlaus, D. Pescia, and H. Melchior, "*Imaging Precessional Motion of the Magnetization Vector*," Science **290**, 492 (2000).
- [96] A. Barman, V. V. Kruglyak, R. J. Hicken, A. Kundrotaite, and M. Rahman, "*Anisotropy, Damping, and Coherence of Magnetization Dynamics in a 10 mm Square Ni₈₁Fe₁₉ Element*," Appl. Phys. Lett. **82**, 3065 (2003).
- [97] I. N. Krivorotov, N. C. Emley, J. C. Sankey, S. I. Kiselev, D. C. Ralph, and R. A. Buhrman, "*Time-domain Measurements of Nanomagnet Dynamics Driven by Spin-Transfer Torques*," Science **307**, 228 (2005).
- [98] Y. Acremann, J. P. Strachan, V. Chembrolu, S. D. Andrews, T. Tyliczszak, J. A. Katine, M. J. Carey, B. M. Clemens, H. C. Siegmann, and J. Stöhr, "*Time-resolved Imaging of Spin Transfer Switching: Beyond the Macrospin Concept*," Phys. Rev. Lett. **96**, 217202 (2006).
- [99] P. Weiss, "*L'hypothèse du Champ Moléculaire et la Propriété Ferromagnétique*," J. Phys. Theor. Appl. **6**, 661 (1907).
- [100] A. H. Morrish, "*The Physical Principles of Magnetism*," IEEE Press, New York, United States (2001).
- [101] W. Heisenberg, "*Zur Theorie des Ferromagnetismus*," Z. f. Phys. **49**, (1928).
- [102] J. Dorfman, "*The Intrinsic Fields in Ferromagnetic Substances*" Nat. **119**, 353 (1928).
- [103] J. Frenkel, "*Elementare Theorie Magnetischer und Elektrischer Eigenschaften der Metalle beim Absoluten Nullpunkt der Temperatur*," Z. f. Phys. **49**, 31 (1928).
- [104] P. Bruno, "*Physical Origins and Theoretical Models of Magnetic Anisotropy*," Jürich (1993).
- [105] H. J. F. Jansen, "*Magnetic Anisotropy in Density-Functional Theory*," Phys. Rev. B **38**, 8022 (1988).
- [106] L. Zhong, M. Kim, X. Wang, and A. J. Freeman, "*Overlayer-induced Anomalous Interface Magnetocrystalline Anisotropy in Ultrathin Co Films*," Phys. Rev. B **53**, 9770 (1996).
- [107] N. Nakajima, T. Koide, T. Shidara, H. Miyauchi, H. Fukutani, A. Fujimori, K. Iio, T. Katayama, M. Nývlt, and Y. Suzuki, "*Perpendicular Magnetic Anisotropy Caused by Interfacial Hybridization via Enhanced Orbital Moment in Co/Pt Multilayers: Magnetic Circular X-Ray Dichroism Study*," Phys. Rev. Lett. **81**, 5229 (1998).
- [108] D.-S. Wang, R. Wu, and A. J. Freeman, "*Magnetocrystalline Anisotropy of Co-Pd Interfaces*," Phys. Rev. B **48**, 15886 (1993).

Bibliography

- [109] B. N. Engel, M. H. Wiedmann, R. A. Van Leeuwen, and C. M. Falco, "*Anomalous Magnetic Anisotropy in Ultrathin Transition Metals*," Phys. Rev. B **48**, 9894 (1993).
- [110] W. H. Meiklejohn and C. P. Bean, "*New Magnetic Anisotropy*," Phys. Rev. **102**, 1413 (1956).
- [111] J. Nogués and I. K. Schuller, "*Exchange Bias*," J. Magn. Magn. Mater. **192**, (1999).
- [112] C. Kittel, "*Theory of the Structure of Ferromagnetic Domains in Films and Small Particles*," Phys. Rev. **70**, 965 (1946).
- [113] E. C. Stoner and E. P. Wohlfarth, "*A Mechanism of Magnetic Hysteresis in Heterogeneous Alloys*," Phil. Trans. R. Soc. Lond. A. **240**, 599 (1948).
- [114] E. H. Frei, S. Shtrikman, and D. Treves, "*Critical Size and Nucleation Field of Ideal Ferromagnetic Particles*," Phys. Rev. **106**, 446 (1957).
- [115] C. Kittel, "*Physical Theory of Ferromagnetic Domains*," Rev. Mod. Phys. **21**, 541 (1949).
- [116] R. Hertel and J. Kirschner, "*Magnetization Reversal Dynamics in Nickel Nanowires*," Physica B: Cond. Matter **343**, 206 (2004).
- [117] R. Hertel, "*Micromagnetic Simulations of Magnetostatically Coupled Nickel Nanowires*," J. Appl. Phys. **90**, 5752 (2001).
- [118] R. Skomski, "*Nanomagnetics*," J. Phys.: Condens. Matter **15**, R841 (2003).
- [119] M. van Kampen, C. Jozsa, J. T. Kohlhepp, P. LeClair, L. Lagae, W. J. M. de Jonge, and B. Koopmans, "*All-Optical Probe of Coherent Spin Waves*," Phys. Rev. Lett. **88**, 227201 (2002).
- [120] E. Beaurepaire, J. C. Merle, A. Daunois, and J. Y. Bigot, "*Ultrafast Spin Dynamics in Ferromagnetic Nickel*," Phys. Rev. Lett. **76**, 4250 (1996).
- [121] R. Knorren, K. H. Bennemann, R. Burgermeister, and M. Aeschlimann, "*Dynamics of Excited Electrons in Copper and Ferromagnetic Transition Metals: Theory and Experiment*," Phys. Rev. B **61**, 9427 (2000).
- [122] G. P. Zhang and W. Hübner, "*Laser-induced Ultrafast Demagnetization in Ferromagnetic Metals*," Phys. Rev. Lett. **85**, 3025 (2000).
- [123] E. Beaurepaire, G. M. Turner, S. M. Harrel, M. C. Beard, J.-Y. Bigot, and C. A. Schmuttenmaer, "*Coherent Terahertz Emission from Ferromagnetic Films Excited by Femtosecond Laser Pulses*," Appl. Phys. Lett. **84**, 3465 (2004).
- [124] B. Koopmans, J. J. M. Ruigrok, F. D. Longa, and W. J. M. d. Jonge, "*Unifying Ultrafast Magnetization Dynamics*," Phys. Rev. Lett. **95**, 267207 (2005).
- [125] B. Koopmans, G. Malinowski, F. Dalla Longa, D. Steiauf, M. Fahnle, T. Roth, M. Cinchetti, and M. Aeschlimann, "*Explaining the Paradoxical Diversity of Ultrafast Laser-induced Demagnetization*," Nat. Mater. **9**, 259 (2010).

Bibliography

- [126] A. Laraoui, V. Halté, M. Vomir, J. Vénuat, M. Albrecht, E. Beaurepaire, and J.-Y. Bigot, "Ultrafast Spin Dynamics of an Individual CoPt_3 Ferromagnetic Dot," *Eur. Phys. J. D* **43**, 251 (2007).
- [127] A. Laraoui, J. Venuat, V. Halte, M. Albrecht, E. Beaurepaire, and J.-Y. Bigot, "Study of Individual Ferromagnetic Disks With Femtosecond Optical Pulses," *J. Appl. Phys.* **101**, 09C105 (2007).
- [128] J. Miltat, G. Albuquerque, and A. Thiaville, "An Introduction to Micromagnetics in the Dynamic Regime," in *Spin Dynamics in Confined Magnetic Structures I*, Springer (2002).
- [129] A. T. J. Miltat and G. Albuquerque, "Spin dynamics in confined magnetic structures I," Springer, Berlin, Heidelberg (2002).
- [130] M. D. Kaufmann, "Magnetization Dynamics in All-optical Pump-probe Experiments: Spin-wave Modes and Spin-current Damping," Ph.D Thesis, Georg-August-Universität, Göttingen, Germany, 2006.
- [131] L. D. Landau and E. M. Lifshitz, "On the Theory of the Dispersion of Magnetic Permeability in Ferromagnetic Bodies," *Phys. Zs. der Sowjetunion* **8**, 153 (1935).
- [132] T. L. Gilbert, "A Lagrangian Formulation of the Gyromagnetic Equation of the Magnetic Field," *Phys. Rev.* **100**, 1243 (1955).
- [133] T. L. Gilbert, "A Phenomenological Theory of Damping in Ferromagnetic Materials," *IEEE Trans. Magn.* **40**, 3443 (2004).
- [134] S. I. Anisimov, B. L. Kapeliovich, and T. L. Perel'man, "Electron Emission from Metal Surface Exposed to Ultrashort Laser Pulses," *Zh. Eksp. Teor. Fiz.* **66**, 776 (1974).
- [135] G. P. Zhang and W. Hübner, "Laser-induced Ultrafast Demagnetization in Ferromagnetic Metals," *Phys. Rev. Lett.* **85**, 3025 (2000).
- [136] B. Koopmans, J. J. M. Ruigrok, F. D. Longa, and W. J. M. de Jonge, "Unifying Ultrafast Magnetization Dynamics," *Phys. Rev. Lett.* **95**, 267207 (2005).
- [137] M. Krauß, T. Roth, S. Alebrand, D. Steil, M. Cinchetti, M. Aeschlimann, and H. C. Schneider, "Ultrafast Demagnetization of Ferromagnetic Transition Metals: The Role of the Coulomb Interaction," *Phys. Rev. B* **80**, 180407 (2009).
- [138] J.-Y. Bigot, M. Vomir, and E. Beaurepaire, "Coherent Ultrafast Magnetism Induced by Femtosecond Laser Pulses," *Nat. Phys.* **5**, 515 (2009).
- [139] G. Lefkidis, G. P. Zhang, and W. Hübner, "Angular Momentum Conservation for Coherently Manipulated Spin Polarization in Photoexcited NiO: An Ab Initio Calculation," *Phys. Rev. Lett.* **103**, 217401 (2009).

Bibliography

- [140] G. P. Zhang, W. Hubner, G. Lefkidis, Y. Bai, and T. F. George, "*Paradigm of the Time-Resolved Magneto-Optical Kerr Effect for Femtosecond Magnetism*," Nat. Phys. **5**, 499 (2009).
- [141] G. Malinowski, F. Dalla Longa, J. H. H. Rietjens, P. V. Paluskar, R. Huijink, H. J. M. Swagten, and B. Koopmans, "*Control of Speed and Efficiency of Ultrafast Demagnetization by Direct Transfer of Spin Angular Momentum*," Nat. Phys. **4**, 855 (2008).
- [142] M. Battiato, K. Carva, and P. M. Oppeneer, "*Superdiffusive Spin Transport as a Mechanism of Ultrafast Demagnetization*," Phys. Rev. Lett. **105**, 027203 (2010).
- [143] J. Griffiths, "*Anomalous High-frequency Resistance of Ferromagnetic Metals*," Nat. **158**, 670 (1946).
- [144] C. Kittel, "*On the Theory of Ferromagnetic Resonance Absorption*," Phys. Rev. **73**, 155 (1948).
- [145] C. Kittel, "*Interpretation of Anomalous Larmor Frequencies in Ferromagnetic Resonance Experiment*," Phys. Rev. **71**, 270 (1947).
- [146] A. Gurevich and G. Melkov, "*Magnetization Oscillations and Waves*," CRC Press, (1996).
- [147] F. Bloch, "*Zur Theorie des Ferromagnetismus*," Z. Physik **61**, 206 (1930).
- [148] C. Herring and C. Kittel, "*On the Theory of Spin Waves in Ferromagnetic Media*," Phys. Rev. **81**, 869 (1951).
- [149] M. Sparks, "*Ferromagnetic Relaxation Theory*," McGraw-Hill, New York (1964).
- [150] T. Holstein and H. Primakoff, "*Field Dependence of the Intrinsic Domain Magnetization of a Ferromagnet*," Phys. Rev. **58**, 1098 (1940).
- [151] L. R. Walker, "*Magnetostatic Modes in Ferromagnetic Resonance*," Phys. Rev. **105**, 390 (1957).
- [152] C. Patton, "*Magnetic Excitations in Solids*," Phys. Rep. **103**, 251 (1984).
- [153] R. W. Damon and J. R. Eshbach, "*Magnetostatic modes of a ferromagnet slab*," J. Phys. Chem. Solids **19**, 308 (1961).
- [154] J. R. Eshbach and R. W. Damon, "*Surface Magnetostatic Modes and Surface Spin Waves*," Phys. Rev. **118**, 1208 (1960).
- [155] S. O. Demokritov, B. Hillebrands, and A. N. Slavin, "*Brillouin Light Scattering Studies of Confined Spin Waves: Linear and Nonlinear Confinement*," Phys. Rep. **348**, 441 (2001).
- [156] B. Hillebrands and J. Hamrle, "*Investigation of Spin Waves and Spin Dynamics by Optical Techniques*," in Handbook of Magnetism and Advanced Magnetic Materials. **3**, Wiley-Interscience (2007).
- [157] M. Faraday, Diary **4**, 7504 (1845).

Bibliography

- [158] J. Kerr, "*On Rotation of the Plane of Polarization by Reflection from the Pole of a Magnet*," Philos. Mag. Series 5 **3**, 321 (1877).
- [159] A. Kundt, "*On the Electromagnetic Rotation of the Plane of Polarization of Light by means of Iron, Cobalt, and Nickel*," Philo. Mag. Series 5 **18**, 308 (1884).
- [160] A. Barman, T. Kimura, Y. Otani, Y. Fukuma, K. Akahane, and S. Meguro, "*Benchmark Time-Resolved Magneto-Optical Kerr Magnetometer*," Rev. Sci. Instrum. **79**, 123905 (2008).
- [161] Z. Qiu and S. Bader, "*Surface Magneto-optic Kerr Effect*," Rev. Sci. Instrum. **71**, 1243 (2000).
- [162] P. N. Argyres, "*Theory of the Faraday and Kerr Effects in Ferromagnetics*," Phys. Rev. **97**, 334 (1955).
- [163] R. P. Hunt, "*Magneto-Optic Scattering from Thin Solid Films*," J. Appl. Phys. **38**, 1652 (1967).
- [164] C.-Y. You and S.-C. Shin, "*Generalized Analytic Formulae for Magneto-Optical Kerr Effects*," J. Appl. Phys. **84**, 541 (1998).
- [165] M. Freiser, "*A Survey of Magneto-optic Effects*," IEEE Trans. Magn. **MAG-4**, 152 (1968).
- [166] T. McDaniel and R. Victora, "*Handbook of Magneto-Optical Data Recording: Materials, Subsystems, Techniques*," Elsevier, (1995).
- [167] Z. Qiu and S. Bader, "*Surface Magneto-optic Kerr Effect (SMOKE)*," J. Magn. Magn. Mater. **200**, 664 (1999).
- [168] P. Bruno, Y. Suzuki, and C. Chappert, "*Magneto-optical Kerr Effect in a Paramagnetic Overlayer on a Ferromagnetic Substrate: A Spin-polarized Quantum Size Effect*," Phys. Rev. B **53**, 9214 (1996).
- [169] H. S. Bennett and E. A. Stern, "*Faraday Effect in Solids*," Phys. Rev. **137**, A448 (1965).
- [170] R. Kubo, "*A General Expression for the Conductivity Tensor*," Can. J. Phys. **34**, 1274 (1956).
- [171] A. Aharoni, "*Local Demagnetization in a Rectangular Ferromagnetic Prism*," Phys. Status Solidi B **229**, 1413 (2002).
- [172] A. Aharoni, L. Pust, and M. Kief, "*Comparing Theoretical Demagnetizing Factors with the Observed Saturation Process in Rectangular Shields*," J. Appl. Phys. **87**, 6564 (2000).
- [173] C. D. Graham and B. E. Lorenz, "*Experimental Demagnetizing Factors for Disk Samples Magnetized along a Diameter*," IEEE Trans. Magn. **43**, 2743 (2007).
- [174] J. Jorzick, S. O. Demokritov, B. Hillebrands, M. Bailleul, C. Fermon, K. Y. Guslienko, A. N. Slavin, D. V. Berkov, and N. L. Gorn, "*Spin Wave Wells in Nonellipsoidal Micrometer Size Magnetic Elements*," Phys. Rev. Lett. **88**, 047204 (2002).

Bibliography

- [175] Y. Obukhov, D. V. Pelekhov, J. Kim, P. Banerjee, I. Martin, E. Nazaretski, R. Movshovich, S. An, T. J. Gramila, S. Batra, and P. C. Hammel, "*Local Ferromagnetic Resonance Imaging with Magnetic Resonance Force Microscopy*," Phys. Rev. Lett. **100**, 197601 (2008).
- [176] M. Pardavi-Horvath, J. Yan, and J. R. Peverley, "*Nonuniform Internal Field in Planar Ferrite Elements*," IEEE Trans. Magn. **37**, 3881 (2001).
- [177] A. V. Farahani and A. Konrad, "*An Iterative Method to Obtain Nonuniform Field Distribution in Magnetic Substrates*," IEEE Trans. Magn. **41**, 3316 (2005).
- [178] M. Beleggia and M. De Graef, "*On the Computation of the Demagnetization Tensor Field for an Arbitrary Particle Shape using a Fourier Space Approach*," J. Magn. Magn. Mater. **263**, L1 (2003).
- [179] S. Tandon, M. Beleggia, Y. Zhu, and M. De Graef, "*On the Computation of the Demagnetization Tensor for Uniformly Magnetized Particles of Arbitrary Shape. Part II: Numerical Approach*," J. Magn. Magn. Mater. **271**, 27 (2004).
- [180] V. V. Kruglyak, P. S. Keatley, R. J. Hicken, J. R. Childress, and J. A. Katine, "*Time Resolved Studies of Edge Modes in Magnetic Nanoelements (Invited)*," J. Appl. Phys. **99**, 08F306 (2006).
- [181] H. Puzskarski, M. Krawczyk, and J.-C. S. Lévy, "*Purely Dipolar versus Dipolar-exchange Modes in Cylindrical Nanorods*," J. Appl. Phys. **101**, 024326 (2007).
- [182] M. Krawczyk and H. Puzskarski, "*Theory of Comb and Bulk-dead Magnetostatic Modes in Elongated Nanorods*," in Nanostructures and their Magnetic Properties, Research Signpost (2008).
- [183] M. Krawczyk and H. Puzskarski, "*The Effect of Cross-sectional Geometry and Size on Magnetostatic Modes in Nanorods*," J. Appl. Phys. **104**, 113920 (2008).
- [184] L. Landau and E. Lifshitz, "*The Classical Theory of Fields*," Oxford: Pergamon Press, (1975).
- [185] M. Krawczyk and H. Puzskarski, "*Plane-wave Theory of Three-Dimensional Magnonic Crystals*," Phys. Rev. B **77**, 054437 (2008).
- [186] V. Laude, M. Wilm, S. Benchabane, and A. Khelif, "*Full Band Gap for Surface Acoustic Waves in a Piezoelectric Phononic Crystal*," Phys. Rev. E **71**, 036607 (2005).
- [187] J. O. Vasseur, P. A. Deymier, B. Djafari-Rouhani, Y. Pennec, and A. C. Hladky-Hennion, "*Absolute Forbidden Bands and Waveguiding in Two-dimensional Phononic Crystal Plates*," Phys. Rev. B **77**, 085415 (2008).
- [188] D. W. Prather, S. Shi, A. Sharkawy, J. Murakowski, and G. J. Schneider, "*Photonic Crystals: Theory, Applications, and Fabrication*," Wiley-New York, New York (2009).

Bibliography

- [189] M. Krawczyk, S. Mamica, M. Mruczkiewicz, J. W. Klos, S. Tacchi, M. Madami, G. Gubbiotti, G. Duerr, and D. Grundler, "*Magnonic Band Structures in Two-dimensional Bi-component Magnonic Crystals with In-plane Magnetization*" J. Phys. D: Appl. Phys. **46**, 495003 (2013).
- [190] S.-K. Kim, "*Micromagnetic Computer Simulations of Spin Waves in Nanometre-scale Patterned Magnetic Elements*," J. Phys. D: Appl. Phys. **43**, 264004 (2010).
- [191] B. Rana, S. Pal, S. Barman, Y. Fukuma, Y. Otani, and A. Barman, "*All-Optical Excitation and Detection of Picosecond Dynamics of Ordered Arrays of Nanomagnets with Varying Areal Density*," Appl. Phys. Express **4**, 113003 (2011).
- [192] B. Rana, D. Kumar, S. Barman, S. Pal, Y. Fukuma, Y. Otani, and A. Barman, "*Detection of Picosecond Magnetization Dynamics of 50 nm Magnetic Dots down to the Single Dot Regime*," ACS Nano **5**, 9559-9565 (2011).
- [193] B. Rana, D. Kumar, S. Barman, S. Pal, R. Mandal, Y. Fukuma, Y. Otani, S. Sugimoto, and A. Barman, "*Anisotropy in Collective Precessional Dynamics in Arrays of $Ni_{80}Fe_{20}$ Nanoelements*," J. Appl. Phys. **111**, 07D503 (2012).
- [194] S. Pal, S. Barman, O. Hellwig, and A. Barman, "*Effect of the Spin-twist Structure on the Spin-wave Dynamics of the $Fe_{55}Pt_{45}/Ni_{80}Fe_{20}$ Exchange Coupled Bi-layers with Varying $Ni_{80}Fe_{20}$ Thickness*," J. Appl. Phys. **115**, 17D105 (2014).
- [195] S. Pal, D. Kumar, and A. Barman, "*Micromagnetic Study of Size-dependent Picosecond Dynamics in Single Nanomagnets*," J. Phys. D: Appl. Phys. **44**, 105002 (2011).
- [196] S. Saha, R. Mandal, S. Barman, D. Kumar, B. Rana, Y. Fukuma, S. Sugimoto, Y. Otani, and A. Barman, "*Tunable Magnonic Spectra in Two-Dimensional Magnonic Crystals with Variable Lattice Symmetry*," Adv. Func. Mater. **23**, 2378 (2013).
- [197] B. Rana, M. Agrawal, S. Pal, and A. Barman, "*Magnetization Reversal Dynamics in Clusters of Single Domain Ni Nanoparticles*," J. Appl. Phys. **107**, 09B513 (2010).
- [198] M. Agrawal, B. Rana, and A. Barman, "*Magnetization Reversal in Chains and Clusters of Exchange-Coupled Nickel Nanoparticles*," J. Phys. Chem. C **114**, 11115 (2010).
- [199] D. Kumar, P. Sabareesan, W. Wang, H. Fangohr, and A. Barman, "*Effect of Hole Shape on Spin-wave Band Structure in One-dimensional Magnonic Antidot Waveguide*," J. Appl. Phys. **114**, 023910 (2013).
- [200] B. K. Mahato, B. Rana, R. Mandal, D. Kumar, S. Barman, Y. Fukuma, Y. Otani, and A. Barman, "*Configurational Anisotropic Spin Waves in Cross-shaped $Ni_{80}Fe_{20}$ Nanoelements*," Appl. Phys. Lett. **102**, 192402 (2013).

Bibliography

- [201] D. Kumar, O. Dmytriiev, S. Ponraj, and A. Barman, "Numerical Calculation of Spin Wave Dispersions in Magnetic Nanostructures," J. Phys. D: Appl. Phys. **45**, 015001 (2012).
- [202] G. Venkat, D. Kumar, M. Franchin, O. Dmytriiev, M. Mruczkiewicz, H. Fangohr, A. Barman, M. Krawczyk, and A. Prabhakar, "Proposal for a Standard Micromagnetic Problem: Spin Wave Dispersion in a Magnonic Waveguide," IEEE Trans. Magn. **49**, 524 (2013).
- [203] R. Mandal, P. Laha, K. Das, S. Saha, S. Barman, A. K. Raychaudhuri, and A. Barman, "Effects of Antidot Shape on the Spin Wave Spectra of Two-dimensional $Ni_{80}Fe_{20}$ Antidot Lattices," Appl. Phys. Lett. **103**, 262410 (2013).
- [204] A. Barman and S. Barman, "Dynamic dephasing of magnetization precession in arrays of thin magnetic elements," Phys. Rev. B **79**, 144415 (2009).
- [205] M. Donahue and D. G. Porter, "OOMMF User's guide, Version 1.0,," NIST Interagency Report No. 6376, National Institute of Standard and Technology, Gaithersburg, MD, URL: <http://math.nist.gov/oommf>, (1999).
- [206] M. R. Scheinfein. *LLG Micromagnetics Simulator*. Available: <http://llgmicro.home.mindspring.com/> (1996).
- [207] "Sputtering by Particle Bombardment," Springer, (2007).
- [208] Applied Research Laboratory at the Pennsylvania State University. Available: https://www.arl.psu.edu/mm_mp_ac_sputtering.php
- [209] L. A. Giannuzzi and F. A. Stevie, "A Review of Focused Ion Beam Milling Techniques for TEM Specimen Preparation," Micron **30**, 197 (1999).
- [210] Synkera Technologies Inc. Available: <http://www.synkerainc.com>
- [211] D. McMullan, "Scanning Electron Microscopy 1928–1965," Scanning **17**, 175 (1995).
- [212] M. A. Moram and M. E. Vickers, "X-ray diffraction of III-nitrides," Rep. Prog. Phys. **72**, 036502 (2009).
- [213] S. Foner, "Versatile and Sensitive Vibrating-Sample Magnetometer," Rev. Sci. Instrum. **30**, 548 (1959).
- [214] M. R. Freeman, R. R. Ruf, and R. J. Gambino, "Picosecond pulsed magnetic fields for studies of ultrafast magnetic phenomena," IEEE Trans. Magn. **27**, 4840 (1991).
- [215] A. Barman, V. V. Kruglyak, R. J. Hicken, J. Scott, A. Kundrotaite, and M. Rahman, "Dependence of anisotropy and damping on shape and aspect ratio in micron sized $Ni_{81}Fe_{19}$ elements," J. Appl. Phys. **95**, 6998 (2004).
- [216] A. Barman, S. Wang, and H. Schmidt, "Ultrafast Magnetization Dynamics in High Perpendicular Anisotropy $[Co/Pt]_n$ Multilayers" J. Appl. Phys. **101**, 09D102 (2007).

Bibliography

- [217] B. Rana and A. Barman, "*Magneto-Optical Measurements of Collective Spin Dynamics of Two-Dimensional Arrays of Ferromagnetic Nanoelements*," *SPIN* **3**, 1330001 (2013).
- [218] S. Pal, B. Rana, O. Hellwig, T. Thomson, and A. Barman, "*Tunable Magnonic Frequency and Damping in $[Co/Pd]_8$ Multilayers with Variable Co Layer Thickness*," *Appl. Phys. Lett.* **98**, 082501 (2011).
- [219] S. Pal, B. Rana, S. Saha, R. Mandal, O. Hellwig, J. Romero-Vivas, S. Mamica, J. W. Klos, M. Mruczkiewicz, M. L. Sokolovskyy, M. Krawczyk, and A. Barman, "*Time-resolved Measurement of Spin-wave Spectra in CoO Capped $[Co(t)/Pt(7\text{\AA})]_{n-1} Co(t)$ Multilayer Systems*," *J. Appl. Phys.* **111**, 07C507 (2012).
- [220] A. Laraoui, J. Vénuat, V. Halté, M. Albrecht, E. Beaurepaire, and J.-Y. Bigot, "*Study of Individual Ferromagnetic Disks with Femtosecond Optical Pulses*," *J. Appl. Phys.* **101**, 09C105 (2007).
- [221] A. Barman, S. Wang, J. D. Maas, A. R. Hawkins, S. Kwon, A. Liddle, J. Bokor, and H. Schmidt, "*Magneto-optical Observation of Picosecond Dynamics of Single Nanomagnets*," *Nano Lett.* **6**, 2939 (2006).
- [222] User's Manual, "Tsunami: Mode-locked Ti:sapphire Laser", *Spectra-Physics*, California, USA (2002).
- [223] User's Manual, "Model 3980: Frequency Doubler and Pulse Selector" *Spectra-Physics*, California, USA (2002).
- [224] User's Manual, "Millenia Pro s-Series: Diode-Pumped, CW Visible Laser System", *Spectra-Physics*, California, USA (2007).
- [225] W. T. Silfvast, "*Laser Fundamentals*," Cambridge University Press, (1996).
- [226] O. Svelto, "*Principles of Lasers*," Springer, (2009).
- [227] R. V. Mikhaylovskiy, E. Hendry, and V. V. Kruglyak, "*Negative Permeability due to Exchange Spin-wave Resonances in Thin Magnetic Films with Surface Pinning*," *Phys. Rev. B* **82**, 195446 (2010).
- [228] O. Dmytriiev, U. A. S. Al-Jarah, P. Gangmei, V. V. Kruglyak, R. J. Hicken, B. K. Mahato, B. Rana, M. Agrawal, A. Barman, M. Mátéfi-Tempfli, L. Piraux, and S. Mátéfi-Tempfli, "*Static and Dynamic Magnetic Properties of Densely Packed Magnetic Nanowire Arrays*," *Phys. Rev. B* **87**, 174429 (2013).
- [229] P. Grünberg and K. Mika, "*Magnetostatic Spin-wave Modes of a Ferromagnetic Multilayer*," *Phys. Rev. B* **27**, 2955 (1983).
- [230] R. E. Camley, T. S. Rahman, and D. L. Mills, "*Magnetic Excitations in Layered Media: Spin Waves and the Light-Scattering Spectrum*," *Phys. Rev. B* **27**, 261 (1983).

Bibliography

- [231] B. Hillebrands, A. Boufelfel, C. M. Falco, P. Baumgart, G. Güntherodt, E. Zirngiebl, and J. D. Thompson, "*Brillouin Scattering from Collective Spin Waves in Magnetic Superlattices*," J. Appl. Phys. **63**, 3880 (1988).
- [232] B. Hillebrands, J. V. Harzer, G. Güntherodt, C. D. England, and C. M. Falco, "*Experimental Evidence for the Existence of Exchange-dominated Collective Spin-wave Excitations in Multilayers*," Phys. Rev. B **42**, 6839 (1990).
- [233] Z. Zhang, P. E. Wigen, and S. S. P. Parkin, "*Pt Layer Thickness Dependence of Magnetic Properties in Co/Pt Multilayers*," J. Appl. Phys. **69**, 5649 (1991).
- [234] B. Hillebrands, "*Spin-wave Calculations for Multilayered Structures*," Phys. Rev. B **41**, 530 (1990).
- [235] R. L. Stamps and B. Hillebrands, "*Dipole-exchange Modes in Single Thin Films and Multilayers with Large Out-of-plane Anisotropy*," J. Magn. Magn. Mater. **93**, 616 (1991).
- [236] J. V. Harzer, B. Hillebrands, R. L. Stamps, G. Güntherodt, D. Weller, C. H. Lee, R. F. C. Farrow, and E. E. Marinero, "*Characterization of Large Magnetic Anisotropies in (100)- and (111)-Oriented Co/Pt Multilayers by Brillouin Light Scattering*," J. Magn. Magn. Mater. **104**, 1863 (1992).
- [237] B. Hillebrands, J. V. Harzer, G. Güntherodt, and J. R. Dutcher, "*Study of Co-based Multilayers By Brillouin Light Scattering*," J. Magn. Soc. Jpn. **17**, 17 (1993).
- [238] M. Buchmeier, H. Dassow, D. E. Bürgler, and C. M. Schneider, "*Intensity of Brillouin Light Scattering from Spin Waves in Magnetic Multilayers with Noncollinear Spin Configurations: Theory and Experiment*," Phys. Rev. B **75**, 184436 (2007).
- [239] J. F. Cochran, "*Brillouin Light Scattering from Periodic Multilayers Composed of Very Thin Magnetic Films*," Phys. Rev. B **64**, 134406 (2001).
- [240] P. Vavassoria, M. Grimsditch, E. E. Fullerton, L. Giovanninia, R. Zivieria, and F. Nizzolia, "*Brillouin Light Scattering Study of an Exchange Coupled Asymmetric Trilayer of Fe/Cr*," Surf. Sci. **454**, 880 (2000).
- [241] A. B. Drovosekov, N. M. Kreĭnes, D. I. Kholin, V. F. Meshcheryakov, M. A. Milyaev, L. N. Romashev, and V. V. Ustinov, "*Ferromagnetic Resonance in Multilayer $[Fe/Cr]_n$ Structures with Noncollinear Magnetic Ordering*," JETP Lett. **67**, 727 (1998).
- [242] A. Barman, V. V. Kruglyak, R. J. Hicken, C. H. Marrows, M. Ali, A. T. Hindmarch, and B. J. Hickey, "*Characterization of Spin Valves Fabricated on Opaque Substrates by Optical Ferromagnetic Resonance*," Appl. Phys. Lett. **81**, 1468 (2002).

Bibliography

- [243] H. Salhi, K. Chafai, O. Msieh, H. Lassri, K. Benkirane, M. Abid, L. Bessais, and E. K. Hlil, "*Spin-wave Excitations in Evaporated Co/Pt Multilayers*," J. Supercond. Nov. Magn. **24**, 1375 (2011).
- [244] S. Mizukami, Y. Ando, and T. Miyazaki, "*Effect of Spin Diffusion on Gilbert Damping for a Very Thin Permalloy Layer in Cu/permalloy/Cu/Pt Films*," Phys. Rev. B **66**, 104413 (2002).
- [245] C. H. Back, D. Weller, J. Heidmann, D. Mauri, D. Guarisco, E. L. Garwin, and H. C. Siegmann, "*Magnetization Reversal in Ultrashort Magnetic Field Pulses*," Phys. Rev. Lett. **81**, 3251 (1998).
- [246] M. Belmeguenai, T. Devolder, and C. Chappert, "*Experimental Analysis of the Fast Magnetization Dynamics in High Perpendicular Anisotropy Co/Pt Nanostructures*," J. Magn. Magn. Mater. **307**, 325 (2006).
- [247] A. Lyberatos, "*Switching Speed Limitations in Perpendicular Magnetic Recording Media*," J. Appl. Phys. **93**, 6199 (2003).
- [248] Y. Y. Zou, J. P. Wang, C. H. Hee, and T. C. Chong, "*Tilted Media in a Perpendicular Recording System for High Areal Density Recording*," Appl. Phys. Lett. **82**, 2473 (2003).
- [249] P. J. Metaxas, J. P. Jamet, A. Mougín, M. Cormier, J. Ferre, V. Baltz, B. Rodmacq, B. Dieny, and R. L. Stamps, "*Creep and Flow Regimes of Magnetic Domain-wall Motion in Ultrathin Pt/Co/Pt Films with Perpendicular Anisotropy*," Phys. Rev. Lett. **99**, 217208 (2007).
- [250] S. Mizukami, E. P. Sajitha, D. Watanabe, F. Wu, T. Miyazaki, H. Naganuma, M. Oogane, and Y. Ando, "*Gilbert Damping in Perpendicularly Magnetized Pt/Co/Pt Films Investigated by All-optical Pump-probe Technique*," Appl. Phys. Lett. **96**, 152502 (2010).
- [251] Y. Nozaki, N. Narita, T. Tanaka, and K. Matsuyama, "*Microwave Assisted Magnetization Reversal in Co/Pd Multilayer with Perpendicular Magnetic Anisotropy*," Appl. Phys. Lett. **95**, 082505 (2009).
- [252] E. P. Sajitha, J. Walowski, D. Watanabe, S. Mizukami, F. Wu, H. Naganuma, M. Oogane, Y. Ando, and T. Miyazaki, "*Magnetization Dynamics in CoFeB Buffered Perpendicularly Magnetized Co/Pd Multilayer*," IEEE Trans. Magn. **46**, 2056 (2010).
- [253] G. Malinowski, F. Dalla Longa, J. H. H. Rietjens, P. V. Paluskar, R. Huijink, H. J. M. Swagten, and B. Koopmans, "*Control of Speed and Efficiency of Ultrafast Demagnetization by Direct Transfer of Spin Angular Momentum*," Nat. Phys. **4**, 855 (2008).
- [254] Y. Tserkovnyak, A. Brataas, and G. E. W. Bauer, "*Enhanced Gilbert Damping in Thin Ferromagnetic Films*," Phys. Rev. Lett. **88**, 117601 (2002).

Bibliography

- [255] R. Urban, G. Woltersdorf, and B. Heinrich, "*Gilbert Damping in Single and Multilayer Ultrathin Films: Role of Interfaces in Nonlocal Spin Dynamics*," Phys. Rev. Lett. **87**, 217204 (2001).
- [256] M. V. Costache, M. Sladkov, S. M. Watts, C. H. van der Wal, and B. J. van Wees, "*Electrical Detection of Spin Pumping due to the Precessing Magnetization of a Single Ferromagnet*," Phys. Rev. Lett. **97**, 216603 (2006).
- [257] M. Grimsditch, R. E. Camley, E. E. Fullerton, S. Jiang, S. D. Bader, and C. H. Sowers, "*Exchange-spring Systems: Coupling of Hard and Soft Ferromagnets as Measured by Magnetization and Brillouin Light Scattering*," J. Appl. Phys. **85**, 5901 (1999).
- [258] R. J. Astalos and R. E. Camley, "*Magnetic Permeability for Exchange-spring Magnets: Application to Fe/Sm-Co*," Phys. Rev. B **58**, 8646 (1998).
- [259] M. J. Pechan, N. Teng, J. Stewart, J. Z. Hilt, E. E. Fullerton, J. S. Jiang, C. H. Sowers, and S. D. Bader, "*Anisotropy determination in Epitaxial Sm-Co/Fe Exchange Springs*," J. Appl. Phys. **87**, 6686 (2000).
- [260] F. Yıldız, O. Yalçın, M. Özdemir, B. Aktaş, Y. Köseoğlu, and J. S. Jiang, "*Magnetic properties of Sm-Co/Fe exchange spring magnets*," J. Magn. Magn. Mater. **272**, E1941 (2004).
- [261] D. S. Schmool, "*Spin Dynamic in Exchange-spring Nanosystems: A Short Review*," Nanosc. Nanotech. Lett. **3**, 515 (2011).
- [262] R. Skomski, A. Kashyap, and J. Zhou, "*Atomic and Micromagnetic Aspects of L_{10} Magnetism*" Scr. Mater. **53**, 389 (2005).
- [263] F. Albertini, L. Nasi, F. Casoli, S. Fabbri, P. Luches, G. C. Gazzadi, A. d. Bona, P. Vavassori, S. Valeri, and S. F. Contri, "*Local Modifications of Magnetism and Structure in FePt (001) Epitaxial Thin Films by Focused Ion Beam: Two-Dimensional Perpendicular Patterns*," J. Appl. Phys. **104**, 053907 (2008).
- [264] J. Kim, H. Song, J. Jeong, K. Lee, J. Sohn, T. Shima, and S. Shin, "*Ultrafast Magnetization Relaxation of L_{10} -ordered $Fe_{50}Pt_{50}$ Alloy Thin Film*," Appl. Phys. Lett. **98**, 092509 (2011).
- [265] S. Mizukami, S. Iihama, N. Inami, T. Hiratsuka, G. Kim, H. Naganuma, M. Oogane, and Y. Ando, "*Fast Magnetization Precession Observed in L_{10} -FePt Epitaxial Thin Film*," Appl. Phys. Lett. **98**, 052501 (2011).
- [266] H. J. Richter, O. Hellwig, S. Florez, C. Brombacher, and M. Albrecht, "*Anisotropy Measurements of FePt Thin Films*," J. Appl. Phys. **109**, 07B713 (2011).
- [267] D. S. Schmool, A. Apolinário, F. Casoli, and F. Albertini, "*Ferromagnetic Resonance Study of Fe/FePt Coupled Films With Perpendicular Anisotropy*," IEEE Trans. Magn. **44**, 3087 (2008).

Bibliography

- [268] P. M. S. Monteiro and D. S. Schmool, "*Magnetization Dynamics in Exchange-coupled Spring Systems with Perpendicular Anisotropy*," Phys. Rev. B **81**, 214439 (2010).
- [269] C. Mathieu, J. Jorzick, A. Frank, S. O. Demokritov, A. N. Slavin, B. Hillebrands, B. Bartenlian, C. Chappert, D. Decanini, F. Rousseaux, and E. Cambril, "*Lateral Quantization of Spin Waves in Micron Size Magnetic Wires*," Phys. Rev. Lett. **81**, 3968 (1998).
- [270] E. V. Tartakovskaya, "*Quantized Spin-wave Modes in Long Cylindrical Ferromagnetic Nanowires in a Transverse External Magnetic Field*," Phys. Rev. B **71**, 180404 (2005).
- [271] G. Goglio, S. Pignard, A. Radulescu, L. Piraux, I. Huynen, D. Vanhoenacker, and A. Vander Vorst, "*Microwave Properties of Metallic Nanowires*," Appl. Phys. Lett. **75**, 1769 (1999).
- [272] A. Encinas-Oropesa, M. Demand, L. Piraux, I. Huynen, and U. Ebels, "*Dipolar Interactions in Arrays of Nickel Nanowires Studied by Ferromagnetic Resonance*," Phys. Rev. B **63**, 104415 (2001).
- [273] A. Encinas-Oropesa, M. Demand, L. Piraux, U. Ebels, and I. Huynen, "*Effect of Dipolar Interactions on the Ferromagnetic Resonance Properties in Arrays of Magnetic Nanowires*," J. Appl. Phys. **89**, 6704 (2001).
- [274] M. Demand, A. Encinas-Oropesa, S. Kenane, U. Ebels, I. Huynen, and L. Piraux, "*Ferromagnetic Resonance Studies of Nickel and Permalloy Nanowire Arrays*," Journal of Magnetism and Magnetic Materials **249**, 228 (2002).
- [275] R. Arias and D. L. Mills, "*Theory of Spin Excitations and the Microwave Response of Cylindrical Ferromagnetic Nanowires*," Phys. Rev. B **63**, 134439 (2001).
- [276] R. Arias and D. L. Mills, "*Theory of Collective Spin Waves and Microwave Response of Ferromagnetic Nanowire Arrays*," Phys. Rev. B **67**, 094423 (2003).
- [277] R. Arias and D. L. Mills, "*Magnetostatic Modes in Ferromagnetic Nanowires*," Phys. Rev. B **70**, 094414 (2004).
- [278] R. Arias and D. L. Mills, "*Magnetostatic Modes in Ferromagnetic Nanowires II. A Method for Cross Sections with Very Large Aspect Ratio*," Phys. Rev. B **72**, 104418 (2005).
- [279] R. Arias, "*Influence of Roughness on the Magnetostatic Modes of Ferromagnetic Nano-wires*," Physica B: Cond. Matter **384**, 25 (2006).
- [280] E. V. Tartakovskaya, "*Inelastic Neutron Scattering Cross Section in Ferromagnetic Nanowires*," Physica B: Cond. Matter **385**, 468 (2006).
- [281] T. M. Nguyen, M. G. Cottam, H. Y. Liu, Z. K. Wang, S. C. Ng, M. H. Kuok, D. J. Lockwood, K. Nielsch, and U. Gösele, "*Spin Waves in Permalloy Nanowires: The Importance of Easy-plane Anisotropy*," Phys. Rev. B **73**, 140402 (2006).

Bibliography

- [282] A. A. Stashkevich, Y. Roussigné, P. Djemia, S. M. Chérif, P. R. Evans, A. P. Murphy, W. R. Hendren, R. Atkinson, R. J. Pollard, A. V. Zayats, G. Chaboussant, and F. Ott, "*Spin-wave Modes in Ni Nanorod Arrays Studied by Brillouin Light Scattering*," *Phys. Rev. B* **80**, 144406 (2009).
- [283] J. De La Torre Medina, M. Darques, L. Piraux, and A. Encinas, "*Application of the Anisotropy Field Distribution Method to Arrays of Magnetic Nanowires*," *J. Appl. Phys.* **105**, 023909 (2009).
- [284] A. Sklyuyev, M. Ciureanu, C. Akyel, P. Ciureanu, and A. Yelon, "*Microwave Studies of Magnetic Anisotropy of Co Nanowire Arrays*," *J. Appl. Phys.* **105**, 023914 (2009).
- [285] V. Boucher, C. Lacroix, L.-P. Carignan, A. Yelon, and D. Ménard, "*Resonance Modes in Arrays of Interacting Ferromagnetic Nanowires Subjected to a Transverse Static Magnetic Field*," *Appl. Phys. Lett.* **98**, 112502 (2011).
- [286] V. O. Dolocan, "*Spatial Distribution of Spin-wave Modes in Cylindrical Nanowires of Finite Aspect Ratio*," *J. Phys.: Cond. Matter* **23**, 446005 (2011).
- [287] V. O. Dolocan, "*Spin-torque Effect on Spin Wave Modes in Magnetic Nanowires*," *Appl. Phys. Lett.* **101**, 072409 (2012).
- [288] M. Hayashi, L. Thomas, R. Moriya, C. Rettner, and S. S. P. Parkin, "*Current-controlled Magnetic Domain-wall Nanowire Shift Register*," *Science* **320**, 209 (2008).
- [289] S. S. P. Parkin, M. Hayashi, and L. Thomas, "*Magnetic Domain-wall Racetrack Memory*," *Science* **320**, 190 (2008).
- [290] Y. Huai, F. Albert, P. Nguyen, M. Pakala, and T. Valet, "*Observation of Spin-transfer Switching in Deep Submicron-sized and Low-resistance Magnetic Tunnel Junctions*," *Appl. Phys. Lett.* **84**, 3118 (2004).
- [291] S. Mangin, D. Ravelosona, J. A. Katine, M. J. Carey, B. D. Terris, and E. E. Fullerton, "*Current-induced Magnetization Reversal in Nanopillars with Perpendicular Anisotropy*," *Nat. Mater.* **5**, 210 (2006).
- [292] V. V. Kruglyak, S. O. Demokritov, and D. Grundler, "*Magnonics*" *J. Phys. D: Appl. Phys.* **43**, 264001 (2010).
- [293] F. J. A. den Broeder, W. Hoving, and P. J. H. Bloemen, "*Magnetic Anisotropy of Multilayers*," *J. Magn. Magn. Mater.* **93**, 562 (1991).
- [294] O. Hellwig, T. Hauet, T. Thomson, E. Dobisz, J. D. Risner-Jamgaard, D. Yaney, B. D. Terris, and E. E. Fullerton, "*Coercivity Tuning in Co/Pd Multilayer Based Bit Patterned Media*," *Appl. Phys. Lett.* **95**, 232505 (2009).

Bibliography

- [295] V. Kambersky, "On Ferromagnetic Resonance Damping in Metals," Czech J. Phys. **Sect. B 26**, 1366 (1976).
- [296] F. K. Mirzade, "Finite-amplitude Strain Waves in Laser-excited Plates," J. Phys.: Cond. Matter **20**, 275202 (2008).
- [297] C.-H. Hsia, T.-Y. Chen, and D. H. Son, "Size-dependent Ultrafast Magnetization Dynamics in Iron Oxide (Fe_3O_4) Nanocrystals," Nano Lett. **8**, 571 (2008).
- [298] C.-H. Hsia, T.-Y. Chen, and D. H. Son, "Time-resolved Study of Surface Spin Effect on Spin-lattice Relaxation in Fe_3O_4 Nanocrystals," J. Am. Chem. Soc. **131**, 9146 (2009).
- [299] A. Laraoui, V. Halté, M. Vomir, J. Vénuat, M. Albrecht, E. Beaurepaire, and J. Y. Bigot, "Ultrafast Spin Dynamics of an Individual $CoPt_3$ Ferromagnetic Dot," Eur. Phys. J. D **43**, 251 (2007).
- [300] J. Y. Bigot, M. Vomir, L. H. F. Andrade, and E. Beaurepaire, "Ultrafast Magnetization Dynamics in Ferromagnetic Cobalt: The Role of the Anisotropy," Chem. Phys. **318**, 137 (2005).
- [301] W. Hübner and K. H. Bennemann, "Simple Theory for Spin-lattice Relaxation in Metallic Rare-earth Ferromagnets," Phys. Rev. B **53**, 3422 (1996).
- [302] L. D. Landau and E. M. Lifshitz, "On the Theory of the Dispersion of Magnetic Permeability in Ferromagnetic Bodies," Phys. Z. Sowjetunion **8**, 153 (1935).
- [303] F. J. A. den Broeder, H. C. Donkersloot, H. J. G. Draaisma, and W. J. M. de Jonge, "Magnetic Properties and Structure of Pd/Co and Pd/Fe Multilayers," J. Appl. Phys. **61**, 4317 (1987).
- [304] R. Arias and D. L. Mills, "Extrinsic Contributions to the Ferromagnetic Resonance Response of Ultrathin Films," Phys. Rev. B **60**, 7395 (1999).
- [305] P. Landeros, R. E. Arias, and D. L. Mills, "Two Magnon Scattering in Ultrathin Ferromagnets: The Case where the Magnetization is out of Plane," Phys. Rev. B **77**, 214405 (2008).
- [306] G. Malinowski, K. C. Kuiper, R. Lavrijsen, H. J. M. Swagten, and B. Koopmans, "Magnetization Dynamics and Gilbert Damping in Ultrathin $Co_{48}Fe_{32}B_{20}$ Films with Out-of-plane Anisotropy," Appl. Phys. Lett. **94**, 102501 (2009).
- [307] O. Hellwig, A. Berger, T. Thomson, E. Dobisz, Z. Z. Bandic, H. Yang, D. S. Kercher, and E. E. Fullerton, "Separating dipolar broadening from the intrinsic switching field distribution in perpendicular patterned media," Appl. Phys. Lett. **90**, 162516 (2007).
- [308] M. Krawczyk and H. Puzkarski, "Plane-wave Theory of Three-dimensional Magnonic Crystals," Phys. Rev. B **77**, 054437 (2008).

Bibliography

- [309] R. S. Iskhakov, N. A. Shepeta, S. V. Stolyar, L. A. Chekanova, and V. Y. Yakovchuk, "*Spin-wave Resonance in Co/Pd Magnetic Multilayers and NiFe/Cu/NiFe Three-layered films*," JETP Lett. **83**, 28 (2006).
- [310] R. L. Stamps and R. E. Camley, "*Spin Waves in Antiferromagnetic Thin Films and Multilayers: Surface and Interface Exchange and Entire-cell Effective-medium Theory*," Phys. Rev. B **54**, 15200 (1996).
- [311] J. T. Haraldsen and R. S. Fishman, "*Spin-wave Dynamics of Magnetic Heterostructures: Application to Dy/Y Multilayers*," J. Phys.: Cond. Matter **22**, 186002 (2010).
- [312] M. Krawczyk, S. Mamica, J. W. Kłos, J. Romero-Vivas, M. Mruczkiewicz, and A. Barman, "*Calculation of spin wave spectra in magnetic nanograins and patterned multilayers with perpendicular anisotropy*," J. Appl. Phys. **109**, 113903 (2011).
- [313] Z. Liu, R. Brandt, O. Hellwig, S. Florez, T. Thomson, B. Terris, and H. Schmidt, "*Thickness Dependent Magnetization Dynamics of Perpendicular Anisotropy Co/Pd Multilayer Films*," J. Magn. Magn. Mater. **323**, 1623 (2011).
- [314] O. Hellwig, T. Hauet, T. Thomson, E. Dobisz, J. D. Risner-Jamtgaard, D. Yaney, B. D. Terris, and E. E. Fullerton, "*Coercivity Tuning in Co/Pd Multilayer Based Bit Patterned Media*," Appl. Phys. Lett. **95**, 232505 (2009).
- [315] S. Maat, K. Takano, S. S. P. Parkin, and E. E. Fullerton, "*Perpendicular Exchange Bias of Co/Pt Multilayers*," Phys. Rev. Lett. **87**, 087202 (2001).
- [316] A. Kashyap, R. Skomski, A. K. Solanki, Y. F. Xu, and D. J. Sellmyer, "*Magnetism of $L1_0$ Compounds with the Composition MT ($M=Rh, Pd, Pt, Ir$ and $T=Mn, Fe, Co, Ni$)*," J. Appl. Phys. **95**, 7480 (2004).
- [317] J. Hamrle, J. Pištora, B. Hillebrands, B. Lenk, and M. Münzenberg, "*Analytical Expression of the Magneto-optical Kerr Effect and Brillouin Light Scattering Intensity Arising from Dynamic Magnetization*," J. Phys. D: Appl. Phys. **43**, 325004 (2010).
- [318] Available: <http://refractiveindex.info/>
- [319] The average anisotropy field, H_{ani} is calculated as $H_{ani} = (2K_{u,av}/M_S)$, where $K_{u,av} = (SK_{u,i}/St_i)$ and $M_S = (Sm_i m_B / St_i)$. Summations are performed over atomic planes (Co and Pt) in the unit cell; t_i is the thickness of the i^{th} layer equal 0.2 nm and 0.233 nm for Co and Pt layer, respectively. $S = 0.068 \text{ nm}^2$ is the surface area in the plane of the unit cell.
- [320] D. Tripathy and A. O. Adeyeye, "*Perpendicular Anisotropy and Out-of-plane Exchange Bias in Nanoscale Antidot Arrays*," New J. Phys. **13**, 023035 (2011).

Bibliography

- [321] V. Neu, C. Schulze, M. Faustini, J. Lee, D. Makarov, D. Suess, S.-K. Kim, D. Grosso, L. Schultz, and M. Albrecht, "*Probing the Energy Barriers and Magnetization Reversal Processes of Nanoperforated Membrane based Percolated Media*," *Nanotech.* **24**, 145702 (2013).
- [322] B. Lenk, H. Ulrichs, F. Garbs, and M. Münzenberg, "*The building blocks of magnonics*," *Phys. Rep.* **507**, 107 (2011).
- [323] M. Kostylev, G. Gubbiotti, G. Carlotti, G. Socino, S. Tacchi, C. Wang, N. Singh, A. O. Adeyeye, and R. L. Stamps, "*Propagating Volume and Localized Spin Wave Modes on a Lattice of Circular Magnetic Antidots*," *J. Appl. Phys.* **103**, 07C507 (2008).
- [324] H. Ulrichs, B. Lenk, and M. Münzenberg, "*Magnonic Spin-wave Modes in CoFeB Antidot Lattices*," *Appl. Phys. Lett.* **97**, 092506 (2010).
- [325] S. Neusser, B. Botters, and D. Grundler, "*Localization, Confinement, and Field-controlled Propagation of Spin Waves in Ni₈₀Fe₂₀ Antidot Lattices*," *Phys. Rev. B* **78**, 054406 (2008).
- [326] S. Neusser, G. Duerr, S. Tacchi, M. Madami, M. L. Sokolovskyy, G. Gubbiotti, M. Krawczyk, and D. Grundler, "*Magnonic Minibands in Antidot Lattices with Large Spin-wave Propagation Velocities*," *Phys. Rev. B* **84**, 094454 (2011).
- [327] R. Zivieri, S. Tacchi, F. Montoncello, L. Giovannini, F. Nizzoli, M. Madami, G. Gubbiotti, G. Carlotti, S. Neusser, G. Duerr, and D. Grundler, "*Bragg Diffraction of Spin Waves from a Two-dimensional Antidot Lattice*," *Phys. Rev. B* **85**, 012403 (2012).
- [328] D. Kumar, J. W. Kłos, M. Krawczyk, and A. Barman, "*Magnonic Band Structure, Complete Bandgap, and Collective Spin Wave Excitation in Nanoscale Two-Dimensional Magnonic Crystals*," *J. Appl. Phys.* **115**, 043917 (2014).
- [329] S. Tacchi, G. Duerr, J. W. Kłos, M. Madami, S. Neusser, G. Gubbiotti, G. Carlotti, M. Krawczyk, and D. Grundler, "*Forbidden Band Gaps in the Spin-wave Spectrum of a Two-Dimensional Bicomponent Magnonic Crystal*," *Phys. Rev. Lett.* **109**, 137202 (2012).
- [330] S. Mamica, M. Krawczyk, M. L. Sokolovskyy, and J. Romero-Vivas, "*Large Magnonic Band Gaps and Spectra Evolution in Three-dimensional Magnonic Crystals Based on Magnetoferritin Nanoparticles*," *Phys. Rev. B* **86**, 144402 (2012).
- [331] J. W. Kłos, D. Kumar, J. Romero-Vivas, H. Fangohr, M. Franchin, M. Krawczyk, and A. Barman, "*Effect of Magnetization Pinning on the Spectrum of Spin Waves in Magnonic Antidot Waveguides*," *Phys. Rev. B* **86**, 184433 (2012).
- [332] J. M. Shaw, S. E. Russek, T. Thomson, M. J. Donahue, B. D. Terris, O. Hellwig, E. Dobisz, and M. L. Schneider, "*Reversal Mechanisms in Perpendicularly Magnetized Nanostructures*," *Phys. Rev. B* **78**, 024414 (2008).

Bibliography

- [333] P. S. Keatley, P. Gangmei, M. Dvornik, R. J. Hicken, J. Grollier, and C. Ulysse, "*Isolating the Dynamic Dipolar Interaction between a Pair of Nanoscale Ferromagnetic Disks*," Phys. Rev. Lett. **110**, 187202 (2013).
- [334] B. Pigeau, C. Hahn, G. de Loubens, V. V. Naletov, O. Klein, K. Mitsuzuka, D. Lacour, M. Hehn, S. Andrieu, and F. Montaigne, "*Measurement of the Dynamical Dipolar Coupling in a Pair of Magnetic Nanodisks Using a Ferromagnetic Resonance Force Microscope*," Phys. Rev. Lett. **109**, 247602 (2012).
- [335] M. P. Kostylev, A. A. Stashkevich, and N. A. Sergeeva, "*Collective Magnetostatic Modes on a One-dimensional Array of Ferromagnetic Stripes*," Phys. Rev. B **69**, 064408 (2004).
- [336] W. H. Meiklejohn and C. P. Bean, "*New Magnetic Anisotropy*," Phys. Rev. **105**, 904 (1957).
- [337] E. E. Fullerton, J. S. Jiang, and S. D. Bader, "*Hard/soft Magnetic Heterostructures: Model Exchange-Spring Magnets*," J. Magn. Magn. Mater. **200**, 392 (1999).
- [338] B. K. Kuanr, Y. V. Khivintsev, I. Harward, R. E. Camley, Z. J. Celinski, M. Bedenbecker, and H. H. Gatzten, "*Increasing Operational Frequency in Microwave Devices by Using [SmCo/NiFe] Multilayered Structures*," Magnetics, IEEE Transactions on **43**, 2648 (2007).
- [339] E. Goto, N. Hayashi, T. Miyashita, and K. Nakagawa, "*Magnetization and Switching Characteristics of Composite Thin Magnetic Films*," J. magn. Magn. Mater. **36**, 2951 (1965).
- [340] Y. Choi, J. S. Jiang, J. E. Pearson, S. D. Bader, J. J. Kavich, J. W. Freeland, and J. P. Liu, "*Controlled interface profile in Sm-Co/Fe exchange-spring magnets*," Appl. Phys. Lett. **91**, 072509 (2007).
- [341] B. Laenens, N. Planckaert, J. Demeter, M. Trekels, C. L'abbé, C. Strohm, R. Rüffer, K. Temst, A. Vantomme, and J. Meersschant, "*Spin Structure in Perpendicularly Magnetized Fe-FePt Bilayers*," Phys. Rev. B **82**, 104421 (2010).
- [342] V. M. Uzdin, A. Vega, A. Khrenov, W. Keune, V. E. Kuncser, J. S. Jiang, and S. D. Bader, "*Noncollinear Fe Spin Structure in (Sm-Co)/Fe Exchange-spring Bilayers: Layer-resolved ⁵⁷Fe Mössbauer Spectroscopy and Electronic Structure Calculations*," Phys. Rev. B **85**, 024409 (2012).
- [343] M. Franchin, G. Bordignon, T. Fischbacher, G. Meier, J. Zimmermann, P. de Groot, and H. Fangohr, "*Spin-polarized Currents in Exchange Spring Systems*," J. Appl. Phys. **103**, 07A504 (2008).
- [344] We have also performed test simulations using the OOMMF software and the results obtained from those simulations agree with the results presented here. We confirmed that another micromagnetic software "Nmag" does not have interlayer exchange coupling.

Bibliography

- [345] K. Kang, L. H. Lewis, J. S. Jiang, and S. D. Bader, "*Recoil Hysteresis of Sm-Co/Fe Exchange-spring Bilayers*," J. Appl. Phys. **98**, 113906 (2005).
- [346] E. A. Anderson, S. Isaacman, D. S. Peabody, E. Y. Wang, J. W. Canary, and K. Kirshenbaum, "*Viral Nanoparticles Donning a Paramagnetic Coat: Conjugation of MRI Contrast Agents to the MS2 Capsid*," Nano Lett. **6**, 1160 (2006).
- [347] D. A. Allwood, G. Xiong, C. C. Faulkner, D. Atkinson, D. Petit, and R. P. Cowburn, "*Magnetic Domain-Wall Logic*," Science **309**, 1688 (2005).
- [348] H. Zeng, M. Zheng, R. Skomski, D. J. Sellmyer, Y. Liu, L. Menon, and S. Bandyopadhyay, "*Magnetic Properties of Self-assembled Co Nanowires of Varying Length and Diameter*," J. Appl. Phys. **87**, 4718 (2000).
- [349] T. Koyama, D. Chiba, K. Ueda, K. Kondou, H. Tanigawa, S. Fukami, T. Suzuki, N. Ohshima, N. Ishiwata, Y. Nakatani, K. Kobayashi, and T. Ono, "*Observation of the Intrinsic Pinning of a Magnetic Domain Wall in a Ferromagnetic Nanowire*," Nat. Mater. **10**, 194 (2011).
- [350] G. Meier, M. Bolte, R. Eiselt, B. Krüger, D.-H. Kim, and P. Fischer, "*Direct Imaging of Stochastic Domain-Wall Motion Driven by Nanosecond Current Pulses*," Phys. Rev. Lett. **98**, 187202 (2007).
- [351] Z. K. Wang, H. S. Lim, V. L. Zhang, J. L. Goh, S. C. Ng, M. H. Kuok, H. L. Su, and S. L. Tang, "*Collective Spin Waves in High-Density Two-Dimensional Arrays of FeCo Nanowires*," Nano Lett. **6**, 1083 (2006).
- [352] V. R. Caffarena, A. P. Guimarães, W. S. D. Folly, E. M. Silva, and J. L. Capitaneo, "*Magnetic Behavior of Electrodeposited Cobalt Nanowires Using Different Electrolytic Bath Acidities*," Mater. Chem. Phys. **107**, 297 (2008).
- [353] Z. Liu, P.-C. Chang, C.-C. Chang, E. Galaktionov, G. Bergmann, and J. G. Lu, "*Shape Anisotropy and Magnetization Modulation in Hexagonal Cobalt Nanowires*," Adv. Func. Mater. **18**, 1573 (2008).
- [354] J. Mallet, K. Yu-Zhang, C.-L. Chien, T. S. Eagleton, and P. C. Searson, "*Fabrication and Magnetic Properties of fcc $\text{Co}_x\text{Pt}_{1-x}$ Nanowires*," Appl. Phys. Lett. **84**, 3900 (2004).
- [355] J. Rivas, A. Kazadi Mukenga Bantu, G. Zaragoza, M. C. Blanco, and M. A. López-Quintela, "*Preparation and Magnetic Behavior of Arrays of Electrodeposited Co Nanowires*," J. Magn. Mater. **249**, 220 (2002).
- [356] S. Shamaïla, D. P. Liu, R. Sharif, J. Y. Chen, H. R. Liu, and X. F. Han, "*Electrochemical Fabrication and Magnetization Properties of CoCrPt Nanowires and Nanotubes*," Appl. Phys. Lett. **94**, 203101 (2009).

Bibliography

- [357] S. Shamaila, R. Sharif, S. Riaz, M. Khaleeq-ur-Rahman, and X. F. Han, "*Fabrication and Magnetic Characterization of Co_xPt_{1-x} Nanowire Arrays*," Appl. Phys. A **92**, 687 (2008).
- [358] S. Sharma, A. Barman, M. Sharma, L. R. Shelford, V. V. Kruglyak, and R. J. Hicken, "*Structural and Magnetic Properties of Electrodeposited Cobalt Nanowire Arrays*," Solid State Commun. **149**, 1650 (2009).
- [359] A. Aharoni, "*Introduction to the Theory of Ferromagnetism*," Oxford University Press, New York (2000).
- [360] M. Demand, A. Encinas-Oropesa, S. Kenane, U. Ebels, I. Huynen, and L. Piraux, "*Ferromagnetic Resonance Studies of Nickel and Permalloy Nanowire Arrays*," J. Magn. Magn. Mater. **249**, 228 (2002).
- [361] M. V. Kamalakar, A. K. Raychaudhuri, X. Wei, J. Teng, and P. D. Prewett, "*Temperature Dependent Electrical Resistivity of a Single Strand of Ferromagnetic Single Crystalline Nanowire*," Appl. Phys. Lett. **95**, 013112 (2009).
- [362] M. V. Kamalakar and A. K. Raychaudhuri, "*Low Temperature Electrical Transport in Ferromagnetic Ni Nanowires*," Phys. Rev. B **79**, 205417 (2009).
- [363] M. Sato and Y. Ishii, "*Simple and Approximate Expressions of Demagnetizing Factors of Uniformly Magnetized Rectangular Rod and Cylinder*," J. Appl. Phys. **66**, 983 (1989).